





# **DNA-based biomimetics as modular tools to study reconstituted and cellular systems**

**Inaugural-Dissertation**

zur

Erlangung des Doktorgrades  
der Mathematisch-Naturwissenschaftlichen Fakultät  
der Universität zu Köln

vorgelegt von

Jessica Sophie Lorenz  
aus Karl-Marx-Stadt

Köln (2018)

Berichtersteller:

Prof. Dr. Ines Neundorf  
Prof. Dr. Karsten Niefind  
Dr. David Michael Smith

Tag der mündlichen Prüfung:

12. Januar 2018





für meine Eltern  
Marion & Joachim



You have to follow your nose,  
and if you think what you are doing is interesting and exciting,  
you have to have the courage to do it.

(Ned Seeman)



### Abstract

Deoxyribonucleic acid (DNA) is the fundamental basis of virtually all living organisms. The central dogma in molecular biology refers to DNA as the carrier of the genetic information that is first being transcribed into ribonucleic acids (RNA) and further translated into proteins. This dogma has been refined, as nucleic acids were also discovered to act as structural and regulatory components within cells. In recent years, the new research field DNA nanotechnology emerged, in which DNA is used as a molecular building block, whose predictable base pairing allows the fabrication of self-assembled two- and three dimensional (2D and 3D) DNA nanostructures, which moreover can be spatially functionalized with a broad range of biomolecules on the nanometer scale. This unique feature as well as its versatility, biodegradability and low toxicity has led to great interest for various applications in a wide range of areas. Moreover, the design of DNA-based biomimetic systems has emerged as a valuable tool for systematically exploring the complexity of cells, which is also at the center of the work shown here.

In the course of this work, short functional peptides were covalently attached to wire-frame DNA nanostructures as well as simple three-arm branched DNA junctions and double-stranded (ds) DNA. In a first approach, DNA tetrahedra and DNA trimers were covalently coupled to cell-penetrating peptides (CPP), which mediated a more efficient cellular uptake. Thus, it can be assumed that CPP retain their function, even when they are covalently attached to DNA, which was one of the main questions within this thesis.

The second approach, comprising the main part of this dissertation, focused on the generation and *in vitro* characterization of the impact of synthetic actin crosslinkers on both reconstituted actin networks and cells. The precise regulation of structural and, thus, mechanical properties of living cells is essential for functionalities such as motility, stability and shape. These properties are mainly attributed to the cytoskeleton, whose main constituents are semiflexible actin filaments as well as numerous actin-binding proteins (ABP), which organize the filaments into a variety of higher order structures, e.g. networks and bundles. ABP that form transient, physical crosslinks between filaments, due to their empirical nature and complexity, do not allow straightforward, systemic studies in which different key parameters can be altered independently. To overcome this limitation, naturally occurring actin crosslinkers such as  $\alpha$ -actinin and fascin were mimicked by synthetically fabricated crosslinkers based on DNA and peptides. These were generated through the covalent attachment of actin-binding peptides on both sides of a double-stranded DNA spacer and thus solely differed in their affinity towards filamentous actin. Bulk shear rheology experiments on reconstituted actin networks

## Abstract

---

revealed that both, the weakly-binding LifeAct<sup>®</sup> crosslinker (wLX) and the strongly-binding Phalloidin crosslinker (sPX) generated the same characteristic mechanical fingerprint as the natural crosslinkers  $\alpha$ -actinin and fascin, respectively. Moreover, they showed a concentration-dependent impact on different structural morphologies of actin networks as well as an inhibition of actin polymerization.

Interestingly, these synthetic crosslinkers also interfered with intracellular systems, as crosslinker-treated cells showed several altered behaviors. Actin remodeling dynamics, as well as migration and invasion were reduced, whereas proliferation and apoptosis rates were not affected. Additionally, synthetic crosslinkers possibly impact the process of epithelial-mesenchymal transition (EMT), in which cells lose their epithelial properties and become transformed into cells with enhanced motile and invasive functions. This process comprises complex signal transduction pathways, which also depend upon the polymerization and depolymerization status of actin. A typical signature of EMT, the formation of actin criss-cross stress fibers, was suppressed in wLX-treated, EMT-induced cells, which could also be correlated to results of advanced cell mechanical measurements. However, the exact mechanism of how synthetic crosslinkers affect cellular functions still remains unclear. Further investigations are required to reveal the underlying cause, and furthermore whether they suppress EMT, in which case they could become a potential candidate for the treatment of, for instance, ocular fibrosis.

### Kurzzusammenfassung

Die Desoxyribonukleinsäure (DNA) stellt die fundamentale Grundlage praktisch aller lebenden Organismen dar. Das zentrale Dogma der Molekularbiologie bezieht sich auf DNA als Träger der genetischen Information, die zunächst in Ribonukleinsäuren (RNA) transkribiert und anschließend in Proteine translatiert wird. Da Nukleinsäuren ebenfalls als strukturelle und regulatorische Komponenten innerhalb von Zellen wirken, wurde dieses Dogma überdacht. So entstand in den letzten Jahren das neue Forschungsfeld „DNA-Nanotechnologie“, welches DNA als molekularen Baustein nutzt. Die vorhersehbare Basenpaarung ermöglicht die Herstellung selbstorganisierter zwei- und dreidimensionaler (2D und 3D) Nanostrukturen, welche zusätzlich mit einer Vielzahl verschiedener Biomoleküle im Nanometer-Maßstab funktionalisiert werden können. Auf Grund dieser einzigartigen Eigenschaft sowie der Vielseitigkeit, geringen Toxizität und biologischen Abbaubarkeit, fanden DNA-Strukturen verschiedene Anwendungen in einer Vielzahl von Bereichen. Darüber hinaus hat sich das Design DNA-basierter, biomimetischer Systeme als ein wertvolles Instrument zur systematischen Erforschung der Komplexität von Zellen erwiesen, welches ebenfalls im Mittelpunkt der hier gezeigten Arbeit steht.

Im Rahmen dieser Arbeit wurden kurze funktionelle Peptide kovalent an DNA-Nanostrukturen gebunden. In einem ersten Ansatz wurden DNA-Tetraeder und DNA-Trimere kovalent an zellpenetrierende Peptide (CPP) gekoppelt, welche eine effizientere zelluläre Aufnahme vermittelten.

Der zweite Ansatz, welcher den Großteil dieser Dissertation umfasst, konzentrierte sich auf die Generierung und *in vitro*-Charakterisierung des Einflusses synthetischer Aktin-*Crosslinker* sowohl auf rekonstituierte Aktinnetzwerke als auch auf Zellen. Die genaue Regulation struktureller und dadurch mechanischer Eigenschaften lebender Zellen ist essentiell für Funktionalitäten wie Motilität, Stabilität und Form. Diese Eigenschaften werden hauptsächlich dem Zytoskelett zugeschrieben, dessen Hauptbestandteile semiflexible Aktinfilamente sowie zahlreiche Aktin-bindende Proteine (ABP) sind, welche die Filamente in eine Vielzahl von Strukturen höherer Ordnung, wie z.B. Netzwerke oder Bündel, organisieren. ABP, die transiente, physikalische Vernetzungen zwischen Filamenten bilden, erlauben aufgrund ihrer empirischen Natur und Komplexität keine direkten systemischen Studien, in denen verschiedene Schlüsselparameter unabhängig voneinander verändert werden können. Um diese Einschränkung zu überwinden, wurden natürlich vorkommende Aktin-*Crosslinker*, wie  $\alpha$ -Actinin und Fascin, durch DNA- und Peptid-basierte, synthetisch hergestellte *Crosslinker* nachgeahmt. Diese wurden durch die kovalente Bindung Aktin-bindender Peptide an beiden

## Kurzzusammenfassung

---

Seiten eines doppelsträngigen DNA-*Spacers* erzeugt und unterschieden sich daher nur in ihrer Affinität gegenüber filamentösem Aktin. Rheologische Untersuchungen rekonstituierter Aktin-Netzwerke zeigten, dass sowohl der schwach bindende LifeAct®-*Crosslinker* (wLX) als auch der stark bindende Phalloidin-*Crosslinker* (sPX) den gleichen charakteristischen mechanischen Fingerabdruck wie die natürlichen *Crosslinker*  $\alpha$ -Actinin bzw. Fascin erzeugen. Darüber hinaus zeigten sie einen konzentrationsabhängigen Einfluss auf Struktur-morphologien von Aktin-Netzwerken sowie eine Hemmung der Aktin-Polymerisation.

Interessanterweise interferierten synthetische *Crosslinker* ebenfalls mit intrazellulären Systemen und es zeigte sich, dass *Crosslinker*-behandelte Zellen einige veränderte Verhaltensweisen aufwiesen. Sowohl die Aktin-Remodellierungsdynamik als auch die Migration und Invasion waren reduziert, während Proliferations- und Apoptoseraten nicht beeinflusst wurden. Darüber hinaus beeinflussen synthetische *Crosslinker* möglicherweise den Prozess des epithelial-mesenchymalen Übergangs (EMT), wobei Zellen ihre epithelialen Eigenschaften verlieren und in Zellen mit mesenchymalen Charakteristika, u.a. einer erhöhten Invasivität, transformiert werden. Dieser Prozess umfasst komplexe Signaltransduktionswege, die von der Polymerisations- und Depolymerisationsdynamik von Aktin abhängen. EMT-induzierte Zellen, welche vorab mit wLX behandelt wurden, unterdrückten die Bildung charakteristischer Stressfasern, welche ein typisches Merkmal von EMT darstellen. Dies korrelierte zusätzlich mit Ergebnissen durchgeführter zellmechanischer Untersuchungen. Mit welchem Mechanismus die synthetischen *Crosslinker* zelluläre Funktionen beeinflussen, bleibt jedoch unklar. Um die zugrundeliegende Ursachen aufzudecken, sind fortführende Untersuchungen erforderlich. Dies umfasst ebenfalls eine potentielle Inhibierung von EMT, in welchem Fall synthetische *Crosslinker* zukünftig möglicherweise für die Behandlung von Fibrosen, z.B. im Auge, eingesetzt werden könnten.

## Table of contents

<i>List of abbreviations</i> _____	VII
<i>List of figures</i> _____	XI
<i>List of tables</i> _____	XIII
<b>1 Introduction</b> _____	<b>1</b>
<b>2 Theoretical Background</b> _____	<b>5</b>
<b>2.1 DNA tetrahedron</b> _____	<b>5</b>
<b>2.2 Functionalization of DNA and corresponding conjugation approaches</b> _____	<b>6</b>
2.2.1 Terminal deoxynucleotide transferase (TdT) reaction _____	6
2.2.2 NHS ester chemistry _____	7
2.2.3 Maleimide chemistry _____	8
2.2.4 Strain-promoted alkyne-azide cycloaddition (SPAAC) _____	8
<b>2.3 Cell-penetrating peptides (CPP)</b> _____	<b>9</b>
<b>2.4 The actin cytoskeleton</b> _____	<b>13</b>
<b>2.5 Naturally occurring actin crosslinkers</b> _____	<b>18</b>
2.5.1 Alpha-actinin - the “weak” binder _____	18
2.5.2 Fascin - the “strong” binder _____	20
<b>2.6 Synthetic actin crosslinkers</b> _____	<b>20</b>
<b>2.7 Actin-binding peptides</b> _____	<b>22</b>
2.7.1 LifeAct® _____	22
2.7.2 Phalloidin _____	22
<b>2.8 Reconstituted actin networks (<i>in vitro</i>)</b> _____	<b>23</b>
2.8.1 Shear rheology of reconstituted actin networks _____	23
2.8.2 Structure and mechanics of reconstituted actin networks _____	26
<b>2.9 Epithelial-mesenchymal transition (EMT)</b> _____	<b>29</b>
<b>3 Objective</b> _____	<b>35</b>

## Table of contents

---

<b>4</b>	<b>Material and Methods</b>	<b>37</b>
4.1	Chemicals	37
4.2	Enzymes, standards and kits	38
4.3	Buffers and solutions	39
4.4	Organisms	41
4.4.1	Bacteria	41
4.4.2	Human cell lines	41
4.5	Culture media	42
4.6	Media additives	43
4.7	Plasmids	43
4.8	DNA oligonucleotides	43
4.9	Peptides	45
4.10	Proteins	46
4.11	Equipment and expendables	46
4.12	Software	48
4.13	Isolation of plasmid DNA from <i>E. coli</i> cells	49
4.14	Determination of DNA concentration	49
4.15	Electrophoretic separation of DNA	50
4.15.1	Agarose gel electrophoresis	50
4.15.2	Native Polyacrylamide gel electrophoresis (PAGE)	50
4.16	Ethanol precipitation	50
4.17	Spin filtration	51
4.18	Cloning	51
4.18.1	Restriction digest of Plasmid DNA	51
4.18.2	Hybridization of cloning insert	51
4.18.3	Ligation	52
4.19	Transformation	52
4.19.1	Preparation of competent <i>E. coli</i> cells	52
4.19.2	Transformation of <i>E. coli</i>	52
4.20	Amplification of DNA fragments through polymerase chain reaction	53
4.21	DNA Sequence analysis	54

## Table of contents

---

<b>4.22</b>	<b>Cultivation and storage of <i>E. coli</i> cells</b>	<b>54</b>
<b>4.23</b>	<b>Folding of DNA structures</b>	<b>54</b>
4.23.1	Folding of DNA tetrahedra	54
4.23.2	Folding of DNA trimers	55
<b>4.24</b>	<b>Size exclusion chromatography (SEC)</b>	<b>56</b>
<b>4.25</b>	<b>Heterobifunctional linkers</b>	<b>56</b>
<b>4.26</b>	<b>Functionalization of DNA tetrahedra with CPP</b>	<b>57</b>
4.26.1	DNA tetrahedra functionalized with CPP chains	57
4.26.2	DNA tetrahedra functionalized with single CPP molecules	61
<b>4.27</b>	<b>Functionalization of DNA trimers with CPP</b>	<b>63</b>
<b>4.28</b>	<b>Engineering synthetic actin crosslinkers</b>	<b>64</b>
<b>4.29</b>	<b>Stability of DNA structures</b>	<b>66</b>
<b>4.30</b>	<b>Atomic force microscopy (AFM)</b>	<b>67</b>
4.30.1	AFM imaging of DNA tetrahedra in fluids	68
4.30.2	AFM imaging of Eight-helix tubes (8HT) in air	68
<b>4.31</b>	<b>Actin preparation</b>	<b>69</b>
<b>4.32</b>	<b>Bulk shear rheology</b>	<b>69</b>
<b>4.33</b>	<b>Static light scattering (SLS)</b>	<b>70</b>
<b>4.34</b>	<b>Spinning disc confocal microscopy</b>	<b>70</b>
<b>4.35</b>	<b>Macroscopic behavior of actin in an inclined cuvette</b>	<b>71</b>
<b>4.36</b>	<b>Actin polymerization / depolymerization assay (pyrene assay)</b>	<b>71</b>
<b>4.37</b>	<b>Basic cell culture techniques</b>	<b>72</b>
4.37.1	Changing culture medium	72
4.37.2	Passaging cells	72
4.37.3	Freezing, thawing and quality control of human cell lines	73
4.37.4	Determination of cell count and viability	73
4.37.5	Fixation of cells	74
4.37.6	Staining of cells	74
4.37.6.1	Staining of living cells	74
4.37.6.2	Staining of fixed cells	75
4.37.7	Internalization of DNA into cells with Lipofectamine™ 3000	75
4.37.7.1	Lipofectamine™ 3000 concentration-dependent internalization of DNA	75
4.37.7.2	Cytotoxicity of Lipofectamine™ 3000	76
4.37.8	Transient transfection of human cell lines	76

## Table of contents

---

<b>4.38</b>	<b>Localization and stability studies of CPP-conjugated DNA structures</b>	<b>77</b>
<b>4.39</b>	<b>Labeling of intracellular actin structures with Cy3-wLX</b>	<b>78</b>
<b>4.40</b>	<b>Cell-based assays</b>	<b>78</b>
4.40.1	Apoptosis assay	78
4.40.2	WST-1 Proliferation assay	79
4.40.3	2D Migration assay	81
4.40.4	3D Migration and invasion assay	82
4.40.5	EMT induction of MCF-10A cells	84
4.40.5.1	Gelatin zymography	85
4.40.5.2	Immunocytochemistry staining for EMT markers	86
4.40.6	Real-time deformability cytometry (RT-DC)	86
4.40.7	Confocal laser scanning microscopy (LSM)	87
<b>5</b>	<b>Results and Discussion</b>	<b>89</b>
<b>5.1</b>	<b>CPP-conjugated DNA nanostructures as carriers for biomolecules</b>	<b>89</b>
5.1.1	Covalent conjugation of sC18 to DNA tetrahedra	89
5.1.2	AFM imaging of CPP-conjugated DNA tetrahedra	91
5.1.3	Separation of DNA tetrahedron monomers from aggregates	93
5.1.4	Uptake and localization of CPP-conjugated DNA structures	94
<b>5.2</b>	<b>Synthetic actin crosslinkers</b>	<b>98</b>
5.2.1	Generation of wLX and sPX	98
5.2.2	Stability of DNA structures	99
<b>5.3</b>	<b>Functional effects of wLX and sPX on reconstituted actin networks</b>	<b>102</b>
5.3.1	Mechanical fingerprints of wLX and sPX	102
5.3.2	Concentration-dependent stiffening of actin networks	105
5.3.3	Different structural morphologies of actin networks	106
5.3.4	Reversibility of crosslinking induced by an enzymatic switch	109
<b>5.4</b>	<b>Interaction of synthetic crosslinkers with actin filaments</b>	<b>112</b>
5.4.1	Polymerization / Depolymerization of actin filaments (pyrene assay)	112
5.4.2	Impact of wLX on actin remodeling dynamics in cells	113
5.4.3	Labeling of actin filaments within cells	114
<b>5.5</b>	<b>Functional effects of wLX on cells</b>	<b>118</b>
5.5.1	Proof of concept	118
5.5.2	Impact of wLX on vital functions of cells	119
5.5.3	Effect of wLX on motile functions and invasiveness of cells	122
5.5.4	Possible impact of synthetic crosslinkers on EMT	124

## Table of contents

---

<b>5.6</b>	<b>Hypotheses of how wLX effect actin-correlated processes</b>	<b>130</b>
5.6.1	Interference with signaling pathways	130
5.6.2	Mechanical influence of wLX on cells	132
5.6.3	Steric interference of actin dynamics caused by wLX	132
<b>6</b>	<b><i>Conclusion and outlook</i></b>	<b>135</b>
<b>7</b>	<b><i>References</i></b>	<b>141</b>
<b>8</b>	<b><i>Supplemental information</i></b>	<b>159</b>
<b>9</b>	<b><i>Publications</i></b>	<b>173</b>
<b>10</b>	<b><i>Danksagung</i></b>	<b>175</b>
<b>11</b>	<b><i>Eidesstattliche Erklärung</i></b>	<b>177</b>
<b>12</b>	<b><i>Curriculum vitae</i></b>	<b>179</b>



### List of abbreviations

In addition to standard abbreviations for metric units (e.g. ml), time units (e.g. min) and chemical symbols as well as formulas (e.g. NaCl), the abbreviations listed below are used throughout this thesis.

2D	Two-dimensional
3D	Three-dimensional
8HT	Eight-helix tubes
A	Adenine
aa	Amino acid
ABP	Actin-binding protein
AC	Alternating contact
AFM	Atomic force microscopy
APS	Ammonium persulfate
ATP	Adenosine triphosphate
BHQ	Black hole quencher
BME	Basement membrane extract
bp	Base pair
C	Cytosine
CAMPs	Cationic antimicrobial peptides
CDS	Cell dissociation solution
Cy3	Cyanine 3
Cy5	Cyanine 5
Da	Dalton
DAPI	4',6-diamidino-2-phenylindole
DBCO	Dibenzocyclooctyne
dd H <sub>2</sub> O	Double distilled water, Millipore water
DMSO	Dimethyl sulfoxide
DNA	Deoxyribonucleic acid
DPBS	Dulbecco's phosphate-buffered saline
ds	Double-stranded
DTT	Dithiothreitol
dUTP	Deoxyuridine triphosphate
ECM	Extracellular matrix
EDTA	Ethylenediaminetetraacetic acid

## List of abbreviations

---

EMT	Epithelial-mesenchymal transition
<i>et al.</i>	And others
EtBr	Ethidium bromide
EtOH	Ethanol
FRAP	Fluorescence recovery after photobleaching
FRET	Förster resonance energy transfer
F-actin	Filamentous actin
G	Guanine
G-actin	Globular actin
GFP	Green fluorescent protein
K <sub>D</sub>	Dissociation constant
LB	Lysogeny broth
LSM	Laser scanning microscopy
MMP	Matrix metalloproteinase
MWCO	Molecular weight cut off
NHS ester	N-hydroxysuccinimidyl ester
nt	Nucleotide
OD	Optical density
PAGE	Polyacrylamide gel electrophoresis
PCR	Polymerase chain reaction
PTO	Phosphorothioate
R <sub>cf</sub>	Relative centrifugal force
Rpm	Revolutions per minute
SDS	Sodium dodecyl sulfate
SEC	Size exclusion chromatography
SPAAC	Strain-promoted alkyne-azide cycloaddition
sPX	Strong phalloidin crosslinker
ss	Single-stranded
Sulfo-SMCC	Sulfo-Succinimidyl 4-[N-maleimidomethyl]cyclohexane-1-carboxylate)
T	Thymine
TCEP	Tris (2-carboxyethyl)-phosphine hydrochloride
TdT	Terminal deoxynucleotidyl transferase
TEMED	N, N, N', N'-tetramethylenediamine
Tet	Tetrahedron
TGF-β	Transforming growth factor β
UV	Ultraviolet

## List of abbreviations

---

v/v	Volume per volume
w/	With
w/o	Without
w/v	Weight per volume
wLX	Weak LifeAct <sup>®</sup> crosslinker
WST-1	Water-soluble tetrazolium salt 1



## List of figures

Figure 1   AFM image of an Eight-helix tube (8HT) network formed at 4 $\mu$ M	3
Figure 2   Temperature-based self-assembly of DNA tetrahedra	5
Figure 3   Mechanism of TdT reaction using aminoallyl-dUTP	7
Figure 4   Amine-reactive NHS esters	8
Figure 5   Sulfhydryl-reactive maleimides	8
Figure 6   Reaction mechanism of SPAAC	9
Figure 7   Endocytotic pathways	12
Figure 8   Schematic illustration of the actin cytoskeleton in a migrating cell	14
Figure 9   Treadmilling/Dendritic nucleation model for actin networks at the leading edge of a cell	16
Figure 10   Mimicking the naturally occurring crosslinker $\alpha$ -actinin with wLX	21
Figure 11   Principles of shear rheology	24
Figure 12   Viscous and elastic properties of a reconstituted actin network	26
Figure 13   Schematic of epithelial-mesenchymal transition (EMT)	30
Figure 14   Simplified schematic of Smad and non-Smad signaling in TGF- $\beta$ -induced EMT	32
Figure 15   MRTF-mediated regulation of SRF-dependent cytoskeletal target genes	33
Figure 16   Chemical structures of utilized heterobifunctional linkers	57
Figure 17   Schematic of engineering DNA tetrahedra carrying CPP chains	58
Figure 18   Reduction of disulfides with TCEP	60
Figure 19   Reaction mechanism of conjugation of DNA and peptide via sulfo-SMCC	60
Figure 20   Schematic of engineering DNA tetrahedra coupled to single CPP molecules	61
Figure 21   Reaction mechanism of conjugation of DNA and peptide via DBCO-NHS ester	62
Figure 22   Functionalization of DNA trimers with single CPP molecules	63
Figure 23   Engineering synthetic actin crosslinkers	64
Figure 24   Coupling of azidopropionic acid sulfo-NHS ester to amine-Phalloidin	65
Figure 25   Formation of Formazan through cleavage of WST-1	80
Figure 26   Schematic of 2D migration assay	81
Figure 27   Schematic of 3D migration and 3D invasion assay	83
Figure 28   Functionalization of DNA tetrahedra with CPP chains	90
Figure 29   Functionalization of DNA tetrahedra with CPP	90
Figure 30   AFM images of CPP-functionalized and unmodified DNA tetrahedra	92
Figure 31   Size exclusion chromatography (SEC) of DNA tetrahedra	93
Figure 32   Localization of CPP-functionalized and unmodified DNA tetrahedra in HeLa cells	96
Figure 33   Localization of CPP-functionalized and unmodified PTO-capped DNA trimers in HeLa cells	97
Figure 34   Analysis of synthetic actin crosslinker production	99
Figure 35   Stability of PTO-modified and unmodified DNA structures in presence of nucleases	100

## List of figures

---

Figure 36	Degradation of unmodified and PTO-capped DNA structures in presence of nucleases	101
Figure 37	Evolution of the elasticity during actin polymerization in presence of wLX over time	103
Figure 38	Evolution of the elasticity during actin polymerization in presence of sPX over time	104
Figure 39	Concentration-dependent elasticity of actin networks enriched wLX and sPX	106
Figure 40	Structural phases of actin networks crosslinked by wLX	107
Figure 41	Structural phases of actin networks polymerized in presence of wLX	108
Figure 42	Reversibility of synthetic actin crosslinkers	110
Figure 43	Reversibility of synthetic actin crosslinkers	111
Figure 44	Polymerization and depolymerization of actin in presence of LifeAct® and wLX	113
Figure 45	Influence of wLX on actin remodeling dynamics in NMuMG cells	114
Figure 46	Labeling of actin filaments within HeLa cells	116
Figure 47	Co-localization of DNA and actin structures in HeLa cells transfected with wLX	117
Figure 48	2D migration of crosslinker-transfected HeLa cells into cell-free area over time	119
Figure 49	Proliferation of crosslinker-treated MDA-MB-231 cells	120
Figure 50	Apoptosis assay of crosslinker-treated MDA-MB-231 cells	121
Figure 51	3D migration and 3D invasion of crosslinker-transfected MDA-MB-231 cells	123
Figure 52	Influence of wLX on EMT induction in human lens epithelial cells (FHL-124)	125
Figure 53	Detection of MMP-2 and MMP-9 levels via gelatin zymography	126
Figure 54	Immunocytochemistry staining for EMT markers after induction with TGF- $\beta$	128
Figure 55	Mean elastic moduli of MCF-10 treated w/ or w/o TGF- $\beta$ post transfection with wLX and corresponding controls	129
Figure 56	Possible influence of wLX in MRTF-mediated SRF signal transduction during EMT	131

## List of figures in supplemental information

Figure S 1	Step-wise assembly of DNA tetrahedra	159
Figure S 2	CPP-conjugation to PTO-capped DNA trimers	160
Figure S 3	Cleavage of sPX by EcoRV-HF®	161
Figure S 4	Evolution of the elasticity during actin polymerization in presence of fascin over time	162
Figure S 5	Structural phases of actin networks polymerized in presence of sPX	163
Figure S 6	Cloning of pTag-LifeAct-GFP-N	164
Figure S 7	DNA sequence of pTag-LifeAct-GFP-N	166
Figure S 8	3D migration and invasion of wLX-treated MDA-MB-231 cells after 36 h	167
Figure S 9	Real-time deformability cytometry (RT-DC) of MCF-10A treated w/ or w/o TGF- $\beta$	168
Figure S 10	Cytotoxic effect of Lipofectamine™ 3000 in MCF-10A and MDA-MB-231 cells	169
Figure S 11	Internalization of DNA at different Lipofectamine™ 3000 concentrations	170
Figure S 12	Internalization efficacies of Cy3-labeled 60bp DNA in different cell lines	171

## List of tables

Table 1		<i>Classification of cell-penetrating peptides</i>	_____	10
Table 2		<i>Examples of actin-binding proteins studied in vivo and in reconstituted actin networks</i>	____	27
Table 3		<i>Classification of epithelial-mesenchymal transition (EMT)</i>	_____	29
Table 4		<i>DNA oligonucleotides</i>	_____	44
Table 5		<i>Peptides</i>	_____	45
Table 6		<i>Properties of cantilevers used for AFM measurements</i>	_____	67
Table 7		<i>Working concentrations of utilized dyes for live-cell imaging</i>	_____	74
Table 8		<i>Volumes of transfection mixtures for different cavities</i>	_____	76

## List of tables in supplemental information

Table S 1		<i>Internalization efficacies of Cy3-labeled 60bp DNA in different cell lines</i>	_____	172
-----------	--	---	-------	-----



### 1 Introduction

Cells constitute the fundamental structural, functional and biological building block of all living organisms. They are intrinsically complex and represent a collection of multiple subsystems. In order to understand their complex behavior, it is necessary to break them down into their individual components. This can be accomplished by the usage of very minimal, *in vitro* systems, which lack the overcrowded environment of the inner of a cell as well as the tendency to biochemically interact with other cellular systems. Even minor changes to a single protein component within one of these systems, for instance a point mutation in the genome, can cause severe diseases. To unravel the impact of such disorders from the level of their basic molecular interactions, reconstituted systems can be utilized. As an example, a point mutation in the actin-binding domain (ABD) of the  $\alpha$ -actinin 4 gene (ACTN4) causes a form of kidney damage known as focal segmental glomerulosclerosis (FSGS). Ehrlicher *et al.* found that this point mutation led to an increased affinity of the crosslinker  $\alpha$ -actinin to actin, which in turn resulted in a slowed down intracellular dynamics. By using reconstituted systems, they speculated that this mutation caused cellular structures to become excessively solid, which in turn caused the failure of the filtration barrier in kidney<sup>1</sup>. Many more diseases are caused by the change of single nucleotide bases in the genome, for instance sickle cell disease<sup>2</sup> or cardiomyopathy<sup>3</sup>. Studying these cases often requires genetic engineering of model cell and animal models, which is usually tricky and time consuming. As an alternative, nanoscale fabrication of biomimetic components can be utilized, in order to create rudimentary model systems that mimic their natural, biological counterparts.

The underlying materials and tools for fabricating these components need to fulfill several requirements: First, they must provide the ability to synthesize components on the size scale of proteins, second, they should be completely molecular modular to enable the systematic integration of bio-interactive functional components, and third, the components must be able to interact with the targeted biological system or behave like their biological counterpart. DNA and other nucleotide materials fulfill these requirements because of their programmable structural properties. DNA is a polymer, whose length can be controllably scaled at a resolution of 3.4 Å, since this is the distance between single nucleotide bases<sup>4</sup> within the well-known double-stranded structure of its most commonly found B-form. Nature already uses nucleic acids for structural reasons, for example as ribozymes, which are ribonucleic acid (RNA) molecules that catalyze specific biochemical reactions similar to enzymes; non-coding RNAs, whose structural features are for instance important during translation; or G-quadruplexes, which are present at the end of chromosomes (telomeres) and therefore may be involved in

maintaining chromosome stability<sup>5</sup>. The discovery of nucleic acid structures that also act as structural molecules has led to a rethinking of the central dogma of molecular biology, in which the primary function of DNA is considered to be the carrier of the genetic information of virtually all living organisms that is transcribed into RNA followed by the translation into proteins.

One of the pioneers of this rethinking is the protein crystallographer Nedrian Seeman. In 1982, he had the idea to look at DNA from a different perspective from the usual dogma, i.e. using DNA as a programmable molecular building block to create two-dimensional (2D) and three-dimensional (3D) structures. This laid the foundation of the new research field of DNA nanotechnology<sup>6</sup>. He focused on the ability of DNA to hybridize via the Watson-Crick base pairing<sup>7</sup> with a complementary DNA strand in a predictable manner to form double-stranded (ds) DNA. Moreover, inspired by a branched nucleic acid structure known as the Holliday junction that for instance occurs during genetic recombination in cells, he considered DNA motifs, consisting of more than two strands that hybridize into branched, multi-arm junctions. These junctions can link with other branched junctions to form lattices or even more complex 3D architectures via the hybridization of “sticky ends”, which are short overhangs of single-stranded (ss) DNA<sup>6</sup>. During the following years, several types of self-assembled 2D and 3D structures, including covalently-closed wire-frame structures or extended lattices with nanometer-sized features, which were achieved through the introduction of crossovers between DNA double strands, have been designed and fabricated<sup>8–15</sup>. In 2005, Goodman *et al.* presented a wire-frame structure, a DNA tetrahedron<sup>16</sup>, which, due to its simple design, high production yield, fast assembly time and optimal size to encapsulate proteins<sup>17</sup>, has formed the basis for a number of subsequent studies<sup>18</sup>.

In the diverse and fast-growing field of DNA nanotechnology<sup>19</sup>, several techniques, such as “DNA origami”<sup>20</sup>, “DNA bricks”<sup>21</sup> or “tile-based self-assembly”<sup>22</sup> emerged to create DNA nanostructures of different geometries, shapes and rigidities. The last named technique for instance was recently utilized to generate DNA nanotubes with programmable diameters, as depicted in Figure 1. This is a great example of how DNA structures can be applied to mimic subcellular systems, in this case semi-rigid biopolymers such as microtubules, intermediate filaments, keratin or actin, which are found in cells and tissues. Whereas the underlying structural parameters of these natural biopolymers cannot be controllably altered, DNA nanotubes can be precisely tuned with regard to their filament stiffness, which makes them a useful tool to study the impact of the persistence length on macroscopic bulk structures of such biopolymers. This study revealed that the underlying stiffness of the filaments has a far greater impact on bulk network stiffness than had been previously assumed through commonly accepted models<sup>23,24</sup>. Moreover, this DNA-enabled biomimetic strategy has also been used to study active systems containing molecular motors<sup>25</sup>.

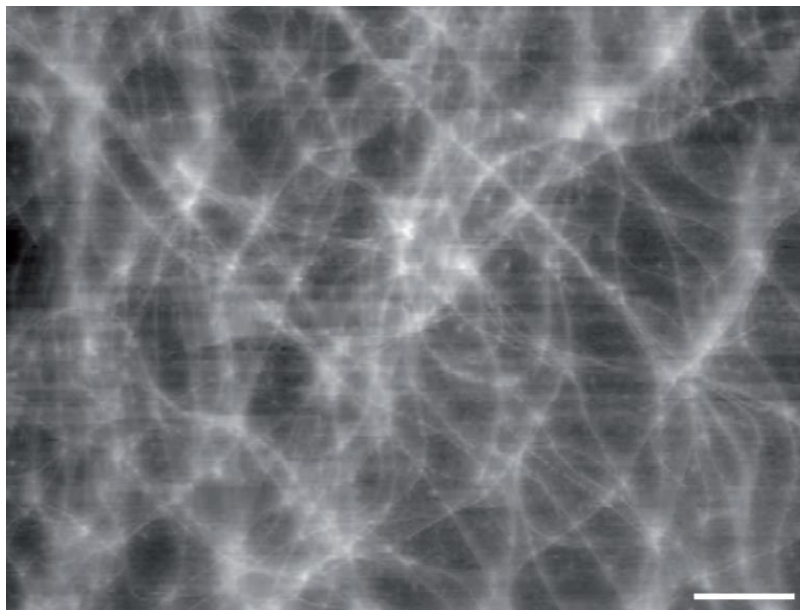


**Figure 1 | AFM image of an Eight-helix tube (8HT) network formed at 4  $\mu\text{M}$ .** A major limitation of structural biopolymers in cells and tissues is that the persistence length cannot be freely tuned to study its impact on macroscopic bulk structures. This limitation was resolved by employing structurally programmable DNA nanotubes, enabling controlled alteration of the filament stiffness<sup>23,24</sup>. DNA nanotubes (8HT) were imaged via atomic force microscopy (AFM) in air, as described in 4.30.2. Scale bar was set to 1  $\mu\text{m}$ .

Besides supplying the underlying structure, DNA nanostructures can be used to position single biomolecules or nanoparticles with nanometer precision, in order to additionally provide the structure with certain functions. Due to this important feature, as well as its biocompatibility, extremely specific base pairing and stability, DNA structures have been applied in research fields such as molecular electronics<sup>26</sup>, plasmonics<sup>27</sup>, biochemistry<sup>28,29</sup> and medicine<sup>18,30</sup>. Comparable to how viruses interact with a host cell, via receptor-ligand interaction, functionalized DNA nanostructures interact on the nanometer scale. Schüller *et al.*, for instance, precisely decorated the outer surface of DNA origami tubes with cytosine-phosphate-guanine (CpG)-sequences, which are highly indicative of bacteria DNA and recognized by the Toll-like receptor 9 (TLR9) in endosomes, to induce a TLR9-specific immune response in cells. They found that CpG-bound DNA origami tubes caused a five-fold increased immune response compared to free CpGs, which underlines the potency of spatially localizing bio-active molecules onto functionalized DNA nanostructures<sup>31</sup>. Additionally, smaller and simpler DNA structures have been functionalized with biomolecules or particles for various applications (2.1).

As protein-receptor stimulation often targets only small interaction regions, these specific binding sites can often be isolated as short peptides, which can also bind and activate the considered target, although in most cases with less potency. These peptides have some advantages over their native protein counterparts, since they are short and scalably

## Introduction

---

synthesizable with various chemical modifications (e.g. functional conjugation groups) of choice. This makes them suitable candidates to add specific biological functions to DNA structures which in turn are then usable in many applications.

With regard to this dissertation, different peptides carrying specific chemical modifications were covalently attached to wire-frame DNA structures, three-arm junction structures or simple ds DNA spacers in order to create biomimetic constructs on the size scale of proteins. These constructs were then tested on minimal, reconstituted systems as a way to determine how different parameters, e.g. binding affinity, globally affect living cellular systems. In one subproject, the uptake efficacy of DNA tetrahedra into cells was found to be increased with the addition of cell-penetrating peptides (CPP), whereas in another subproject, synthetic, DNA-peptide structures that mimic crosslinking proteins of the cellular biopolymer actin were generated to modulate the properties and dynamics of actin networks. For both projects, it was of great interest to test whether the attached functional materials stay intact and retain their function even when covalently affixed to DNA. Particularly for the second subproject, two fundamental questions came up: First, do these biomimetic constructs have an impact on reconstituted systems, i.e. can these minimal systems, which are not as overcrowded as the intracellular environment, be tuned with these functionalized DNA structures? Second, do they have the capability to function on specific systems within cells? The following section introduces the utilized DNA nanostructures as well as strategies to functionalize them. Moreover, peptides as well as the corresponding cellular system they interact with are presented in more detail.

## 2 Theoretical Background

### 2.1 DNA tetrahedron

DNA is a powerful building block which allows the programmed self-assembly of molecular scaffolds, cages and multifunctional carriers with nanoscale dimensions by the nature of predictable base pairing. DNA nanostructures offer multiple binding sites for a wide variety of biomolecular compounds and allow programmable features such as conformational changes triggered by receptor-ligand interactions. Due to the fact that each point in the structure is equally addressable, DNA nanotechnology represents a smart technique for the nanometer scale arrangement of molecules on 2D or 3D structures. One of the simplest and most rigid DNA system that allows variations in spacing, orientation and local stoichiometry is the DNA tetrahedron<sup>16</sup>. This molecule consists of four oligonucleotides, 63 nt each, which run around one face and hybridize to form a wire-frame tetrahedron with double-stranded edges of ~ 7 nanometers (Figure 2). The single-step self-assembly of DNA tetrahedra is achieved by mixing these four partially complementary oligonucleotides in equimolar quantities in 1X TM buffer, followed by a temperature-based annealing from 95 °C to 4 °C within a few minutes.

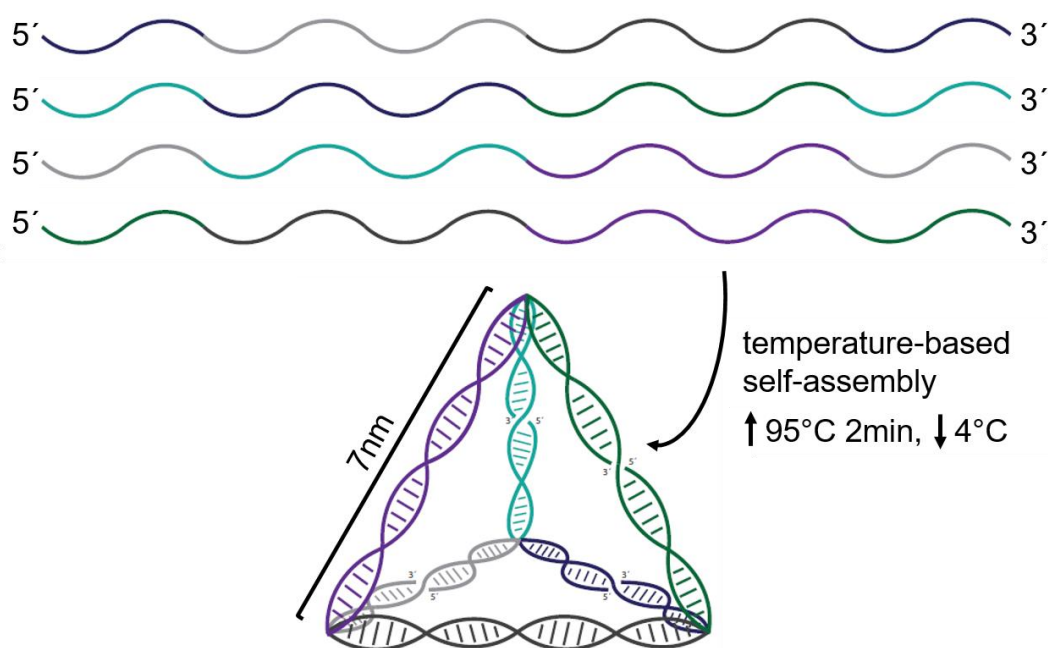


**Figure 2 | Temperature-based self-assembly of DNA tetrahedra.** Four partially complementary oligonucleotides (63 nt each,) identified by color, are mixed in equimolar amounts in 1X TM buffer (4.3) and self-assembled to a wire-frame tetrahedron with double-stranded edges of ~ 7 nm by heating up to 95 °C for 2 min followed by a rapid cooling to 4 °C<sup>16</sup>.

Originally, four of the six edges of the DNA tetrahedron contain nicks, i.e. breaks in the ds DNA backbone, where the 5' and the 3' end of each sequence meet after looping around one face of the structure<sup>16</sup>. Each of these gaps allows the attachment of functional molecules, either on the 3' or the 5' end of each individual DNA strand. In this work, DNA sequences were designed to result in DNA tetrahedra with one gap in one plane and three gaps in an opposite plane, whereby the local stoichiometry of attached peptides could be increased. So far, tetrahedral DNA structures have been used in various applications, for instance tetrahedron-based microarrays<sup>32</sup>, for siRNA delivery<sup>33</sup>, for protein encapsulation<sup>17,34</sup>, as molecular beacon to detect tumor-related mRNA<sup>35</sup> or for drug delivery<sup>36,37</sup>.

Previous studies have shown that DNA nanostructures fuse with the cellular membrane and enter the cell via endocytosis, presumably via caveolae-mediated endocytosis. Moreover, DNA nanostructures end up in lysosomes as they were observed to co-localize with lysosomal markers<sup>38</sup>. However their uptake might be not as effective since negatively charged DNA structures are electrostatically repulsed from negatively charged cell membrane. In order to increase the cellular uptake without the usage of transfection agents, which are toxic at high concentrations, so-called cell-penetrating peptides (CPP, 2.3) were covalently attached to the DNA tetrahedra and DNA trimers in the work presented here. In the following, different methods to chemically conjugate peptides to DNA strands are introduced.

## 2.2 Functionalization of DNA and corresponding conjugation approaches

In order to add function to DNA structures (covalent conjugation of e.g. peptides), several conjugation approaches were tested and are described in the following.

### 2.2.1 Terminal deoxynucleotide transferase (TdT) reaction

The enzyme terminal deoxynucleotide transferase (TdT) is a specialized polymerase which catalyzes the template independent addition of (modified) nucleotides to the 3' hydroxyl end of ss or ds DNA. During the reaction, the free hydroxyl group on the C3 atom of the 2-deoxyribose reacts with the  $\alpha$ -phosphate of the aminoallyl-dUTP. This leads to the cleavage of the phosphoanhydride bond and the release of pyrophosphate (PPi). Through the addition of desoxy-UTP to the 3' end of the DNA a new hydroxyl group is available and the enzyme can add another dUTP. This results in a tailing of DNA with dUTP molecules in dependence on the molar excess of dUTP compared to free 3' DNA strands (Figure 3). In this work, TdT was utilized to add a tail of NHS ester reactive aminoallyl-dUTPs, which were finally covalently conjugated to peptides via heterobifunctional linkers (4.25).

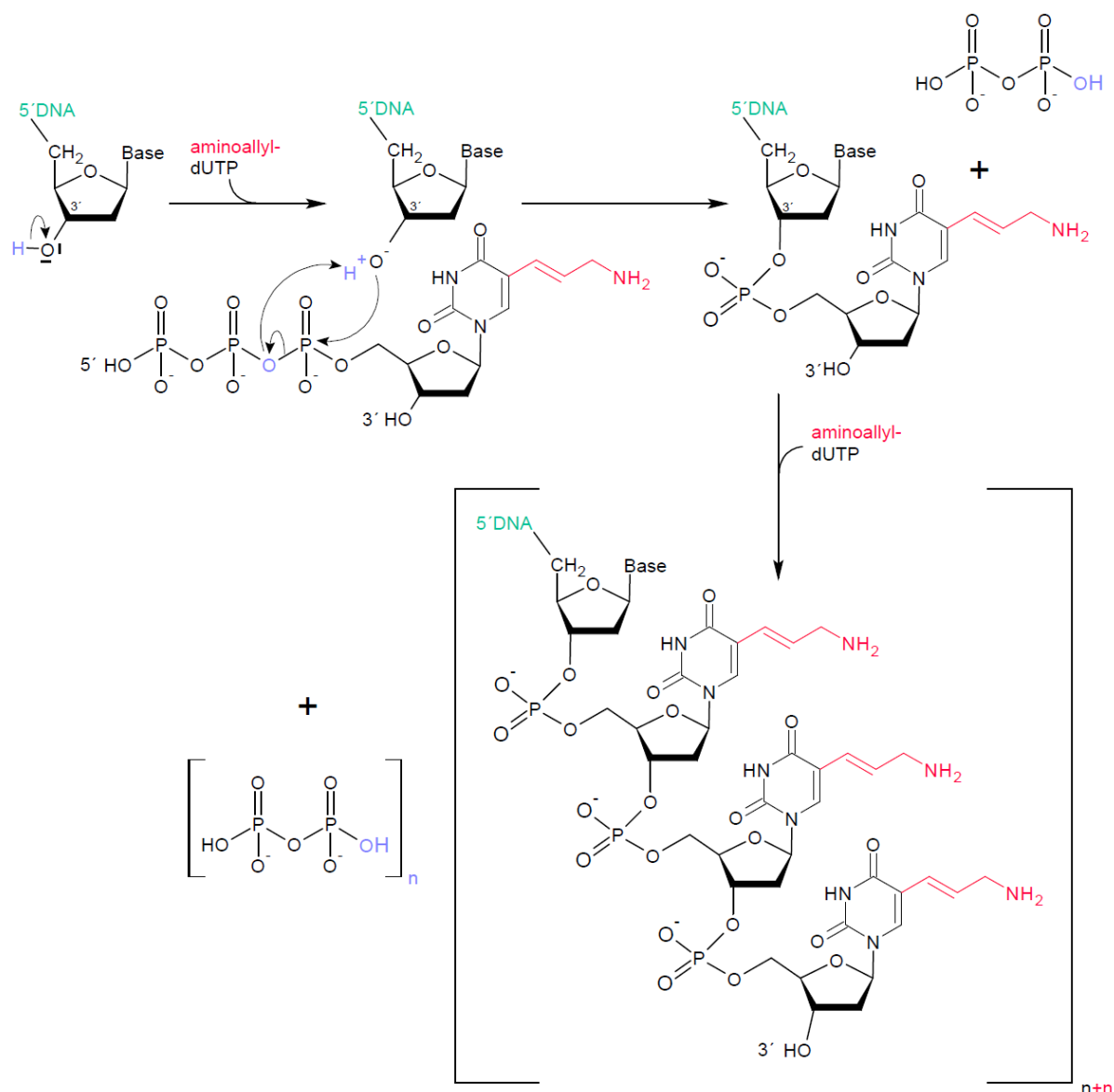


**Figure 3 | Mechanism of TdT reaction using aminoallyl-dUTP.** Depending on the molar ratio of free 3'-ends of DNA strands to aminoallyl-dUTP molecules, the enzyme attaches a tail of dUTPs (n+n).

## 2.2.2 NHS ester chemistry

N-hydroxysuccinimide (NHS) esters react with primary amines ( $-NH_2$ ) in amine-free buffers within physiologic to slightly alkaline milieu (pH 7 - 9). NHS is released and a stable amide bond between two conjugated molecules is formed (Figure 4). For all conjugation approaches, NHS ester-containing linker molecules were utilized. Therefore, DNA was either amine-modified via TdT as described in 2.2.1 or purchased with single 5'  $NH_2$ -modification.

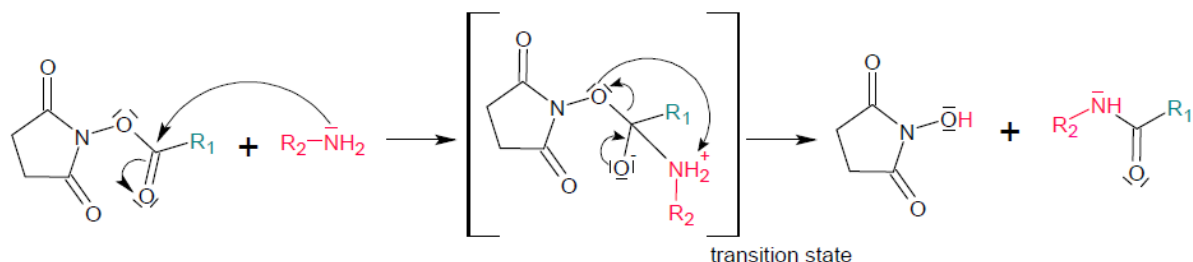


**Figure 4 | Amine-reactive NHS esters.** The primary amine of molecule  $R_2$  reacts with NHS ester-conjugated molecule  $R_1$  under the formation of a stable amide bond and the release of NHS. Arrows indicate the reaction mechanism. Molecules involved in the reaction are shown with their free electrons.

### 2.2.3 Maleimide chemistry

Maleimides specifically react with sulfhydryl groups ( $-SH$ ) in a pH range of 6.5 – 7.5 and form stable thioether bonds (Figure 5). In order to covalently couple cysteine-containing proteins or peptides to maleimides, disulfide bonds have to be reduced to free thiols. Most reducing agents, such as DTT and  $\beta$ -mercaptoethanol, are thiol-containing compounds and need to be excluded from maleimide reaction buffers since they would otherwise compete for coupling sites. Alternatively, TCEP that does not contain thiol groups can be used to reduce disulfides (Figure 18). In this work, thiol-reactive maleimides were utilized in form of sulfo-SMCC to covalently couple cysteine-containing peptides to DNA structures.

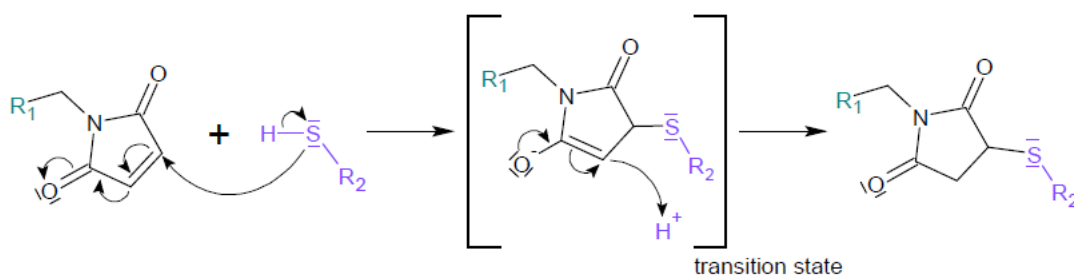


**Figure 5 | Sulfhydryl-reactive maleimides.** Sulfhydryl group of molecule  $R_2$  reacts with maleimide-conjugated molecule  $R_1$  and forms a stable thioether bond. Arrows indicate the reaction mechanism. Molecules involved in the reaction are shown with their free electrons.

### 2.2.4 Strain-promoted alkyne-azide cycloaddition (SPAAC)

The strain-promoted alkyne-azide cycloaddition (SPAAC), also known as copper-free click chemistry, is a bioorthogonal reaction of a thermostable cyclooctyne with an azide building a triazole. The reaction was first developed by Bertozzi *et al.* in 2004<sup>39</sup> and the reaction mechanism is shown in Figure 6. However, their work was based on the work by

Sharpless *et al.*<sup>40</sup> who invented a modified version of the Huisgen cycloaddition, which specifically describes the 1,3 – dipolar cycloaddition between an azide and an alkyne under the formation of a triazole but which generally does not run readily under mild, physiological conditions. In order to easily proceed the reaction at neutral pH, room temperature and in aqueous solution, Sharpless *et al.* added copper(I) as a catalyst, which gave the reaction the name “copper-catalyzed alkyne-azide cycloaddition” (CuAAC, copper-catalyzed click chemistry). Since copper is strongly cytotoxic, Bertozzi *et al.* developed the copper-free click chemistry, which runs quickly under physiological conditions, does not require the catalyst and thus can be applied in living systems without cellular toxicity<sup>41,42</sup>. Since SPAAC is a quick reaction that results in high yields, peptides of interest were, if possible, purchased with a N-terminal N<sub>3</sub> group.

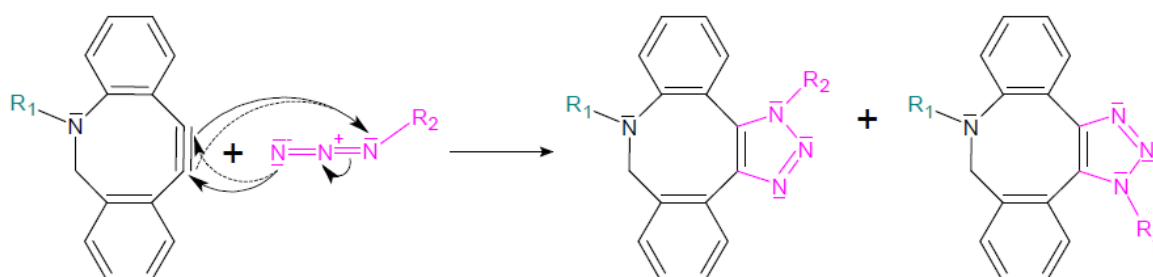


**Figure 6 | Reaction mechanism of SPAAC.** Strained alkyne (e.g. DBCO) reacts with an azide in a covalent manner forming a triazole. Due to the angle distortion of the cyclooctyne, the reaction is sped up and does not require a catalyst. Most cyclooctynes react to form regioisomeric mixtures. Arrows indicate the reaction mechanism.

### 2.3 Cell-penetrating peptides (CPP)

The delivery of bioactive molecules or drugs into cells is an intensively studied research field. Since these molecules are often either too big to passively diffuse through the membrane or are repulsed due to their charge or polarity, they need a carrier in order to internalize into cells. In recent years, different approaches such as electroporation, encapsulation into liposomes, viral transfection vectors or microinjection were developed. However, these methods often show limitations such as insufficient efficacies or high cytotoxic effects.

Over the past 20 years, so-called cell-penetrating peptides (CPP) have been intensively studied. These peptides are generally short (i.e. up to 40 amino acids) and show the ability to transport cargos of different size and charge into different cell types, without a high cytotoxicity. Previous studies describe the internalization of different cargos such as proteins<sup>43</sup>, antisense oligonucleotides<sup>44</sup>, liposomes<sup>45</sup> and nanoparticles<sup>46</sup> with the help of CPP. The most popular

## Theoretical Background

representative CPP are Tat(48-60)<sup>47</sup>, a short fragment of the HIV 1 TAT transactivation factor that was discovered by Frankel *et al.* in 1988 to show the ability to internalize into cells<sup>48</sup> and Penetratin, a short fragment of helix 3 (43-58) of the transcription factor antennapedia (Antp) homeodomain from *Drosophila*<sup>49</sup>. Other important CPP are V22<sup>50</sup>, Transportan<sup>51</sup> and Polyarginin<sup>52</sup>. An overview about the classification of CPP is shown in Table 1.

**Table 1 | Classification of cell-penetrating peptides.** CPP are classified by origin or chemical properties<sup>53</sup>.

By origin		Examples for CPP
Natural	Sequence derived/truncated from natural protein sequence (protein transduction domain)	TAT, Penetratin
Synthetic	Sequence developed by theoretical considerations	Polyarginine (e.g. R <sub>9</sub> )
Chimeric	Fusion peptides of natural and synthetic sequences	Transportan
By chemical properties		Examples for CPP
Cationic	At least 8 positive charges, less anionic amino acid residues	Tat, Polyarginine (e.g. R <sub>9</sub> )
Amphiphatic	Both, hydrophobic and hydrophilic amino acid residues	Transportan (primary amphiphatic through primary structure) and Penetratin (secondary amphiphatic through secondary structure)
Hydrophobic	Hydrophobic amino acid residues	Signal sequence of integrin $\beta$

Henriques *et al.* described that antimicrobial peptides, due to their cationic and amphiphilic properties, act similarly to cell-penetrating peptides<sup>54</sup>. These cationic antimicrobial peptides (CAMPs) are able to inactivate bacterial or viral pathogens through permeabilization of their membranes. Fragments of the CAMP cathelicidin (CAP18)<sup>55</sup> were investigated for their antimicrobial activity and highly cationic sequences (residues 106 - 125, short C18) were identified. This C-terminal region featured an amphiphatic alpha-helical conformation that might be responsible for antimicrobial activity<sup>56</sup>. Additionally, it was shown that these cationic alpha-helical antimicrobial peptides can be a useful tool for gene delivery<sup>57</sup>. A shortened version of C18, named sC18 (corresponding to residues 106 - 121 of CAP18) that was first reported by Neundorff *et al.* in 2009<sup>58</sup>, was utilized in the work presented here to increase the internalization efficacy of DNA tetrahedra and DNA trimers.

## Theoretical Background

---

sC18 consists of 16 amino acid residues (GLRKRLRKFRNKIKEK, Table 5) and belongs to the group of amphipathic CPP<sup>58</sup>. The peptide has nine positively and one negatively charged residues and a theoretical pI of 12.02 (calculated with ProtParamTool (4.12)). Thus, under physiological conditions it is highly positively charged. As most other CPP, sC18 was also described to internalize into cells via endocytosis<sup>58</sup>, which describes the process of active uptake of molecules into cells by invaginating regions of the plasma membrane.

Two mechanisms of endocytosis exist: phagocytosis and pinocytosis. During phagocytosis (“cell eating”), macromolecules, cell debris or even whole bacteria are up taken by specialized cells, including macrophages, monocytes and neutrophils. In contrast, pinocytosis (“cell drinking”) involves the invagination of fluids or smaller particles and is carried out by most cell types<sup>59</sup>. Conner *et al.* classified the different types of pinocytosis as depicted in Figure 7: macropinocytosis<sup>59–62</sup>, clathrin-mediated endocytosis (CME)<sup>60,63,64</sup>, caveolae-mediated endocytosis<sup>65–70</sup>, and clathrin- and caveolae-independent endocytosis<sup>71</sup>. The intracellular fate of internalized compounds strongly depends on the previously mentioned pathways used. Most common fates after internalization into cells are degradation in lysosomes, recycling back to the plasma membrane as well as trafficking to organelles like the Golgi apparatus or translocation into the cytosol<sup>60</sup>.

In order to investigate the mechanism of the endocytotic uptake of sC18 in more detail, Neundorf *et al.* conducted co-localization studies of carboxyfluorescein-labeled sC18 with transferrin-TexasRed, a marker for clathrin-mediated endocytosis. They found, at least for HeLa and MCF-7 cells, a co-localization of the peptide and the marker within some vesicles, which indicates a cellular uptake of sC18 by CME. Most of sC18 does not escape from endosomes, as no translocation into the cytosol was seen at 37 °C. Rather this CPP ends up in lysosomes that contain acidic hydrolases as well as other enzymes, where it is digested<sup>58</sup>.

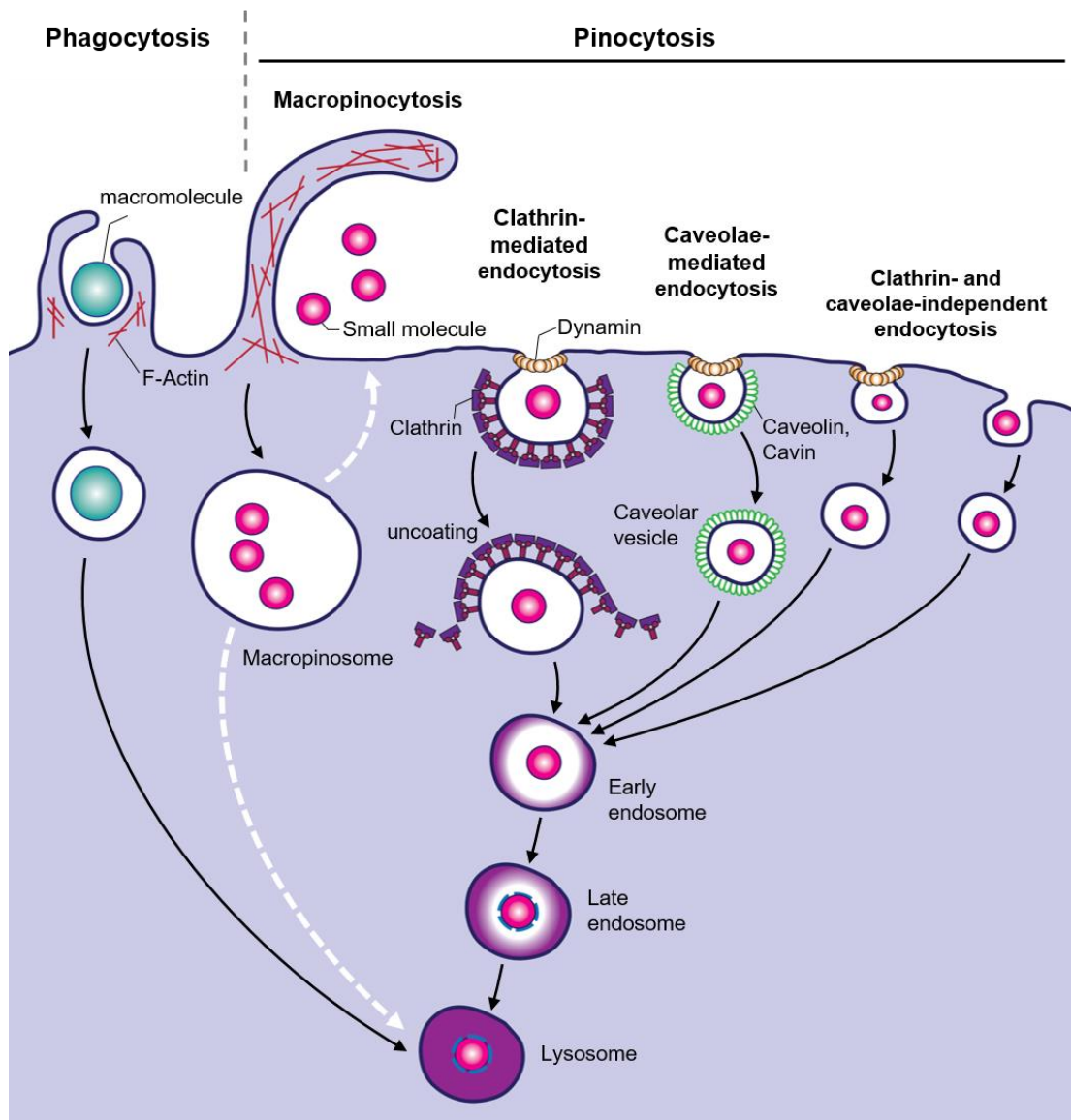


**Figure 7 | Endocytotic pathways.** Phagocytosis describes the uptake of larger molecules, cell debris or even whole bacteria, whereas during pinocytosis fluids or smaller molecules are uptaken. The subtypes of pinocytosis, classified by Conner *et al.*<sup>59</sup> are shortly described in the following. **Macropinocytosis**<sup>59–62</sup>: Macropinocytosis displays the most effective way to internalize large amounts of extracellular fluid. Large membrane protrusions are formed in an actin-driven process which further collapse onto and fuse with the plasma membrane to build large endocytic vesicles, called macropinosomes. The fate of macropinosomes is cell specific. **Clathrin-mediated endocytosis (CME)**<sup>60,63,64</sup>: Clathrin forms triskelions, that assemble into basket-like lattices and induces the deformation of the plasma membrane into clathrin-coated pits on the cytoplasmic side of the membrane. The binding of a GTPase, called dynamin, mediates the fission of the membrane and the formation of vesicles. Clathrin-coated vesicles become uncoated and fuse with early endosomes, which are slightly acidic (pH 6). Early endosomes are able to mature into late endosomes, which have a pH below 6. These fuse with lysosomal vesicles of pH 5 that contain acidic hydrolases as well as other enzymes, which are responsible for the degradation of endocytosed molecules. **Caveolae-mediated endocytosis**<sup>65–70</sup>: Caveolae are cholesterol- and sphingolipid-rich bulb-shaped invaginations of the plasma membrane, which are formed by caveolin. Similar to CME, binding of dynamin causes the invagination of the plasma membrane and vesicles are subsequently pinched off. The intracellular pathway of vesicles is probably similar to what was previously reported for CME. **Clathrin- and caveolae-independent endocytosis**<sup>71</sup>: Some of their uptake pathways are constitutive, whereas others are triggered by specific signals. They also differ in their mechanisms and kinetics of formation, associated molecular machinery and cargo destination. Illustration redrawn from Mayor & Pagano (2007)<sup>71</sup> and Holm (2011)<sup>72</sup>.

### 2.4 The actin cytoskeleton

All eukaryotic cells exhibit a cytoskeleton, which is responsible for a variety of tasks. It is responsible for three broad and important functions: it spatially organizes the contents of the cell, it connects the cell physically and biochemically to the external environment, and it generates coordinated forces that enable the cell to move, change their shape and to provide a certain mechanical stability. These processes depend on an interconnected network of filamentous polymers and regulatory proteins, which are the constituents of the cell's cytoskeleton<sup>73</sup>. Its three main components are microtubules, which for instance are responsible for separating chromosomes and long-range transport of large particles, intermediate filaments that function as intracellular ligaments and tendons as they primarily fulfill structural tasks, and actin filaments, which provide the mechanical structure and motility of a cell<sup>74,75</sup>. In the following, the major component, i.e. the actin cytoskeleton, will be explained in more detail with focus on the process of actin polymerization and depolymerization as well as on diverse actin-based structures with distinct architectures that assemble during migration of cells.

Actin is an ATP-binding protein with a molecular mass of ~42 kDa that is present in cells either as monomers (called G-actin or globular actin) or as filaments (known as F-actin, filamentous actin or microfilaments). Actin filaments are long helical polymers that assemble by the reversible endwise polymerization of monomers, thereby ATP is hydrolyzed to ADP and inorganic phosphate ( $P_i$ ) is released. As the two ends of each filament have distinct biochemical properties, actin filaments are polar. The fast-growing end, where polymerization primarily occurs, is called the barbed end (plus end), whereas the slower-growing end is designated the pointed end (minus end). G-actin polymerization and F-actin depolymerization are under tight control by monomer- and filament-binding proteins that regulate the monomer pool, orchestrate the formation of filaments, organize filaments into arrays, and depolymerize filaments for monomer recycling, which is an important feature of actin dynamics<sup>76</sup>. Actin filaments are organized into bundles and networks by a variety of crosslinking proteins. The resulting filament length as well as the type of crosslink strongly determines the mechanical properties of the whole structure.

All cells contain an actin cortex, which is a dense network of filamentous actin that is located just beneath the plasma membrane. These filaments are generally oriented with their barbed ends facing toward the plasma membrane<sup>77</sup> and are connected to it via several transmembrane proteins. Thus, the actin cortex supports the plasma membrane to resist tension, which makes it to one of the main determinants of cell shape and motility<sup>78,79</sup>. Moreover, cortical actin polymerization is of importance in the invagination of extracellular materials via phagocytosis and pinocytosis as well as in the formation of acto-myosin contractile structures in nonmuscle cells such as stress fibers and the contractile ring<sup>79</sup>. Furthermore, it is thought that spatially restricted cortical polymerization is the driving force to

## Theoretical Background

form membrane protrusions, such as lamellipodia and filopodia, during cell locomotion. These protrusive structures exhibit distinct filament geometries as depicted in Figure 8.

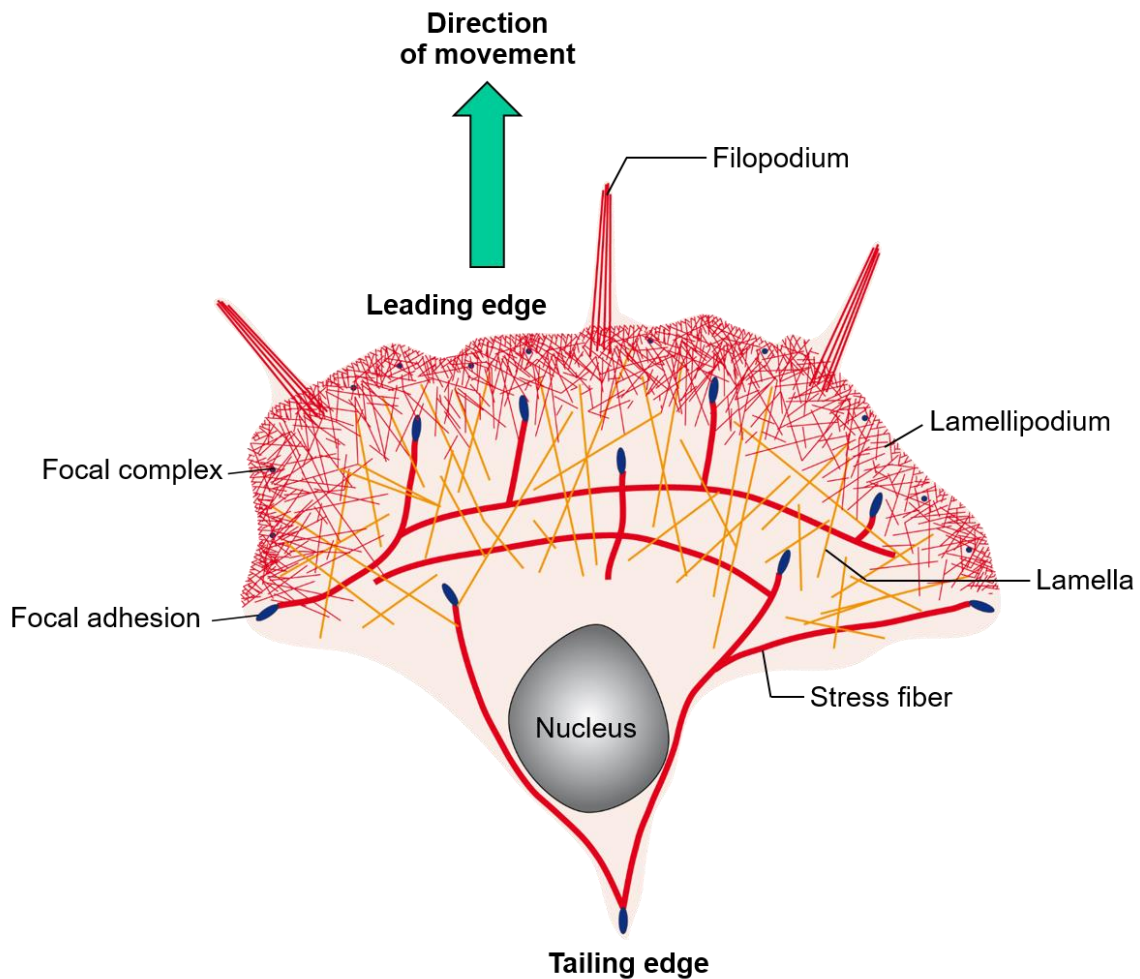


**Figure 8 | Schematic illustration of the actin cytoskeleton in a migrating cell.** This overview shows major cellular structures that occur in a migrating cell. The schematic cell drawn here does not correspond to a specific cell type. In order to migrate, a cell first acquires a characteristic polarized morphology in response to extracellular signals. At the cell front, actin polymerization drives the extension of membrane protrusions such as lamellipodia, which contain branched actin filaments, and filopodia that exhibit non-branched actin filaments which are tightly bundled by several proteins including fascin. At the leading edge of the lamellipodium the cell forms adhesions that connect the extracellular matrix to the actin cytoskeleton to anchor the protrusion and tract the cell body. Finally, in order to move forward, the cell retracts its trailing edge by combining actomyosin contractility and disassembly of adhesions at the rear. Illustration modified from Le Clainche & Carlier (2008)<sup>80</sup>.

Sheet-like lamellipodia contain a network of branched “dendritic” actin filaments<sup>81</sup> that are suggested to be able to push along a broad length of the plasma membrane and are thought to be the major engine for cell movement<sup>82</sup>. In contrast, spike-like filopodia with their long, parallel bundle organization are particularly well designed to serve as the cell’s sensory and guiding organelles, which function to explore the local environment and form cell - substrate or cell - cell interactions<sup>83</sup>. Behind the highly dynamic leading edge there is a more stable region, called the lamella, which contributes to cell migration by coupling the actin

network to myosin II-mediated contractility and substrate adhesion, i.e. stress fibers<sup>84</sup>. Stress fibers are contractile actin bundles composed of actin and nonmuscle myosin II (NMMII) found in nonmuscle cells<sup>85</sup>. In order to form this highly regulated actomyosin structure, they additionally contain crosslinking proteins such as  $\alpha$ -actinin<sup>86</sup>. Stress fibers span through the cytoplasm and are often anchored to focal adhesions, which connect the extracellular matrix (ECM) to the actin cytoskeleton<sup>87,88</sup>.

### Model of actin polymerization at the leading edge of a cell

Prior work has shown that *in vitro* polymerization of actin in presence of actin crosslinkers, for instance  $\alpha$ -actinin, results either in an isotropic gel of filaments or parallel bundles<sup>89</sup>. For a long time, it remained unclear how cells use these proteins to assemble an ordered and polarized structure. In order to assemble such an ordered network, a cellular component that initiates actin polymerization and crosslinking in a highly localized manner is needed. This long sought cellular nucleator of actin filaments was discovered to be the Arp2/3 complex<sup>90-93</sup>. The WASp/Scar complex was found to be the regulator of the nucleation activity of the Arp2/3 complex<sup>94-97</sup>. WASp proteins are named after the Wiskott-Aldrich syndrome, in which mutations in the gene encoding WASp cause immune and blood deficiencies. Scar is also known as WAVE since the same protein was discovered independently by two groups, however nowadays the name WAVE is more commonly used<sup>98</sup>. Based on these findings, Pollard *et al.* postulated a concrete, quantitative mechanism for the assembly and disassembly of lamellipodia at the leading edge of a cell, which they called the dendritic-nucleation model<sup>76,99</sup>.

As depicted in Figure 9, their model proposes that (1) external signals activate surface receptors in a first place. The associated signal transduction pathways then produce (2) active Rho-GTPases, such as Rac, Cdc42 and RhoG<sup>83</sup>, and phosphatidylinositol 4,5-bisphosphate (PIP<sub>2</sub>), which in turn (3) activate WASp/Scar proteins. Their activation leads again to an (4) activation of the Arp2/3 complex, which binds to the sides or tip of a preexisting actin filament and (5) induces the formation of a new daughter filament that branches off the mother filament<sup>79,100</sup>. These filaments grow rapidly from their barbed ends and (6) push the membrane forward. Pushing of the membrane, the actual protrusive event, is believed to occur not by elongation of the actin filament per se but by an “elastic Brownian ratchet” mechanism, in which thermal energy bends the nascent short filaments, storing elastic energy. Unbending of an elongated filament against the leading edge would then provide the driving force for protrusion<sup>83,100</sup>. After a short time, i.e. within a second or two, (7) elongation of barbed ends is terminated by capping protein. Since new Arp2/3 complexes are incorporated during filament branching, the system requires their continuous activation. If nucleation activity drops to zero,

## Theoretical Background

capping stops polymerization automatically<sup>101</sup>. Actin subunits in this branched network quickly hydrolyze their bound ATP to ADP-P<sub>i</sub> but slowly dissociate the  $\gamma$ -phosphate (filament aging). Thus, ATP hydrolysis and the dissociation of P<sub>i</sub> is postulated to regulate actin filament disassembly<sup>102</sup>. In a next step, (9) actin depolymerization factor ADF/cofilin, which binds to ADP rather than ATP or ADP-P<sub>i</sub>, mediate severing and depolymerization of older filaments at a rate that is controlled by some of the same signals that stimulate assembly. For instance, PIP<sub>2</sub> that was previously mentioned to be part of the activation of WASp/Scar proteins, displace capping protein from barbed ends<sup>103</sup>. ADP-bound actin monomers are recycled by (10) profilin, which exchanges ADP to ATP, whereby (11) the pool of ATP-actin monomers is refilled. A phosphorylation of ADF/cofilins (12) by LIM kinase blocks the interaction of ADP-actin filaments and monomers with ADF/cofilins<sup>104</sup>. LIM kinase itself is activated by p21-activated kinase (PAK), which in turn is regulated by Rho-family GTPases<sup>105</sup>. ADF/cofilin is dephosphorylated and thus activated by a specific phosphatase called *slingshot*<sup>106</sup>.

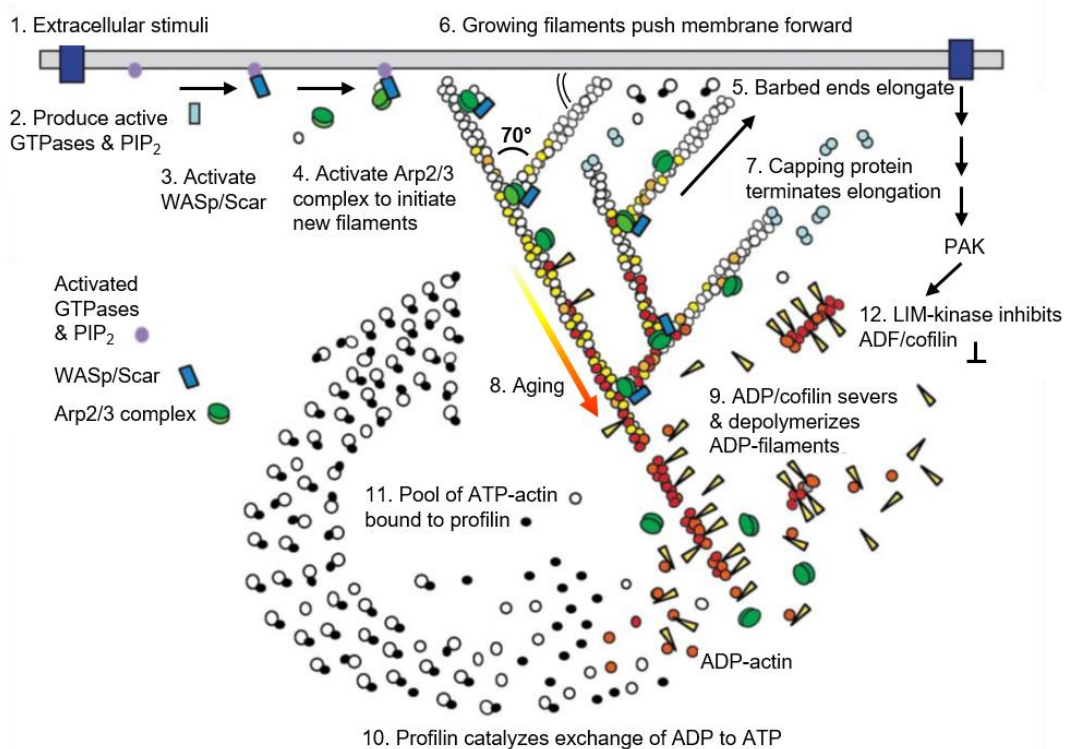


**Figure 9 | Treadmilling/Dendritic nucleation model for actin networks at the leading edge of a cell.** (1) Extracellular signals activate receptors. (2) The associated signal transduction pathways produce active Rho-family GTPases and PIP<sub>2</sub> that (3) activate WASp/Scar proteins. (4) WASp/Scar proteins bring together Arp2/3 complex and an actin monomer on the side of a preexisting filament to form a branch. (5) Rapid growth at the barbed end of the new branch (6) pushes the membrane forward. (7) Capping protein terminates growth within a second or two. (8) Filaments age by hydrolysis of ATP bound to each actin subunit (white subunits turn yellow) followed by dissociation of the  $\gamma$ -phosphate (subunits turn red). (9) ADF/cofilin promotes phosphate dissociation, severs ADP-actin filaments and promotes dissociation of ADP-actin from filament ends. (10) Profilin catalyzes the exchange of ADP for ATP (turning the subunits white), returning subunits to (11) the pool of ATP-actin bound to profilin, ready to elongate barbed ends as they become available. (12) Rho-family GTPases also activate PAK and LIM kinase, which phosphorylates ADF/cofilin. This tends to slow down the turnover of the filaments<sup>76</sup>. Image from Pollard *et al.* (2000)<sup>76</sup>.

## Theoretical Background

---

Furthermore, there are plenty of other proteins, which play supporting roles in the dendritic actin network. Cortactin, for instance, stabilizes branches whereas  $\alpha$ -actinin (2.5.1) and filamin A stabilize the entire network by crosslinking actin filaments<sup>79</sup>. The length of actin filaments in lamellipodia depends on the balance of actin-binding proteins. Furthermore, an increase of capping protein activity, for instance, diverts actin monomers from elongation to nucleation which reduces actin filament length and increases nucleation by the Arp2/3 complex<sup>107</sup>. An increase of VASP in turn promotes filament elongation which results in longer filaments<sup>108</sup>. Another actin-binding protein, which promotes both, actin disassembly as well as polymerization is gelsolin. Gelsolin is a very potent,  $\text{Ca}^{2+}$ -dependent actin filament severing protein. After breaking actin filaments, gelsolin remains attached to the barbed end as a cap, thus preventing polymerization. Uncapping of gelsolin from these filaments generates many polymerization-competent ends from which actin can grow to rebuild the cytoskeleton to new specifications. Thus, gelsolin can also promote actin polymerization due to severing followed by an uncapping of filaments<sup>109</sup>.

Filopodial protrusion, in contrast, is thought to occur by a filament treadmilling mechanism, in which actin filaments within a bundle elongate at their barbed ends and release actin monomers from their pointed ends<sup>79</sup>. Within this structure, elongation of filaments is favored over branching. Many proteins including Ena/VASP proteins, which bind barbed ends of actin filaments and antagonize both capping and branching, thereby allowing continuous elongation of filaments, are enriched in filopodia. Same was described for formins such as mDia1 that protects barbed ends from capping and thereby promotes actin filament elongation without branching<sup>80</sup>. Moreover, actin filaments are bundled by fascin (2.5.2), which thereby might generate the stiffness needed to allow efficient pushing of the plasma membrane in filopodia<sup>79,83</sup>.

Cell motion depends on the protrusion of the leading edge, the traction of the cell body as well as the retraction of the tail. Within these processes, as already mentioned, the mechanical coupling of actin dynamics and the substrate is controlled by cell matrix adhesion which functions as a “molecular clutch”. If the polymerizing actin network and the substrate are connected, membrane protrusion occurs. Additionally, this connection leads to the conversion of the actomyosin tension into traction of the cell body and retraction of the tail. In contrast, if there is no connection between adhesions and the actin cytoskeleton, no protrusion occurs because actin treadmilling is mainly converted into retrograde flow<sup>80,110</sup>.

The actin cytoskeleton is highly regulated and has a wide variety of architectures that are associated with specific functional structures<sup>73</sup>. The mechanisms of actin polymerization as well as their corresponding regulators are not still not yet fully understood and require further investigation. For instance, in order to further reveal the influence that actin-binding proteins or peptides have upon the mechanical properties of actin filament networks, minimal systems

of purified proteins reconstituted *in vitro* are used. Section 2.8 introduces a method, which is utilized to explore the impact of actin-crosslinking proteins on the actin mechanics and gives some examples of characterized actin crosslinkers, which naturally occur in cells.

### 2.5 Naturally occurring actin crosslinkers

Cells exhibit a broad range of actin-binding proteins, including actin crosslinkers, such as filamin<sup>111</sup>, scruin<sup>112</sup>, espin<sup>113</sup>,  $\alpha$ -actinin<sup>114</sup> or fascin<sup>115,116</sup> (see Table 2). Both of the latter named actin crosslinkers are introduced in more detail in the following sections, as these two proteins were to be mimicked by synthetically produced crosslinking constructs (2.6) within this work.

#### 2.5.1 Alpha-actinin - the “weak” binder

Alpha-actinin is a ubiquitously conserved actin crosslinking protein found in both muscle and nonmuscle cells at points where actin is anchored to a variety of intracellular structures. It is member of a highly conserved family of actin-binding proteins, the spectin superfamily<sup>117</sup>. Alpha-actinin functions as a homodimer, consisting of two identical peptides that are arranged in an antiparallel fashion. It was reported to have a subunit molecular weight of 94 – 103 kDa<sup>118,119</sup> that appeared in electron micrographs<sup>120</sup> as a 30 - 40 nm long rod with globular regions at each end. Studies of the  $\alpha$ -actinin amino acid sequence as well as data obtained from proteolysis experiments showed that it is composed of three domains. The N-terminal 250 amino acid (aa) residues form an actin-binding domain (ABD)<sup>121</sup>. The central rod-like domain is formed by four spectrin-like, triple-helical coiled-coil repeats, each of 122 amino acid residues. These spectrin repeats as well as the linker sequences between them confer an important mechanical property on  $\alpha$ -actinin: the molecule has significant elasticity, which allows it to resist mechanical strain, a useful feature for a protein found in many types of cellular adhesion<sup>114</sup>. The C-terminal calmodulin (CaM)-like domain, consisting of 150 residues, contains two EF-hand motifs (helix-loop-helix), which bind  $\text{Ca}^{2+}$  and thereby regulate the actin-binding affinity<sup>122,123</sup>. An illustration of the conformation of  $\alpha$ -actinin is given in Figure 10.

A number of different  $\alpha$ -actinin isoforms were identified<sup>119,124–127</sup> and are grouped into two distinct classes: muscle and nonmuscle cytoskeletal isoforms. Whereas binding of nonmuscle actinin to actin is calcium sensitive, binding of muscle isoforms is calcium insensitive<sup>124</sup>. Skeletal, cardiac and smooth muscle isoforms (isoforms 2 and 3) are localized in the Z-disk, which is the boundary between sarcomeres in striated muscle, where it cross-links actin filaments from adjacent sarcomeres, forming a lattice-like structure that stabilizes the muscle contractile apparatus<sup>128</sup>. Whereas  $\alpha$ -actinin 2 is found in the cardiac and oxidative skeletal

muscle,  $\alpha$ -actinin 3 is overexpressed in glycolytic skeletal muscle fibers<sup>129</sup>. The following section introduces the functions of nonmuscle  $\alpha$ -actinins in more detail.

### Alpha-actinin of nonmuscle cells

Alpha-actinin of nonmuscle cells occurs at the cytoplasmic face in multiple subcellular regions, including cell-cell and cell-matrix contact sites, cellular protrusions, lamellipodia as well as stress fiber dense regions, indicating that it plays multiple important roles in the cell. This includes the linkage of the cytoskeleton to many different transmembrane proteins in a variety of junctions and the regulation of the activity of multiple receptors. Furthermore, it serves as a scaffold to connect the cytoskeleton to diverse signaling pathways<sup>114</sup>.

Both nonmuscle isoforms (isoforms 1 and 3) were found to be associated with stress fibers and focal adhesions<sup>117,130</sup>. However, their distribution differs in highly motile cells. Alpha-actinin isoform 4 is more concentrated in circular dorsal ruffles and was reported to be closely associated with newly formed macropinosomes<sup>131,132</sup>. Point mutations in the ABD of the  $\alpha$ -actinin 4 gene (ACTN4), which cause a form of kidney damage known as focal segmental glomerulosclerosis (FSGS), showed an increased affinity for F-actin that resulted in slowing down of intracellular dynamics<sup>1</sup>. The major nonmuscle isoform 1 was shown to be distributed along stress fibers in a distinct, periodic array<sup>86</sup>. Moreover, it was shown to localize at highly dynamic regions, such as lamellipodia at the leading edges of migrating cells<sup>133,134</sup>. Due to the fact that nonmuscle  $\alpha$ -actinin 1 has been reported to play diverse roles in both actin-filament as well as integrin  $\beta$ 1<sup>135</sup> and  $\alpha$ -catenin<sup>134</sup> binding, its protein expression levels have been correlated with many cell functions, such as adhesive strength, cell motility, cell growth rates, as well as metastatic transformation<sup>136,137</sup>. Glück *et al.* reported, for instance, that the downregulation of  $\alpha$ -actinin in 3T3 fibroblasts led to an increased cell motility, whereas an overexpression showed a strongly reduced migration<sup>137</sup>. Moreover they found that an overexpression of  $\alpha$ -actinin 1 in SVT2 cells led to a complete suppression of their ability to form tumors in syngeneic BALB/c mice, which suggests, that  $\alpha$ -actinin, which is also localized in cell junctions, may have an effective suppressive effect on the tumorigenic properties<sup>136</sup>.

The biomechanical behavior of reconstituted actin networks enriched with  $\alpha$ -actinin is described in section 2.8.2.

### 2.5.2 Fascin - the “strong” binder

Fascin is a 55 kDa monomeric protein that crosslinks actin filaments *in vitro* into unipolar and tightly packed, stiff bundles with well-defined diameters<sup>115,138,139</sup>. In living cells, it assists in the organization of two major forms of actin-based structures which are cortical cell protrusions that mediate cell interactions and migration, and cytoplasmic microfilament bundles that contribute to cell architecture and to intracellular movements<sup>116</sup>. Fascin particularly localizes to a number of highly dynamic cellular structures that require strong mechanical support, such as stress fibers, microvilli, filopodia as well as lamellipodia<sup>140,141</sup>. Moreover, fascin is highly expressed in specialized cells which are particularly rich in filopodia, such as neurons and mature dendritic cells, as well as in many transformed cells such as HeLa cells<sup>142,143</sup>. In vertebrates, three forms of fascin are encoded on the genome: fascin 1 (also known as fascin), which is broadly expressed by mesenchymal tissues and in the nervous system<sup>144</sup>, fascin 2, which is found in retinal photoreceptor cells<sup>145</sup> and fascin 3, which only occurs in testis<sup>146</sup>.

Fascin consists of four beta-trefoil domains and, as an actin-crosslinking protein, contains at least two actin-binding sites. One site is located in the first beta-trefoil domain between amino acid residues 33 - 47 at the amino terminus. The other actin-binding site is assumed to lie between aa 277 - 493<sup>142</sup>. The amino acid residue Ser 39<sup>147</sup>, which is located within the first actin-binding site, plays an important role. The actin-bundling activity of fascin is inhibited by phosphorylation of Ser 39 by protein kinase C $\alpha$  (PKC $\alpha$ ) that blocks the activity of the N-terminal actin-binding site<sup>143</sup>. PKC $\alpha$  is a regulator of focal adhesions. It is activated by integrin-mediated adhesion and has significant regulatory effects on cell migration. Anilkumar *et al.* found that the specific blockade of the fascin/PKC $\alpha$  interaction increases cell migration on fibronectin in conjunction with increased fascin protrusions and remodeling of focal adhesions. Thus, the interaction of fascin and PKC $\alpha$  represents a point of intersection that regulates the balance between contractile adhesions and protrusions and thereby modulates cell migratory behavior<sup>148</sup>.

The biomechanical behavior of reconstituted actin networks in presence of fascin is described in section 2.8.2.

### 2.6 Synthetic actin crosslinkers

In contrast to permanent, chemical crosslinks in classical polymer systems, biological crosslinks such as those introduced in the previous sections have a far broader parameter space defined by the molecular details of their binding and connective regions. Factors such as affinity, size, flexibility, orientation, and biochemical switches allow these components to

## Theoretical Background

function beyond simply imposing local affine responses against external deformations<sup>149–152</sup>. The coexistence of bundles and regular networks are ubiquitous in mixtures of actin with the naturally occurring crosslinker  $\alpha$ -actinin, possibly due to its low binding affinity<sup>153–156</sup>. Likely, molecular and physical details of the naturally occurring crosslinkers enable the structural polymorphism that is important to the mechanical behaviors of cells. This, however, imposes a central limitation to systematic investigations and development of biomimetic or bio-inspired materials: using different native biological crosslinkers to explore the phase space of one parameter (e.g. using  $\alpha$ -actinin and fascin to vary binding strength) is unavoidably coupled with unwanted variations of several other parameters<sup>89,140</sup>. Genetic mutation can be used to perturb crosslinker properties such as binding kinetics or size<sup>1,157,158</sup>, however, its empirical nature and complexity inhibits systematic studies where different key parameters can be modified in a completely decoupled manner. This natural limitation was resolved in the work presented here by engineering purely synthetic actin crosslinkers (4.28), whose core building block is a 20 nm long, double-stranded DNA, which can be covalently coupled to actin-binding peptides on both sides via a copper-free click chemistry approach (SPAAC). Thus, the basic geometry of the crosslinkers are conserved while properties such as binding affinity towards actin can be tuned independently by varying the attached actin-binding peptides. Here, either LifeAct<sup>®</sup> (2.7.1) or Phalloidin (2.7.2) was covalently conjugated to both ends of the DNA spacer as the means to mimic  $\alpha$ -actinin (2.5.1) as a weak, or fascin (2.5.2) as a strong binder, respectively. For simplicity, the weak LifeAct<sup>®</sup>-based and the strong Phalloidin-based crosslinkers are denoted as wLX and sPX in the following. The imitation of natural crosslinkers by synthetic ones is exemplarily shown for  $\alpha$ -actinin and wLX in Figure 10.

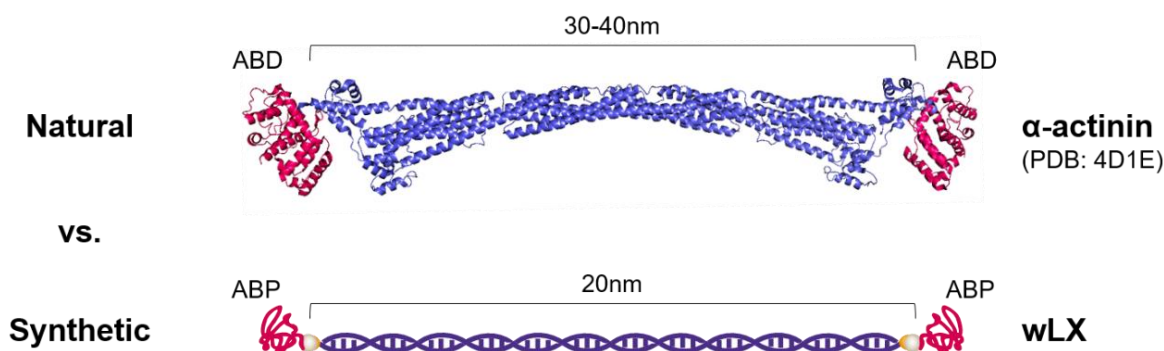


**Figure 10 | Mimicking the naturally occurring crosslinker  $\alpha$ -actinin with wLX.** This illustration exemplarily shows the imitation of the naturally occurring weakly-binding actin crosslinker  $\alpha$ -actinin (PDB code: 4D1E) with the DNA-based LifeAct<sup>®</sup> crosslinker (wLX). ABD, actin-binding domain (aa residues 34 – 254); ABP, actin-binding peptide (in this case LifeAct<sup>®</sup>). Spacer domains are colored in blue: i.e. aa residues 255 - 892 for  $\alpha$ -actinin, which is 30 - 40 nm in length; 60bp DNA spacer for wLX, which is 20 nm in length. Illustration of  $\alpha$ -actinin was conducted with PyMOL.

### 2.7 Actin-binding peptides

#### 2.7.1 LifeAct®

In 1998, Asakura *et al.* discovered an F-actin-binding protein of a molecular mass of ~140 kDa, which was named Abp140. They found that Abp140 directly interacts with F-actin and binds along the sides of F-actin. In addition, immunofluorescence studies as well as green fluorescent protein (GFP) fusions revealed that Abp140 co-localized with filamentous actin structures<sup>159,160</sup>. Riedl *et al.* found that the first 17 amino acids (MGVADLIKKFESISKEE) of Abp140 were sufficient to mediate actin localization comparable to the full-length protein. Interestingly they also reported that this short peptide, named LifeAct®, is conserved among close relatives of *Saccharomyces cerevisiae* but absent from other organisms, which made it an attractive *in vivo* actin marker for higher eukaryotes within the last years<sup>161</sup>. LifeAct®-GFP fusions stained filamentous actin structures such as lamellipodia, filopodia or stress fibers in eukaryotic cells and tissues. Also, they observed no signs of cytotoxicity, abnormal morphology or of growth retardation in transiently or stably transfected cell lines<sup>161</sup>. Furthermore, Riedl *et al.* measured the affinity of LifeAct® to F-actin with a dissociation constant  $K_D$  of  $2.3 \pm 0.9 \mu\text{M}$  and found that LifeAct® did not affect nucleation and elongation phases of actin polymerization as well as depolymerization rates *in vitro* (pyrene assay)<sup>161</sup>.

#### 2.7.2 Phalloidin

Phalloidin is a toxin that belongs to the group of phallotoxins and was isolated from the death cap mushroom *Amanita phalloides* by Feodor Lynen and Ulrich Wieland in 1937<sup>162</sup>. It is a bicyclic heptapeptide that contains a cysteine-tryptophan linkage (tryptathionine bond). Phalloidin was found to bind tightly and specifically to filamentous actin with a  $K_D$  of  $\sim 9 \text{ nM} \pm 2 \text{ nM}$  and reported to stabilize actin filaments from a variety of depolymerizing agents<sup>163,164</sup>. Simulations on F-actin gave evidence that Phalloidin interacts with three actin subunits and therefore stabilize subunit interactions<sup>165</sup>. Moreover, Estes *et al.* showed that phalloidin decreases the critical concentration for actin polymerization *in vitro* as it reduces the dissociation rate constant of monomers from filament ends<sup>166</sup>. Phalloidin was also reported to inhibit the binding of ADF/cofilin to actin filaments<sup>167</sup>. Due to its strong binding to F-actin, fluorochrome-conjugated phalloidins are widely used in microscopy to visualize actin structures within cells.

### 2.8 Reconstituted actin networks (*in vitro*)

As mentioned in section 2.4, F-actin assembles at different structural morphologies in order to provide the cell with certain functions. Whereas the actin cortex, which determines the shape and the mechanical strength of a cell, is composed of a network of crosslinked filaments, closely-packed actin bundles provide support or create membrane protrusions which are important for cellular motility. Processes, such as cell motion, cell division as well as intracellular transport require strongly regulated spatial and temporal remodeling of actin networks. In order to control the network assembly and disassembly, the morphology and the biomechanical properties of the actin network, cells make use of actin-binding proteins (ABP). However, since a lot of these proteins occur simultaneously in the cytoskeleton, it is rather difficult to conclude any correlation of the network morphology and the viscoelastic response *in vivo*. In order to investigate this correlation *in vitro* in a non-overcrowded environment, reconstituted actin networks, a very minimal system, are used. Thereby, different actin/ABP mixtures can be investigated while the biochemical network composition can be precisely controlled. Isolated and purified actin can be maintained as G-actin (monomers) by eliminating nearly all salts present, including calcium ions rather than magnesium ions and storing it under mildly alkaline conditions, i.e. 1X G-buffer conditions (4.3). This G-actin solution can then be induced to form filaments by adding a concentrated buffer mix, i.e. 20X KME-buffer (4.3) that alters pH, switches divalent cations, and increases salt concentrations into the physiological range<sup>168</sup>. Moreover, fluorescently labeled actin derivatives, such as pyrene-actin, are a useful tool to study the kinetics of actin polymerization and depolymerization *in vitro* as the fluorescence intensity increases linearly with the degree of polymerization<sup>169,170</sup>. According to this reconstitution of actin networks, the physical as well as biochemical effects of ABP can be independently correlated to both the network mechanics and the structural morphology. In order to characterize complex actin filament assemblies, different experimental techniques such as rheology, light scattering, microscopy, conventional biochemical methods as well as theoretical modellings and simulations were combined in recent years. A rather old but common technique to investigate the biomechanical properties of reconstituted actin networks is shear rheology, which is described in the following section.

#### 2.8.1 Shear rheology of reconstituted actin networks

Rheology is utilized to investigate both, the elastic as well as the viscous properties of a material. Those materials, which behave as a combination of elastic and viscous components, are named viscoelastic materials. As actin shows this kind of characteristic, it is classified a viscoelastic biopolymer. The influence of actin-binding proteins and/or actin crosslinkers on the mechanical properties of actin networks are of great interest in science and have been

## Theoretical Background

studied intensively via shear rheology, which is defined as the characterization of flow or deformation originating from an applied shear stress.

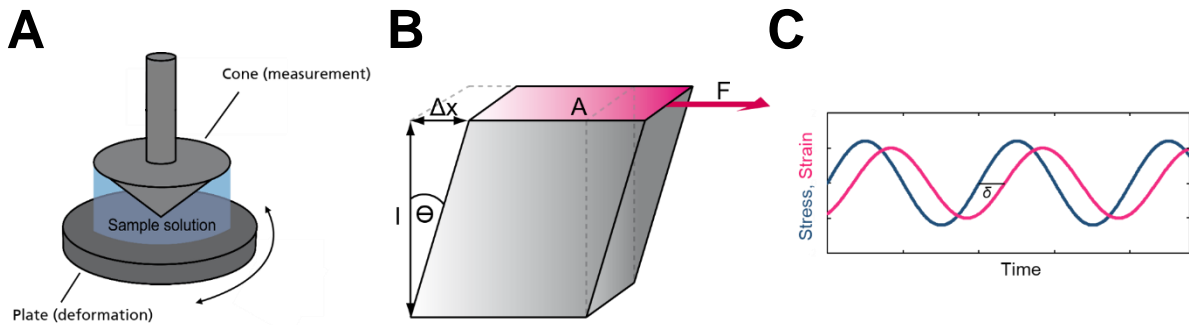


**Figure 11 | Principles of shear rheology.** (A) Illustration of an actin sample that is polymerized between a plate and a cone (picture kindly provided by Jörg Schnauß). (B) The sample experiences a certain stress, which is, in correlation to its biomechanical properties, transmitted through the sample. The responding strain is measured on the fixed plate. (C) Doing this in an oscillatory fashion, the complex shear modulus  $G^*$  can be derived, which includes both, the elastic response as well as the viscous response of the system. The shear modulus describes the tendency of a sample to shear, i.e. the deformation of shape at a constant volume.

In rheology, schematically illustrated in Figure 11 A, the actin sample is sitting between a rotating cone and a fixed plate. On the upper side of the actin sample, a certain shear stress is applied. The shear stress  $\sigma$ , as shown in Equation 1, is defined as the force  $F$  per area  $A$  on which the force acts (Figure 11 B).

$$\sigma = \frac{F}{A}$$

Equation 1

Depending on its viscoelastic properties, the applied force is transmitted through the actin sample and the response of the system, i.e. the strain, is measured with respect to the lower fixed plate. The shear strain  $\gamma$  is defined as the transverse displacement  $\Delta x$  over the initial length  $l$ , as seen in Equation 2.

$$\gamma = \frac{\Delta x}{l}$$

Equation 2

The shear modulus  $G$ , also known as the modulus of rigidity, is defined as the ratio of shear stress to the shear strain, as given in Equation 3.

$$G = \frac{\sigma}{\gamma} = \frac{F/A}{\Delta x/l}$$

Equation 3

Performing the measurement in an oscillatory fashion, i.e. at a certain angular frequency  $\omega$ , the complex shear modulus  $G^*(\omega)$  [Pa] can be derived, as shown in Equation 4. The complex shear modulus can be divided into the elastic/shear modulus (Equation 5) and the viscous/loss modulus (Equation 6), corresponding to  $G'$  and  $G''$ , respectively. The elastic modulus  $G'$  at a frequency of 1 Hz is referred as to the plateau modulus  $G_0$ .

$$G^*(\omega) = G'(\omega) + iG''(\omega)$$

Equation 4

$$G'(\text{elastic modulus}) = \frac{\sigma}{\gamma} \cos \delta$$

Equation 5

$$G''(\text{viscous modulus}) = \frac{\sigma}{\gamma} \sin \delta$$

Equation 6

The corresponding phase angle  $\delta$  (Figure 11 C) measures the relative importance of viscous to elastic contributions for a material at a given frequency and is defined as followed in Equation 7. An ideal, purely elastic material (solid-like) behaves with  $\delta = 0^\circ$ , whereas a purely viscous material, i.e. a material behaving as a Newtonian fluid, behaves with  $\delta = 90^\circ$ . Viscoelastic materials are defined to show phase angles between  $0^\circ$  and  $90^\circ$ . Pure, viscoelastic actin networks displayed a phase angle around  $40^\circ$  (5.3.1). An example of the time course of the stress function (blue curve) and the corresponding strain function (magenta curve) for a viscoelastic material is given in Figure 11 C.

$$\tan \delta(\omega) = \frac{G''(\omega)}{G'(\omega)}$$

Equation 7

The viscous ( $G''$ ) as well as elastic ( $G'$ ) moduli of a reconstituted actin network are exemplarily illustrated in Figure 12. As the elastic properties dominate in actin networks,  $G'$  is emphasized in this work.

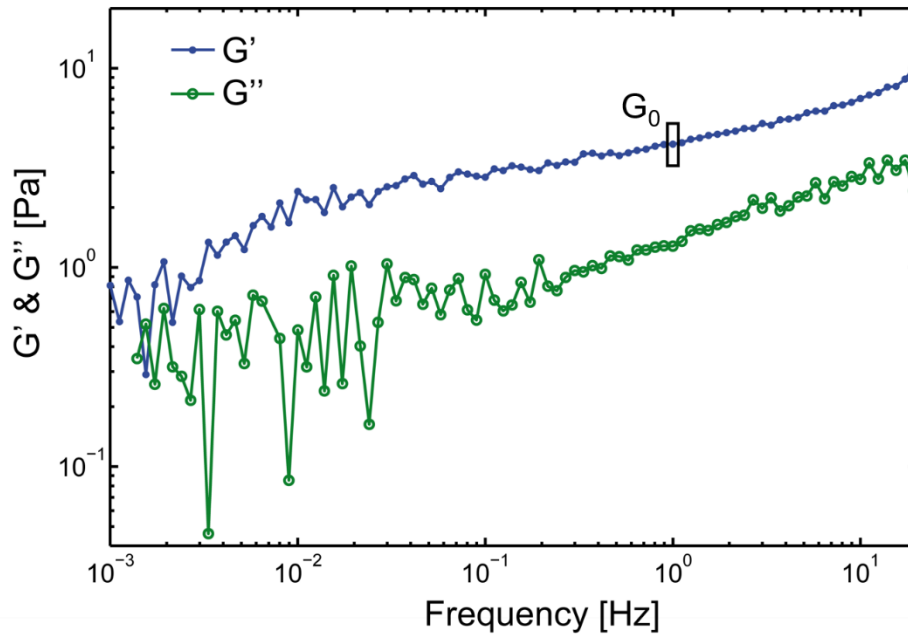


**Figure 12 | Viscous and elastic properties of a reconstituted actin network.** Actin was polymerized at a concentration of 24  $\mu\text{M}$  and measured via shear rheology. The elastic modulus  $G'$  (blue curve) as well as the viscous response  $G''$  (green curve) are plotted over the applied frequency. The applied strain was 5 %.  $G_0$ , which is the elastic modulus  $G'$  at a frequency of 1 Hz, is exemplarily black edged.

## 2.8.2 Structure and mechanics of reconstituted actin networks

Both the structural morphology and the viscoelastic properties of the formed actin network strongly depend on the concentration as well as on the biochemical and micromechanical properties of the crosslinker, i.e. the affinity of the actin-binding domains towards F-actin, the number of binding domains as well as the length and flexibility of the spacer in between. Two generic types of F-actin assemblies can be distinguished: networks of individual crosslinked actin filaments and actin bundles. However, in particular regions of the cytoskeleton either one of these assembly types may dominate or they may appear in coexistence. The main goal of ongoing and past research is to understand the local structures and rearrangements invoked by the different actin crosslinkers<sup>150</sup>. Several naturally occurring actin crosslinkers, such as  $\alpha$ -actinin<sup>151,171,172</sup>, filamin<sup>173–175</sup>, fascin<sup>139,140,174</sup> as well as crosslinker mutants<sup>176</sup> have been explored concerning their influence on the biomechanical properties as well as on the structural morphology of actin networks *in vitro*. Besides microscopic analysis, this includes the investigation of such networks via shear rheology. Table 2 gives an exemplary overview about the *in vitro* found structural morphologies that can be correlated to the *in vivo* function of some actin crosslinkers as well as actin-binding proteins.

## Theoretical Background

**Table 2 | Examples of actin-binding proteins studied *in vivo* and in reconstituted actin networks**

<b>Actin crosslinker</b>	<b><i>In vivo</i> function</b>	<b>Structural morphology of reconstituted actin networks</b>
<b>Large actin crosslinker</b>		
$\alpha$ -actinin	$\alpha$ -actinin is the most prominent actin-bundling protein in stress fibers and is also found in cellular protrusions such as lamellipodia <sup>114</sup> .	At low concentrations, $\alpha$ -actinin forms orthogonally crosslinked actin networks whereas at higher concentrations bundles are formed <sup>89,177</sup> .
Filamin	Filamin is omnipresent in eukaryotic cells. It is found in stress fibers and reported to be involved in signaling processes <sup>111</sup> .	Below a certain threshold concentration, filamin crosslinks actin filaments into an orthogonal network, whereas above this concentration filamin builds branched actin bundles, which are curved due to internal stresses <sup>111,173,175,178</sup> .
<b>Small actin crosslinker</b>		
Fascin	Fascin is found in dynamic, cortical cell protrusions such as filopodia <sup>82</sup> .	Above a critical concentration, fascin forms actin networks of straight, parallel bundles <sup>179</sup> .
Espin	Espin is an actin-bundling protein found in brush border microvilli and hair cell stereocilia <sup>113,113</sup> .	Espin forms long, straight and parallel actin bundles similar to fascin <sup>180</sup> .
<b>Actin-binding protein</b>	<b><i>In vivo</i> function</b>	<b>Structural morphology of reconstituted actin networks</b>
Heavy meromyosin (HMM, i.e. a subfragment of myosin II)	HMM is the larger subfragment of the molecular motor myosin II that contains the ATPase region and the actin-binding region. HMM does not occur in cells as it is obtained by chymotrypsin digestion of myosin II <sup>181</sup> .	HMM binds, in absence of ATP, to actin filaments in the rigor state and thus can form interfilamental crosslinks. Actin/HMM networks were shown to be homogeneously and isotropically crosslinked without embedded bundle structures <sup>182</sup> .
Tropomyosin	Tropomyosin was shown to protect F-actin from disassembly through ADF/cofilin <sup>183</sup> .	Tropomyosin binds end to end to actin filaments, spanning over seven actin subunits along the filament <sup>184</sup> and does not form interfilamental crosslinks. Thus, actin/tropomyosin networks consist of single, entangled actin filaments.

As already mentioned, structural morphologies of actin networks depend on crosslinker properties such as concentration, length and affinity. For instance, in order to induce a major effect on the global structure and mechanics of a solution of actin filaments, a critical crosslinker concentration is needed. Below this threshold, some crosslinkers such as

$\alpha$ -actinin<sup>89</sup> and HMM<sup>185</sup> induce local heterogeneities. Those heterogeneities increase with increasing crosslinker concentration until the crosslinking proteins are equally distributed and cause a global change in the network structure. This transition was previously reported for  $\alpha$ -actinin as different structural morphologies were induced in a concentration-dependent manner. Entangled actin solutions were weakly crosslinked at low  $\alpha$ -actinin concentrations and an increase in concentration led to composite networks of crosslinked actin filaments and bundles. At high  $\alpha$ -actinin concentrations bundled networks and even clusters of actin bundles were observed<sup>150</sup>.

Moreover, it was shown that small crosslinkers such as fascin<sup>179</sup> and espin<sup>180</sup> tend to tightly pack actin filaments into bundles, whereas larger actin crosslinkers, such as  $\alpha$ -actinin<sup>89,177</sup> and filamin<sup>111,173,175</sup> induce a more complex behavior, as they formed crosslinked networks of actin filaments at low concentrations and purely bundled or composite networks at high concentrations. This was also supported by engineered actin crosslinkers that had actin-binding domains separated by different numbers of *Dictyostelium discoideum* filament rods, i.e. they differed in length but not in affinity towards F-actin. In this case, the shortest crosslinkers showed the highest F-actin bundling propensity<sup>158</sup>.

Furthermore, the affinity of the actin crosslinker towards F-actin is an important factor. Wachsstock *et al.* studied the impact of the  $\alpha$ -actinin affinity and found that different affinities towards actin cause different bundling threshold concentrations<sup>89</sup>. The impact of the weakly-binding crosslinker  $\alpha$ -actinin (2.5.1) and the strongly-binding crosslinker fascin (2.5.2) on the biomechanical properties of reconstituted actin networks was intensively investigated in the past. Within rheological measurements, F-actin/ $\alpha$ -actinin solutions caused a monotonic increase of  $G'$  with increasing  $\alpha$ -actinin concentrations. Accordingly, the phase angles displayed a monotonic decrease with increasing crosslinker concentration, which indicates the system became more elastic. The strong crosslinker fascin did also show this monotonic increase of  $G'$  until a certain concentration was reached. However, above this threshold concentration, actin/fascin networks displayed a non-monotonic behavior. Initially, the elastic modulus drastically increased until reaching a peak which subsequently relaxed to a more viscous dominated state. The corresponding phase angles increased at high fascin concentrations, indicating the system becoming more viscous. The behavior of the drastic increase of  $G'$  followed by a drop in elasticity was referred to as the “elasticity burst”<sup>140</sup>. In 2011, Lieleg *et al.* showed that actin networks simultaneously polymerized with fascin formed pre-stressed structures which are bent beyond their equilibrium configuration<sup>139</sup> due to the fact that filament elongation<sup>186</sup> is faster than dissociation of the strongly-binding crosslinker<sup>187</sup>. The relaxation, i.e. the decrease of  $G'$ , could be induced by glassy dynamics aiming to release the stress towards equilibrium<sup>139</sup>, and/or occur due to filament breakage, as filaments are subjected to significant bending forces<sup>188</sup>.

## 2.9 Epithelial-mesenchymal transition (EMT)

The epithelial-mesenchymal transition (EMT) describes a biological process, in which a polarized epithelial cell that normally interacts with basement membrane via its basal surface, is transformed to a non-polarized mesenchymal cell, which imparts the transformed cell with enhanced capabilities of migration, invasiveness, evasion of apoptosis and increased production of extracellular matrix (ECM) components. The degradation of the underlying basement membrane as well as the ability to migrate away from the epithelial layer represents a signal for the completion of an EMT. Several molecular processes are involved in both the initiation and the completion of EMT, which include the activation of transcription factors, expression of characteristic cell-surface receptors, reorganization and expression of cytoskeletal proteins, production of matrix metalloproteinases (MMPs) that degrade ECM components, as well as changes in the expression of specific microRNAs. Moreover, factors regulating EMT are often used as biomarkers to study different phases of EMT. EMT is involved in many cellular processes, including development, fibrosis, and cancer, and depending on its function it is classified into three EMT subtypes as described in Table 3<sup>189</sup>.

**Table 3 | Classification of epithelial-mesenchymal transition (EMT)<sup>189</sup>**

<b>EMT subtype</b>	<b>Characteristics</b>
Type 1	This subtype is associated with implantation, embryo formation and organ development. It is organized to generate diverse cell types that share common mesenchymal phenotypes. Moreover, this type neither causes fibrosis nor an invasive phenotype. Type 1 EMTs can generate mesenchymal cells that have the potential to undergo a mesenchymal-epithelial transition (MET) in order to build secondary epithelia.
Type 2	This EMT subtype is associated with wound healing, tissue regeneration and organ fibrosis. Further, these EMTs are associated with inflammation and terminate once inflammation is attenuated.
Type 3	This type of EMT is present in neoplastic cells that have previously undergone genetic changes, specifically in genes that favor clonal outgrowth and the development of localized tumors. Cancer cells undergoing a type 3 EMT may invade and metastasize and thereby generate the final, life-threatening form of cancer progression.

Tumor cell dissemination is critical in cancer progression and involves various processes, including EMT (type 3), leading to the formation of metastases at remote loci. As EMT progress, epithelial cell-cell contacts are dissolved and cells lose their apical-basal polarity<sup>189</sup>. Additionally, epithelial junction proteins, for instance epithelial (E)-cadherin, and

## Theoretical Background

other epithelial markers are downregulated and the expression of mesenchymal adhesion and marker proteins, such as  $\alpha$ -smooth muscle actin (SMA), is increased<sup>190</sup>. Moreover, the actin cytoskeleton is drastically reorganized and phenotypic changes occur to enable the cell to acquire a front-rear polarity and motility. In the end, cells gain invasive properties due to an increased expression and secretion of MMPs. Furthermore, these cells are able to synthesize components of the ECM, i.e. collagen and fibronectin, to reconstitute their micro-environment<sup>189,191,192</sup>. Conversely, after reaching a secondary colonization site, cancer cells that have acquired mesenchymal properties are able to revert to an epithelial phenotype through mesenchymal-epithelial transition (MET), thus reacquiring the properties of the original tumor following metastasis<sup>193</sup>. Figure 13 schematically gives an overview about changes that cells undergo during EMT, involving upregulated proteins (markers) for both phenotypes, respectively.

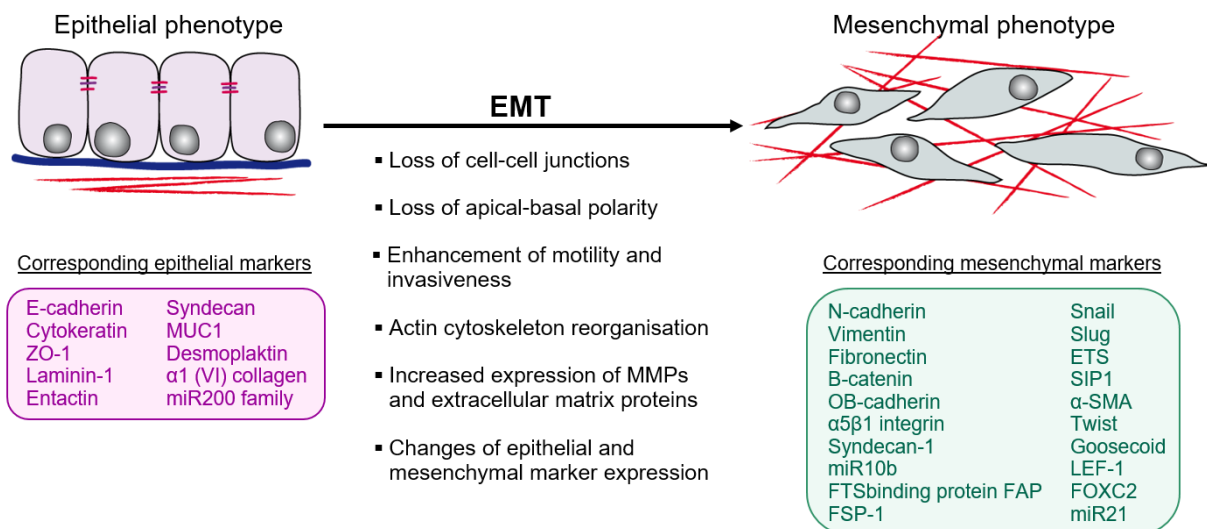


**Figure 13 | Schematic of epithelial-mesenchymal transition (EMT).** During EMT, cells lose their epithelial characteristics and acquire mesenchymal properties. This involves the loss of epithelial cell - cell contacts and apical-basal polarity. Moreover, transformed cells gain mesenchymal markers and invasive properties, characterized by a reorganization of the actin cytoskeleton and an increased expression of matrix metalloproteases (MMPs) as well as extracellular matrix components. Picture modified from Katsuno *et al.* (2013)<sup>193</sup> and Kalluri & Weinberg (2009)<sup>189</sup>.

In case of many carcinomas (type 3 EMT), EMT-inducing signals, such as hepatocyte growth factor (HGF), epithelial growth factor (EGF), platelet-derived growth factor (PDGF) and transforming growth factor beta (TGF- $\beta$ ), appear to be responsible for the induction or functional activation of a broad range of EMT-inducing transcription factors<sup>189</sup>. In the following, the induction of EMT mediated by TGF- $\beta$  is introduced in more detail with special focus on cancer cell progression.

### TGF- $\beta$ signaling in EMT

Two possible signaling pathways have been identified as mediators of TGF- $\beta$ -induced EMT: the Smad and the non-Smad pathways, as depicted in Figure 14. Both signaling pathways are initiated upon the interaction of TGF- $\beta$  with a tetrameric cell surface complex of two type II and two type I transmembrane kinase receptors, T $\beta$ RII and T $\beta$ RI. Following TGF- $\beta$  binding, T $\beta$ RII directly phosphorylates T $\beta$ RI. Within the Smad pathway, the intracellular mediators Smad2 and Smad3 then are phosphorylated. Two activated Smad2/3 proteins combine with one Smad4 to form a trimeric Smad complex that is translocated into the nucleus<sup>194,195</sup>. In conjunction with other nuclear cofactors, Smad signaling regulates the expression of the three families of EMT-inducing transcription factors, Snail/Slug, zinc finger E-box binding homeobox 1 and 2 (ZEB1/2), and Twist<sup>196</sup>. These transcription factors repress the expression of epithelial markers, in turn activate the expression of mesenchymal markers<sup>193</sup> and thus promote EMT. For instance, Vincent *et al.* reported the direct interaction of the Smad3/4 complex with regulatory promoter sequences of Snail, which form an active complex that binds to regulatory promoter sequences of the genes encoding the epithelial junction proteins occludin and E-cadherin, leading to TGF- $\beta$ -induced repression of their expression<sup>197</sup>. In addition to Smad signaling, TGF- $\beta$  also initiates non-Smad signaling from the T $\beta$ RII/T $\beta$ RI complexes, leading to the activation of pathways that are more commonly seen as effectors of receptor tyrosine kinase signaling, such as PI3K-Akt-mTOR and Rho-GTPases pathways<sup>198</sup>, leading to increased motility and invasion, as well as changes in protein synthesis and cytoskeletal reorganization<sup>193,199,200</sup>. Reorganization of the actin network is associated with the myocardin-related transcription factor (MRTF) - serum-response factor (SRF) signaling pathway, which connects both the canonical and the non-canonical pathway (see Figure 15).

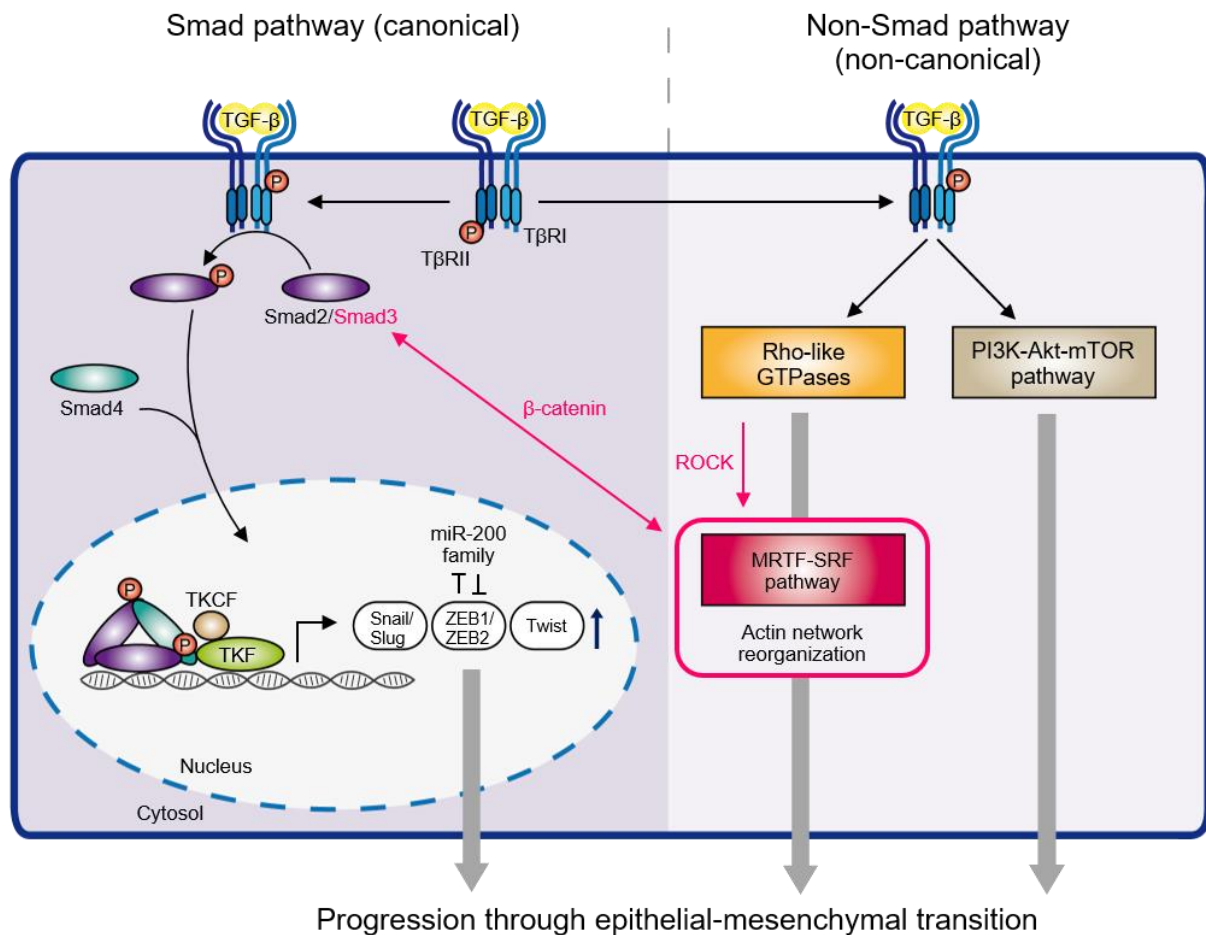


**Figure 14 | Simplified schematic of Smad and non-Smad signaling in TGF- $\beta$ -induced EMT.** TGF- $\beta$  signaling induces EMT through Smad (canonical) and non-Smad (non-canonical) pathways, where, upon ligand binding, two type II (T $\beta$ RII) and two type I (T $\beta$ RI) transmembrane kinase receptors phosphorylate and activate Smad2 and Smad3. Those activated Smad proteins complex with Smad 4 and translocate into the nucleus where it regulates the transcription of target genes through interactions with other transcription factors (TKF) and transcription cofactors (TKCF). Thereby, three families of EMT-inducing transcription factors are upregulated: Snail/Slug family, zinc finger E-box binding homeobox 1 and 2 (ZEB1 and ZEB2) family and Twist family. These transcription factors are responsible for the repression of the expression of epithelial markers and the upregulation of the expression of mesenchymal markers. Other pathways, which do not involve Smad proteins, are also activated by TGF- $\beta$ . For instance, TGF- $\beta$  activates small GTPases, including Rho, which leads to an increase in migration and invasion as well as changes in protein synthesis and reorganization of the actin cytoskeleton. The MRTF-SRF signaling pathway affects the reorganization of the actin cytoskeleton and connects the canonical and non-canonical Smad pathway, illustrated in magenta. A more detailed overview is shown in Figure 15. Abbreviations: TGF- $\beta$ , transforming growth factor  $\beta$ ; T $\beta$ RI, TGF- $\beta$  receptor type I; T $\beta$ RII, TGF- $\beta$  receptor type II; TKF, transcription factor; TKCF, transcription cofactor; P, phosphorylated. Schematic modified from Katsuno *et al.* (2013)<sup>193</sup>.

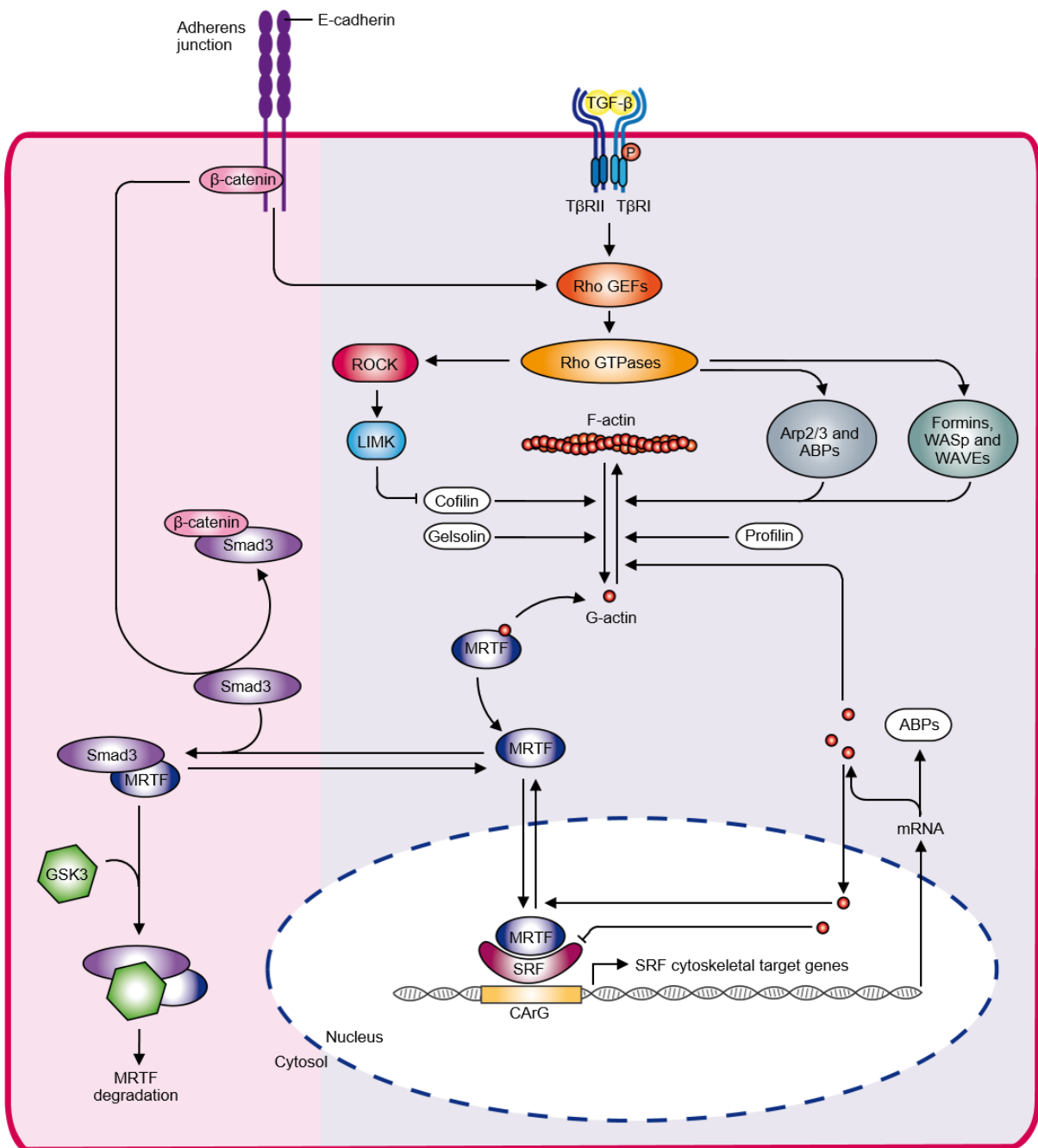


**Figure 15 | MRTF-mediated regulation of SRF-dependent cytoskeletal target genes.** The MRTF-SRF signaling pathway affects the reorganization of the actin cytoskeleton and connects both the Smad and the non-Smad pathway. A detailed description of the MRTF-SRF signaling pathway is to be found in the text below. Abbreviations: TGF- $\beta$ , transforming growth factor  $\beta$ ; T $\beta$ RI, TGF- $\beta$  receptor type I; T $\beta$ RII, TGF- $\beta$  receptor type II; Rho GEFs, Rho guanine nucleotide exchange factors; ROCK, Rho-associated kinase; LIMK, LIM kinase; WASp, Wiskott-Aldrich syndrome protein; WAVEs, WASp-family verpulin homologues; Arp2/3, Actin-related protein 2/3; ABPs, Actin-binding proteins; GSK3, Glycogen synthase kinase-3 $\beta$ ; MRTF, Myocardin-related transcription factor; SRF, Serum-response factor; CArG, palindromic CC(A/T)<sub>6</sub>GG DNA sequence; P, phosphorylated. Image modified from Olson & Nordheim (2010)<sup>201</sup> and Charbonney *et al.* (2011)<sup>202</sup>

The activation of several membrane receptors, for instance TGF- $\beta$  receptors and E-cadherins at adherens junctions, affects the cytoskeletal actin dynamics, as they modulate the activity of Rho GTPases<sup>203</sup> through Rho guanine nucleotide exchange factors (Rho GEFs). Rho-associated kinase (ROCK), formins, Wiskott-Aldrich syndrome protein (WASp), WASP-family verprolin homologues (WAVEs), actin-related protein 2/3 (Arp2/3) complex, as well as other actin-binding proteins (ABPs) are effectors of Rho GTPases and orchestrate actin polymerization by incorporating G-actin into F-actin<sup>204</sup>. High levels of cytoplasmic G-actin retain MRTF in the cytoplasm, whereas an incorporation of G-actin into filamentous actin liberates MRTF to translocate into the nucleus. In the nucleus it forms a complex with the transcription factor SRF<sup>205</sup>, which then binds to the CArG region (palindromic CC(A/T)<sub>6</sub>GG DNA sequence) and triggers the expression of a subset of SRF target genes, i.e. mostly cytoskeletal genes. Nuclear MRTF can be complexed by nuclear G-actin, which inhibits MRTF-mediated stimulation of SRF-dependent transcription and facilitates MRTF nuclear export<sup>206</sup>. SRF target genes include actin itself as well as many genes that modulate actin dynamics, such as gelsolin, vinculin and cofilin. These ABP might stimulate cytoplasmic actin polymerization, complex cytoplasmic MRTF or increase levels of nuclear G-actin to downregulate MRTF-mediated transcription, and stimulate nuclear export of MRTF. The disassembly of epithelial cell contacts is an initiating event in the process of EMT. The subsequent release of catenins, such as  $\alpha$ -catenin and p120 catenin, activates actin dynamics through interaction with Rho GTPases<sup>207</sup>. Moreover, E-cadherin contributes to MRTF activation through the liberation of  $\beta$ -catenin, which neutralizes Smad3, a strong inhibitor of MRTF. Additionally,  $\beta$ -catenin maintains the stability of MRTF by suppressing the Smad3-mediated recruitment of glycogen synthase kinase-3 $\beta$  (GSK3) to MRTF, an event that otherwise leads to MRTF ubiquitination and degradation, which results in a consequent loss of SRF/MRTF-dependent proteins<sup>202</sup>.

SRF target genes, which are regulated through MRTF, encode many proteins that are related to actin cytoskeletal activities. According to their contributions to actin function, SRF-regulated gene products are grouped into three categories, which are: structural effectors (e.g. actin itself, integrin  $\beta$ 1, vinculin, tropomyosin 1), effectors of actin turnover (e.g. cofilin 1, gelsolin, villin) and regulators of actin dynamics (e.g., filamin A, talin 1, MMP-9). MMP-9 is involved in extracellular matrix remodeling, angiogenesis and migration<sup>201</sup>. Finally, Schrott *et al.* generalized that SRF affects actin treadmilling by regulating the expression of additional proteins involved in actin turnover downstream of RhoA<sup>208</sup>.

### 3 Objective

DNA nanostructures consist of partially complementary sequences that self-assemble into double-stranded objects in a temperature-dependent process. Since the underlying DNA sequence is known, the exact attachment of functional groups to DNA strands through different chemical reactions is possible. The nanometer-precise arrangement of biofunctional molecules such as peptides at specific distances is unique and a major benefit of those constructs. This has led to great interest for several medical applications and is also part of this thesis.

The first aim of this work was to establish a “plug and play” platform for the covalent attachment of functional peptides to DNA nanostructures. Therefore, different conjugation methods should be tested and finally high product yields achieved. Once peptide-conjugated DNA structures were available, three major questions were to be answered:

- 1) Do the attached biofunctional materials retain their functionality when there are covalently bound to DNA structures?
- 2) Can these peptide-functionalized DNA constructs be applied to tune reconstituted *in vitro* systems?
- 3) Are these biomimetic DNA structures able to function on particular systems inside of living cells?



## 4 Material and Methods

For all methods, sterile filter tips (Greiner Bio-One International GmbH, Austria) and reaction tubes were utilized. DNA LoBind reaction tubes (Eppendorf AG, Germany) were used for DNA containing samples. All buffers and solutions were prepared using Millipore water and, if not stated differently, sterilized through autoclavation.

### 4.1 Chemicals

Aminoallyl-dUTP	Thermo Fisher Scientific, USA
Ammonium persulfate	Carl Roth GmbH, Germany
ATP	Thermo Fisher Scientific, USA
Azidopropionic acid sulfo-NHS ester	Jena Bioscience GmbH, Germany
Biochrom AG™ Donor Horse Serum	Thermo Fisher Scientific, USA
Calcein AM, cell-permeant dye	Thermo Fisher Scientific, USA
Camptothecin	Abcam, UK
Cell carrier buffer	Zellmechanik Dresden GmbH, Germany
CellTracker™ Blue CMAC	Thermo Fisher Scientific, USA
Cholera Toxin	Sigma-Aldrich, Germany
Cultrex® 10X Coating Buffer	Biozol Diagnostica, Germany
Cultrex® 5X BME Solution	Biozol Diagnostica, Germany
Cultrex® 10X Cell Dissociation Solution	Biozol Diagnostica, Germany
DBCO-NHS ester	Jena Bioscience GmbH, Germany
DMEM/Ham's F-12, stable glutamine	Biochrom AG, Germany
DNA Gel Loading Dye (6X)	Thermo Fisher Scientific, USA
Dimethyl sulfoxide	Sigma-Aldrich, Germany
dNTP Mix	Thermo Fisher Scientific, USA
DPBS, no calcium, no magnesium (1X)	Thermo Fisher Scientific, USA
Ethanol, absolute	Carl Roth GmbH, Germany
Ethidium bromide	Carl Roth GmbH, Germany
Fluorescein Phalloidin	Thermo Fisher Scientific, USA
Fluoroshield™ with DAPI	Sigma-Aldrich, Germany
Fluoroshield™	Sigma-Aldrich, Germany

## Material and Methods

---

Gelatin solution, Type B, 2 % in dd H <sub>2</sub> O	Sigma-Aldrich, Germany
Gibco® Trypsin-EDTA (0.05 %), phenol red	Thermo Fisher Scientific, USA
Gibco FluoroBrite DMEM	Thermo Fisher Scientific, USA
Hoechst® 33342	Thermo Fisher Scientific, USA
HyClone™ Fetal Bovine Serum	Thermo Fisher Scientific, USA
Hydrocortisone	Sigma-Aldrich, Germany
Insulin	Sigma-Aldrich, Germany
Latrunculin B	Sigma-Aldrich, Germany
Lipofectamine® 3000	Thermo Fisher Scientific, USA
LysoTracker™ Deep Red	Thermo Fisher Scientific, USA
MEM Amino Acids Solution (50X)	Thermo Fisher Scientific, USA
MEM Vitamin Solution (100X)	Thermo Fisher Scientific, USA
Opti-MEM® I Reduced-Serum Medium	Thermo Fisher Scientific, USA
Penicillin-Streptomycin (10,000 U/ml)	Thermo Fisher Scientific, USA
Pierce™ Immobilized TCEP Disulfide Reducing Gel	Thermo Fisher Scientific, USA
Poly-L-ornithine	Sigma-Aldrich, Germany
Roti®-Histofix 4 %	Carl Roth GmbH, Germany
Rotiphorese® Gel 40 (29:1): 40 % acrylamide/ bisacrylamide	Carl Roth GmbH, Germany
SYBR® Gold nucleic acid gel stain	Life Technologies, USA
SYBR® Green I nucleic acid gel stain	Life Technologies, USA
TCEP	Sigma-Aldrich, Germany
TEMED	Carl Roth GmbH, Germany
Trypan Blue Stain 0.4 %	Biozym, Germany
WST-1	Roche, Switzerland

All other chemicals including salts, buffer reagents etc. were obtained from Sigma-Aldrich, Carl Roth GmbH or AppliChem.

### 4.2 Enzymes, standards and kits

The restriction enzymes *Bam*HI-HF®, *Eco*RI-HF® and *Eco*RV-HF® were purchased from New England Biolabs (USA) and used according to manufacturers' instructions.

## Material and Methods

---

Dnase I	Thermo Fisher Scientific, USA
Exonuclease III	New England Biolabs, USA
E.Z.N.A. <sup>®</sup> Endo-Free Plasmid Mini Kit I	VWR, USA
Gel Loading Dye, Purple (6X)	New England Biolabs, USA
GeneRuler <sup>™</sup> 1 kb DNA Ladder	Thermo Fisher Scientific, USA
GeneRuler <sup>™</sup> Low Range DNA Ladder	Thermo Fisher Scientific, USA
Glucose Oxidase from <i>Aspergillus niger</i>	Sigma-Aldrich, Germany
Hot Start <i>Taq</i> DNA Polymerase	New England Biolabs, USA
Human EMT 3-Color Immunocytochemistry Kit	Bio-Techne Corporation, USA
NucleoSpin <sup>®</sup> Gel and PCR Clean up Kit	Macherey - Nagel, Germany
PageRuler <sup>™</sup> Unstained Protein Ladder	Thermo Fisher Scientific, USA
PE Annexin V Apoptosis Detection Kit I	BD Bioscience, USA
Pierce <sup>™</sup> BCA Protein Assay Kit	Thermo Fisher Scientific, USA
RNase A	Sigma-Aldrich, Germany
T4 DNA Ligase	New England Biolabs, USA
Terminal Transferase, recombinant	Roche, Switzerland

### 4.3 Buffers and solutions

10X TM	100 mM Tris base pH 8.1, 50 mM MgCl <sub>2</sub>
1X TM	10 mM Tris base pH 8.1, 5 mM MgCl <sub>2</sub>
10X TM II	100 mM Tris base pH 8.1, 500 mM MgCl <sub>2</sub>
1X TM II	10 mM Tris base pH 8.1, 50 mM MgCl <sub>2</sub>
Elution buffer	10 mM Tris base pH 7.4, 450 mM NaCl <sub>2</sub>
1X TBE	89 mM Tris base, 89 mM Boric acid, 2 mM EDTA
5X TBEM	445 mM mM Tris base, 445 mM Boric acid, 10 mM EDTA, 25 mM MgCl <sub>2</sub>
1X TBEM	89 mM Tris base, 89 mM Boric acid, 2 mM EDTA, 5 mM MgCl <sub>2</sub>
1X TAE	40 mM Tris-Acetate pH 8, 1 mM EDTA
Agarose solution	1 % (w/v) Agarose, 50 ml 1X TAE, 2 µl EtBr
10X SDS running buffer	250 mM Tris base, 1.92 M Glycine, 1 % (w/v) SDS

## Material and Methods

---

5X Non-reducing sample buffer	4 % (v/v) SDS, 20 % (v/v) Glycerol, 0.01 % (v/v) Bromophenol blue, 125 mM Tris-HCl pH 6.8
Washing buffer	50 mM Tris-HCl pH 7.5, 5 mM CaCl <sub>2</sub> , 1 μM ZnCl <sub>2</sub> , 2.5 % (v/v) Triton-X-100
Incubation buffer	50 mM Tris-HCl pH 7.5, 5 mM CaCl <sub>2</sub> , 1 μM ZnCl <sub>2</sub> , 1 % (v/v) Triton-X-100
Staining solution	0.125 % (w/v) Coomassie Brilliant Blue R-250, 45.5 % (v/v) EtOH, 9.2 % (v/v) Acetic acid
Destaining solution	30 % (v/v) EtOH, 10 % (v/v) Acetic acid
1X PBS-T	137 mM NaCl, 2.7 mM KCl, 10 mM Na <sub>2</sub> HPO <sub>4</sub> , 1.8 mM KH <sub>2</sub> PO <sub>4</sub> , 0.1 % (v/v) Tween-20, pH 7.4
Blocking solution	10 % HyClone™ Fetal Bovine Serum, 1 % BSA, 0.3 % Triton-X100
TFB I	50 mM MnCl <sub>2</sub> , 100 mM KCl, 10 mM CaCl <sub>2</sub> , 15 % (v/v) Glycerol, 30 mM Potassium acetate, pH 6.1
TFB II	10 mM MOPS, 10 mM KCl, 75 mM CaCl <sub>2</sub> , 15 % (v/v) Glycerol, pH 7
10X G-buffer	50 mM Tris-HCl pH 7.8, 1 mM CaCl <sub>2</sub> , 2 mM ATP, 10 mM DTT, 0.1 % (w/v) NaN <sub>3</sub>
1X G-buffer	5 mM Tris-HCl pH 7.8, 0.1 mM CaCl <sub>2</sub> , 0.2 mM ATP, 1 mM DTT, 0.01 % (w/v) NaN <sub>3</sub>
20X KME	20 mM MgCl <sub>2</sub> , 2 M KCl, 4 mM EGTA
20X F-buffer	100 mM Tris-HCl pH 7.8, 4 mM ATP, 20 mM MgCl <sub>2</sub> , 2 mM CaCl <sub>2</sub> , 2 M KCl, , 20 mM DTT, 0.2 % NaN <sub>3</sub> , 1 mM EGTA
10X F-buffer	50 mM Tris-HCl pH 7.8, 2 mM ATP, 10 mM MgCl <sub>2</sub> , 1 mM CaCl <sub>2</sub> , 1 M KCl, 10 mM DTT, 0.1 % (w/v) NaN <sub>3</sub> , 0.5 mM EGTA
1X F-buffer	5 mM Tris-HCl pH 7.8, 0.2 mM ATP, 1 mM MgCl <sub>2</sub> , 0.1 mM CaCl <sub>2</sub> , 0.1 M KCl, 1 mM DTT, 0.01 % (w/v) NaN <sub>3</sub> , 0.05 mM EGTA
10X Anti-bleaching buffer	10 mM Tris-HCl pH 8, 50 mM NaCl, 0.4 % (w/v) Glucose

### 4.4 Organisms

#### 4.4.1 Bacteria

*E. coli* DH5 $\alpha$  (Thermo Fisher Scientific, USA)

Genotype: F<sup>-</sup>  $\Phi$ 80*lacZ* $\Delta$ M15  $\Delta$ (*lacZYA-argF*) U169 *recA1 endA1 hsdR17*(r<sub>k</sub><sup>-</sup>, m<sub>k</sub><sup>+</sup>) *phoA supE44 thi-1 gyrA96 relA1*  $\lambda$ <sup>-</sup>

#### 4.4.2 Human cell lines

All cell lines were purchased at the American Type Culture Collection (ATCC), USA.

##### HeLa

HeLa is the oldest and most commonly immortal human epithelial cell line used in scientific research. These cells were isolated from a cervical adenocarcinoma of Henrietta Lacks, a 31-year old woman, in 1951 without her knowledge or consent. The cell line was named 'HeLa' because of the first two letters of the patient's first and last name<sup>209</sup>.

##### MDA-MB-231

MDA-MB-231 is a well-established, highly invasive and tumorigenic epithelial cell line originating from the metastatic sites (pleural effusions) of adenocarcinomas in the mammary gland of a 51-year old European woman<sup>210</sup>. These cells are aneuploid since chromosomes N8 and N15 are missing. MDA-MB-231 are spindle-shaped cells which grow randomly, can become confluent and are distinct from fibroblasts<sup>211</sup>.

##### MCF-10A

MCF-10A is a well-known non-tumorigenic epithelial cell line. Cells were originally isolated from the benign mammary gland of a 36 year old Caucasian woman suffering from extensive fibrocystic disease<sup>212</sup>. These cells are immortal, but otherwise normal, noncancerous breast epithelial cells. MCF-10A cells are strongly adherent: depending on the cell density, it takes about 15 min - 20 min to detach them from plastic surfaces using 0.05 % Gibco<sup>®</sup> Trypsin-EDTA (4.37.2).

### 4.5 Culture media

#### Media for *E. coli* growth:

LB medium <sup>213</sup>	1 % (w/v) Tryptone, 0.5 % (w/v) Yeast extract, 1 % (w/v) NaCl For plates: 1.5 % (w/v) Agar Agar were added
SOC medium <sup>214</sup>	2 % (w/v) Tryptone, 0.5 % (w/v) Yeast Extract, 10 mM NaCl, 2.5 mM KCl, 10 mM MgCl <sub>2</sub> , 10 mM MgSO <sub>4</sub> · 7 H <sub>2</sub> O, 20 mM Glucose NaCl, KCl, MgCl <sub>2</sub> , MgSO <sub>4</sub> and Glucose were sterile filtered and added after autoclavation.

#### Media for human cell lines:

HeLa	RPMI 1640 supplemented with 15 % (v/v) HyClone™ Fetal Bovine Serum, 1X MEM Amino Acids Solution (50X) and 1X MEM Vitamin Solution (100X)
MDA-MB-231	DMEM, high Glucose, GlutaMAX™ supplemented with 10 % (v/v) HyClone™ Fetal Bovine Serum
MCF-10A	DMEM/Ham's F-12, stable glutamine, supplemented with 5 % (v/v) Biochrom AG™ Donor Horse Serum, 20 ng/ml Epidermal Growth Factor (EGF), 10 µg/ml Insulin, 100 ng/ml Cholera Toxin, 500 ng/ml Hydrocortisone, 1 % (v/v) Penicillin/Streptomycin
2X Freeze medium	50 % (v/v) cell specific growth medium, supplemented with 30 % (v/v) Serum (HyClone™ Fetal Bovine Serum for HeLa and MDA-MB-231; Biochrom AG™ Donor Horse Serum for MCF-10A cells), 20 % (v/v) DMSO as cryoprotectant

All bacteria media were autoclaved at 121 °C, 2.1 bar for 20 min prior to usage. Human cell culture media were mixed and sterile filtered using a TPP® Filtermax rapid bottle-top filter (Dr. Ilona Schubert Laborfachhandel) with a pore size of 0.22 µm.

### 4.6 Media additives

LB media as well as agar plates for the selection of positive *E. coli* DH5 $\alpha$  clones after transformation were supplemented with 50  $\mu$ g/ml Kanamycin. Kanamycin stock solutions were prepared in Millipore water at a concentration of 50 mg/ml.

Epithelial-to-mesenchymal-transition (EMT) was induced by the addition of transforming growth factor beta (TGF- $\beta$ ). For those experiments, MCF-10A medium as well as Opti-MEM<sup>®</sup> I Reduced-Serum Medium were supplemented with 10 ng/ml TGF- $\beta$ .

### 4.7 Plasmids

pTagGFP-N  
(Evrogen, Russia)

pTagGFP-N is an eukaryotic expression vector encoding green-fluorescent protein TagGFP and designed to generate TagGFP-tagged fusions or to express TagGFP in human cells. The vector backbone comprises immediate early promoter of cytomegalovirus ( $P_{CMV\ IE}$ ) for protein expression, SV40 origin for replication in human cells expressing SV40 T-antigen, pUC origin of replication for propagation in *E. coli* and f1 origin for ss DNA production. The multiple cloning site (MCS) is located between  $P_{CMV\ IE}$  and TagGFP coding sequence. SV40 early promoter provides Neo<sup>R</sup> gene expression to select stably transfected eukaryotic cells using G418. Bacterial promoter provides Kan<sup>R</sup> gene expression in *E. coli*.

pTag-LifeAct-GFP-N  
(this work)

The vector pTagGFP-N was used to integrate the DNA sequence, encoding LifeAct<sup>®</sup>, via *EcoRI* and *BamHI* into the MCS (4.18).

### 4.8 DNA oligonucleotides

All DNA oligonucleotides were purchased from Biomers.net GmbH (Germany) as lyophilized product and further solubilized with Millipore water to a final concentration of 100  $\mu$ M, respectively. Nucleotides marked with \* indicate a PTO modification. Bolded sequences are highlighting an *EcoRV* digestion site.

## Material and Methods

**Table 4 | DNA oligonucleotides**

Name	Sequence 5'→3'
<b>DNA tetrahedron</b>	
TetS1	AGGCAGTTGAGACGAACATTCCTAAGTCTGAAATTTATCACC CGCCATAGTAGACGTATCACC
TetS2	CTTGCTACACGATTCAGACTTAGGAATGTTTCGACATGCGAGG GTCCAATACCGACGATTACAG
TetS3	GGTGATAAAACGTGTAGCAAGCTGTAATCGACGGGAAGAGC ATGCCATCCACTACTATGGCG
TetS4	CCTCGCATGACTCAACTGCCTGGTGATACGAGGATGGGCAT GCTCTTCCCGACGGTATTGGAC
TetS1*	CTAAGTCTGAAATTTATCACCCGCCATAGTAGACGTATCACC AGGCAGTTGAGACGAACATTC
TetS2 - Cy3	Cy3 - CTTGCTACACGATTCAGACTTAGGAATGTTTCGACATGC GAGGGTCCAATACCGACGATTACAG
TetS4 - Cy5	Cy5 - CCTCGCATGACTCAACTGCCTGGTGATACGAGGATGG GCATGCTCTTCCCGACGGTATTGGAC
TetS1* - NH <sub>2</sub>	NH <sub>2</sub> - TCTAAGTCTGAAATTTATCACCCGCCATAGTAGACGTA TCACCAGGCAGTTGAGACGAACATTC
TetS2 - NH <sub>2</sub>	NH <sub>2</sub> - TCTTGCTACACGATTCAGACTTAGGAATGTTTCGACATG CGAGGGTCCAATACCGACGATTACAG
TetS3 - NH <sub>2</sub>	NH <sub>2</sub> - TGGTGATAAAACGTGTAGCAAGCTGTAATCGACGGGA AGAGCATGCCATCCACTACTATGGCG
TetS4 - NH <sub>2</sub>	NH <sub>2</sub> - TCCTCGCATGACTCAACTGCCTGGTGATACGAGGATG GGCATGCTCTTCCCGACGGTATTGGAC
<b>DNA Trimer</b>	
AB - NH <sub>2</sub>	NH <sub>2</sub> - ACTATCTTTGGTCTATTATCTTGAGTCATC
B*C - NH <sub>2</sub>	NH <sub>2</sub> - GATGACTCAAGATAAACACACACACAACACTA
C*A* - NH <sub>2</sub>	NH <sub>2</sub> - TAGTTGTGTGTGTGTTAGACCAAAGATAGT
AB - PTO - NH <sub>2</sub>	NH <sub>2</sub> - A*C*T*A*T*CTTTGGTCTATTATCTTGAGT*C*A*T*C*
B*C - PTO - NH <sub>2</sub>	NH <sub>2</sub> - G*A*T*G*A*CTCAAGATAAACACACACACA*A*C*T*A*
C*A* - PTO - NH <sub>2</sub>	NH <sub>2</sub> - T*A*G*T*T*GTGTGTGTGTTAGACCAAAGA*T*A*G*T*
C*A* - PTO - Cy3	Cy3 - T*A*G*T*T*GTGTGTGTGTTAGACCAAAGA*T*A*G*T*
B*C - PTO - BHQ2	G*A*T*G*ACTCAAGATAAACACACACACAA*C*T*A - BHQ2
<b>Crosslinker</b>	
60fw-NH <sub>2</sub>	NH <sub>2</sub> - GCTTTCTTCTCTAAATACATCTTCACGTC <b>GATATCACCA</b> TAACTCAGGTAAGGAGGTCAA
60rv-NH <sub>2</sub>	NH <sub>2</sub> - TTGACCTCCTTACCTGAGTTATGGT <b>GATATCGACGTGA</b> AGATGTATTTAGAGAAGAAAGC
60fw-NH <sub>2</sub> -PTO	NH <sub>2</sub> - G*C*T*T*T*C*T*T*T*C*T*A*A*A*T*A*C*A*T*C*T*T*C*A*C* G*T*C* <b>G*A*T*A*T*C</b> *A*C*C*A*T*A*A*C*T*C*A*G*G*T*A*A*G* G*A*G*G*T*C*A*A*

## Material and Methods

60rv-NH <sub>2</sub> -PTO	NH <sub>2</sub> - T*T*G*A*C*C*T*C*C*T*T*A*C*C*T*G*A*G*T*T*A*T*G*G* T*G*A*T*A*T*C*G*A*C*G*T*G*A*A*G*A*T*G*T*A*T*T*T*A*G*A* G*A*A*G*A*A*A*G*C*
60fw	GCTTTCTTCTCTAAATACATCTTCACGTCGATATCACCATAAC TCAGGTAAGGAGGTCAA
60rv-Cy3	Cy3 - TTGACCTCCTTACCTGAGTTATGGTGATATCGACGTGA AGATGTATTTAGAGAAGAAAGC
60fw-Cy3	Cy3 - GCTTTCTTCTCTAAATACATCTTCACGTCGATATCACCA TAACTCAGGTAAGGAGGTCAA
60rv-BHQ2	TTGACCTCCTTACCTGAGTTATGGTGATATCGACGTGAAGAT GTATTTAGAGAAGAAAGC – BHQ2
60fw-5'NH <sub>2</sub> - 3'TT-Cy3	NH <sub>2</sub> - GCTTTCTTCTCTAAATACATCTTCACGTCGATATCACCA TAACTCAGGTAAGGAGGTCAATT - Cy3
<b>LifeAct<sup>®</sup> insert</b>	
LifeAct-fw-EcoRI	AATTCATGGGCGTGGCCGACCTGATCAAGAAGTTCGAGAGC ATCAGCAAGGAGGAG
LifeAct-rv-BamHI	GATCCTCCTCCTTGCTGATGCTCTCGAACTTCTTGATCAGGT CGGCCACGCCATG
<b>PCR primer</b>	
Kol-PCR-rv-pTaqGFP	TCTTGAAGAAGTCGTTTCATC
Kol-PCR-fw-LifeAct	ATGGGCGTGGCCGACCTGAT

## 4.9 Peptides

All peptides were obtained as lyophilized products and solubilized with Millipore water or methanol to a final concentration of 2 mM - 5 mM, respectively.

**Table 5 | Peptides**

Name		Sequence N→C	Source
sC18 variants	Cys - sC18	CGLRKRLRKFRNKIKEK	Prof. Dr. Ines Neundorf, University of Cologne
	Azide - sC18	<b>B</b> GLRKRLRKFRNKIKEK	<b>B</b> : Azidolysin
Azide-LifeAct <sup>®</sup>		Ac-MGVADLIKKFESISKEEGG- azidolysine-amid	PSL Peptide Specialty Laboratories GmbH, Germany
Amino-Phalloidin		Cyclo(-Ala-D-Thr-Cys-cis-Hyp-Ala- Trp-(4R)-4-hydroxy-4-Me-Orn) (Sulfide bond between Cys and indol-2-yl)	Bachem AG, Switzerland

### 4.10 Proteins

EGF Recombinant Human Protein	Thermo Fisher Scientific, USA
Pyrene Muscle Actin (Rabbit skeletal muscle)	Cytoskeleton Inc., USA
Muscle Actin (Rabbit skeletal muscle)	Isolated from rabbit muscles, Fraunhofer IZI, Leipzig
Recombinant Human TGF-beta 1	Bio-Techne GmbH, Germany
Recombinant Human Fascin protein	Abcam, UK

### 4.11 Equipment and expendables

7900HT Fast Real-Time PCR System	Applied Biosystems, USA
8-well on cover glass II	Sarstedt, Germany
8-well on glass, detachable	Sarstedt, Germany
AFM cantilever ACTA-10	AppNano, USA
AFM cantilever USC-F0.3-k0.3	Asylum Research, USA
Äkta Avant 25	GE Healthcare Europe GmbH, Germany
Amicon <sup>®</sup> -Ultra-4 centrifugal filter units, 10K MWCO	EMD Millipore, Germany
Amicon <sup>®</sup> -Ultra-0.5 centrifugal filter units, 3K MWCO, 30 K MWCO	EMD Millipore, Germany
Atomic force microscope NanoWizard 3.0	JPK Instruments AG, Germany
BioPhotometer (spectrophotometer)	Eppendorf AG, Germany
BioSep <sup>™</sup> SEC-s2000 column	Phenomenex, USA
CELLSTAR <sup>®</sup> Filter Cap Cell Culture Flasks, TC- treated	Greiner Bio-One International GmbH, Austria
CELLSTAR <sup>®</sup> multiwell plates (96-well, 24-well, 12- well, 6-well)	Greiner Bio-One International GmbH, Austria
Centrifuge 5424 R	Eppendorf AG, Germany
Combitips Advanced <sup>®</sup>	Eppendorf AG, Germany
Cover slips, 24 mm x 60 mm	VWR, USA
Cultrex <sup>®</sup> 24 Insert Cell Invasion / Migration Chamber	Biozol Diagnostica, Germany
CryoPure tube 2.0 ml	Sarstedt, Germany
Culture-Inserts, 2-well	Ibidi, Germany
DNA LoBind reaction tube (1.5 ml, 2 ml)	Eppendorf AG, Germany

## Material and Methods

---

Dynamic Shear Rheometer (ARES)	TA Instruments, USA
Eppendorf ThermoMixer® C	Eppendorf AG, Germany
Flow cytometer iQue™ Screener	IntelliCyt®, USA
Gel documentation system Gel Jet Imager	Intas, Germany
Gel electrophoresis apparatus Power Supply Power Pac Basic	BioRad Laboratories, Germany
HeraeusMultifuge® 3SR+	Thermo Fisher Scientific, USA
Incubator Function Line B20	Thermo Fisher Scientific, USA
Incubator HERAccl® 240	Thermo Fisher Scientific, USA
KIMTECH SCIENCE® Precision Wipes	Kimberly-Clark Professional, Germany
LightCycler® 480 Sealing Foil	Roche Life Science, Switzerland
LSM 710/AxioObserver	Carl Zeiss Microscopy GmbH, Germany
Leica DM IRB phase contrast microscope	Leica Microsystems GmbH, Germany
Leica DMIL LED inverted microscope	Leica Microsystems GmbH, Germany
Luna II™ automated cell counter	Biozym, Germany
Luna™ cell counting slides	Biozym, Germany
Magnetic stirrer MR Hei-Tec	Heidolph, Germany
Mettler Toledo™ XP6U Micro Comparator	Mettler-Toledo, Germany
Mica “V1”, 12 mm round	Plano GmbH, Germany
MicroAmp® Fast Optical 96-Well Reaction Plate	Applied Biosystems, USA
Microliter centrifuge Micro 200 R	Andreas Hettich GmbH & Co.KG, Germany
Microplate 96-well (black), fluorotrac	Greiner Bio-One International GmbH, Austria
Microscope slides, 25 mm x 75 mm	VWR, USA
Mini-PROTEAN® Tetra Handcast Systems	BioRad Laboratories, Germany
Mr. Frosty™ freezing container	Thermo Fisher Scientific, USA
Multipette® M4	Eppendorf, Germany
NanoDrop ND-1000 UV/Vis	PEQLAB Biotechnologie GmbH, Germany
New Brunswick™ Innova® 44 incubator shaker	New Brunswick Scientific, USA
Parafilm® M	Sigma-Aldrich, Germany

## Material and Methods

---

pH Meter Lab 870	SI Analytics GmbH, Germany
Polymax 1040 waving platform shaker	Heidolph Instruments GmbH & Co. KG, Germany
Quintix® Analytical Balance 2102-1S	Sartorius Lab Instruments GmbH, Germany
Real-time deformability cytometer (RTDC) AcCellerator	Zellmechanik Dresden GmbH, Germany
Reprorubber® Thin Pour	JPK Instruments AG, Germany
Rotilabo®-syringe filters CME 0.22 µm	Carl Roth GmbH, Germany
Spinning disc confocal microscope (Inverted Axio Observer.Z1/Yokogawa CSU-X1A 5000)	Carl Zeiss Microscopy GmbH, Germany
SPROUT® MINI CENTRIFUGE 12V	Heathrow Scientific® LLC, USA
Sterile tweezers	Dr. Ilona Schubert Laborfachhandel, Germany
TECAN Infinite® M1000	Tecan Group AG, Switzerland
TPP® Filtermax rapid bottle-top filter, 0.22 µm	Dr. Ilona Schubert Laborfachhandel, Germany
TProfessional Thermocycler	Biometra GmbH, Germany
UVette®	Eppendorf AG, Germany
Vortex-Genie® 2	Scientific Industries Inc., USA
Water bath	GFL Gesellschaft für Labortechnik mbH, Germany
Zetasizer Nano ZSP	Malvern Instruments, UK

### 4.12 Software

Gel-Dokumentationssoftware Intas GDS	Intas, Germany
JPK SPM and DP software (AFM measurements and data processing)	JPK Instruments AG, Germany
Gwyddion (processing AFM images)	<a href="http://gwyddion.net/">http://gwyddion.net/</a>
PyMOL (3D structures of proteins)	<a href="https://pymol.org/2/">https://pymol.org/2/</a>
ForeCyt v4.1	IntelliCyt®, USA
ShapeOut (evaluation RTDC measurements)	Zellmechanik Dresden GmbH, Germany
ZEN2 blue	Carl Zeiss Microscopy, Germany
Magellan 5	Tecan Group AG, Switzerland

## Material and Methods

---

ImageJ (plus Mitobo plugin)	<a href="https://imagej.nih.gov/ij/">https://imagej.nih.gov/ij/</a> ; <a href="https://imagej.net/MiToBo">https://imagej.net/MiToBo</a>
ChemSketch (drawing chemical formula)	<a href="http://www.acdlabs.com/resources/freeware/chemsketch/">http://www.acdlabs.com/resources/freeware/chemsketch/</a>
ProtParamTool	ExPasy ( <a href="http://www.expasy.ch">http://www.expasy.ch</a> )
Reverse translation tool	<a href="http://www.bioinformatics.org/sms2/rev_trans.html">http://www.bioinformatics.org/sms2/rev_trans.html</a>
Codon usage database	<a href="http://www.kazusa.or.jp/codon/">http://www.kazusa.or.jp/codon/</a>
Adobe Illustrator CS4	Adobe Systems, USA
Microsoft Office 2016	Microsoft, USA
Citavi 5	Swiss Academic Software, Switzerland
Ligation calculation tool	<a href="https://nebiocalculator.neb.com/#!/ligation">https://nebiocalculator.neb.com/#!/ligation</a>

### 4.13 Isolation of plasmid DNA from *E. coli* cells

Plasmid-DNA, which was further used in human cell culture, was isolated from *E. coli* using the E.Z.N.A.<sup>®</sup> Endo-Free Plasmid Mini Kit I (VWR) according to manufacturers' instructions. Plasmid-DNA was stored at -20 °C in elution buffer.

### 4.14 Determination of DNA concentration

DNA concentration was measured by absorbance (UV/VIS) spectroscopy at 260 nm using the NanoDrop ND-1000 UV/VIS spectrophotometer (PEQLAB Biotechnologie GmbH). Using the Lambert-Beer equation (Equation 8), with  $A$  = absorbance at 260 nm,  $\varepsilon$  = extinction coefficient at 260 nm [ $\mu\text{l} \cdot \text{ng}^{-1} \cdot \text{cm}^{-1}$ ],  $c$  = DNA concentration [ $\text{ng} \cdot \mu\text{l}^{-1}$ ] and  $d$  = layer thickness [cm], the amount of absorbed light can be related to the concentration of the absorbing DNA.

$$A = \varepsilon \times c \times d$$

Equation 8

The average extinction coefficient of ds DNA at 260 nm is  $0.02 \mu\text{l} \cdot \text{ng}^{-1} \cdot \text{cm}^{-1}$ , of ss DNA it is  $0.027 \mu\text{l} \cdot \text{ng}^{-1} \cdot \text{cm}^{-1}$ . DNA purities were estimated from the ratio of absorbance at 260 nm and 280 nm ( $A_{260}/A_{280}$ ).

### 4.15 Electrophoretic separation of DNA

#### 4.15.1 Agarose gel electrophoresis

For analytic separation of plasmid-DNA and DNA fragments, 1 % (w/v) agarose gels containing EtBr were used (4.3). DNA samples (100 ng each) were mixed with 6X DNA loading buffer and separated with a constant voltage of 100 V. After 60 min, DNA was visualized using the gel documentation system Gel Jet Imager (Intas). GeneRuler™ 1 kb DNA Ladder (Thermo Fisher Scientific) was run on the agarose gel as a molecular weight standard to determine the size of DNA fragments.

#### 4.15.2 Native Polyacrylamide gel electrophoresis (PAGE)

In order to analyze the functionalization of short, ss DNA fragments as well as small DNA nanostructures, such as the DNA tetrahedron, native PAGE gels were utilized. Six % - 20 % (v/v) PAGE gels, containing 6 % - 20 % (v/v) Acrylamide-bisacrylamide (29 : 1), 1X TBE (4.3), 1 % (w/v) APS and 0.1 % TEMED, were prepared using the Mini-PROTEAN® Tetra Handcast System (Bio-Rad). DNA samples (100 ng) were mixed with 6X DNA loading buffer and added into rinsed gel slots. Native PAGE gels were run at 100 V - 120 V for 60 min - 90 min at room temperature in 1X TBE buffer. After running, gels were stained for 5 min with SYBR® Gold nucleic acid gel stain (1 : 10,000 dilution in 1X TBE) and further visualized under UV-light using the Gel documentation system Gel Jet Imager (Intas). GeneRuler™ Low Range DNA Ladder (Thermo Fisher Scientific) was run on native PAGE gels as a molecular weight standard.

PAGE gels containing DNA tetrahedra, both gel and running buffer were supplemented with 5 mM MgCl<sub>2</sub> in order to stabilize the DNA structures.

### 4.16 Ethanol precipitation

For purification of modified oligonucleotides, samples were mixed with 0.1X volumes 3 M sodium acetate and 2X volumes of absolute ethanol followed by a 5 min incubation in liquid nitrogen. Right after, samples were centrifuged for 1 h at 4 °C and 16,500 rcf. The supernatant was carefully removed and the pellet was air dried for 5 min to 10 min. Purified DNA was dissolved in 1X DPBS or Millipore water and stored at -20 °C prior to usage.

### 4.17 Spin filtration

To purify DNA structures from excess peptides or other conjugation molecules, Amicon<sup>®</sup>-Ultra Centrifugal Filter Devices (EMD Millipore) varying in size (e.g. Amicon<sup>®</sup>-Ultra-0.5, Amicon<sup>®</sup>-Ultra-4) and MWCO (e.g. 3 K, 10 K, 30 K) were used according to manufacturer's instructions. All devices were pre-rinsed with corresponding buffer or Millipore water.

### 4.18 Cloning

#### 4.18.1 Restriction digest of Plasmid DNA

Vector pTagGFP-N was digested with *Bam*HI and *Eco*RI according to manufacturers' instructions. Linearized vector was further purified with NucleoSpin<sup>®</sup> Gel and PCR Clean up Kit (Macherey - Nagel) and analyzed via 1 % (w/v) agarose gel electrophoresis.

#### 4.18.2 Hybridization of cloning insert

The aim of the cloning was the generation of a vector encoding the LifeAct<sup>®</sup> sequence<sup>161</sup> with whom HeLa cells could be transfected to visualize actin structures within cells. In order to receive the correct DNA sequence that could be transcribed and translated in HeLa cells (4.4.2) later on, the original peptide sequence was back translated under the codon usage of *Homo sapiens sapiens* (4.12). Additionally, the obtained sequence was extended with *Eco*RI and the complementary strand with *Bam*HI digestion sites. Since LifeAct<sup>®</sup> is a short peptide, the corresponding DNA sequence is likewise short. Thus, the DNA sequence was not obtained by gene amplification but synthesized through Biomers.net GmbH (Germany). Complementary sequences, already containing *Bam*HI or *Eco*RI digestion sites (4.8), were hybridized at 50 nM in a final volume of 20  $\mu$ l using the TProfessional Thermocycler (Biometra GmbH).

Denaturation	95 °C	2 min
Hybridization	81 °C	10 min
Storage	4 °C	

The resulting ds DNA fragment had *Bam*HI and *Eco*RI overhangs of four nucleotides each, as they would be generated during digestion with corresponding restriction enzymes.

### 4.18.3 Ligation

Using the ligation calculator (4.12), the mass of insert required at a molar insert : vector ratio of 5 : 1 for a typical ligation reaction with T4 DNA Ligase (New England Biolabs) was calculated. The reaction mixture was incubated for 1 h at room temperature and heat inactivated for 10 min at 65 °C afterwards.

Reaction mixture:

	Concentration	Mastermix (1X)
Linearized, purified pTagGFP-N (4730 bp)	23.41 nM	1.46 $\mu$ l
Hybridized DNA fragment (56 bp)	50 nM	1.71 $\mu$ l
10X T4 DNA Ligase buffer		2 $\mu$ l
T4 DNA Ligase	1 U/ml	1 $\mu$ l
dd H <sub>2</sub> O		13.83 $\mu$ l
		$\Sigma = 20 \mu$ l

### 4.19 Transformation

#### 4.19.1 Preparation of competent *E. coli* cells

Competent *E. coli* cells were prepared according to Green & Rogers (2013)<sup>215</sup>. Five ml LB medium were inoculated with 50  $\mu$ l of *E. coli* DH5 $\alpha$  cells and cultured overnight at 37 °C in a New Brunswick™ Innova® 44 incubator shaker (New Brunswick Scientific). The next day, 100 ml LB medium were inoculated with 1 ml stationary *E. coli* overnight culture and grown at 37 °C and 200 rpm until an OD<sub>600</sub> of 0.45 - 0.55 was reached. After placing them on ice for 10 min, cells were centrifuged for 4 min at 4 °C and 4,000 rpm. The supernatant was discarded and the pellet resuspended in 30 ml ice-cold TFB I buffer. After 45 min incubation on ice, cells were again pelleted at 4,000 rpm for 4 min at 4 °C and resuspended in 4 ml ice-cold TFB II buffer. Aliquots of 50  $\mu$ l each were pipetted into 1.5 ml reaction tubes, immediately frozen in liquid nitrogen and stored at -80 °C.

#### 4.19.2 Transformation of *E. coli*

For transformation of *E. coli* DH5 $\alpha$ , 5  $\mu$ l of inactivated ligation solution was pipetted to 50  $\mu$ l partially thawed cells. The mixture was incubated for 30 min on ice and then heat-shocked for 30 s at 42 °C. After heat-shock, samples were placed on ice for 5 min. Right after,

400  $\mu$ l ice-cold SOC medium were added and cells incubated for 60 min at 37 °C and 300 rpm in an Eppendorf ThermoMixer® C (Eppendorf AG). Transformed cells were plated at different concentrations on kanamycin-selective agar plates and incubated overnight at 37 °C. As a negative control, untransformed *E. coli* DH5 $\alpha$  cells were plated. Since these cells do not carry the pTagGFP-N vector, they should not grow on kanamycin-containing agar plates.

### 4.20 Amplification of DNA fragments through polymerase chain reaction

Polymerase chain reaction (PCR) was utilized to amplify DNA fragments. DNA amplification was performed using Hot Start *Taq* DNA Polymerase (New England Biolabs) according to manufacturers' instructions. PCR products were analyzed by agarose gel electrophoresis (4.15.1).

#### Colony PCR

To determine the presence of the LifeAct® insert in the plasmid construct of previously transformed competent *E. coli* DH5 $\alpha$  cells, a colony PCR was performed. Positive clones were identified using insert specific primers (4.8, supplemental Figure S 7). After transformation, single colonies were picked from agar plates using an inoculation needle and resuspended in 5  $\mu$ l dd H<sub>2</sub>O in 0.2  $\mu$ l PCR reaction tubes. After resuspension, 15  $\mu$ l of the following reaction mixture were added to a final volume of 20  $\mu$ l.

Reaction mixture:

	Mastermix (1X)
10 $\mu$ M Kol_PCR_rv_pTaqGFP	1 $\mu$ l
10 $\mu$ M Kol_PCR_fw_LifeAct	1 $\mu$ l
10 mM dNTP Mix	0.4 $\mu$ l
10X Hot Start <i>Taq</i> DNA Polymerase buffer	2 $\mu$ l
Hot Start <i>Taq</i> DNA Polymerase	0.1 $\mu$ l
dd H <sub>2</sub> O	10.4 $\mu$ l
	$\Sigma = 15 \mu$ l

As negative control, 0.1  $\mu$ l pTagGFP-N (empty vector) was pipetted into 4.9  $\mu$ l dd H<sub>2</sub>O in a 0.2 ml PCR reaction tube and 15  $\mu$ l of the reaction mixture were added. Gene amplification was performed in a TProfessional Thermocycler (Biometra GmbH).

Reaction protocol:

Initial denaturation	95 °C	2 min	
Denaturation	95 °C	30 s	} 40 cycles
Annealing	52 °C	30 s	
Elongation	60 °C	45 s	
Final elongation	60 °C	5 min	
Storage	4 °C		

### 4.21 DNA Sequence analysis

Plasmid-DNA was verified by DNA sequencing. Samples of 50 ng/μl to 100 ng/μl were analyzed at GATC Biotech AG (Germany).

### 4.22 Cultivation and storage of *E. coli* cells

*E. coli* was generally grown at 37 °C in shaking cultures using various media (4.5). Cell growth was determined in an UVette® (Eppendorf AG) by measuring the optical density at 600 nm (OD<sub>600</sub>) using the spectrophotometer BioPhotometer (Eppendorf AG). Plasmid-carrying cells were selected through corresponding antibiotics in media and agar plates (4.5, 4.6). Agar plates were incubated overnight at 37 °C in the microbiological incubator Function Line B20 (Thermo Scientific Heraeus). For long-term storage of *E. coli* cells, glycerol stocks were prepared. Therefore, 250 μl of 80 % (v/v) glycerol were added to 750 μl of mid-log phase *E. coli* cells and stored at -80 °C.

### 4.23 Folding of DNA structures

#### 4.23.1 Folding of DNA tetrahedra

Four partially complementary oligonucleotides with 63 nt each were hybridized to form DNA tetrahedra<sup>16</sup>. DNA sequences (Table 4) were mixed in equimolar amounts in 1X TM buffer (4.3). The folding of the structure with S1 and S1\* differed in the assembly of tetrahedra with either two nicks each face or three nicks on one face and one nick on another face. DNA tetrahedra were typically hybridized at 500 nM to 1 μM. The reaction mixture was heated to 95 °C for 2 min and rapidly cooled down to 4 °C using a TProfessional Thermocycler

## Material and Methods

---

(Biometra GmbH). The assembly was analyzed via 6 % (v/v) native PAGE (4.15.2) and visualized by AFM imaging (4.30.1, Figure 30).

Example reaction mixture to assemble 500 nM DNA tetrahedra:

10 $\mu$ M TetS1/TetS1*	2.5 $\mu$ l
10 $\mu$ M TetS2	2.5 $\mu$ l
10 $\mu$ M TetS3	2.5 $\mu$ l
10 $\mu$ M TetS4	2.5 $\mu$ l
10X TM	5 $\mu$ l
dd H <sub>2</sub> O	35 $\mu$ l
<hr/>	
$\Sigma = 50 \mu$ l	

### 4.23.2 Folding of DNA trimers

Similar to the self-assembly of DNA tetrahedra, DNA trimers were formed. Here, three partially complementary DNA strands of 30 nt each were designed to form a three-arm junction when they hybridize. To illustrate the geometry, the open ends of a DNA trimer were designated A, B, and C, respectively. The names of the DNA strands (Table 4) indicate their complementarity to the part of the other sequences. As an example, strand AB is complementary to A\* of the C\*A\* strand and B is complementary to B\* of the B\*C strand. DNA sequences were mixed in equimolar amounts to a final concentration of 2  $\mu$ M in 100 mM KH<sub>2</sub>PO<sub>4</sub> pH 7.2. DNA trimers were assembled in a TProfessional Thermocycler (Biometra GmbH) and subsequently analyzed via 10 % (v/v) native PAGE.

Example reaction mixture and assembly program:

50 $\mu$ M AB	4 $\mu$ l	Denaturation	95 °C	2 min
50 $\mu$ M B*C	4 $\mu$ l	Hybridization	48 °C	15 min
50 $\mu$ M C*A	4 $\mu$ l	Storage	4 °C	$\infty$
1 M KH <sub>2</sub> PO <sub>4</sub> pH 7.2	10 $\mu$ l			
dd H <sub>2</sub> O	78 $\mu$ l			
<hr/>				
$\Sigma = 100 \mu$ l				

### 4.24 Size exclusion chromatography (SEC)

Even though the self-assembly of DNA tetrahedra was at a high yield, a decent amount of aggregations formed. In order to separate correctly formed structures from aggregates, DNA tetrahedra were purified with SEC using an Äkta Avant 25 (GE Healthcare Europe GmbH) chromatography system. DNA tetrahedra were assembled at 500  $\mu$ l of 1  $\mu$ M (4.23.1) in 1X TM II buffer (4.3) and injected into a 0.5 ml injection loop using a plastic syringe. The sample was then applied onto a BioSep™SEC-s2000 column (Phenomenex), pre-equilibrated with 1X TM II (mobile phase buffer). The flow rate was set to 0.6 ml/min and the DNA structures were isocratically eluted with elution buffer (4.3). DNA was detected at 260 nm and peak fractions collected. Samples were analyzed via 8 % (v/v) native PAGE (4.15.2). Fractions of same peaks were pooled, concentrated and buffer exchanged to 1X TM buffer via spin filtration using Amicon®-Ultra-0.5 centrifugal filter units with 30 K MWCO (4.17).

### 4.25 Heterobifunctional linkers

Bifunctional linkers possess different reactive groups at either end and are used to covalently couple molecules, such as DNA, peptides, proteins or dyes that carry specific functional groups. These crosslinking reagents allow for both single-step conjugations as well as for sequential conjugations. Figure 16 shows heterobifunctional linker molecules that were utilized in this work. Detailed reaction mechanisms of individual functional groups are to be found in section 2.2.2, 2.2.3 and 2.2.4, respectively.

Sulfo-SMCC is a water-soluble linker reactive to primary amine groups via N-hydroxysuccinimide (NHS) ester (red) and thiols via maleimide group (purple). This linker was used to covalently couple DNA to cysteine-containing peptides (Figure 19). DBCO-NHS ester also reacts with primary amines via NHS ester (red) but can be further clicked to azide-containing molecules via its DBCO group (green, Figure 21). Also involved in copper-free click chemistry is the bifunctional linker azidopropionic acid sulfo-NHS ester. Again it has activity for primary amine groups but can be clicked to strained alkynes in a SPAAC reaction (2.2.4).

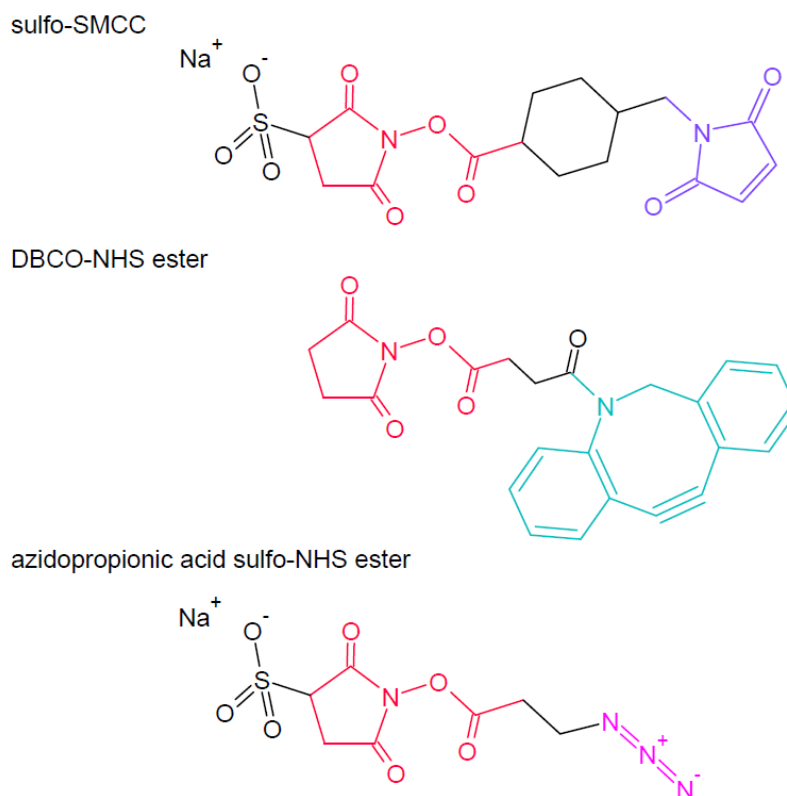


**Figure 16 | Chemical structures of utilized heterobifunctional linkers.** All three used linker molecules contain (sulfo)-NHS esters (red) that react with primary amines. Sulfo-SMCC contains a maleimide group that is reactive for sulfhydryl groups. Both DBCO-NHS ester as well as azidopropionic acid sulfo-NHS ester are utilized in copper-free click chemistry. A DBCO group (green) reacts with an azide (pink) under the formation of a triazole. The reaction mechanisms of these functional groups are described in 2.2.2, 2.2.3 and 2.2.4, respectively.

## 4.26 Functionalization of DNA tetrahedra with CPP

In order to tune the dynamics of the active cellular uptake and internal trafficking of DNA nanostructures, DNA tetrahedra were modified with cell-penetrating peptides (CPP). In the following, two different conjugation strategies, leading to either DNA tetrahedra with CPP chains or DNA tetrahedra with single CPP attached, are introduced.

### 4.26.1 DNA tetrahedra functionalized with CPP chains

Before the manufacturing process is described in more detail, a brief overview of the individual steps is pictured in Figure 17. Initially, a tail of aminoallyl-dUTPs was added to single Tet sequences using TdT. After purification, DNA tetrahedra with amino-modified sequences were assembled and sulfo-SMCC, a bifunctional linker, which reacts with primary amine groups as well as sulfhydryl groups, was added. Excess linker molecules were removed

through spin filtration and cysteine-containing CPP, which were previously reduced with TCEP, were added to react with the maleimide group of sulfo-SMCC in a covalent manner.

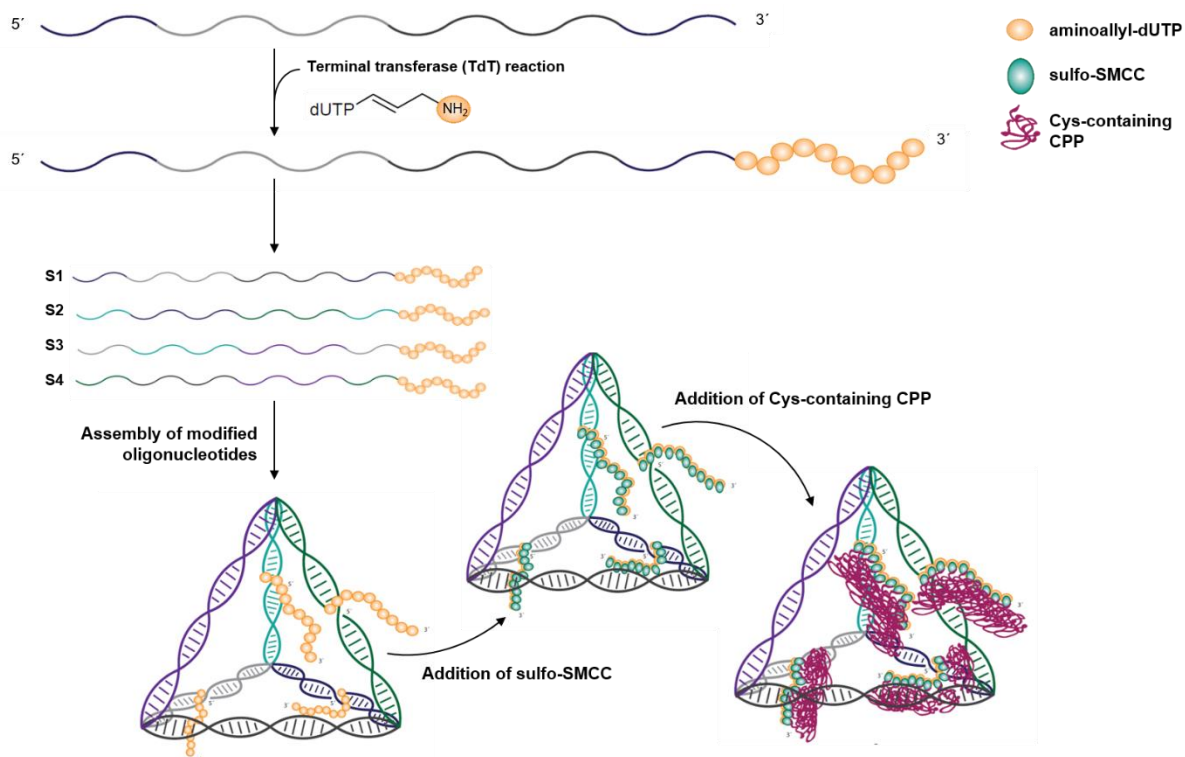


**Figure 17 | Schematic of engineering DNA tetrahedra carrying CPP chains.** Partially complementary Tet sequences were modified with aminoallyl-dUTP at the 3' end using TdT. After the assembly of modified strands, sulfo-SMCC was covalently attached to the DNA structure via NHS ester. In a last step, TCEP reduced CPP containing a free sulfhydryl group were bound to the DNA tetrahedron in a covalent manner via the maleimide group of the bifunctional linker.

In the following, the conjugation strategy for the generation of DNA tetrahedra carrying CPP chains is explained in more detail.

#### Terminal deoxynucleotidyl transferase (TdT) reaction

In order to enable the multiple binding of sulfo-SMCC and thus CPP, Tet sequences (4.8) were enzymatically modified with aminoallyl-dUTPs on the 3'-ends using Terminal deoxynucleotidyl transferase (TdT, Roche). The reaction mechanism is illustrated in Figure 3 and explained in 2.2.1. The reaction mixture for each Tet sequence was incubated for 30 min at 37 °C in an Eppendorf ThermoMixer® C (Eppendorf AG). To stop the reaction, the samples were placed on ice and 2 µl of 0.2 M EDTA were added. Aminoallyl-dUTP elongated DNA sequences were purified either by ethanol precipitation (4.16) or using the NucleoSpin® Gel and PCR Clean up Kit (Macherey - Nagel) according to manufacturers' instructions. DNA samples were eluted with pre-warmed 100 mM KH<sub>2</sub>PO<sub>4</sub>, instead of the elution buffer delivered with the kit since this buffer contained Tris which would disturb the following NHS ester

## Material and Methods

---

reaction. DNA concentrations were determined using a NanoDrop ND-1000 UV/VIS spectrophotometer (PEQLAB Biotechnologie GmbH) (4.14).

The TdT reaction mixture consisted of:

approximately 100 pmol free 3' ends of TetS1 / S1* / S2 / S3 / S4	
200 $\mu$ M aminoallyl-dUTP in different ratios (1 : 3 or 1 : 10)	
5X TdT reaction buffer	4 $\mu$ l
25 mM CoCl <sub>2</sub>	4 $\mu$ l
TdT	0.1 $\mu$ l
dd H <sub>2</sub> O	x $\mu$ l
	$\Sigma = 20 \mu$ l

### Assembly of amine-modified Tet sequences

Aminoallyl-dUTP elongated Tet sequences were mixed in equimolar amounts and folded as explained in 4.23.1 at 500 nM. Modified DNA tetrahedra were not folded in 1X TM buffer but in 100 mM KH<sub>2</sub>PO<sub>4</sub>.

### Addition of sulfo-SMCC

The heterobifunctional linker sulfo-SMCC (Figure 16) was freshly prepared prior to use at a stock concentration of 10 mM in DMSO and subsequently added in a 50-fold molar excess towards DNA. The reaction mixture was incubated overnight at room temperature. The next day, samples were spin filtered using Amicon<sup>®</sup>-Ultra-0.5 centrifugal filter units with 3 K MWCO (4.17) to get rid of excess sulfo-SMCC which would interfere with the maleimide reaction in the next step.

### Reduction of Cystein-containing CPP with TCEP and addition to DNA tetrahedra

CPP (Cys - sC18) were solubilized at a concentration of 2 mM - 5 mM with Millipore water (4.9). Since Cys - sC18 peptides contain N-terminal cysteines, they tend to form dimers via disulfide bridges. In order to bind them to DNA tetrahedra, disulfide bonds had to be cleaved by reduction with tris(2-carboxyethyl)phosphine (TCEP)<sup>216</sup> (Figure 18). TCEP is particularly useful when cysteine residues are coupled to maleimides. It is stable in aqueous solutions, tolerates a wide pH range and does not undergo rapid oxidation that often occurs with other reducing agents such as dithiothreitol (DTT) and  $\beta$ -mercaptoethanol<sup>217,218</sup>. In order to remove TCEP after reduction, TCEP conjugated agarose beads were utilized (Pierce<sup>™</sup> Immobilized TCEP disulfide reducing gel, Thermo Fisher Scientific). Sixty  $\mu$ l of TCEP disulfide reducing gel were spun for 1 min at 1,000 rcf. After the supernatant was removed, TCEP agarose beads

## Material and Methods

were mixed with 30  $\mu$ l 2 mM Cys - sC18 and incubated for 2 h at room temperature. The mixture was then spun again for 1 min at 1,000 rcf and the supernatant, containing reduced peptides, was transferred into a new reaction tube. Reduced peptides were added to SMCC-conjugated DNA tetrahedra in a 100-fold molar excess and incubated at 4  $^{\circ}$ C overnight.

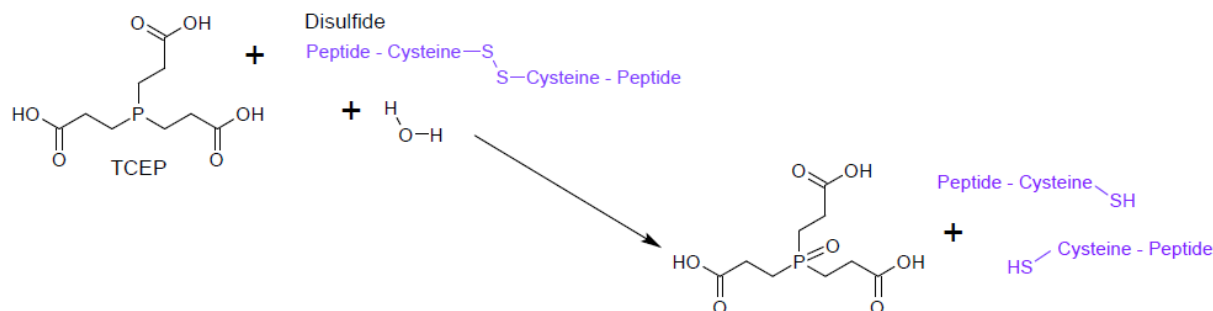


**Figure 18** | Reduction of disulfides with TCEP<sup>219</sup>. Disulfide bonds that occur within cysteine-containing peptides or proteins can be rapidly cleaved by tris(2-carboxyethyl)phosphine. This reduction is rather important when coupling thiol-containing molecules to maleimides.

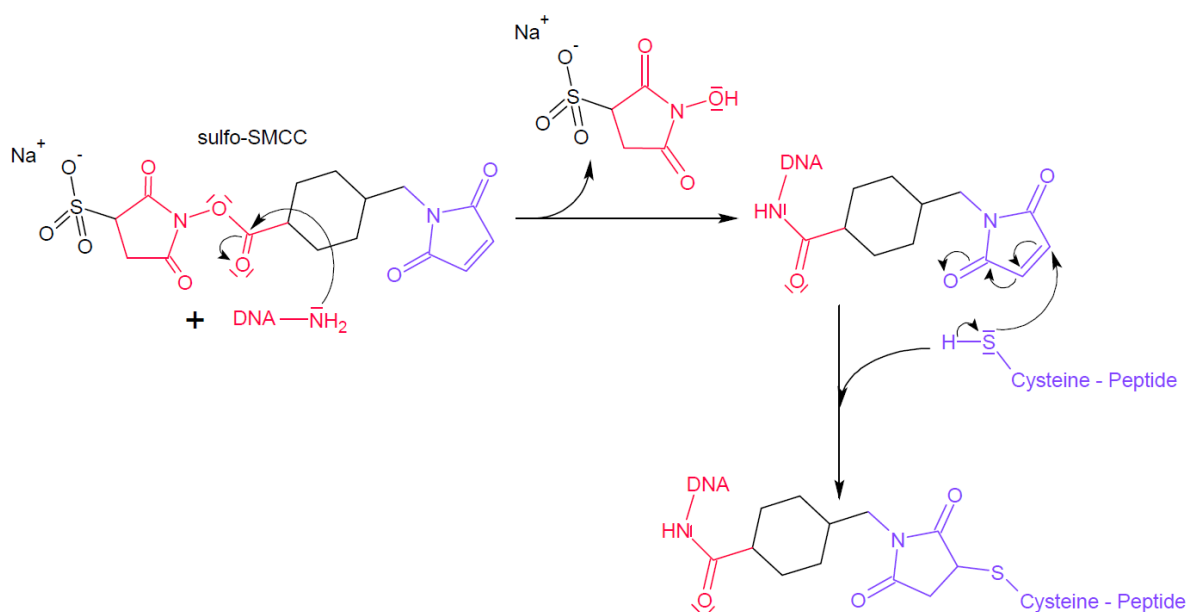


**Figure 19** | Reaction mechanism of conjugation of DNA and peptide via sulfo-SMCC. The primary amine group of the DNA reacts with the sulfo-NHS ester of sulfo-SMCC in a first step under the release of sulfo-NHS (red). In a second step, the DNA bound linker molecule reacts with sulfhydryl-groups of previously reduced cysteine-containing peptides via its maleimide group (purple).

The whole conjugation process was stepwise analyzed via 6 % (v/v) native PAGE (4.15.2). The final structure was also investigated via AFM imaging (4.30.1, Figure 30).

#### 4.26.2 DNA tetrahedra functionalized with single CPP molecules

To gain a better overview about the fabrication process, the different steps are illustrated in Figure 20. In order to generate DNA tetrahedra with single CPP functionalization, Tet sequences already containing a 5' NH<sub>2</sub> modification were first conjugated to DBCO-NHS esters. After purification, DBCO-modified Tet strands were clicked to an azide-containing CPP via copper-free click chemistry (SPAAC). Finally, CPP-conjugated oligonucleotides were assembled to functionalized DNA tetrahedra.

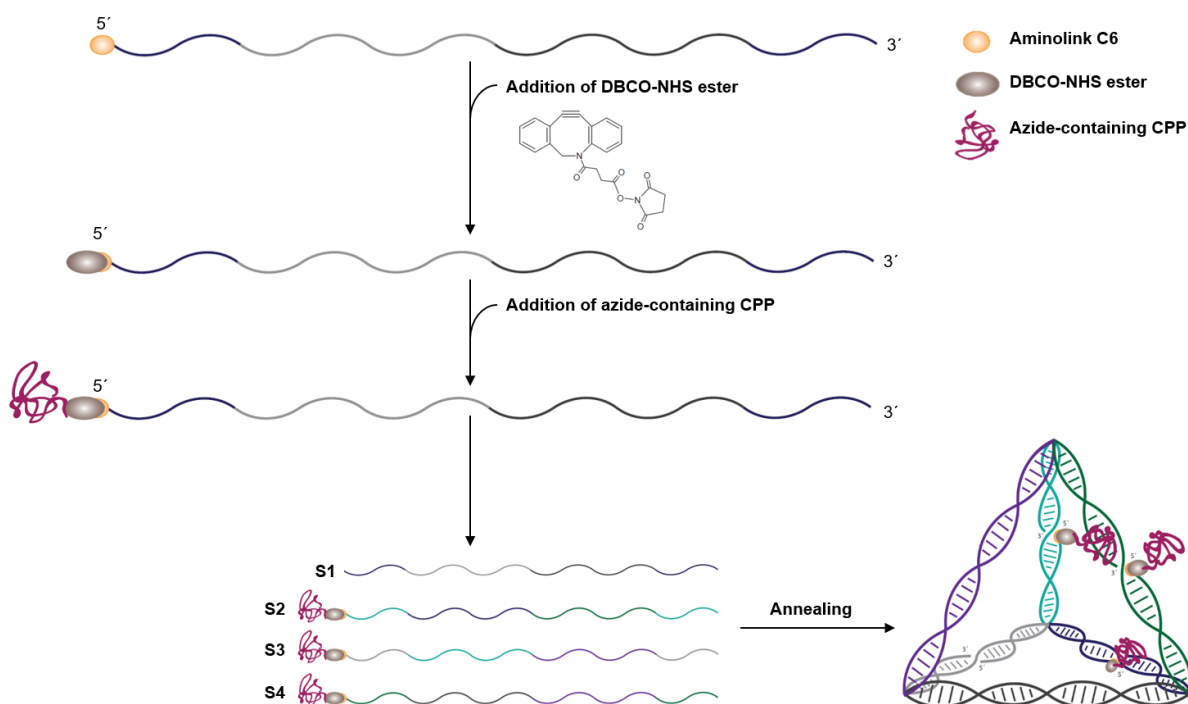


**Figure 20 | Schematic of engineering DNA tetrahedra coupled to single CPP molecules.** Partially complementary Tet sequences already synthesized with a 5' NH<sub>2</sub> modification were covalently coupled to DBCO-NHS esters. In the next step azide-containing CPP were clicked to DBCO-functionalized strands (SPAAC, see 2.2.4). Purified, CPP-conjugated strands were assembled to the full DNA structure.

In the following, the conjugation strategy for the fabrication of DNA tetrahedra functionalized with single CPP molecules is explained in more detail and an overview about the chemical reactions is given in Figure 21.

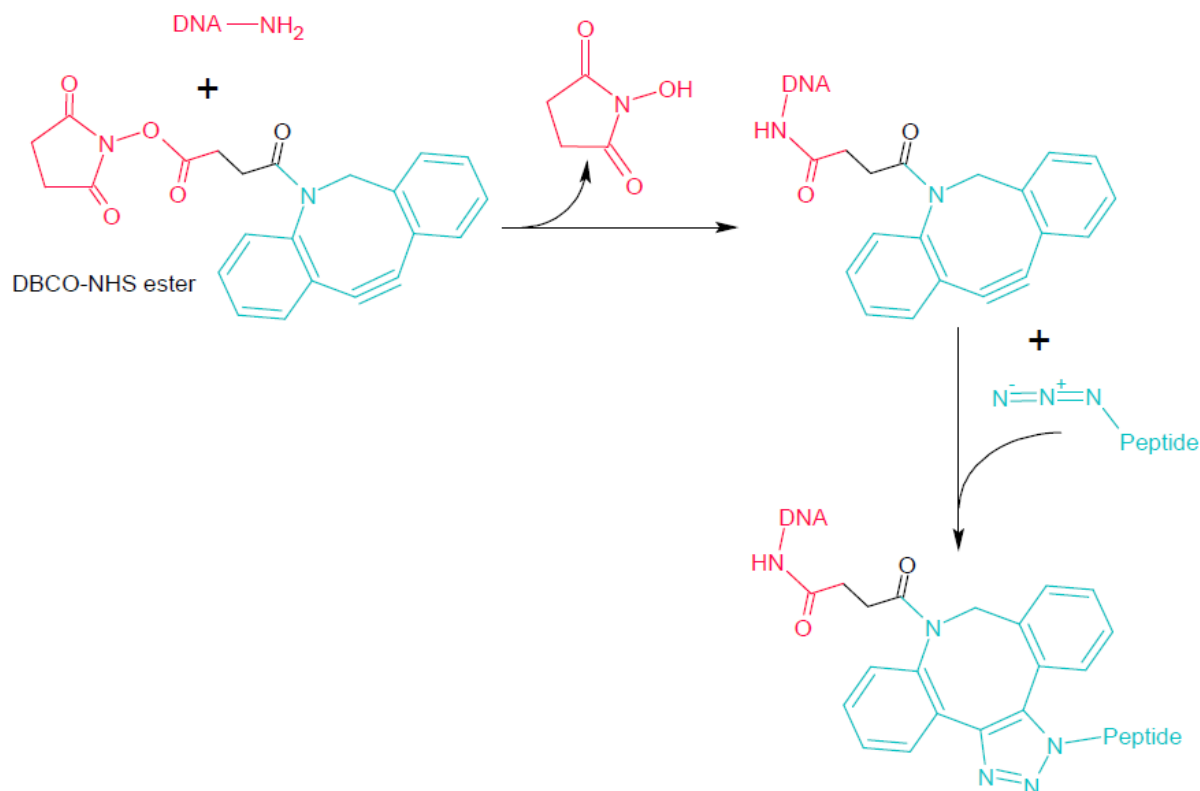


**Figure 21 | Reaction mechanism of conjugation of DNA and peptide via DBCO-NHS ester.** Amine-reactive DBCO-NHS esters react with  $\text{NH}_2$  groups of DNA (red). NHS is released and DNA covalently coupled to DBCO, which further reacts with an azide-containing peptide under the formation of a triazole in a covalent manner (green).

#### Addition of DBCO-NHS ester

The heterobifunctional linker DBCO-NHS ester (Figure 16) was freshly prepared prior to use at a stock concentration of 10 mM in DMSO. The dissolved linker was subsequently added to 5'  $\text{NH}_2$  Tet sequences (4.8) in a 100-fold molar excess and incubated overnight at room temperature. Next day, samples were purified using the NucleoSpin® Gel and PCR Clean up Kit (Macherey - Nagel) according to manufacturers' instructions. DBCO-functionalized oligonucleotides were eluted in pre-warmed 1X TM buffer and DNA concentrations were determined using a NanoDrop ND-1000 UV/VIS spectrophotometer (PEQLAB Biotechnologie GmbH) (4.14).

#### Addition of Azide-containing CPP

Azide-containing CPP (azide - sC18) were freshly solubilized at a concentration of 2 mM - 5 mM with Millipore water (4.9). In the next step, peptides were added to DBCO-modified oligonucleotides in a 50-fold to 100-fold molar excess and incubated overnight. Samples were eluted with 1X TM buffer after the subsequent purification with the NucleoSpin® Gel and PCR Clean up Kit (Macherey - Nagel). Concentrations were spectrophotometrically measured at a NanoDrop.

Annealing of CPP-conjugated oligonucleotides

CPP-conjugated Tet sequences were mixed in equimolar amounts and assembled as explained in 4.23.1 at 500 nM. The whole conjugation process was stepwise monitored via 6 % (v/v) native PAGE (4.15.2). The final structure was also investigated with AFM imaging (4.30.1, Figure 30).

4.27 Functionalization of DNA trimers with CPP

DNA trimers were functionalized with single CPP as previously described with DNA tetrahedra (4.26.2). Amine-modified oligonucleotides (Table 4) were first coupled to DBCO-NHS esters. After purification, DBCO-modified trimer strands were clicked to an azide-containing CPP (Table 5) via copper-free click chemistry (SPAAC). Samples were eluted with 1X TM buffer after the subsequent Kit purification and concentrations were spectrophotometrically determined at a NanoDrop. Finally, CPP-conjugated oligonucleotides were hybridized to a functionalized DNA trimer as explained in 4.23.2 and assembly monitored via 10 % native PAGE (4.15.2).

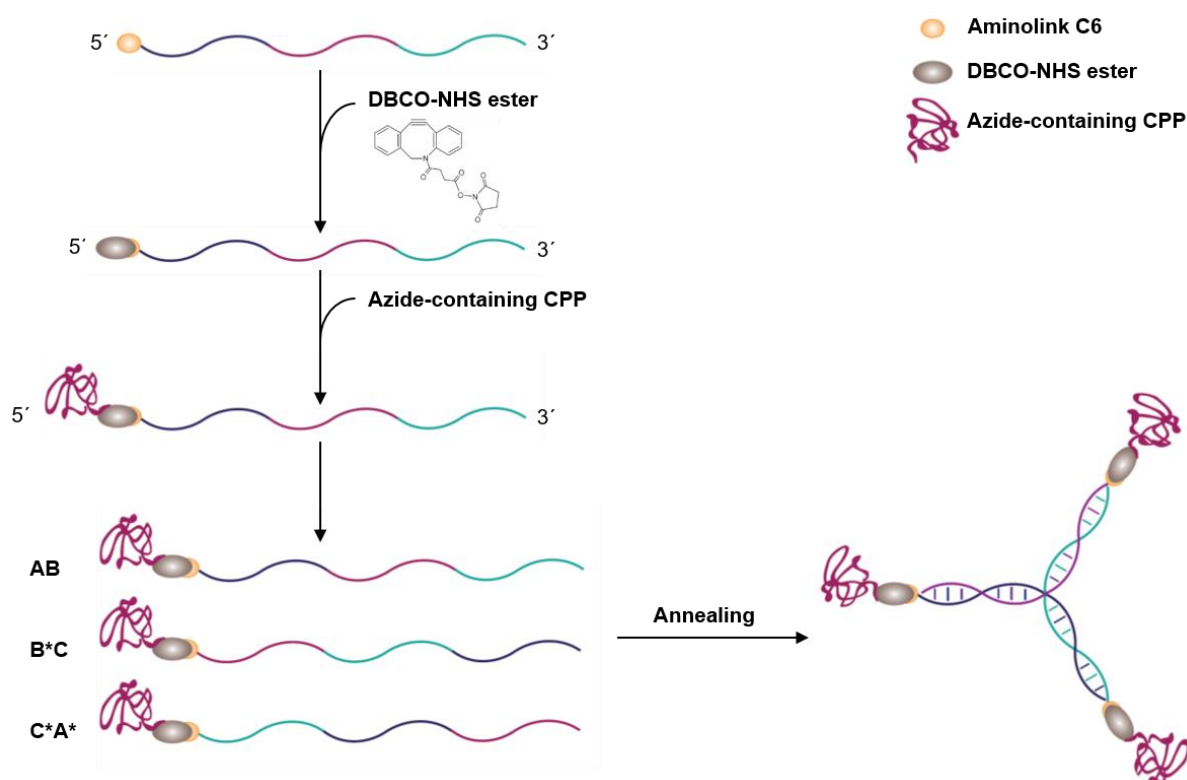


**Figure 22 | Functionalization of DNA trimers with single CPP molecules.** Partially complementary oligonucleotides containing a 5' NH<sub>2</sub> modification were covalently bound to DBCO. In the next step, azide-containing CPP were clicked to DBCO-functionalized strands (SPAAC, see 2.2.4). Kit purified, CPP-conjugated oligonucleotides were assembled to DNA trimers.

#### 4.28 Engineering synthetic actin crosslinkers

At the very beginning, complementary DNA strands are hybridized and covalently conjugated to dibenzocyclooctyne via DBCO-NHS ester on each site of the double strand. After purification, azide-containing actin-binding peptides were clicked to previously attached DBCO groups. An overview about the engineering process is given in Figure 23.

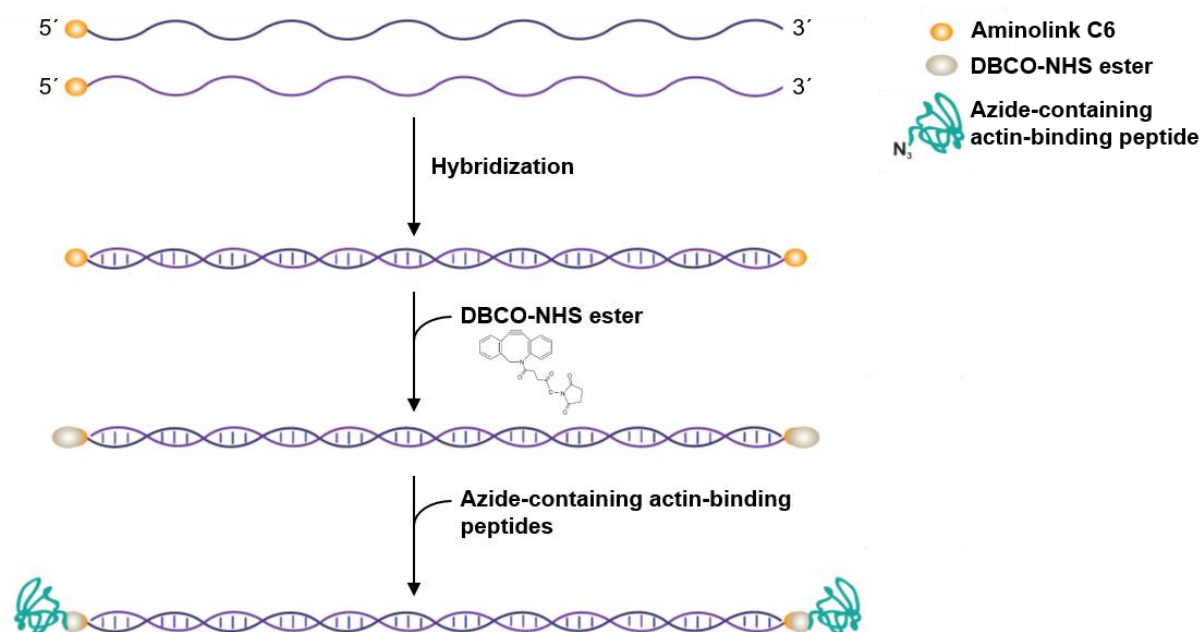


**Figure 23 | Engineering synthetic actin crosslinkers.** A copper-free click chemistry approach<sup>39</sup> was used to covalently attach actin-binding peptides to ds DNA. After hybridization of the complementary strands, DBCO-NHS ester covalently reacts with primary amine groups on each end of the double-stranded DNA-spacer. Subsequently, an azide-containing actin-binding peptide reacts with the previous attached DBCO group in a covalent manner.

In a first step, complementary 60 nt DNA strands (Table 4) were mixed in equimolar amounts and hybridized in 100 mM  $\text{KH}_2\text{PO}_4$  pH 7.2 at a final concentration of 25 mM in a TProfessional Thermocycler (Biometra GmbH) with the following program:

Denaturation	95 °C	2 min
Hybridization	71.6 °C	15 min
Storage	4 °C	∞

DBCO-NHS ester was dissolved in DMSO to a concentration of 10 mM, added in a 100-fold molar excess to previously hybridized DNA, and incubated overnight at room temperature. DBCO-modified ds DNA was purified via ethanol precipitation (4.16) and concentrations were measured using a NanoDrop ND-1000 UV/VIS spectrophotometer (PEQLAB Biotechnologie

## Material and Methods

GmbH) (4.14). Next, azide-containing peptides (i.e. LifeAct<sup>®</sup>, Table 5) were added in a 50 to 100-fold molar excess to DBCO-DNA and incubated over night at room temperature.

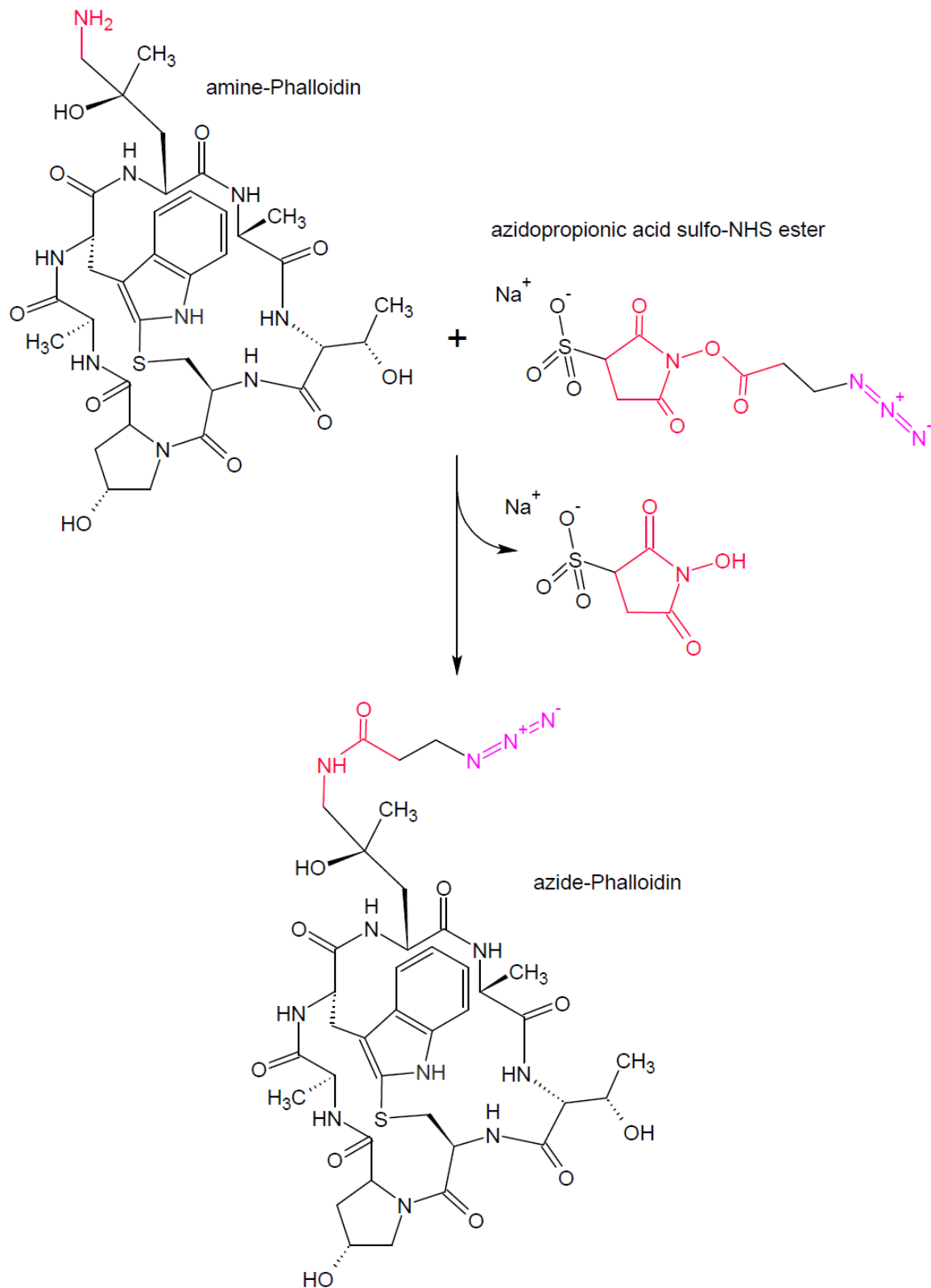


**Figure 24 | Coupling of azidopropionic acid sulfo-NHS ester to amine-Phalloidin.** Phalloidin carrying a primary amine group was covalently conjugated to an azide group via azidopropionic acid sulfo-NHS ester.

Since Phalloidin could not be purchased as azide-coupled molecule, azidopropionic acid sulfo-NHS ester (Figure 24) was coupled to amine-Phalloidin (4.9) to introduce an azide group. Therefore, azidopropionic acid sulfo-NHS ester was dissolved in DMSO to a concentration of 10 mM, mixed in equal molar amounts with amine-Phalloidin in 100 mM  $\text{KH}_2\text{PO}_4$  pH 7.2, and incubated over night at room temperature. No further purifications were performed and peptide was added in a 50 to 100-fold molar excess to DBCO-DNA as described above.

To remove excess peptides, samples were spin filtered using Amicon<sup>®</sup>-Ultra-4 centrifugal filter units with 10K MWCO (4.17) in 1X DBPS (w/o Calcium, w/o Magnesium). The successful synthesis and the purity of wLX and sPX was verified via 10 % (v/v) native PAGE (4.15.2). Synthetic crosslinkers were stored at - 20 °C with no detectable degradation.

### 4.29 Stability of DNA structures

To investigate how stable utilized DNA structures (i.e. DNA trimers and crosslinkers with and without phosphorothioate (PTO) modifications) are against nucleases, they were incubated with DNase I (endonuclease) and Exonuclease III.

In a first approach, PTO-capped as well as uncapped DNA trimers (Table 4) were assembled (4.23.2) at a final concentration of 2  $\mu\text{M}$ . DNA trimers were mixed with Exonuclease III (New England Biolabs) and 10X NEBuffer according to manufacturers' instructions and were incubated for 1 min, 5 min, 10 min, 20 min and 30 min at 37 °C in a Eppendorf ThermoMixer<sup>®</sup> C (Eppendorf AG), respectively. Right after, the enzyme was heat-inactivated for 20 min at 70 °C. Samples were analyzed via 10 % (v/v) native PAGE (4.15.2). Similar experiments were conducted for 60bp DNA that was used for engineering synthetic actin crosslinkers. In this case, full-PTO protected 60bp DNA as well as unprotected 60bp DNA (Table 4) were hybridized as described in 4.28. Double-stranded DNA (100 ng) were mixed with DNase I and corresponding 10X DNase I buffer as well as with Exonuclease III and 10X NEBuffer according to manufacturers' instructions. As controls, samples were mixed with Opti-MEM<sup>®</sup> I Reduced-Serum Medium and dd  $\text{H}_2\text{O}$ . All samples were incubated for 30 min at 37 °C and analyzed via 12 % (v/v) native PAGE.

In a second approach, DNA strands containing a 5' Cyanine 3 and the complementary strand a 3' BHQ2 (black hole quencher 2) were utilized. As long as Cy3 and BHQ2 are close together, fluorophore's emission is suppressed. In case of degradation through nucleases, BHQ2 and Cy3 are not close anymore and the fluorescence signal increases. The 5' Cy3-60fw and 3' BHQ2-60rv strand (Table 4) without PTO-modifications were hybridized as previously mentioned (4.28.). Furthermore, PTO-capped Cy3-BHQ2 DNA trimers as well as uncapped Cy3-BHQ2 DNA trimers (Table 4) were assembled (4.23.2). Samples were mixed as described

## Material and Methods

below and pipetted in triplicates à 100 µl into black 96-well plates (Microplate 96-well (black), fluorotrac, Greiner Bio-One).

Reaction mixture:

	Mastermix (1X)	Final concentration
10 µM DNA (i.e. DNA trimer or 60bp DNA)	1.5 µl	150 nM
10X Enzyme buffer	10 µl	1X
10X Anti-bleaching buffer	10 µl	1X
250 U/ml Glucose oxidase	16 µl	40 U/ml
1,000 U/ml DNase I <u>or</u> 10,000 U/ml Exonuclease III	1 µl	10 U/ml <u>or</u> 100 U/ml
dd H <sub>2</sub> O	61.5 µl	
	Σ = 100 µl	

Fluorescence intensities were read out with a TECAN Infinite® M1000 reader (Tecan Group AG) at an excitation of 550 nm and an emission of 570 nm. Samples were measured over 30 min and fluorescence was recorded every 30 s. Fluorescence intensities of triplicates were averaged. DNA trimers and 60bp DNA, which were not treated with nucleases, served as control.

### 4.30 Atomic force microscopy (AFM)

AFM imaging is an ideal technique to determine whether the DNA nanostructure was formed correctly and possibly how it appears with modifications. All AFM images were acquired with a NanoWizard 3.0 (JPK Instruments AG) and recorded in alternating contact (AC) / tapping mode at room temperature at a line rate of 1 Hz - 5 Hz with JPK SPM software. Unmodified and CPP-conjugated DNA tetrahedra were visualized and characterized in fluid using a USC-F0.3-k0.3 cantilever (Asylum Research) whereas DNA tubes were measured in air using an ACTA-10 (AppNano) cantilever. The properties of the cantilevers used in this work are listed below (Table 6).

**Table 6 | Properties of cantilevers used for AFM measurements**

Cantilever	Force constant	Resonance frequency
ACTA-10	37 (13 - 77) N/m	300 (200 - 400) kHz
USC-F0.3-k0.3	0.3 (0.06 - 1.0) N/m	180 (60 - 350) kHz

The sample preparation differed from measurements recorded in air or fluids (4.30.2 and 4.30.1). After the cantilever was secured to the glass block and put into the AFM head, the laser sum signal as well as vertical and lateral deflection was adjusted. Cantilever specific calibrations were made and the AFM head was approached to the surface in contact mode. After reaching the surface of the sample, the cantilever was retracted and the contact mode switched to AC mode. This step involved the selection of a set point according to the calibrated frequency. After the AFM head again reached the sample's surface, the measurement started. Since SPM software produces images of different channels per scan, JPK DP software was applied to select height or phase images. Further analysis and processing was performed with Gwyddion software.

### **4.30.1 AFM imaging of DNA tetrahedra in fluids**

Cleaned and freshly cleaved mica surface was incubated with 100  $\mu$ l poly-L-ornithine for 10 min and washed three times with 100  $\mu$ l 1X TM buffer (4.3) to remove unbound DNA and debris. Positively charged poly-L-ornithine is used to bind negatively charged DNA on the mica. Two  $\mu$ l - 5  $\mu$ l of the Amicon<sup>®</sup>-purified sample was pipetted on the previously prepared mica surface and incubated for 10 min at room temperature. Directly after, the surface was washed twice with 100  $\mu$ l 1X TM buffer. In order to measure the sample under stable conditions, a plastic ring was glued (Reprorubber<sup>®</sup> Thin Pour, JPK Instruments AG) around the mica surface to construct a chamber that was filled up with 1X TM buffer. The cantilever bearing the USC-F0.3-k0.3 tip was secured to the glass block and, in order to prevent air bubbles between cantilever and glass block, a drop of 1X TM buffer was applied on the back of the chip. The glass block was then put into the AFM head and the cantilever was used with a spring constant of  $\sim$  0.29 N/m and a resonance frequency of  $\sim$  168 kHz.

### **4.30.2 AFM imaging of Eight-helix tubes (8HT) in air**

Pre-hybridized 8HT were deposited on a cleaned and freshly cleaved mica surface (Plano GmbH) attached to a microscope slide. After a settling time of 10 min samples were spun at 6,000 rpm (SPROUT<sup>®</sup> Mini centrifuge, Heathrow Scientific<sup>®</sup> LLC) in short intervals to minimize the alignment of attached 8HTs. The cantilever bearing the Gold-coated ACTA-10 tip was secured to the glass block, put into the AFM head and used with a spring constant of  $\sim$  54 N/m and a resonance frequency of  $\sim$  300 kHz.

### 4.31 Actin preparation

Globular actin (G-actin) was prepared from rabbit muscle (rabbits provided by Fraunhofer IZI, Leipzig) in two steps<sup>220</sup>. First, skeletal muscle actin was extracted and dried as acetone powder according to the method of Pardee and Spudich<sup>221</sup> and second, the actual actin prep adapted from the lab of Marie-France Carlier was conducted to isolate solely actin. Monomeric actin (in 1X G-buffer) was polymerized to F-actin by the addition of 20X KME-buffer (4.3) at a final concentration of 24  $\mu\text{M}$  and 1X F-buffer.

### 4.32 Bulk shear rheology

Immediately after inducing actin polymerization by the addition of 20X KME-buffer to G-actin enriched w/ or w/o synthetic crosslinkers, a sample volume of 175  $\mu\text{l}$  was loaded to the dynamic shear rheometer (ARES, TA Instruments, USA) equipped with a cone (diameter 25 mm, 0.04 rad). The network between the cone and the plate was surrounded with a 2.5 ml 1X F-buffer bath (4.3) similarly as described previously<sup>222,223</sup> to avoid a direct contact of the sample with air. The sample chamber was sealed with a cap equipped with wet sponges to suppress evaporation. Measurements were performed at 20 °C and followed the sequence: (i) The time evolution of the polymerization was monitored for 2 h (one data point per minute;  $\gamma = 5\%$ ;  $f = 1\text{ Hz}$ ), which was subsequently followed by a (ii) short frequency sweep ( $\gamma = 5\%$ ;  $f = 0.01\text{ Hz}$  to 30 Hz; 5 data points per decade), (iii) long frequency sweep ( $\gamma = 5\%$ ;  $f = 0.001\text{ Hz}$  to 30 Hz; 21 data points per decade), (iv) short frequency sweep, (v) strain sweep ( $f = 1\text{ Hz}$ ;  $\gamma = 0.0125\%$  to 100%; 20 data points per decade), (vi) short frequency sweep, and (vii) strain sweep. The sequence has been designed to test the robustness of the system over time and the frequency of 1 Hz has been chosen to display the values for  $G_0$ .

### ***EcoRV*-HF<sup>®</sup>-digestion of sPX**

To investigate the necessity of two actin-binding domains on one crosslinker for the stiffening of reconstituted actin networks, bulk rheology measurements on actin with functional, undigested as well as *EcoRV*-HF<sup>®</sup>-digested sPX that were incubated for 1 h at 37 °C were performed. Crosslinker DNA was designed with an *EcoRV* digestion site almost in the middle of the double strand (4.8). A digestion of this results in a 32bp and a 28bp fragment. Prior to rheology measurements, 1624 ng sPX (final concentration of 0.24  $\mu\text{M}$  in 175  $\mu\text{l}$  final sample volume) were incubated with 5  $\mu\text{l}$  of *EcoRV*-HF<sup>®</sup> (20,000 units/ml, New England Biolabs) and 1.75  $\mu\text{l}$  of 10X CutSmart<sup>®</sup> buffer (New England Biolabs) in a final volume of 20  $\mu\text{l}$  for 1 h at 37 °C. No inactivation of the enzyme was performed. After *EcoRV*-HF<sup>®</sup>-incubation, the

digested sample was directly added to actin, 10X G-buffer and 20X KME-buffer to a final volume of 175  $\mu$ l. Thereby, actin polymerization was induced and rheological measurements were performed as previously described. In addition, *EcoRV*-HF<sup>®</sup>-digestion of sPX was proved via 10 % (v/v) native PAGE (4.15.2).

### 4.33 Static light scattering (SLS)

Static light scattering (Malvern Instruments Ltd., Zetasizer Nano ZSP, UK) was used to observe the dependence of actin morphology<sup>140,224</sup> on synthetic crosslinker concentrations. The scattering of the incident He-Ne-Laser beam (633 nm, 10 mW) by the sample (20  $\mu$ l) in a quartz cuvette (Malvern, ZEN2112) was detected at a fixed angle of 173 °. To prevent evaporation during long-term measurements, the cuvette was sealed with mineral oil (molecular biological grade, BioReagent, Sigma Aldrich Co., Germany). The final actin concentration was 24  $\mu$ M. The crosslinker concentration ranged from 0  $\mu$ M to 9.6  $\mu$ M ( $R = 0$  to 0.4). The scattering of the sample was measured every minute for 1.5 h and scattering intensities were arithmetically averaged after 30 min of equilibration.

### 4.34 Spinning disc confocal microscopy

Monomeric actin was mixed under 1X G-buffer conditions (4.3) at a molar ratio of 3 : 1 with Phalloidin-tetramethylrhodamine B isothiocyanate (Phalloidin-TRITC, Sigma-Aldrich) for visualization. Synthetic crosslinkers with two LifeAct<sup>®</sup> binding domains (wLX) were added to yield a final  $R = 0.333$ ,  $R = 0.01$ , and  $R = 0.001$  or with two Phalloidin binding domains (sPX) to yield a final  $R = 1$ ,  $R = 0.1$ , and  $R = 0.01$ , respectively. Polymerization was initialized by increasing the salt concentration to 1X F-Buffer conditions (4.3) after mixing all components, leading to a final actin concentration of 3  $\mu$ M. Immediately after starting the polymerization process the premixed solution was deposited into a sample chamber as described previously<sup>154</sup>. Measurements were performed on a spinning disc confocal microscope (inverted Axio Observer.Z1/Yokogawa CSU-X1A 5000 (Carl Zeiss Microscopy GmbH, Germany), 100x oil immersion objective (Plan-Apochromat 100x/1.40 Oil DIC M27)) and recorded with a Hamamatsu Camera at an exposure time of 50 ms. Image series were exported using the ZEN 2 software provided by the company (Carl Zeiss Microscopy GmbH).

#### **4.35 Macroscopic behavior of actin in an inclined cuvette**

Three different samples, i.e. 24  $\mu\text{M}$  actin only, 24  $\mu\text{M}$  actin enriched with sPX ( $R = 0.4$ ) and 24  $\mu\text{M}$  actin supplemented with sPX ( $R = 0.4$ ) that was incubated for 1 h at 37 °C with 300 U *EcoRV*-HF<sup>®</sup> (New England Biolabs) prior to the experiment, were prepared similar as described above. Final samples were pipetted into a small cuvette at a volume of 150  $\mu\text{l}$  each. Additionally, a small amount of free Phalloidin-TRITC was added to dye the solution for a better contrast and visibility. After 40 min resting time at room temperature, the cuvette with the respective sample was placed on an inclined plane with a 20 ° angle. Images were recorded every second using a commercially available digital camera.

#### **4.36 Actin polymerization / depolymerization assay (pyrene assay)**

In order to investigate whether the synthetic actin crosslinkers interfere with actin polymerization or depolymerization, a pyrene assay using pyrene muscle actin (Cytoskeleton Inc.) was conducted. Those actin monomers had been modified to contain covalently linked pyrene molecules at the cysteine 374 residue via N-(1-pyrene) iodoacetamide. The fluorescent signal of monomer pyrene-actin is enhanced during its polymerization into filaments, making it an ideal tool for monitoring both actin polymerization as well as depolymerization.

Lyophilized pyrene-actin was reconstituted according to manufacturers' instructions and further diluted to 0.6 mg/ml (i.e. 13.95  $\mu\text{M}$ ) with 1X G-buffer (4.3). To depolymerize actin oligomers, the solution was placed on ice. After 1 h, pyrene-actin was spun for 30 min at 14,000 rpm and 4 °C to remove any residual nucleating centers. Working concentrations of pyrene-actin varied between 6  $\mu\text{M}$  and 10  $\mu\text{M}$ . The reaction was performed in a black 96-well plate (Microplate 96-well (black), fluorotrac, Greiner Bio-One) at room temperature.

Example for reaction mixture for pyrene-actin w/o crosslinkers:

	Final concentration	Volume
13.95 $\mu\text{M}$ pyrene-actin in 1X G-buffer	6 $\mu\text{M}$	43 $\mu\text{l}$
10X G-buffer	1X	5.7 $\mu\text{l}$
10X Anti-bleaching buffer	1X	10 $\mu\text{l}$
400 U/ml Glucose oxidase (GOx)	40 U/ml	10 $\mu\text{l}$
dd H <sub>2</sub> O		26.3 $\mu\text{l}$
20X KME	1X	5 $\mu\text{l}$
		$\Sigma = 100 \mu\text{l}$

All components, except for 20X KME buffer, were mixed (4.3). Prior to induction of polymerization, a fluorescence baseline at 405 nm base was recorded. The process of pyrene-actin filament formation induced by the addition of 20X KME buffer was monitored over time and fluorescence measured every 1 min or 5 min. After 90 min, depolymerization was induced by the addition of Latrunculin B (Sigma-Aldrich) to a final concentration of 200  $\mu$ M and fluorescence measured for another 90 min.

Glucose and GOx served as an anti-bleaching agent and GOx was added to the mixture at last in order to prevent a rapid degradation of glucose. Synthetic crosslinkers were added at  $R = 1$ ,  $R = 0.2$ ,  $R = 0.1$ ,  $R = 0.08$ ,  $R = 0.02$  and  $R = 0.01$ .

### 4.37 Basic cell culture techniques

HeLa, MDA-MB-231 and MCF-10A cells were cultivated in their corresponding cell culture medium (4.5) in 75 cm<sup>2</sup> CELLSTAR<sup>®</sup> Filter cap cell culture flasks (Greiner Bio-One) as a monolayer culture in 5 % CO<sub>2</sub> humidified atmosphere at 37 °C in an incubator HERAcCell<sup>®</sup> 240 (Thermo Fisher Scientific). All culture media and buffers were pre-warmed to 37 °C in a water bath (GFL Gesellschaft für Labortechnik mbH) prior to usage.

#### 4.37.1 Changing culture medium

Since cells constantly consume nutrients and thereby produce waste products, culture medium was routinely renewed every 2 – 3 days. Phenol red, which was supplemented in all culture media, served as pH indicator. A color change of the medium from red to orange/yellow indicated an acidification due to waste products and the necessity to change the medium. Therefore, old medium was aspirated and cells washed with 5 ml 1X DPBS (without Ca<sup>2+</sup> and Mg<sup>2+</sup>). DPBS was removed and 10 ml fresh medium were added to cover the cells. Cells were placed into the incubator.

#### 4.37.2 Passaging cells

Many cell types, especially cell lines that double quite fast (~ every 24 h), change their growth rate as well as gene expression depending on the cell density in the culture vessel. This occurs particularly when cells grow fully confluent, meaning that 100 % of the growth area is covered by a monolayer of cells. In order to maintain a consistent proliferative phenotype and to regulate the population density, cells were routinely sub-cultured every 3<sup>rd</sup> to 5<sup>th</sup> day. Again, old medium was aspirated and cells washed with 5 ml 1X DPBS (Volume for 75 cm<sup>2</sup> flasks). DPBS was removed and cell trypsinized by the addition of 2 ml 0.05 % Gibco<sup>®</sup> Trypsin-

EDTA (Thermo Fisher Scientific). Trypsinization times differed between cell lines. Whereas HeLa and MDA-MB-231 cells were incubated with trypsin for only 2 -3 min, MCF-10A cells needed about 18 min to fully detach from the surface. After cells were detached, 5 ml fresh medium, containing FCS to inactivate trypsin, were added and mixed with the detached cells. Then, the whole cell suspension was transferred into a sterile 15 ml falcon® tube. After a centrifugation time of 5 min at 1150 rpm in a HeraeusMultifuge® 3SR+ (Thermo Fisher Scientific), the supernatant was discarded and cells were resuspended in 1 ml fresh medium. Ten ml fresh medium were pipetted into a new 75 cm<sup>2</sup> culture vessels and 100 µl to 500 µl of the cell suspension were added. Culture vessel was swayed slightly back and forth in order to equally distribute the cells. Cells were placed into the incubator.

### 4.37.3 Freezing, thawing and quality control of human cell lines

For long-term storage of human cell lines, cryopreservation was performed<sup>225</sup>. During this process, cell solutions are frozen with a cryoprotectant, usually DMSO, to impede cell death or damage due to the formation of ice crystals. To generate cryostocks, 500 µl 2X Freeze medium (4.5) were mixed with 500 µl cell suspension of 3 - 10 x 10<sup>6</sup> cells/ml in 2 ml CryoPure tubes (Sarstedt). Stocks were cooled slowly, i.e. - 1 °C/min, to - 80 °C using a Mr. Frosty™ freezing container (Thermo Fisher Scientific) and subsequently stored in the vaporous phase of liquid nitrogen at - 156 °C.

To culture frozen cryostocks of cells, cells were rapidly, but not fully, thawed at 37 °C in a water bath for ~ 1 min. Directly after, cryostock solution was transferred into a 15 ml falcon® tube containing 5 ml fresh medium and spun for 5 min at 1150 rpm in a HeraeusMultifuge® 3SR+ (Thermo Fisher Scientific). The supernatant was discarded and cell pellet resuspended in 2 ml fresh medium, which was then transferred into a 75 cm<sup>2</sup> CELLSTAR® Filter cap cell culture flask (Greiner Bio-One), containing 10 ml fresh culture medium.

In order to maintain cell culture quality, cell stocks were screened for bacteria and fungi using a Leica DMIL LED inverted microscope (Leica Microsystems GmbH), and tested for viable cell counts as well as growth potential. Additionally, cells were checked for the presence of *Mycoplasma* species every three months. Since these small bacteria are difficult to detect with conventional light microscopy and resistant to antibiotics, they often remain undetected. However, they may cause cellular changes, such as changes in metabolism and cell growth. All cell lines were checked for *Mycoplasma* contamination via qPCR at GATC Biotech AG.

### 4.37.4 Determination of cell count and viability

Cell count and viability was determined by a Luna II™ automated cell counter (Biozym). Therefore, 10 µl cell suspension were pre-mixed with 10 µl Trypan Blue Stain 0.4 % (Biozym)

and 10  $\mu$ l of this mixture were subsequently transferred into a Luna™ cell counting slide (Biozym). Cell count and viability were read out by the device.

### 4.37.5 Fixation of cells

Cells were grown on detachable 8-well glass slides (Sarstedt). To fix them, e.g. after transfection with wLX, old medium was removed and cells washed three times for 2 min with 1X PBS-T (4.3). PBS-T buffer was removed and wells filled with 300  $\mu$ l 4 % Roti®-Histofix (Paraformaldehyde diluted in PBS, Carl Roth GmbH) each. After 10 min incubation at room temperature, Roti®-Histofix was removed and wells washed three times for 2 min with 1X PBS-T. After washing, chambers were removed from the glass slide, which was then covered with mounting medium Fluoroshield™ (Sigma-Aldrich) and finally sealed with a cover slip (VWR). Fixed cell samples were stored protected from light in a transport box at room temperature.

### 4.37.6 Staining of cells

#### 4.37.6.1 Staining of living cells

In order to fluorescently image intracellular structures of living cells, dye molecules that are able to pass the cell membrane were used. Nuclei were stained utilizing Hoechst® 33342, lysosomes were observed with LysoTracker™ Deep Red and to visualize the cytosol, CellTracker™ Blue CMAC was used. All dyes were prepared in stock solutions according to manufacturers' instructions and further diluted in Opti-MEM® to desired working concentrations, which are listed in Table 7.

**Table 7 | Working concentrations of utilized dyes for live-cell imaging**

Dye	Working concentration
Hoechst® 33342	5 $\mu$ M
LysoTracker™ Deep Red	0.5 $\mu$ M
CellTracker™ Blue CMAC	10 $\mu$ M

After incubation with DNA structures, cells were washed with 300  $\mu$ l 1X DPBS and subsequently incubated with 300  $\mu$ l of corresponding dye solution for 15 min in the incubator. After this, cells were washed three times with 1X DPBS. In order to drastically reduce background fluorescence caused by phenol red in cell media, chambers were filled up with

300 µl Gibco FluoroBrite DMEM. Cells were imaged via confocal laser scanning microscopy using a LSM 710 (Carl Zeiss Microscopy GmbH). Corresponding settings for LSM imaging are described in 4.40.7.

### 4.37.6.2 Staining of fixed cells

Compared to staining of living cells, fixed cells are stained with dyes that cannot pass cellular membranes or those which are very toxic, such as phalloidin. Since cells are permeabilized with 1X PBS-T buffer after fixation (4.37.5), dyes can easily flow into cells and stain intracellular structures. During this work, actin structures were visualized utilizing Fluorescein (FITC)-Phalloidin (Thermo Fisher Scientific). FITC-Phalloidin was diluted to a working concentration of 100 nM in 1X PBS-T. Sixty µl of this solution were added to previously fixed and permeabilized cells and incubated for 20 min at room temperature. Then, cells were washed three times for 2 min with 1X PBS-T buffer. Chambers were detached from glass slide, mounting medium was added and cells sealed with a cover slip. In order to co-stain for nuclei, mounting medium Fluoroshield™ containing DAPI (Sigma-Aldrich) was utilized.

### 4.37.7 **Internalization of DNA into cells with Lipofectamine™ 3000**

The uptake of DNA-structures or ds DNA strongly depends on the amount of Lipofectamine™ 3000 transfection reagent (Thermo Fisher Scientific) in the transfection mixture. Since Lipofectamine™ 3000 is known to be cytotoxic at high concentrations, it was necessary to determine which concentration still gives good internalization rates but does not induce apoptosis of cells (supplemental Figure S 10, Figure S 11, Figure S 12 and supplemental Table S 1). Concerning this issue, the following experiments were conducted.

#### 4.37.7.1 Lipofectamine™ 3000 concentration-dependent internalization of DNA

In order to determine, which Lipofectamine™ 3000 concentration gives high internalization efficacies, cells were transfected with a dilution series of Lipofectamine-complexed 300 nM Cy3-labeled 60nt ss DNA. MDA-MB-231 cells (4.4.2) were seeded at  $1 \times 10^6$  cells/ml in 100 µl in 96-well plates and incubated overnight at 37 °C in the incubator. The next day, medium was removed and cells washed with 1X DPBS. Fifty µl of transfection mixture containing 0 % (v/v) to 12 % (v/v) Lipofectamine™ 3000 were added. After transfection (4.37.8) for 2 h, the transfection mixture was removed and cells washed twice with 50 µl 1X DPBS. In order to analyze them via flow cytometry, cells were detached and suspension was analyzed via iQue™ Screener (IntelliCyt®) (4.11) under the excitation and detection of Cy3 in the FL2 channel. Mean fluorescence intensities of cell population transfected with different Lipofectamine concentrations were analyzed and compared.

### 4.37.7.2 Cytotoxicity of Lipofectamine™ 3000

Since Lipofectamine™ 3000 is cytotoxic at high concentrations, a dilution series should gain information about the concentration, which still achieves a correspondingly high internalization efficacy (4.37.7.1) without killing the cells. Therefore, cells were seeded at  $1 \times 10^6$  cells/ml in 100  $\mu$ l in 96-well plates and incubated overnight at 37 °C in 5 % CO<sub>2</sub> humidified atmosphere. The next day, medium was removed and cells washed with 1X DPBS. Fifty  $\mu$ l transfection mixture containing 0 % (v/v) to 12 % (v/v) Lipofectamine™ 3000 were added. After transfection (4.37.8) for 2 h, cells were analyzed for apoptosis (4.40.1).

### 4.37.8 Transient transfection of human cell lines

Transfection of HeLa, MDA-MB-231 and MCF-10A cells was performed using Lipofectamine™ 3000. Volumes of transfection mixtures used depended on the size of the wells and are listed in Table 8.

**Table 8 | Volumes of transfection mixtures for different cavities**

Microplate/insert	Volume of transfection mixture/well
6-well	1000 $\mu$ l
12-well	500 $\mu$ l
96-well	50 $\mu$ l
2-well culture insert (2D migration)	70 $\mu$ l

For a transfection mixture of 50  $\mu$ l total, 0.75  $\mu$ l Lipofectamine™ 3000 were pipetted to 25  $\mu$ l Opti-MEM® I Reduced-Serum Medium (Thermo Fisher Scientific) and incubated for 5 min at room temperature. Meanwhile, DNA (e.g. crosslinker sample) was diluted in 25  $\mu$ l Opti-MEM® to twice of the desired concentration. After 5 min, 25  $\mu$ l of the Lipofectamine™ 3000/Opti-MEM® mixture was pipetted to previously diluted DNA resulting in a final DNA concentration of typically 150 nM to 600 nM. The transfection mixture, at a Lipofectamine™ 3000 concentration of 0.75 % (v/v), was complexed for 30 min at room temperature. For larger or smaller volumes of transfection mixtures, the volumes of Lipofectamine™ 3000 and Opti-MEM® were adjusted according to the previously described ratios.

Cells were seeded one or two days before transfection. For some assays, cells were starved for 24 h with Opti-MEM® I Reduced-Serum Medium before transfection to attain high internalization rates. After washing with 1X DBPS, cells were fully covered with transfection

mixture and incubated for 4 h to 6 h at 37 °C in the incubator. Finally, the transfection mixture was removed and replaced with fresh either serum-containing or serum-free media. Transfected monolayer cultures were cultured at 37 °C for 24 h to 72 h.

### Determination of DNA internalization efficacies

Before conducting all following cell based assays, it was necessary to investigate how effective utilized cell lines internalize DNA nanostructures when complexed with 0.75 % (v/v) Lipofectamine™ 3000. Therefore, cells were seeded at  $2 \times 10^5$  cells/ml in 500  $\mu$ l in 24-well plates and incubated overnight in the incubator. The next day, cells were washed with 1X DPBS and subsequently transfected (4.37.8) for 2 h or 4 h with 300 nM or 600 nM Cy3-labeled 60bp DNA (Table 4), that was hybridized as described for synthetic actin crosslinker production (4.28). In order to remove fluorescent DNA constructs that were not internalized and probably bind unspecific to cell surfaces, cells were washed twice with 1X DPBS. Cells were detached and suspension was analyzed at the flow cytometer iQue™ Screener (IntelliCyt®) (4.11) under excitation and detection of Cy3 in the FL2 channel. Cells treated only with Lipofectamine™ 3000 but without DNA served as control. Internalization efficacy was determined by the relative number of positively classified cells compared to negative control populations.

### 4.38 Localization and stability studies of CPP-conjugated DNA structures

The intracellular localization of CPP-conjugated DNA tetrahedra as well as their stability within cells was investigated via confocal laser scanning microscopy (LSM). Therefore, DNA tetrahedra coupled to the FRET pair Cy3 and Cy5, referred to as FRETrahedra, were utilized. FRETrahedra that could be further modified with CPP, were assembled using Cy3 and Cy5-labeled strands as well as two amine-modified sequences (Table 4). Covalent conjugation to sC18 was performed as described in 4.26.2. HeLa cells (4.4.2) were seeded at  $1.66 \times 10^5$  cells/ml in 300  $\mu$ l in 8-well chamber slides (8-well on cover glass II, Sarstedt) and incubated for 24 h at 37 °C in 5 % CO<sub>2</sub> humidified atmosphere. Cells were washed with 1X DPBS and CPP-coupled FRETrahedra as well as unmodified FRETrahedra, diluted to 200 nM in Opti-MEM®, were incubated with HeLa cells for 24 h in the incubator. Right after, cells were stained with 10  $\mu$ M CellTracker™ Blue CMAC for 15 min as described in 4.37.6.1. Live-cell imaging was conducted via confocal laser scanning microscopy (4.40.7).

Similar to CPP-FRETrahedra localization, the intracellular localization of PTO-capped, CPP-conjugated Cy3-DNA trimers was investigated. PTO-capped Cy3-DNA trimers (Table 4) were sC18-functionalized as described in 4.27. Cells were treated as described above but

incubated for 2 h with 400 nM either unmodified PTO-capped Cy3-DNA timer as well as CPP-functionalized ones. Cells were stained with 5  $\mu$ M Hoechst<sup>®</sup> 33342 and 0.5  $\mu$ M LysoTracker<sup>™</sup> Deep Red for 15 min (4.37.6.1) and subsequently, live-cell imaging was performed.

### 4.39 Labeling of intracellular actin structures with Cy3-wLX

The intracellular localization of Cy3-labeled wLX and thus possible staining of filamentous actin structures was also studied by LSM imaging. Therefore, HeLa cells (4.4.2) were seeded at  $2.5 \times 10^5$  cells/ml in 300  $\mu$ l in 8-well chamber slides (8-well on glass, detachable, Sarstedt) and incubated overnight at 37 °C in the incubator. The next day, cells were washed with 1X DPBS and further transfected for 6 h with either 1000 ng pTag-LifeAct-GFP-N plasmid DNA or 75 nM to 300 nM Cy3-labeled wLX as described in 4.37.8. Directly after transfection, cells were fixed and permabilized as explained in section 4.37.5. In order to stain actin structures differently, untreated HeLa cells were stained with FITC-Phalloidin as a control (4.37.6.2). Nuclei of cells were stained with DAPI-containing mounting medium prior to LSM imaging (4.40.7).

### 4.40 Cell-based assays

#### 4.40.1 Apoptosis assay

During apoptosis, cells change their plasma membrane structure to signal suicide to the environment. In early apoptotic cells, phosphatidylserine (PS) is translocated from the inner leaflet and exposed on the outer leaflet of the plasma membrane<sup>226</sup>. Annexin V, a phospholipid-binding protein, exhibits a high affinity for binding selectively to PS in presence of  $\text{Ca}^{2+}$  ions even if conjugated to fluorochromes such as Phycoerythrin (PE). In order to distinguish between early and later stages of apoptosis, in which cells lose their membrane integrity, a vital dye such as 7-amino-actinomycin (7-AAD) is often additionally used. Whereas viable cells with intact membranes exclude 7-AAD, membranes of dead and damaged cells are permeable to 7-AAD. It preferably intercalates in ds DNA at GC-rich regions and thereby changes its fluorescent properties. Viable cells are negative for both Annexin V and 7-AAD, early apoptotic cells are Annexin V positive and 7-AAD negative, whereas late apoptotic or dead cells are positive for both Annexin V and 7-AAD.

The possible induction of apoptosis triggered by internalized synthetic crosslinkers was investigated with PE Annexin V Detection Kit I (BD Bioscience) according to manufacturers' instructions. MDA-MB-231 cells (4.4.2) were seeded at  $0.5 \times 10^6$  cells/ml in 1 ml in 12-well

plates and incubated overnight in the incubator. The next day, medium was removed, cells washed with 1X DPBS and transfected with 300 nM wLX and control samples as described in 4.37.8. After 4 h, transfection mixture was removed, cells were washed with 1X DPBS and 1 ml fresh serum-containing medium were added. Cells were incubated for 24 h in the incubator. The next day, supernatant was transferred into a new 1.5 ml reaction tube and kept. Cells were washed with 400  $\mu$ l 1X DPBS and subsequently trypsinized by the addition of 50  $\mu$ l 0.05 % Trypsin-EDTA (4.37.2). After 3 min, 800  $\mu$ l FCS-containing medium (4.5) were added, cell suspension transferred into a 1.5 ml tube and cells spun for 5 min at 1150 rpm in a centrifuge 5424 R (Eppendorf AG). The supernatant was discarded and cells resuspended in the previously kept supernatant in order to include apoptotic or dead cells that did not adhere to the surface after 24 h. Cells were again spun for 5 min at 1150 rpm and pellet resuspended in 400  $\mu$ l fresh medium. Cell count was measured using the Luna II™ automated cell counter (Biozym) (4.37.4) and  $1 \times 10^5$  cells each sample were transferred into a new 1.5 ml reaction tube. Cells were washed twice with ice-cold 1X DPBS, resuspended in 100  $\mu$ l cold 1X Annexin binding buffer and transferred into a 96-well plate (V-bottom, Greiner Bio-One International GmbH). Three  $\mu$ l PE Annexin V and 1  $\mu$ l 7-AAD were added and samples incubated for 20 min at room temperature protected from light. Samples were measured with a flow cytometer iQue™ Screener (IntelliCyt®). Annexin V was measured with FL2 channel, whereas 7-AAD was measured with FL3 and a compensation value of 20 % since the spectral emission characteristics of PE-labeled Annexin V overlapped with those of 7-AAD and correspondingly gave false positive signals in the FL3 channel. To correctly adjust the value of compensation as well as the setting of suitable gates, camptothecin (Abcam), which specifically induces apoptosis, served as a positive control. For this purpose,  $1 \times 10^6$  cells were incubated in a volume of 1 ml with 6  $\mu$ M camptothecin for 5 h and  $1 \times 10^5$  cells were subsequently stained with PE-Annexin V and 7-AAD as described above. Cells treated for 24 h with 7 % (v/v) DMSO served as a second positive control in each experiment. The software ForeCyt® v4.1 was used to receive histograms and dot plots as well as corresponding statistical analysis.

### 4.40.2 WST-1 Proliferation assay

MDA-MB-231 cells (4.4.2) were seeded at  $0.5 \times 10^6$  cells/ml in 2 ml in 6-well plates and incubated overnight in the incubator. The next day, cells were transfected (4.37.8) with 300 nM wLX as well as control samples. After an incubation of 4 h in the incubator, transfection mixture was removed, cells washed and detached from plastic surface using 200  $\mu$ l 0.05 % Trypsin-EDTA (4.37.2). After addition of 800  $\mu$ l serum-containing medium, cell suspension was transferred into a 1.5 ml reaction tube and cells spun for 5 min at 1150 rpm. The supernatant was discarded and cells resuspended in fresh medium. Cell count and viability

## Material and Methods

was measured with Luna II™ automated cell counter (Biozym) as described in 4.37.4. Cells were seeded in triplicates at  $0.1 \times 10^6$  cells/ml in 150  $\mu$ l per 96-well of four individual cell culture microplates and incubated for 30 min (plate 0), 24 h (plate 1), 48 h (plate 2) and 72 h (plate 3) at 37 °C in 5 % CO<sub>2</sub> humidified atmosphere, respectively. After 24 h, 48 h and 72 h, 15  $\mu$ l cell proliferation reagent WST-1, containing WST-1 and an electron coupling reagent, were added using a Multipette® M4 (Eppendorf AG). The Slightly red water soluble tetrazolium salt 1 (WST-1) is cleaved to dark red formazan<sup>227</sup> (Figure 25) through membrane-associated, NADH-dependent oxidoreductase enzymes<sup>228</sup>, classified as EC 1. The amount of formazan dye formed directly correlates with the number of metabolically active cells.

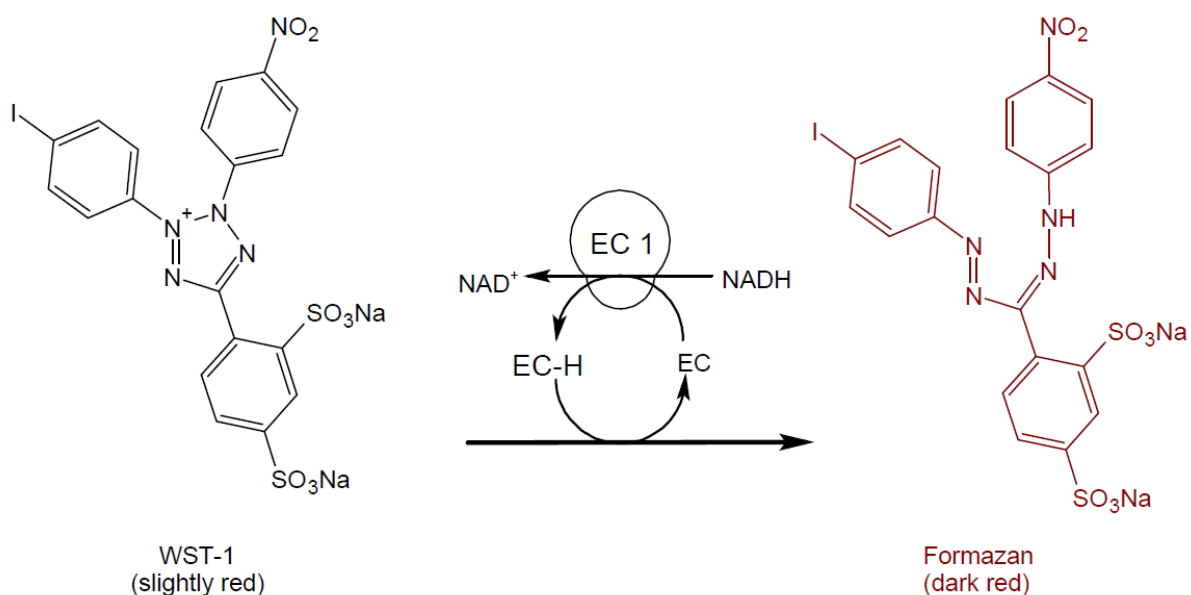


**Figure 25 | Formation of Formazan through cleavage of WST-1.** The slightly red tetrazolium salt WST-1 is cleaved to dark red formazan by cellular enzymes<sup>227</sup>. EC = electron coupling reagent; EC1 = oxidoreductase. Schematic modified from Ishiyama *et al.* (1993)<sup>229</sup>.

Absorbance at 450 nm was measured after an incubation time of 60 min and 90 min in the incubator using a TECAN Infinite® M1000 reader (Tecan Group AG). The reference wavelength was set to 690 nm.

In spite of the fact that theoretically the same cell numbers were seeded, the dilution of cell suspensions may have slightly differed whereby the number of cells effectively seeded varied from sample to sample but not from plate to plate. For this reason, WST-1 proliferation reagent was added to plate 0 exactly 30 min after seeding of cells. Absorbance at 450 nm was measured after 60 min and 90 min incubation as described above. Cells treated with 7 % (v/v) DMSO in serum-containing medium served as a positive control, since DMSO is toxic and provokes cell death.

#### 4.40.3 2D Migration assay

To investigate the migrative potential of crosslinker-transfected cells, HeLa cells (4.4.2) were seeded into a previously placed silicone culture insert (Figure 26). Seventy  $\mu\text{l}$  cell suspension of a concentration of  $5 \times 10^5$  cells/ml were pipetted into both wells of the insert. Additionally, the outer area of the insert was filled with 400  $\mu\text{l}$  serum-containing medium (4.5). Cells were incubated overnight at 37 °C in 5 %  $\text{CO}_2$  humidified atmosphere. The next day, cells were transfected in culture inserts for 4 h as described in 4.37.8. After transfection, transfection mixture was removed and cells were washed with 70  $\mu\text{l}$  1X DPBS in order to remove cell debris or non-adherent cells. Silicone inserts were carefully removed with sterile tweezers and wells were filled with 2 ml serum-containing medium. Unused wells of the 24-well plate were filled with Millipore water in order to ensure good humidity in the plate and to prevent cells from drying out. The plate was closed with a special lid, which allowed connecting the gas supply during observation. Plate and lid were sealed with an adhesive tape to reduce leaking gas and then placed onto the sample stage of the microscope.

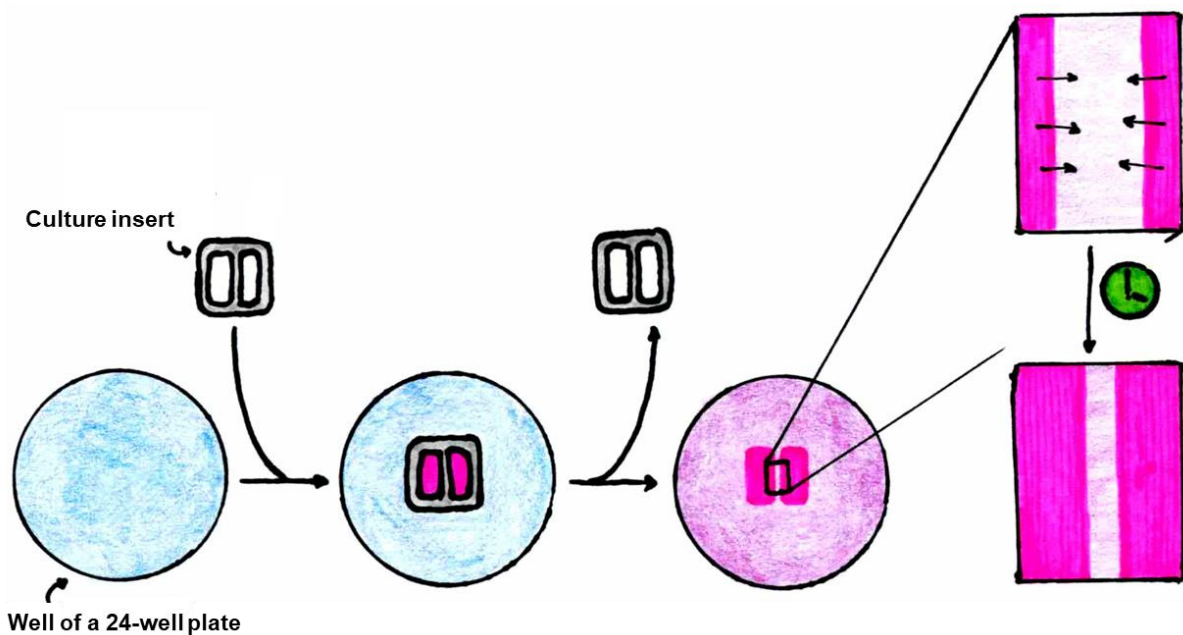


**Figure 26 | Schematic of 2D migration assay.** After placing the culture inserts into well of a 24-well plate cells were seeded into the two wells of the silicone device. After 24 h, cells were transfected (4.37.8) for 4 h and subsequently the insert was removed, leaving a 500  $\mu\text{m}$  gap. Migration of cell fronts was recorded over time.

Long-term observation was conducted using a self-build microscopy setup (COB1) kindly provided by the soft matter physics division of the University of Leipzig. The homemade microscopy system mainly consisted of a temperature-controlled enclosure and a gas supply (5 %  $\text{CO}_2$ /95 % air mixture) in order to control optimal measurement conditions similar to a standard cell culture incubator, an inverted Leica DM IRB phase contrast microscope (Leica

Microsystems GmbH, Germany), a motorized x-y sample stage (Leica DMSTC, Germany), an objective z-piezo positioner (PI P-721 PIFOC, Physik Instrumente GmbH & Co. KG, Germany), two homemade motorized illuminations shutters and a homemade motorized filter cube. Long-term observations were kindly supervised by Steve Pawlizak and Steffen Grosser (University of Leipzig), who built up the microscopy setup and the corresponding *Multi Observation* software. Migration of cells into the free gap was observed over 48 h and phase contrast pictures were recorded every 5 min. Image analysis was conducted with ImageJ and a special plugin, named MITOBO (4.12). This program detects cell-free areas and sets it to “white”, whereas areas where cells grew were set to “black”. By subtracting “white” from “black” areas, the percentages of areas covered with cells were calculated.

#### 4.40.4 3D Migration and invasion assay

To gain better overview of the following 3D migration and 3D invasion assay, a schematic representation is shown in Figure 27. MDA-MB-231 cells (4.4.2) were seeded at  $0.35 \times 10^6$  cells/ml in 2 ml in 6-well plates and incubated overnight in the incubator. The next day, medium was removed, cells washed with 1X DPBS and starved with 1 ml Opti-MEM<sup>®</sup> 24 h prior to transfection. MDA-MB-231 cells were transfected (4.37.8) with 300 nM wLX as well as control samples and incubated for 4 h at 37 °C in 5 % CO<sub>2</sub> humidified atmosphere.

For 3D invasion assays, cell culture inserts (Cultrex<sup>®</sup> 24 Insert Cell Invasion / Migration Chamber, Biozol Diagnostica) were coated with 100 µl of 0.5X or 1X basement membrane extract (BME) solution. Therefore, Cultrex<sup>®</sup> 5X BME solution (Biozol Diagnostica) was diluted 1 : 10 or 1 : 5 with 1X Coating buffer prepared from Cultrex<sup>®</sup> 10X Coating buffer (Biozol Diagnostica). BME-coated inserts were incubated for 4 h in the incubator to polymerize the natural extracellular matrix hydrogel, which forms a reconstituted basement membrane. During 3D migration experiments, cell culture inserts were not coated with BME layer.

After 4 h, transfection mixture was aspirated and cells washed with 1X DPBS. Cells were trypsinized (4.37.2) for 3 min by the addition of 200 µl 0.05 % Trypsin-EDTA. Eight hundred µl serum-containing MDA-MB-231 medium (4.5) were added and cell suspension spun for 5 min at 1150 rpm in a Centrifuge 5424 R (Eppendorf AG). The supernatant was discarded and cells resuspended in 800 µl Opti-MEM<sup>®</sup>. Cell count and viability was measured with Luna II™ automated cell counter (Biozym) as described in 4.37.4. Subsequently, cells suspensions were diluted to  $1 \times 10^6$  cells/ml (for 3D invasion) and  $0.5 \times 10^6$  cells/ml (for 3D migration) with Opti-MEM<sup>®</sup>.

Before seeding, wells of the Cultrex<sup>®</sup> 24 Insert Cell Invasion / Migration plate were filled with 650 µl serum-containing MDA-MB-231 medium. Uncoated cell culture inserts were placed

into wells of the plate and 100  $\mu\text{l}$  of  $0.5 \times 10^6$  cells/ml transfected cells were seeded in order to investigate 3D migration.

To study 3D invasion, BME-coated cell culture inserts were utilized. As mentioned for 3D migration, wells of the Cultrex<sup>®</sup> 24 Insert Cell Invasion / Migration plate were filled with 650  $\mu\text{l}$  serum-containing MDA-MB-231 medium in advance and BME-coated inserts were placed into wells. Directly before seeding samples, 70  $\mu\text{l}$  of excess BME solution were removed from individual inserts and 100  $\mu\text{l}$  of a  $1 \times 10^6$  cells/ml cell suspension was placed on top of the BME layer. Both, migration and invasion samples were incubated for 36 h - 48 h in the incubator.

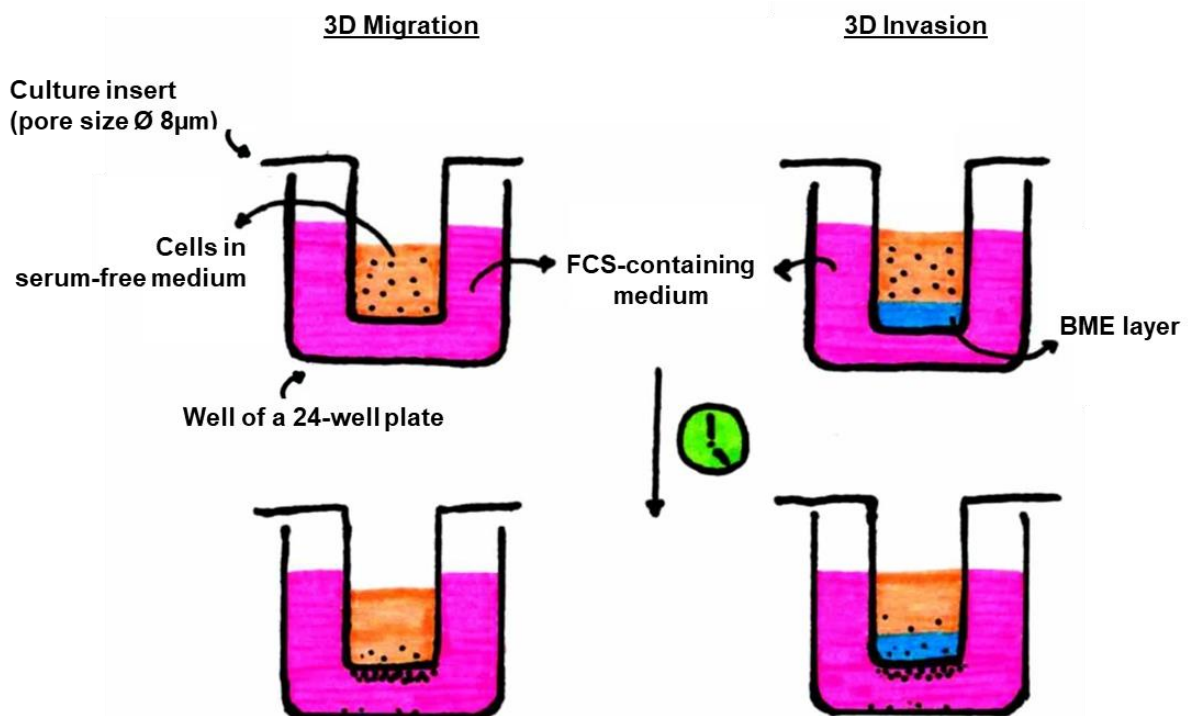


**Figure 27 | Schematic of 3D migration and 3D invasion assay.** For 3D migration experiments (**left**), transfected cells were seeded in serum-free medium in culture inserts with an average pore size of 8  $\mu\text{m}$ . The insert was surrounded by serum-containing medium towards cells migrate over time and squeeze through pores. In terms of 3D invasion (**right**), cells in serum-free medium were seeded on top of a 0.5X – 1X basement membrane extract (BME) layer that they had to degrade in order to finally get through the pores to reach the serum-containing medium. Cells were incubated for 36 h - 48 h and cell count was determined using the cell permeable dye Calcein AM.

The number of cells that have invaded or migrated was quantitated via Calcein AM (Thermo Fisher Scientific). Calcein AM is a cell-permeant dye whose acetomethylester (AM) gets cleaved by intracellular esterases. Generated, free Calcein fluoresces brightly, and this fluorescence may be used for quantification.

Therefore, 50  $\mu\text{g}$  Calcein AM was resuspended in 30  $\mu\text{l}$  DMSO. For 1 ml of 1X Calcein/CDS, 100  $\mu\text{l}$  Cultrex<sup>®</sup> 10X Cell Dissociation Solution (Biozol Diagnostica) were mixed with 900  $\mu\text{l}$  Millipore water and 1.2  $\mu\text{l}$  Calcein AM stock were added. Inserts were taken out of the well using a sterile tweezer and put into an unused well. The supernatant from the

well was removed and well washed with 500  $\mu$ l 1X DPBS. After that, 350  $\mu$ l 1X Calcein/CDS were added and inserts placed back into the well. Subsequently, the supernatant of the insert was removed as well. The plate was placed back into the incubator for 1 h and sides of the plate were tapped after 30 min. Next, inserts were removed and 100  $\mu$ l of the cell suspension were pipetted in triplicates into a black fluorescence 96-well plate (fluorotrac, Greiner Bio-One International GmbH). Fluorescence was read out with a TECAN Infinite® M1000 reader (Tecan Group AG) with an excitation of 485 nm and an emission of 520 nm.

In order to determine cell count, a calibration curve was recorded. Untreated MDA-MB-231 cells were detached and spun as described before. The cell pellet was resuspended in 1X CDS solution and cell count was measured with Luna II™ automated cell counter. A dilution series of cells diluted in 1X CDS was prepared. Fifty  $\mu$ l of each cell concentration was pipetted in triplicates into a black fluorescence 96-well plate. Then, 50  $\mu$ l of 2X Calcein AM/CDS (2.4  $\mu$ l Calcein AM stock/1 ml 1X CDS) were added to cell dilutions. The plate was incubated for 30 min at 37 °C in the incubator and fluorescence read out with an excitation of 485 nm and an emission of 520 nm. Known cell numbers of the dilutions as well as their corresponding fluorescence intensities were plotted and a linear standard curve was generated, which was used to calculate the cell count after invasion and migration.

Additionally, the number of cells seeded into inserts was double checked via Calcein AM staining. Cell solutions of  $1 \times 10^6$  cells/ml as well as  $0.5 \times 10^6$  cells/ml were diluted 1 : 5 and 1 : 2 in 1X CDS, respectively. Samples were also pipetted at 50  $\mu$ l/well in triplicates and 50  $\mu$ l 2X Calcein AM/CDS solution was added. After an incubation of 30 min in the incubator, the fluorescence was measured as already mentioned. Cell count that was seeded into inserts for 3D migration and 3D invasion was more precise and got incorporated into the later calculation of cells that finally passed through the micro-sized pores.

### 4.40.5 EMT induction of MCF-10A cells

MCF-10A cells (4.4.2) were seeded at  $1.66 \times 10^5$  cells/ml in 300  $\mu$ l into chamber slides (8-well on glass, detachable; Sarstedt) and incubated overnight in the incubator. The next day, cells were washed with 1X DPBS and starved with 300  $\mu$ l Opti-MEM® for 24 h. Cells were transfected (4.37.8) for 6 h with 300 nM wLX and corresponding controls which were 300 nM 60bp ds DNA and Lipofectamine™ 3000 only treated cells. The transfection mixture was removed and cells washed with 1X DPBS. Subsequently, 300  $\mu$ l Opti-MEM® supplemented with or without 10 ng/ml TGF- $\beta$  that was previously solubilized in a 4 mM HCl, 0.1 % (w/v) BSA solution at a final concentration of 4  $\mu$ g/ml, was added. Samples were incubated for 48 h in the incubator. In order to assess MMP-2 and MMP-9 activity in EMT-induced and -uninduced samples, a gelatin zymography assay of conditioned medium was

conducted<sup>230,231</sup>. Additionally, same samples were analyzed for E-cadherin and Snail levels by immunocytochemistry. Both methods are described in the following.

### 4.40.5.1 Gelatin zymography

Zymography is a simple, sensitive, quantifiable, and functional assay for analyzing proteolytic activity. It is already widely used for research on extracellular matrix degrading enzymes, in particular the matrix metalloproteinases (MMPs)<sup>232</sup>. Both gelatinase A (MMP-2, 72 kDa) and gelatinase B (MMP-9, 92 kDa) are proteins that are secreted from cells. In order to determine differences in MMP-levels of samples, the supernatant of induced and uninduced cells was analyzed. In a first step, the supernatant of each individual sample was collected and spun for 2 min at 1150 rcf in order to pellet dead cells. The supernatant was transferred into a new 1.5 ml reaction tube and total protein content determined using Pierce™ BCA Protein Assay Kit (Thermo Fisher Scientific) according to manufacturers' instructions. Three hundred ng total protein were mixed with 5X Non-reducing sample buffer (4.3) and loaded onto a 0.75 mm thick 10 % (v/v) SDS-PAGE<sup>233</sup> gel containing 0.1 % (v/v) gelatin. For a better resolution of proteins, a 4 % (v/v) stacking gel was utilized. Typically, SDS-PAGE was run for 1.5 h at room temperature and 130 V in 1X SDS running buffer (4.3).

#### Separating gel (10 % (v/v), 8 ml)

40 % (w/v) Acrylamide-bisacrylamide (29 : 1)	2 ml
1 M Tris pH 8.8	3 ml
dd H <sub>2</sub> O	2.6 ml
2 % (w/v) Gelatin solution	0.4 ml
10 % (w/v) SDS	80 µl
10 % (w/v) APS	80 µl
TEMED	8 µl

#### Stacking gel (4 % (v/v), 5 ml)

40 % (w/v) Acrylamide-bisacrylamide (29 : 1)	0.5 ml
0.5 M Tris pH 6.8	1.25 ml
dd H <sub>2</sub> O	3.25 ml
10 % (w/v) SDS	50 µl
10 % (w/v) APS	50 µl
TEMED	5 µl

After electrophoresis, gel was washed twice with washing buffer (4.3) for 30 min in order to remove SDS from the gel and thereby renature MMPs. Next, gel was rinsed for 10 min at

37 °C with incubation buffer (4.3) that contained cofactors necessary for the gelatinase reaction to occur. This buffer was subsequently replaced with fresh incubation buffer and gel incubated for 24 h at 37 °C. Gel was stained for 45 min with staining solution (4.3) and further incubated with destaining solution (4.3) until clear bands were seen. These bands indicate MMP activity. The molecular weight of the analyzed MMPs was compared to PageRuler™ Unstained Protein Ladder (Thermo Fisher Scientific) that was run as a protein standard on each gel.

#### 4.40.5.2 Immunocytochemistry staining for EMT markers

Additionally, EMT-induced and -uninduced cells were stained for EMT markers such as E-cadherin and Snail using fluorochrome-conjugated antibodies provided within the Human EMT 3-Color Immunocytochemistry Kit (Bio-Techne Corporation). Intensity of fluorescence signal can give evidence of an up or down regulation of these proteins. After fixation with Roti®-Histofix (4.1) and permeabilization with 1X PBS-T buffer (4.3), cells were treated with blocking solution (4.3) for 5 min at room temperature. Cells were incubated for 3 h at room temperature in the dark with anti-human snail NL557-conjugated goat IgG and anti-human E-cadherin NL637-conjugated goat IgG, which were diluted in blocking solution according to manufacturers' instructions. Antibody staining solution was removed and cells washed three times for 2 min with 1X PBS-T. Cells were covered with Fluoroshield™ and sealed with a cover slip. Samples were imaged with confocal laser scanning microscopy (4.40.7).

#### 4.40.6 **Real-time deformability cytometry (RT-DC)**

The mechanical phenotype of crosslinker-transfected MCF-10A cells, which were either treated without or with TGF-β in advance, was determined with real-time deformability cytometry (RT-DC)<sup>234</sup>. MCF-10A cells (4.4.2) were seeded at  $2 \times 10^5$  cells/ml in 1.5 ml in 6-well plates as triplicates and incubated overnight in the incubator. The next day, cells were washed with 1X DPBS and starved overnight with 2 ml Opti-MEM®. Cells were transfected (4.37.8) with 300 nM wLX as well as 300 nM 60bp DNA and Lipofectamine only that served as a control. After an incubation time of 6 h, the transfection mixture was removed and cells washed with 1X DPBS. In order to induce EMT, 2 ml serum-containing MCF-10A medium (4.5) supplemented with 10 ng/ml TGF-β were added. Control cells received serum-containing medium without TGF-β. After an incubation time of 48 h in the incubator, medium was removed and cells washed with 1X DPBS. Cells were trypsinized with 500 μl of 0.05 % Trypsin-EDTA. After 18 min, 900 μl serum-containing MCF-10A medium were added, cell suspension transferred into a 1.5 ml reaction tube and cells spun for 3 min at 2,000 rcf. The cell pellet was carefully resuspended in 100 μl Cell carrier buffer (Zellmechanik Dresden GmbH) without the

formation of air bubbles, which would interfere with the following measurement. Cells were measured with the AcCellerator (Zellmechanik Dresden GmbH) at a flow rate of 0.04  $\mu\text{l/s}$  to 0.12  $\mu\text{l/s}$  in a 20  $\mu\text{m}$  x 20  $\mu\text{m}$  channel in triplicates. Measurements were kindly conducted by Christoph Herold (Zellmechanik Dresden GmbH). The evaluation of data was performed using analysis software ShapeOut, provided by Zellmechanik Dresden GmbH.

### **4.40.7 Confocal laser scanning microscopy (LSM)**

Cells were imaged via confocal laser scanning microscopy (LSM) using a Zeiss LSM 710/AxioObserver and objectives Plan-Apochromat 63x/1.40 Oil DIC M27 or Plan-Apochromat 20x/0.8 M27 (Carl Zeiss Microscopy GmbH). Lasers, including Diode laser (405 nm), Argon laser (488 nm) and Helium-Neon laser (633 nm), were run at 60 % laser power. Images were recorded at a size of (xy) 50  $\mu\text{m}$  x 50  $\mu\text{m}$  to 700  $\mu\text{m}$  x 700  $\mu\text{m}$  and a resolution of 512 x 512 pixels. For some experiments, z-stacks of approximately 15  $\mu\text{m}$  were taken in steps of 1.5  $\mu\text{m}$ . Values for digital gain, offset, pinhole, scanning speed and laser power were set to standard values, but corrected until few specific pixels reached oversaturation. Image processing, including pseudo coloration, was conducted with Zen blue software (Carl Zeiss Microscopy GmbH).



## 5 Results and Discussion

### 5.1 CPP-conjugated DNA nanostructures as carriers for biomolecules

The first part of this work covers the usage of DNA nanostructures, i.e. DNA tetrahedra and DNA trimers, as a platform to covalently attach functional biomolecules, e.g. cell-penetrating peptides (CPP), to increase their cellular uptake without the utilization of transfection agents such as Lipofectamine™ 3000.

#### 5.1.1 Covalent conjugation of sC18 to DNA tetrahedra

In a first approach, chains of CPP should be covalently coupled to DNA tetrahedra (4.26.1). Therefore, a tail of aminoallyl-dUTP (589.2 Da) was added to DNA tetrahedron sequences (Table 4) using TdT. This amino-tail was subsequently used to couple sulfo-SMCC (Figure 16), a heterobifunctional linker that firstly reacts via its NHS ester with the primary amine on the tail, and secondly via its maleimide group with a cysteine-containing CPP (Cys - sC18, Table 5). The whole conjugation process was monitored via 6 % (v/v) native PAGE and is shown in Figure 28. Depending on the ratio of used substrate, different lengths of amino-tails were obtained. In case of a molar ratio of 1 : 3 (DNA : aminoallyl-dUTP), shown in lane 1, the tail was shorter than using a ratio of 1 : 10, which can be seen in lane 2. After adding Sulfo-SMCC (436.37 Da), the small relative gain of molecular weight could not be resolved in the gel (lanes 3 and 4). Sulfo-SMCC-coupled DNA strands were mixed with CPP, incubated overnight and loaded onto 6 % (v/v) native PAGE next day. Samples did not enter into the gel (lanes 5 and 6), therefore detection of a successful conjugation was not possible in this case.

Native PAGE separates molecules by their isoelectric point (pI). Since native PAGE is typically performed at pH 7 – 9, peptides with a high pI are positively charged at this pH. When samples are run from cathode to anode, highly positively charged molecules do not separate in the gel. Hence, it was assumed that if sC18, which is a highly positively charged peptide (2.2), reacted with a large number of maleimides of DNA strands, the overall charge of the DNA-peptide conjugate became too positive to run in the gel.

## Results and Discussion

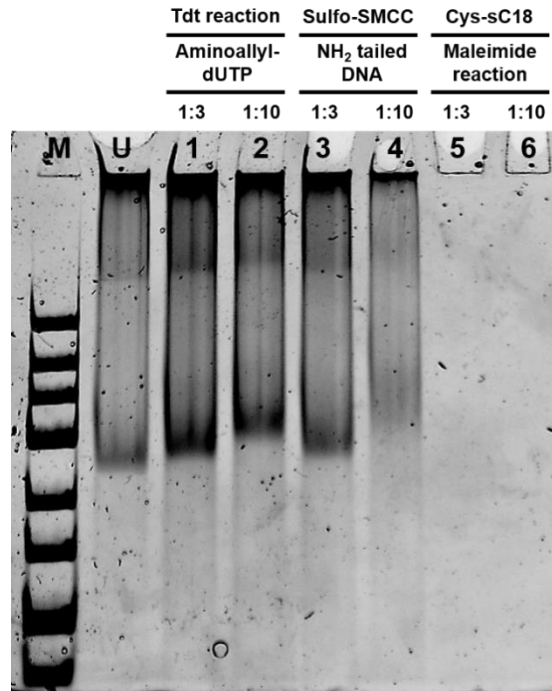


**Figure 28 | Functionalization of DNA tetrahedra with CPP chains.** Tetrahedron sequences were first tailed with aminoallyl-dUTP in different ratios using TdT. Next, sulfo-SMCC was attached via NHS ester to primary amines of dUTPs. Finally, CPP (Cys – sC18) were coupled to maleimides of sulfo-SMCCs via its TCEP-reduced sulfhydryl groups. The conjugation process was monitored via 6 % (v/v) native PAGE and visualized by SYBR<sup>®</sup> Gold Nucleic Acid Gel Strain staining. **M**, GeneRuler™ Low Range DNA Ladder; **U**, unmodified DNA tetrahedra; **1 - 2**, DNA tetrahedra with aminoallyl-dUTP tail (ratios 1:3 and 1:10) via TdT; **3 - 4**, DNA tetrahedra covalently conjugated to sulfo-SMCC via previously introduced NH<sub>2</sub> groups, **5 - 6**, DNA tetrahedra coupled to CPP (azide - sC18), which do not show up in the gel.

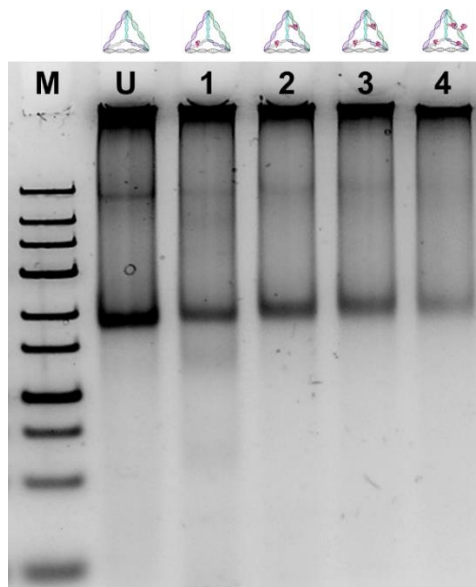


**Figure 29 | Functionalization of DNA tetrahedra with CPP.** Utilizing a SPAAC approach, DNA tetrahedra carrying single CPP modifications were obtained. Covalent conjugation of CPP was observed through 6 % (v/v) native PAGE and visualized by SYBR<sup>®</sup> Gold Nucleic Acid Gel Strain staining. **M**, GeneRuler™ Low Range DNA Ladder; **U**, unmodified DNA tetrahedra; **1 - 4**, DNA tetrahedra with one, two, three and four azide - sC18 attached, respectively.

In order to drastically reduce the number of attached CPP and thereby the probably dominant positive charge, DNA tetrahedra were conjugated to single CPP molecules. Therefore, a copper-free click chemistry approach (SPAAC, 2.2.4) was utilized as explained in section 4.26.2. Figure 29 shows DNA tetrahedra covalently conjugated to one (lane 1), two (lane 2), three (lane 3) and four (lane 4) azide - sC18, respectively. Compared to DNA tetrahedra which were not functionalized with CPP, a band shift from left to right can be seen, which indicates the successful attachment of peptides.

### 5.1.2 AFM imaging of CPP-conjugated DNA tetrahedra

Direct visualization of DNA tetrahedra is rather difficult since the nanostructure is very small. One edge is only about 7 nm in length. Nonetheless, DNA tetrahedra were imaged via atomic force microscopy (AFM). As described in sections 4.30 and 4.30.1, samples were measured in alternating contact (tapping) mode in fluid utilizing an ultra-short cantilever (Table 6). AFM images of unmodified DNA tetrahedra, DNA tetrahedra with CPP-chains that were not visible in native PAGE gels, as well as DNA tetrahedra carrying single CPP modifications are shown in Figure 30. During AFM measurements, structures were flattened into 2D structures due to strong electrostatic interactions between the DNA frame and the mica surface. For this reason, unmodified DNA tetrahedra (Figure 30 A) appeared as triangular structures. The length of individual edges was in the range of 7 nm, from which it can be concluded that structures formed correctly. In contrast, DNA tetrahedra that were modified with CPP chains appeared as circular structures (Figure 30 B). The overall structure was twice as big as unmodified DNA tetrahedra. Nevertheless, the diameter of the formed hole in the middle of these structures was in the range of 7 nm to 9 nm, suggesting that DNA tetrahedra were surrounded by covalently coupled peptide chains. On the other hand, DNA tetrahedra conjugated to four individual CPP molecules, shown in Figure 30 C, did not appear as rounded structures. Even though the image quality was not as good as within the other images, the structures looked similar to those of unmodified DNA tetrahedra, displaying sharp edges rather than a circular configuration.

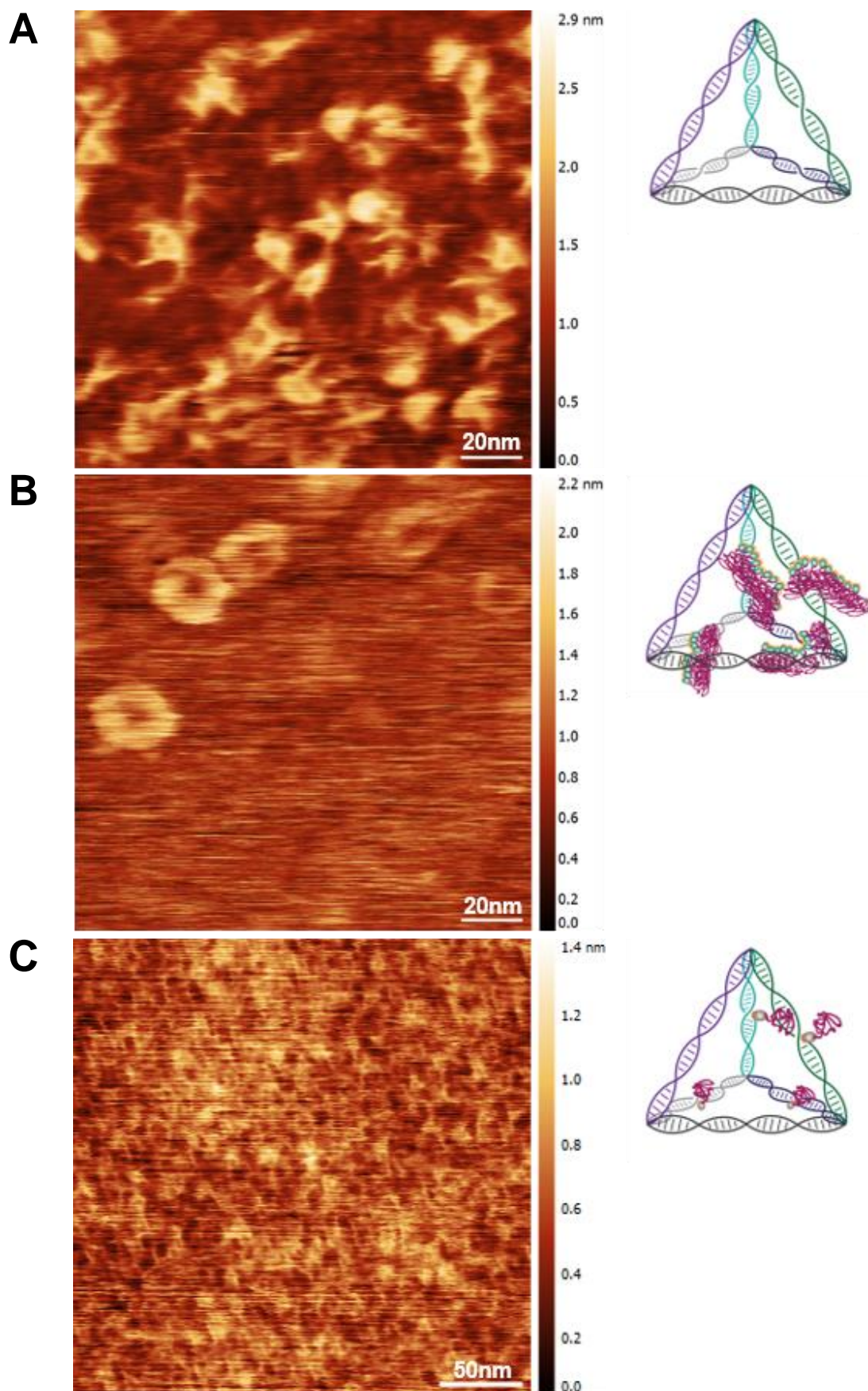


**Figure 30** | AFM images of CPP-functionalized and unmodified DNA tetrahedra. Height measurements of (A) unmodified DNA tetrahedra, (B) DNA tetrahedra with CPP chains as well as (C) DNA tetrahedra with single CPP functionalization were obtained by AFM imaging in tapping mode under aqueous buffer conditions (4.30.1).

### 5.1.3 Separation of DNA tetrahedron monomers from aggregates

Even if the covalent coupling of single CPP molecules as well as CPP chains to DNA tetrahedra was successful, a significant amount of aggregates formed. DNA tetrahedra were self-assembled according to Goodman *et al.* (2005)<sup>16</sup> and as the step-wise formation in supplemental Figure S 1 shows, aggregates firstly occurred when three strands were mixed and hybridized (lane 3). This phenomenon was even stronger when all four strands were involved in the assembly (lane 4). In order to separate these aggregates from DNA tetrahedron monomers, size exclusion chromatography (SEC) was conducted as described in section 4.24. Several buffer conditions for isocratic sample elution were tested. The best separation of the aggregation peak from the monomer peak was obtained with an elution buffer containing 10 mM Tris base pH 7.4, 450 mM NaCl<sub>2</sub>. An illustrative image of the SEC chromatogram as well as the corresponding peak fractions and fractions that were pooled and analyzed via native PAGE are shown in Figure 31. Whereas fractions 1.A.2 to 1.A.8 mainly contained aggregates, monomers appeared mostly in peak fractions 1.B.1 to 1.B.7. Unfortunately, separation of both peaks was not optimal and could not be further optimized during this work. However, all pooled fractions contained less aggregates after buffer exchange compared to unpurified DNA tetrahedron samples.

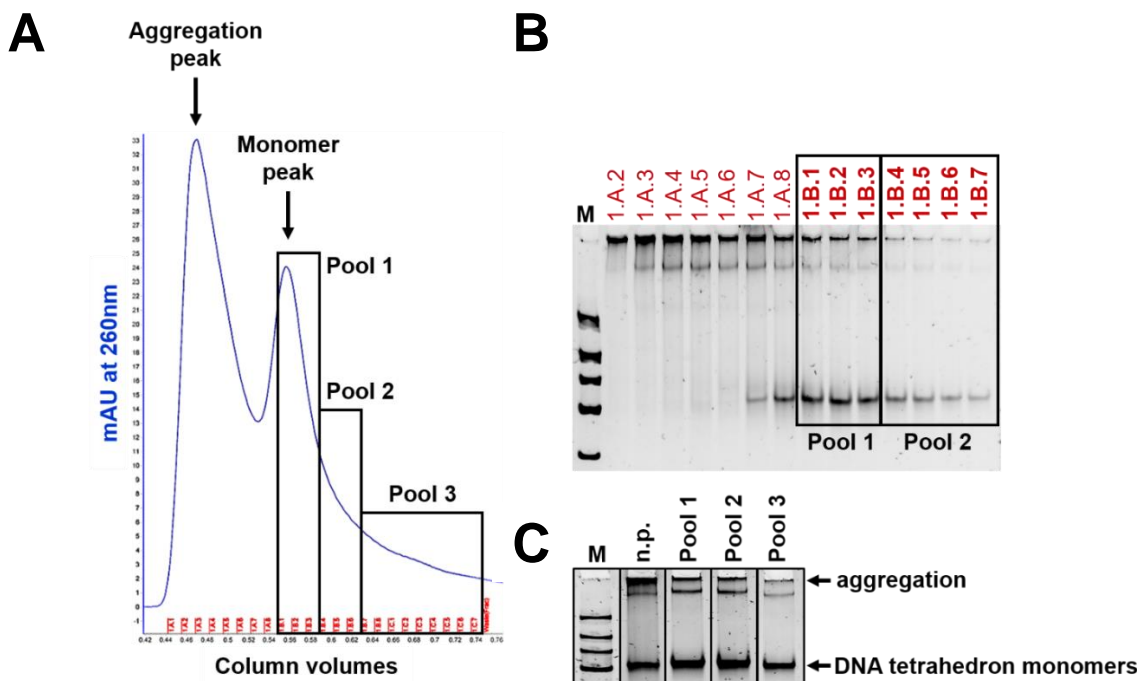


**Figure 31 | Size exclusion chromatography (SEC) of DNA tetrahedra.** In order to remove aggregates from DNA tetrahedron monomers, SEC was performed as described in 4.24. DNA structures were isocratically eluted and peak fractions collected at 260 nm. Fractions were analyzed via native PAGE, samples pooled, concentrated, and buffer exchanged to 1X TM buffer. **(A)** Elution of 1  $\mu$ M sample and pooled fractions, that were partially **(B)** analyzed via 8 % (v/v) native PAGE and visualized by SYBR<sup>®</sup> Gold Nucleic Acid Gel Strain staining. **M**, GeneRuler<sup>™</sup> Low Range DNA Ladder; **1.A.2 – 1.B.7**, partial fractions of chromatography run. **(C)** Native PAGE analysis of pooled fractions. **M**, GeneRuler<sup>™</sup> Low Range DNA Ladder; **n.p.**, unpurified DNA tetrahedra, Pool1 - Pool3, SEC-purified fractions.

A complete separation of CPP-tetrahedron conjugates from aggregates was not at all possible under these buffer conditions. Several other harsh buffers (e.g. containing low concentration of acetonitrile) were tested but did not lead to a separation. In order to still investigate the effect of cellular uptake and localization, DNA tetrahedron-CPP complexes were therefore utilized in presence of remaining aggregates for cell culture experiments.

### 5.1.4 Uptake and localization of CPP-conjugated DNA structures

HeLa cells were treated with sC18-coupled FRETrahedra as well as unmodified FRETrahedra as described in 4.38. The intracellular localization of these structures after 24 h incubation is shown in Figure 32. The upper row shows Cy5 fluorescence of intact DNA structures (green), the middle row Cy3 fluorescence of partly digested or destroyed FRETrahedra (red) and the lower row an overlay of Cy5, Cy3 and CellTracker™ Blue CMAC fluorescence that was utilized to stain the cytosol (blue). Since the fluorescence signal is higher in Figure 32 A compared to Figure 32 B, one can assume that CPP-conjugated DNA tetrahedra internalize into cells better than unconjugated DNA tetrahedra.

This phenomenon was also seen with CPP-conjugated DNA trimers, which were synthesized as described in 4.27, supplemental Figure S 2, and had additional PTO-caps on DNA ends to prevent the structures from degradation through exonucleases within cells. These DNA structures were added to HeLa cells for 2 h at a concentration of 400 nM, as explained in 4.38. The fluorescence signal in Figure 33 A, which shows DNA trimers covalently coupled to two sC18 molecules, was significantly higher than the fluorescence signal of the trimer control that did not carry CPP, shown in Figure 33 B. This result is consistent to what was observed for CPP-conjugated DNA tetrahedra.

DNA tetrahedra enter cells via endocytosis and end up in lysosomes, as reported by Kichler *et al.* (2006)<sup>38</sup>. The same can be assumed for the trimeric DNA structure, since these co-localize with the lysosomal marker LysoTracker™ Deep Red, shown in Figure 33 C and D. An overly of Cy3-fluorescence of the PTO-capped DNA trimer and the fluorescence of lysosome marker can be seen in Figure 33 E and F. Both DNA tetrahedra as well as DNA trimers did not enter the nucleus, also when conjugated to CPP. The increased intracellular fluorescence of CPP-conjugated DNA tetrahedra could appear due to the presence of large aggregates. However, since CPP-coupled DNA trimers were not seen to aggregate (supplemental Figure S 2), it can be assumed that the effect can be at least partially attributed to an increased uptake.

The utilized CPP sC18 was also previously described to enter cells via endocytosis and to end up in lysosomes<sup>58</sup>. As seen from fluorescence images, both, DNA tetrahedra and CPP in combination, did end up in lysosomes. In order to increase the uptake of DNA structures

through CPP but also mediate their release into the cytosol, CPP that promote endosomal escape or lysosome rupture could be used<sup>57</sup>. Neundorf *et al.* described a chimeric version of sC18, named N-E5L-sC18 that was coupled to a short modified sequence of influenza virus hemagglutinin subunit HA2. Since these N-terminal fragments are able to disrupt endosomal membranes they were reported to be used for endosomal release of biologically active substances into the cytosol after encapsulation into endosomes<sup>235,236</sup>. Neundorf *et al.* found that these chimeric CPP also enter cells via endocytosis but showed an increased cytosolic distribution. However, this peptide also showed intrinsic cytotoxic effects against certain cell lines<sup>58</sup>. While not pursued in the context of the work presented here, the utilization of peptides permitting endosomal escape and cytosolic translocation of DNA nanostructures would be interesting for future applications, as they could act as carrier platforms, which would be rapidly uptaken and additionally could target specific molecules in the cytosol.

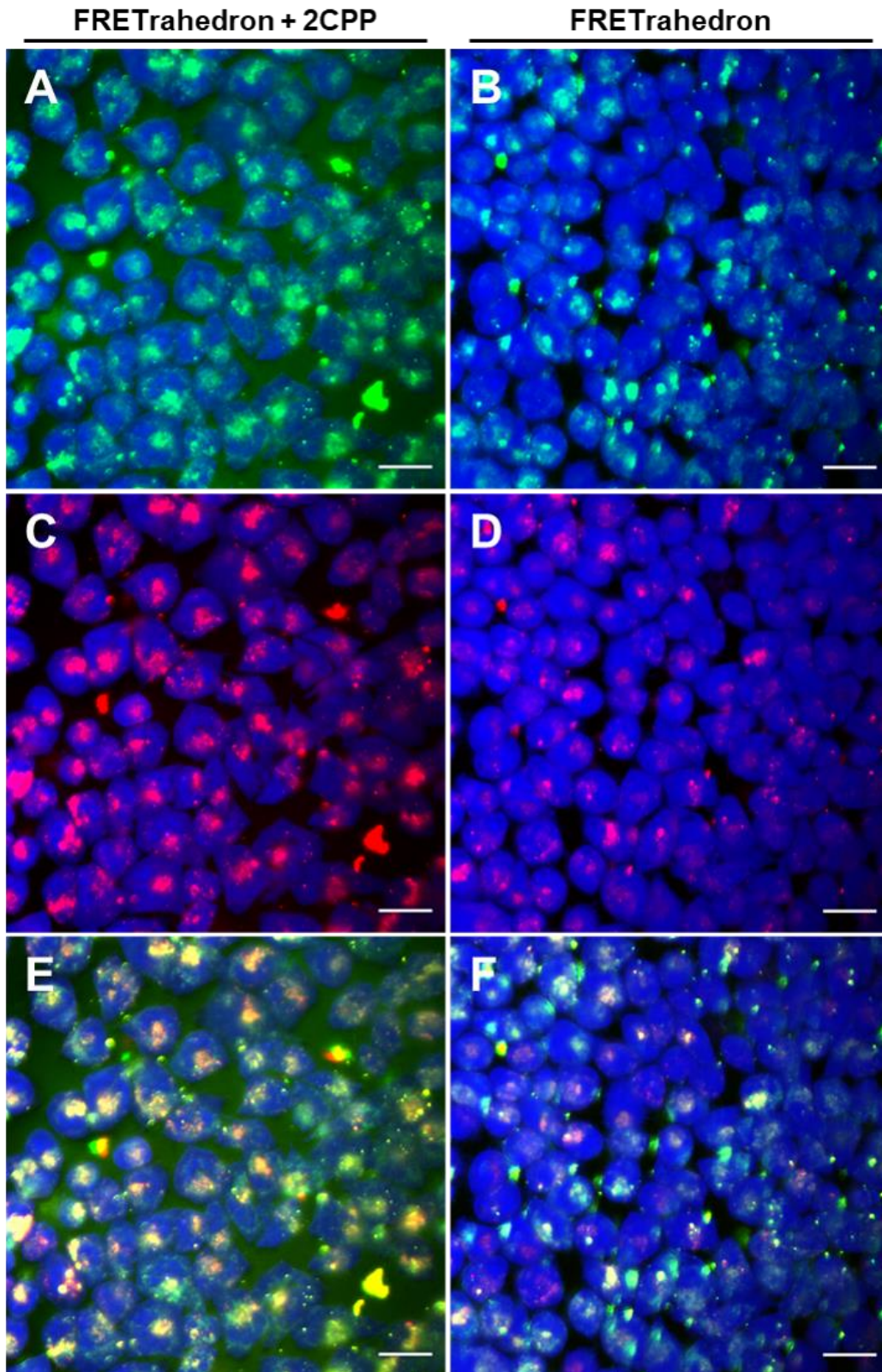


**Figure 32 | Localization of CPP-functionalized and unmodified DNA tetrahedra in HeLa cells.** (Left) DNA tetrahedra containing a FRET pair (Cy3/Cy5) were covalently coupled to two CPP (azide - sC18) via SPAAC (2.2.4). (Right) DNA tetrahedra without CPP functionalization served as control. DNA samples were diluted to 200 nM in Opti-MEM® and cells incubated for 24 h to internalize structures. Staining the cytosol using CellTracker™ Blue CMAC, shown in blue, was performed as described in 4.37.6. LSM images show (A, B) Cy5 fluorescence of intact DNA tetrahedra (green), (C, D) Cy3 fluorescence of degraded DNA structures (red) and (E, F) an overlay. Equal laser intensities and gains were applied. Images were pseudo colored using ZEN blue software and scale bars set to 20  $\mu\text{m}$ .

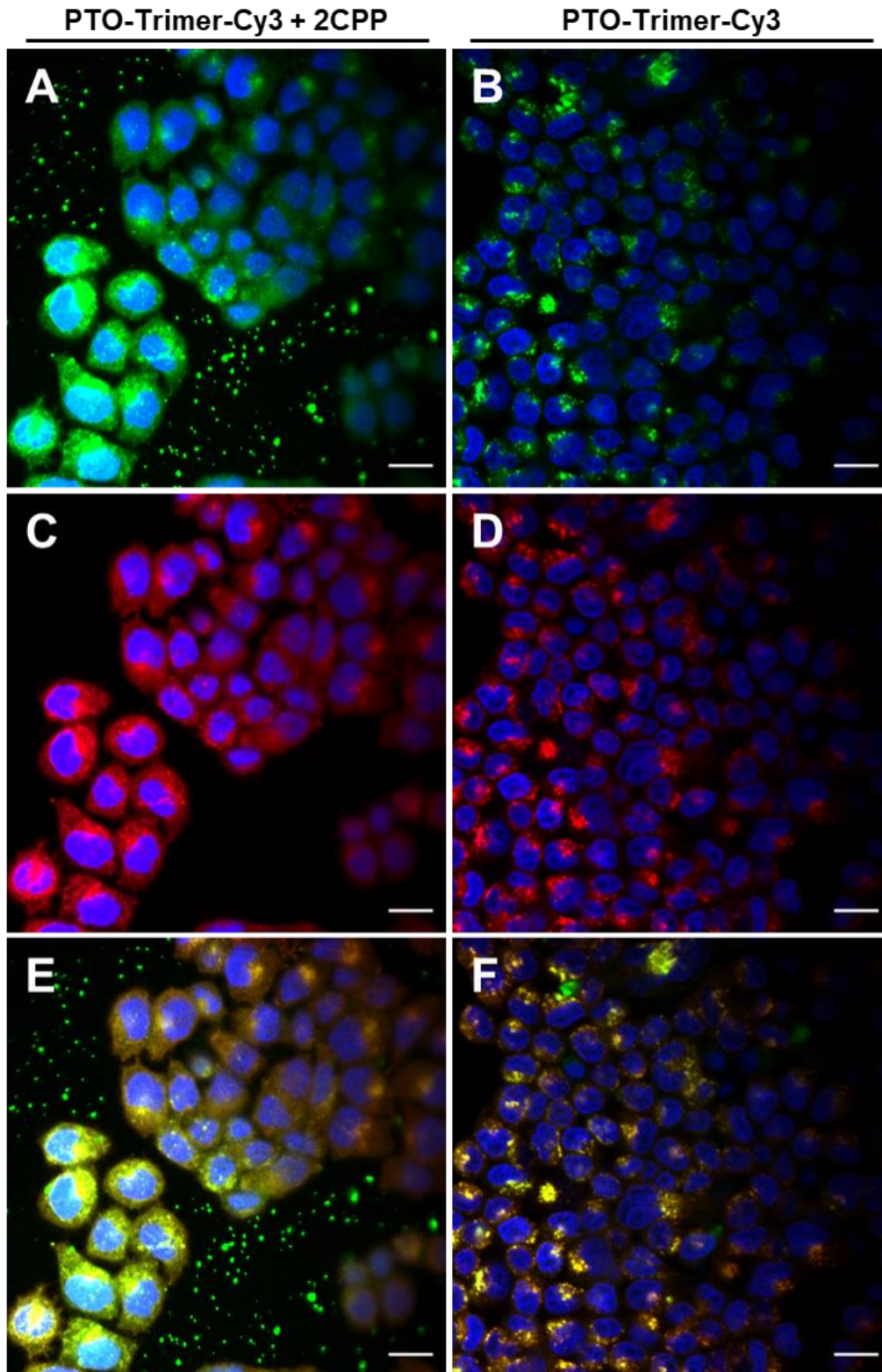


**Figure 33 | Localization of CPP-functionalized and unmodified PTO-capped DNA trimers in HeLa cells. (Left)** PTO-trimers labeled with a Cy3 dye and conjugated to two CPP (azide - sC18) via SPAAC (2.2.4). **(Right)** Unmodified PTO-trimers labeled with a Cy3 dye. DNA samples were diluted to 400 nM in Opti-MEM® and cells incubated for 2 h for cellular uptake. Staining nuclei using Hoechst® 33342 (blue) and lysosomes using LysoTracker™ Deep Red (red), was performed as described in 4.37.6.1. LSM images show **(A, B)** localization of DNA trimers **(A)** with CPP and **(B)** without CPP functionalization, **(C, D)** subcellular localization of lysosomes of cells treated with DNA trimers **(C)** conjugated with CPP and **(D)** without functionalization. **(E, F)** Overlay of trimer and lysosome localization. Equal laser intensities and gains were applied. Images were pseudo colored using ZEN blue software and scale bars set to 20 µm.

### 5.2 Synthetic actin crosslinkers

As previously mentioned, natural occurring actin crosslinkers, due to their empirical nature and complexity, do not allow systemic studies, where different key parameters can be decoupled from each other and individually varied in a systematic manner. This natural limitation was resolved in this work by engineering purely synthetic actin crosslinkers (4.28), whose core building block is a 20 nm long, double-stranded DNA which can be covalently coupled to actin-binding peptides on both sides via a copper-free click chemistry approach (SPAAC, 2.2.4). Thus, the basic geometry of the crosslinkers are conserved while properties such as binding affinity towards actin can be tuned independently by varying the attached actin-binding peptides. The following part of this work addresses the development of synthetic actin crosslinkers, i.e. the weakly-binding LifeAct<sup>®</sup> crosslinker (wLX) and the strongly-binding Phalloidin crosslinker (sPX) as the means to mimic the behaviors of  $\alpha$ -actinin (2.5.1) or fascin (2.5.2), respectively, and the *in vitro* characterization of both reconstituted actin networks as well as living cells.

#### 5.2.1 Generation of wLX and sPX

Synthetic actin crosslinkers were produced as described in 4.28 and the engineering process analyzed via native PAGE (4.15.2), depicted in Figure 34. Different kind of crosslinkers were generated: wLX (Figure 34 A, lane 2), sPX (Figure 34 A, lane 6), Cy3-labeled wLX (Figure 34 B, lane F), as well as full-PTO protected wLX (Figure 34 C, lane S). Additionally, 60bp DNA conjugated to only one LifeAct<sup>®</sup> (Figure 34 A, lane 4) or Phalloidin (Figure 34 A, lane 8) served as control. wLX, sPX and Cy3-wLX were generated in high yields as monomer bands were only slightly visible. Only for the generation of full-PTO-wLX side products, i.e. only one coupled LifeAct<sup>®</sup> instead of two, were observed. However, these samples were nevertheless utilized for shear rheology measurements, cell based assays as well as confocal laser scanning microscopy.

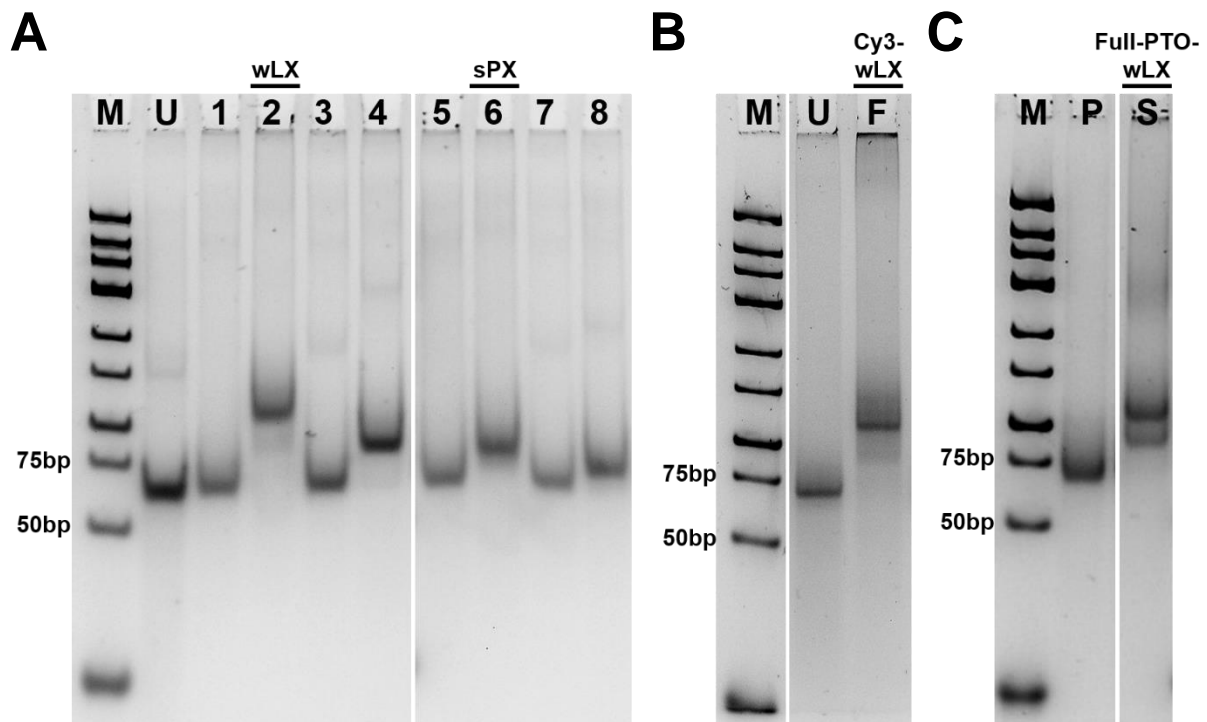


**Figure 34 | Analysis of synthetic actin crosslinker production.** The engineering process of synthetic actin crosslinkers was stepwise monitored via **(A)** 10 % (v/v), **(B)** 12 % (v/v), **(C)** 10 % (v/v) native PAGE and visualized by SYBR<sup>®</sup> Gold Nucleic Acid Gel Strain staining. **M**, GeneRuler<sup>™</sup> Low Range DNA Ladder; **U**, 60bp hybridized DNA; **1 and 5**, two-fold DBCO-functionalized 60bp DNA; **2**, 60bp wLX; **3 and 7**, one-fold DBCO-functionalized 60bp DNA; **4**, 60bp DNA coupled to one LifeAct<sup>®</sup>; **6**, 60bp sPX; **8**, 60bp DNA coupled to one Phalloidin; **F**, Cy3-labeled wLX that was used for staining of actin structures within cells (Figure 46); **P**, full PTO-modified 60bp DNA; **S**, full-PTO wLX that was utilized in cell-based experiments.

### 5.2.2 Stability of DNA structures

Besides the synthesis of crosslinkers, the general stability of two-armed as well as three-armed DNA structures towards endo- and exonucleases was investigated. In a first test, 60bp DNA, either with PTO-modifications for all nucleotides or unmodified (Table 4), were incubated with DNase I or Exonuclease III as explained in 4.29. As shown in Figure 35, DNA that was not fully protected through PTO-modifications did not resist nuclease degradation, whereas PTO-protected 60bp DNA was not degraded (Figure 35 A, lanes D and E). An incubation of DNA with Opti-MEM<sup>®</sup> I Reduced-Serum Medium (Figure 35 A, lanes O) or Millipore water (Figure 35 A, lanes N) did not cause degradation.

In addition, DNA trimers that were capped by five PTO-nucleotides each and were incubated for up to 30 min with Exonuclease III, and their resistance against digestion was compared to those of uncapped DNA trimers. As Figure 35 B indicates, PTO-capped DNA

trimers were stable against Exonuclease III over 30 min whereas unprotected DNA trimers were already digested within one minute, as trimer bands disappeared in the native PAGE gel.

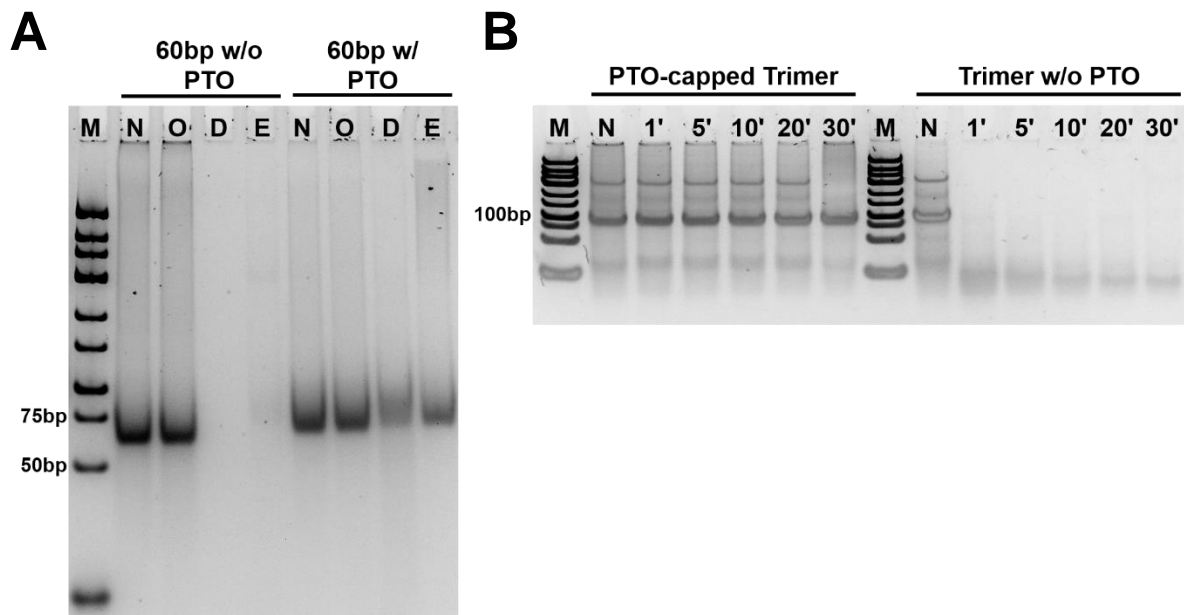


**Figure 35 | Stability of PTO-modified and unmodified DNA structures in presence of nucleases.** (A) 60bp DNA, either without PTO-modifications or as full PTO-DNA, was incubated for 30 min at 37 °C in (N) dd H<sub>2</sub>O, (O) Opti-MEM® I Reduced-Serum Medium, with (D) DNase I or (E) Exonuclease III. Samples were analyzed via 12 % (v/v) native PAGE and visualized by SYBR® Gold Nucleic Acid Gel Strain staining. M, GeneRuler™ Low Range DNA Ladder. (B) PTO-capped DNA trimers as well as trimers without PTO modifications were incubated for indicated times in presence of Exonuclease III. Samples were analyzed via 10 % (v/v) native PAGE and stained as described above. The experimental setup is to be found in 4.29.

In a second approach, the stability of unprotected 60bp DNA as well as PTO-capped DNA trimers, both coupled to a fluorophore-quencher pair (i.e. Cy3 and black hole quencher 2 (BHQ2)) was investigated, as explained in 4.29. As long as DNA is hybridized and not degraded, Cy3 is close enough to have its fluorescence emission quenched by BHQ2. However, when degraded by nucleases, the Cy3 molecule is no longer quenched and its fluorescence emission can be detected.

First, 60bp DNA, without PTO-protected nucleotides but with a Cy3-BHQ2 pair, was incubated with DNase I, Exonuclease III or without any nucleases. The fluorescence emission at 570 nm was recorded over 30 min for individual samples, respectively. As plotted in Figure 36 A, degradation of unprotected 60bp DNA through DNase I started immediately after pipetting the enzyme since the fluorescence signal directly increased at the beginning. After about 15 min, the fluorescence signal reached a plateau, indicating that all DNA was degraded. Similar results were observed for DNA incubated with Exonuclease III. In this case, the fluorescence signal strongly increased after about 8 min and reached a plateau after

approximately 20 min. 60bp DNA that was not incubated with nucleases did not show an increase of fluorescence signal over 30 min, indicating that DNA remained intact.

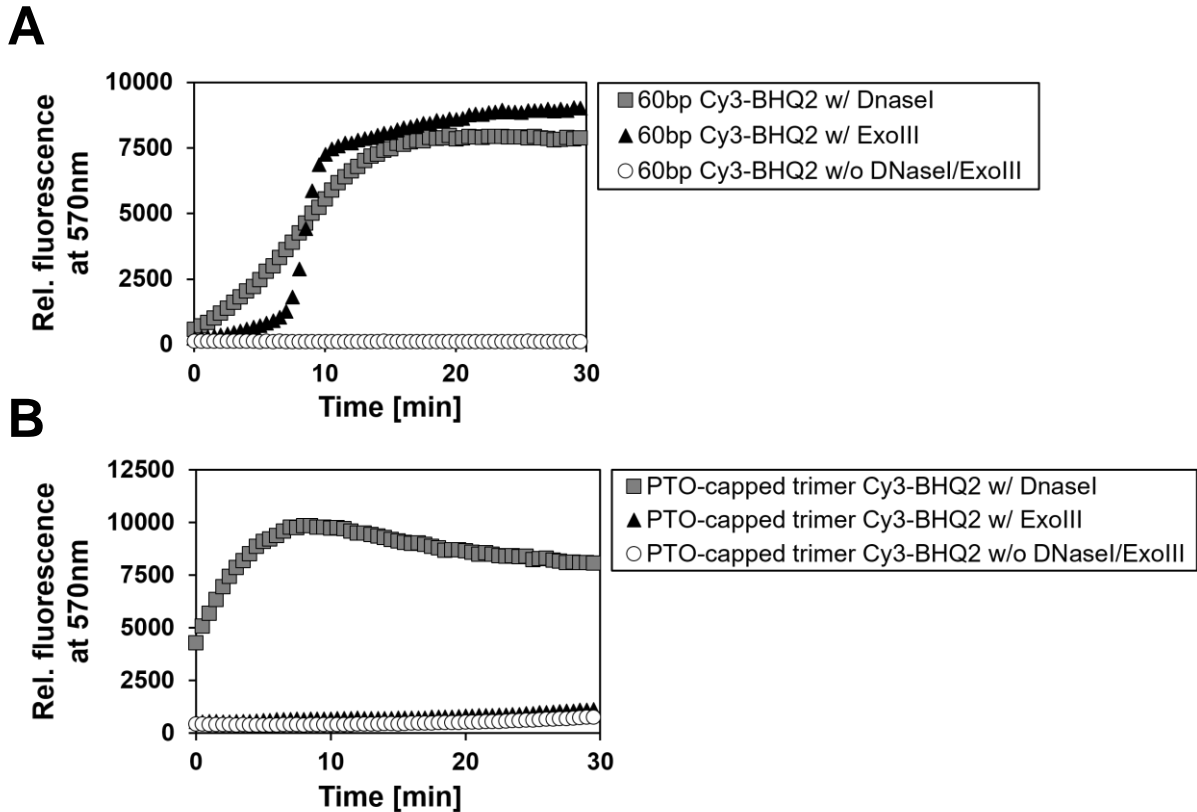


**Figure 36 | Degradation of unmodified and PTO-capped DNA structures in presence of nucleases.** (A) 60bp DNA with a Cy3-BHQ2 pair (fluorophore-quencher pair) but without PTO-modification was incubated w/ DNaseI, w/ Exonuclease III or w/o both nucleases. (B) PTO-capped DNA trimers carrying a Cy3-BHQ2 pair were also incubated w/ DNaseI, w/ Exonuclease III or with none of these enzymes. The increase of relative fluorescence at 570 nm due to enzymatic degradation of DNA was analyzed over time using a TECAN Infinite<sup>®</sup> M1000 with an excitation of 550 nm.

Cy3 - BHQ2 DNA trimers, capped by five PTO-nucleotides, were also incubated with either DNase I, Exonuclease III or none of these nucleases. Again, the fluorescence intensity was measured at 570 nm over time. As depicted in in Figure 36 B, DNA trimers incubated with DNase I showed the same rapid degradation as previously seen for 60bp DNA, since the fluorescence signal increased right after initiating the experiment. In contrast, PTO-capped trimers resisted digestion through Exonuclease III. The fluorescence signal did not increase over time, as seen for the control that was not incubated with a nuclease. However, for DNA trimers incubated with DNase I, the fluorescence signal decreased over time. This is probably due to bleaching of the fluorophore Cy3, although anti-bleaching agents were utilized.

As reported by Putney *et al.* in 1981, DNA can be protected from degradation through nucleases by PTO-modifications of the DNA backbone<sup>237</sup>. As seen from previously described experiments, DNA structures that were only PTO-capped were stable against exonucleases but not endonucleases. When the DNA structure consisted of strands that were fully modified

with PTO-nucleotides it was stable against both, endo- and exonucleases. This result as well as the fact that the full-PTO structures were also producible in high yields, was thought to be of importance for subsequent cell culture experiments, since it meant that the full-PTO wLX could longer stay intact within the cytosol that contains both exo- and endonucleases, and therefore could cause the most possible impact on cellular functions.

### 5.3 Functional effects of wLX and sPX on reconstituted actin networks

In order to investigate the effect of these synthetic crosslinkers on reconstituted actin networks in a quantitative manner, dynamic shear rheology (4.32) was employed. A broad range of crosslinker concentrations were tested in viscoelastic actin filament networks. These ratios are given as  $R = C_{\text{crosslinker}}/C_{\text{actin}}$  in the following.

#### 5.3.1 Mechanical fingerprints of wLX and sPX

In a first approach, actin polymerization was measured with a bulk shear rheometer in presence of different concentrations of wLX. Therefore, monomeric actin was enriched w/ or w/o wLX, polymerization induced by the addition of 20X KME and rheological measurements were immediately started. Corresponding values for the elasticity ( $G'$ ) were plotted over time and are shown in Figure 37. Actin polymerization w/o wLX (black curve) showed a monotonic increase of  $G'$  over time, indicating elongating filaments arranged into an entangled, viscoelastic network. Once the steady state of actin polymerization was reached the elasticity remained stable. These qualitative characteristics were also obtained when actin was polymerized in presence of the weakly-binding wLX (differently shaded red curves). However, additional crosslink-dependent effects emerged as wLX caused an increase of  $G'$  in a concentration-dependent manner. For the highest wLX concentration, i.e. 2.4  $\mu\text{M}$  ( $R = 0.1$ , dark red), the overall elasticity was 6-times higher compared to pure actin. This illustrates the effect of physically, albeit transiently connecting individual filaments. This has also been previously described for the weakly-binding natural occurring crosslinker  $\alpha$ -actinin (2.5.1)<sup>140,238</sup>.

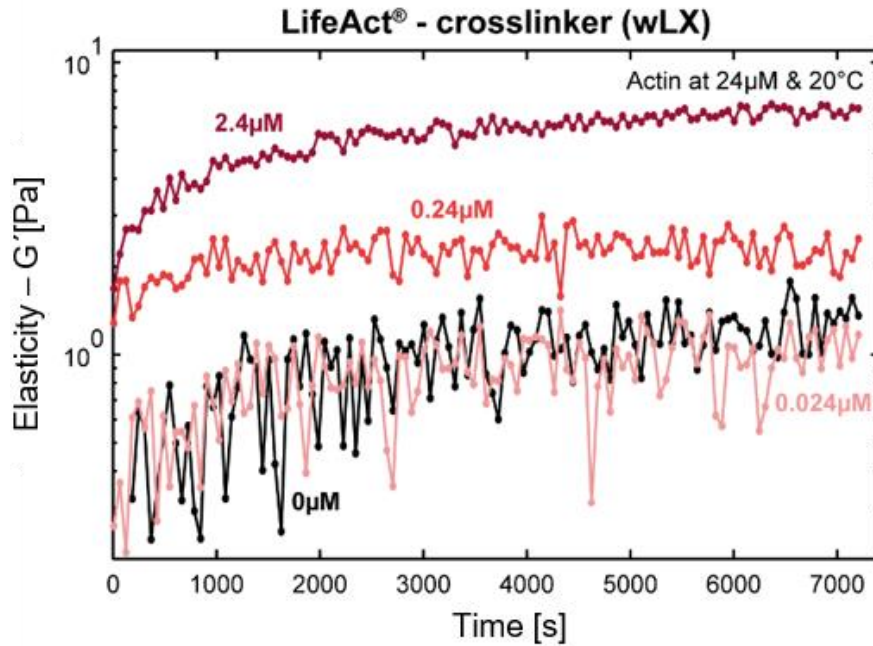


**Figure 37 | Evolution of the elasticity during actin polymerization in presence of wLX over time.** Actin polymerization in presence of wLX was investigated via dynamic shear rheology. The elastic modulus  $G'$  of pure actin ( $24 \mu\text{M}$ , black) enriched with different concentrations of wLX ( $R = 0, 0.001, 0.01, 0.1$ , red shaded curves) was measured over time as explained in 4.32.

A similar behavior, at comparatively lower concentrations, was observed for the strongly-binding sPX. As Figure 38 A illustrates, a 6-fold increase of  $G'$  was observed at a molar ratio of  $R = 0.01$  (blue curve), which is about 10 % of the wLX concentration required to reach a similar magnitude of elasticity. The corresponding phase angles at  $R = 0.01$  and  $0.0025$ , depicted as blue curves in Figure 38 B, were shifted to lower values, indicating their increasing elastic response. Pure, viscoelastic actin networks in contrast, displayed a phase angle around  $40^\circ$ . Again, equivalent behavior was reported for human fascin, the natural analogue to sPX, where the described signatures of gelation have been shown for similarly low ratios<sup>140</sup>. However, at higher sPX concentrations, i.e.  $R = 0.1$  and  $0.02$ , the elasticity increased non-monotonically. Initially,  $G'$  drastically increased until reaching a peak, which suddenly relaxed to a more viscous dominated state, shown in Figure 38 A (green curves). This time evolution is referred to as the “elasticity burst”<sup>140</sup>. The nature of this elasticity burst with its subsequent exponential decay was further revealed through the concurrent evolution of the phase angle  $\delta$  over time. As seen in Figure 38 B (green curves), before the peak of  $G'$  is reached,  $\delta$  remained stably low indicating a predominantly elastic system. During the subsequent decay of  $G'$ , the phase angle monotonically increased and finally reached a stable plateau, representing a correspondingly viscoelastic response. For the highest sPX concentration tested, i.e.  $R = 0.1$  (Figure 38 B, dark green curve) the system predominantly behaved as a viscous fluid, since  $\delta$  values were significantly higher compared to purely entangled actin filaments (Figure 38 B, black curve).

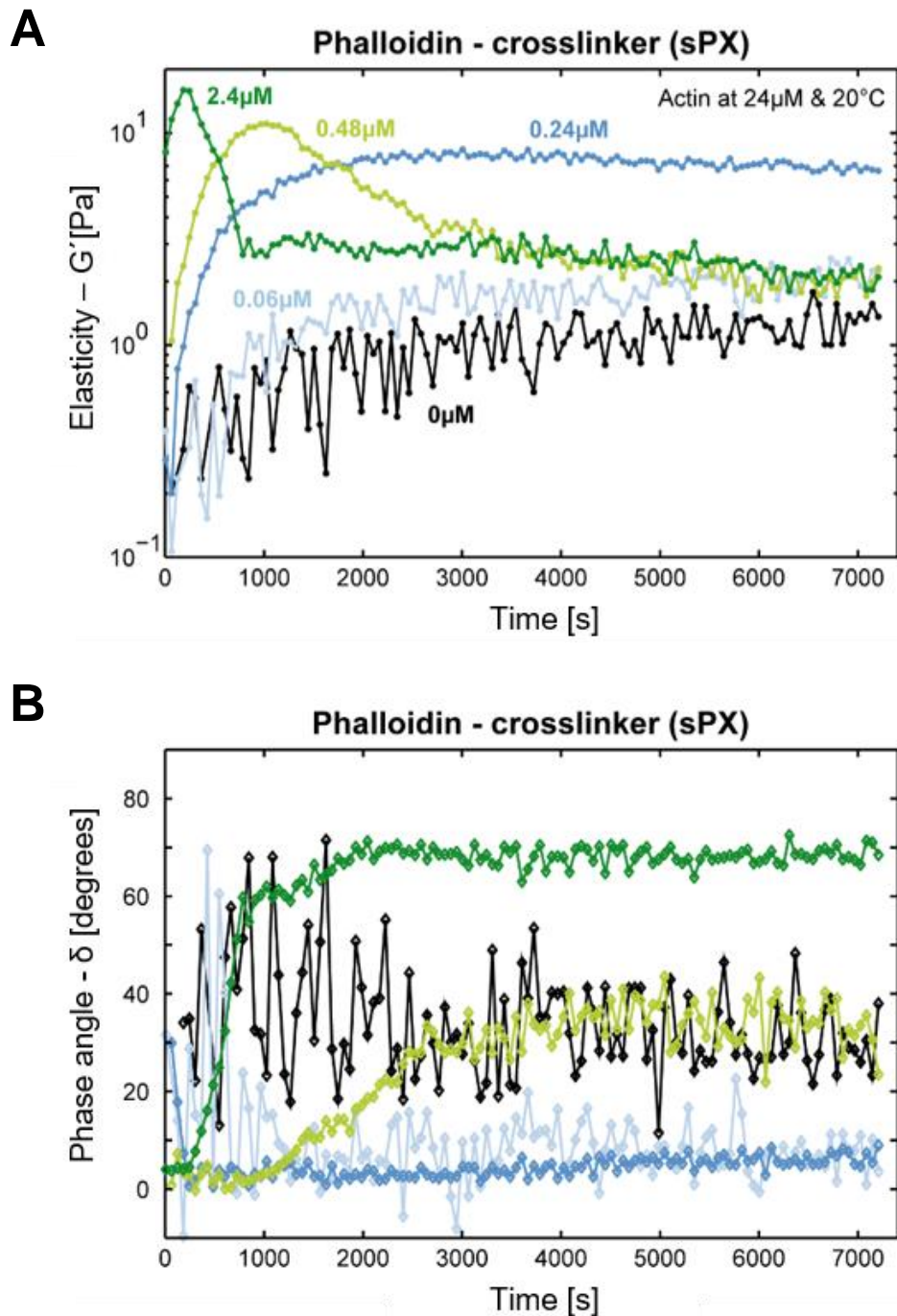


**Figure 38 | Evolution of the elasticity during actin polymerization in presence of sPX over time.** Actin polymerization in presence of wLX was investigated via dynamic shear rheology. **(A)** The elastic modulus  $G'$  of pure actin (24  $\mu\text{M}$ , black) enriched with different concentrations of sPX ( $R = 0, 0.0025, 0.01, 0.02, 0.1$ , different shades of blue and green referring to monomeric increase vs. elastic burst, respectively) was measured over time as explained in 4.32. **(B)** Shows the corresponding phase angles  $\delta$  defined as the arctangent of the ratio  $G''/G'$ , where  $G''$  and  $G'$  are the frequency dependent viscous and elastic shear moduli, respectively, with  $0^{\circ}$  being a purely elastic (solid-like) response and  $90^{\circ}$  being a purely viscous response (colours refer to the same concentrations as in Figure 38 A).

This mechanical fingerprint was also seen in experiments with the strongly-binding natural occurring actin crosslinker fascin (supplemental Figure S 4), confirming the already

reported behaviors<sup>139,140</sup>. Lieleg *et al.* reported in 2011 that simultaneous polymerization with strong crosslinking leads to the generation of pre-stressed structures that are bent beyond their equilibrium configuration<sup>139</sup>. As a result, formed actin networks build up internal stress<sup>139,178</sup>. This occurs due to the fact that polymerization is faster than unbinding of the strong crosslinker, i.e. the typical filament elongation rates ( $\sim 10 \mu\text{M}^{-1} \text{s}^{-1}$ )<sup>186</sup> far exceed the off rates of the actin-binding domains ( $0.12 \text{ s}^{-1}$  for fascin<sup>187</sup>,  $0.00026 \text{ s}^{-1}$  for phalloidin<sup>164</sup>). In this situation, the buildup of stress within the network can occur since fast filament growth can lead to sterically trapped configurations, where relaxation is limited by the slow unbinding rates of crosslinkers. As seen in Figure 38 the build-up pre-stress subsequently relaxed and therefore the system became more viscous. As actin filaments are subjected to significant bending forces, they could break at some point which would lead the system to become more viscous<sup>188</sup>. Moreover, the subsequent age-dependent relaxation could be partially induced by glassy dynamics aiming to release the stress towards equilibrium<sup>139</sup>.

### 5.3.2 Concentration-dependent stiffening of actin networks

Since naturally occurring actin crosslinkers, such as  $\alpha$ -actinin and fascin, were reported to stiffen reconstituted actin networks in a concentration-dependent manner<sup>140</sup>, actin/wLX and actin/sPX networks were rheologically examined over a broad concentration spectrum. As depicted in Figure 39, both wLX (red curve) and sPX (green curve) showed a qualitatively similar, non-monotonic, concentration dependent behavior of the network elasticity. For the lowest respective concentrations,  $G'$  was slightly lower compared to purely entangled actin networks. This could be due to local heterogeneities induced by the crosslinker, which caused a global softening of the network<sup>150,239</sup>. With increasing crosslinker concentrations, as the networks became progressively more percolated, the elasticity rose as demonstrated by the positive slopes in Figure 39. However, the slope for sPX was higher than for wLX, i.e. displaying a power law exponent of 0.62 compared to 0.21 for the weaker case. This indicated that sPX stiffened the network much more efficiently compared to wLX, which also correlates with the binding affinities of Phalloidin and LifeAct<sup>®</sup> for actin. Excitingly, both cases exhibited a local maximum of  $G'$ , which subsequently decreased to a minimum and rose again with a different exponential behavior for the highest concentrations. Although the onset of the different regimes varied, the qualitative curve progression for both binding strengths resembled each other in appearance.

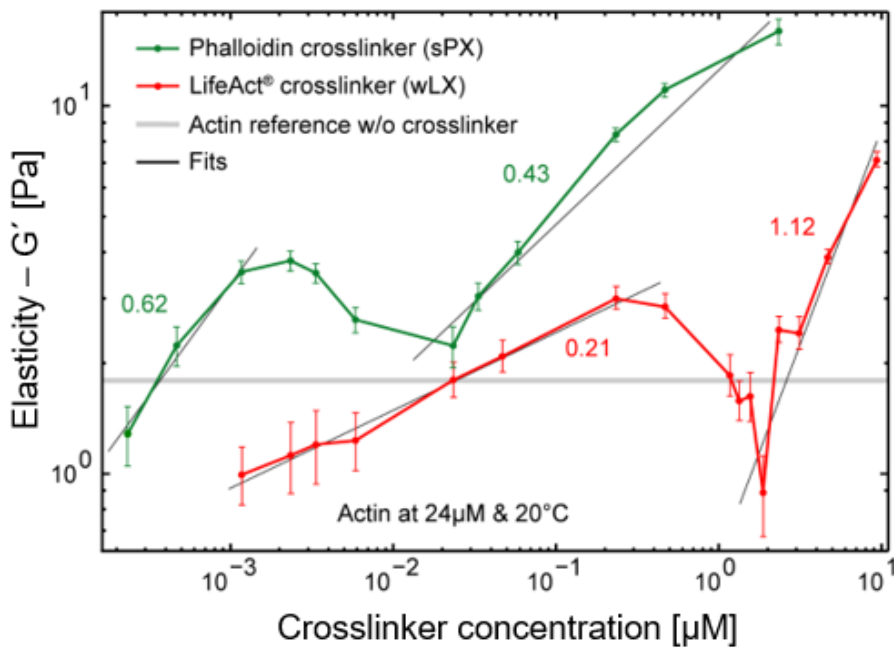


**Figure 39 | Concentration-dependent elasticity of actin networks enriched wLX and sPX.** Elastic moduli of actin networks were investigated for different concentrations of wLX (red curve) and sPX (green curve) via dynamic shear rheology (4.32). Power law fits are shown in black with according power law exponents in the corresponding color next to the graph.

### 5.3.3 Different structural morphologies of actin networks

As reported by Lieleg *et al.* in 2010, the natural actin crosslinker  $\alpha$ -actinin induced different structural morphologies in a concentration-dependent manner<sup>150</sup>. Since both wLX and sPX caused a non-monotonic behavior of the network elasticity with increasing concentration, actin networks enriched with different concentrations of synthetic crosslinkers were investigated concerning their morphology in the next step. For this purpose, light scattering (4.33, Figure 40) as well as spinning disc confocal microscopy (4.34, Figure 41) were conducted and additionally correlated to the corresponding elastic moduli.

As seen in Figure 40 (blue curve), the scattering intensity remained constant below a wLX concentration of  $R \leq 0.01$ . In addition, microscopy images revealed that actin filaments were arranged in a weakly crosslinked network (Figure 41 A). However, above a threshold concentration ( $R = 0.01$ ), the scattering intensity increased while simultaneously  $G'$  (red curve) decreased. Fluorescence images taken at a wLX concentration of  $R = 0.01$  (Figure 41 B) showed the existence of a few actin bundles in a crosslinked actin network. With further increases to the wLX concentration, the scattering intensity as well as the network elasticity rose. Corresponding images taken at wLX concentration of  $R = 0.33$  showed a bundled actin network (Figure 41 C).

## Results and Discussion

These mechanical characteristics can be attributed to three different phases of morphologies, i.e. (I) crosslinked actin network, (II) coexistence network and (III) bundle network, as illustrated in grey shaded parts in Figure 40. In the first regime (I) actin filaments are isotropically arranged in a weakly crosslinked network. Above a certain threshold concentration, the network enters the coexistence regime (II), in which higher wLX concentrations increasingly favor alignment of filaments, yielding a coexistence of bundles within an isotropic background network. In this regime ( $0.01 < R \leq 0.08$ ) bundles can be considered as local anisotropies, hence the effective actin concentration in the percolated background network is reduced which results in a weakening of the overall structure and resulting in the observed decrease of  $G'$ . It was previously suggested in simulation studies that bundled structures occupy more crosslinkers than their isotropic counterparts suggesting that this increasing anisotropy comes at the cost of overall network percolation<sup>240</sup>. The combination of both, a reduced percolation in the background network and concurrently a reduced effective actin concentration might be the reason for the drastic decrease of the elasticity to values even below those found for much smaller crosslinker concentrations<sup>240</sup>. In the third regime (III), bundles assembled to form a percolated bundle network, illustrated by the dominating elastic response of the system. With rising crosslinker density, percolation is increased and therefore the network further stiffened.

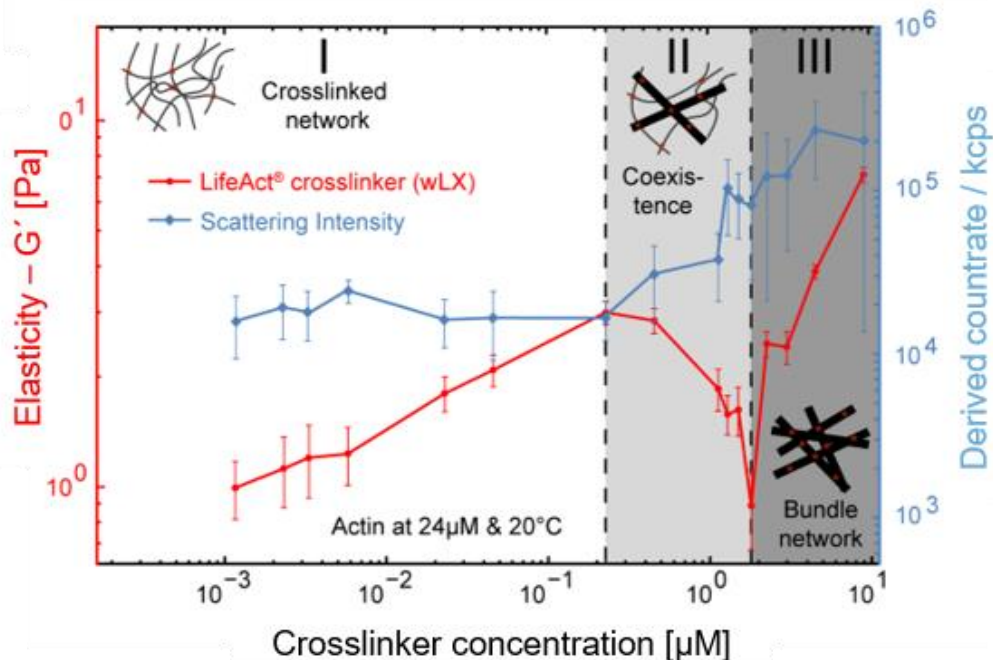


**Figure 40 | Structural phases of actin networks crosslinked by wLX.** Actin networks were investigated in presence of different concentrations of wLX via light scattering (4.33). Light scattering intensities are shown in blue with error bars indicating standard deviations of the mean values. Corresponding elastic moduli (same as in Figure 39) are additionally given in red.

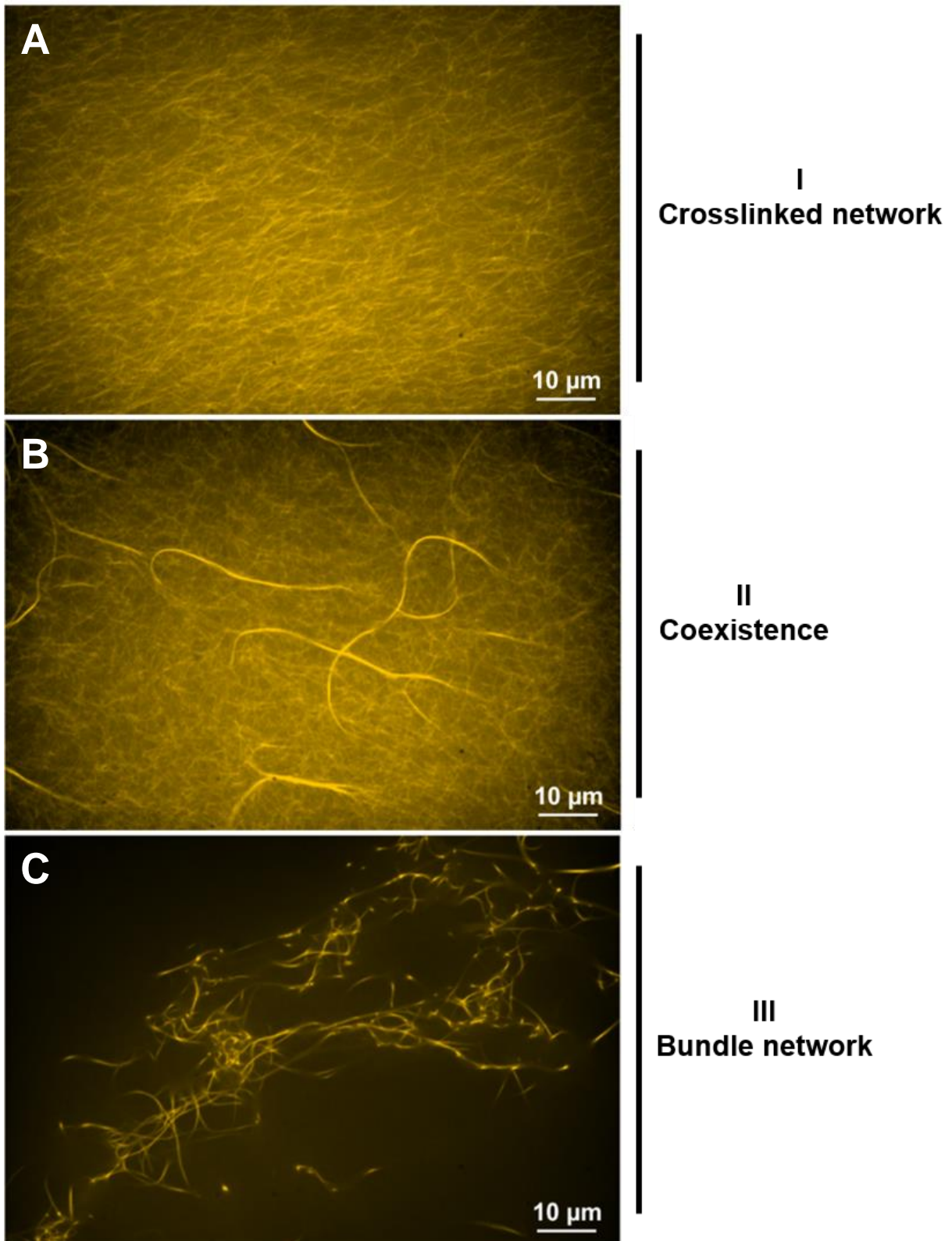


**Figure 41 | Structural phases of actin networks polymerized in presence of wLX.** Actin was polymerized at 3  $\mu\text{M}$  in presence of wLX at (A)  $R = 0.001$ , (B)  $R = 0.01$  and (C)  $R = 0.333$ , respectively. Actin was mixed with TRITC-Phalloidin at a molar ratio of 3 : 1 for visualization with spinning disc confocal microscopy. The detailed experimental setup is explained in 4.34.

This qualitative structural trend was also seen in actin networks containing sPX. However, light scattering analysis of sPX crosslinked actin networks was not suitable due to the time dependent evolution of structural anisotropies described in section 5.3.1. However, clear differences became apparent when samples were investigated with fluorescence microscopy (supplemental Figure S 5).

The observed tri-phasic behavior was described for actin networks containing the weakly-binding synthetic crosslinker wLX. However, it can be expected, as prior findings indicate<sup>89,150</sup>, that the characteristics will be generally valid for other synthetic and natural actin crosslinkers.

### 5.3.4 Reversibility of crosslinking induced by an enzymatic switch

In addition to mimicking natural mechanical signatures, the modular, DNA-based design of the synthetic crosslinkers also allows the integration of simple regulatory mechanisms in the form of orthogonal state-switches. Here, the sequence of the DNA spacer included a recognition site for the restriction enzyme *EcoRV* so that the crosslinker could be cleaved into two segments, thereby effectively "breaking" the link between filaments. Therefore, the time-dependent elasticity of actin polymerization was studied either in presence of intact sPX, *EcoRV*-HF<sup>®</sup>-cleaved sPX or *EcoRV*-HF<sup>®</sup> only. For this purpose, sPX concentrations below the threshold of the elastic burst were chosen (i.e.  $R = 0.01$ ;  $c = 0.24 \mu\text{M}$ ). As Figure 42 A demonstrates, a cleavage of sPX through *EcoRV*-HF<sup>®</sup> prior to measurement (light green curve) led to a drastic decrease of  $G'$  compared to intact sPX (dark green curve) and reached values close to the actin control (black curve) that was incubated with *EcoRV*-HF<sup>®</sup> but without crosslinkers. Still *EcoRV*-HF<sup>®</sup>-cleaved sPX showed a slightly higher elasticity than the actin control which likely could be resulting from few numbers of undigested crosslinkers, as it was confirmed by native PAGE analysis (supplemental Figure S 3).

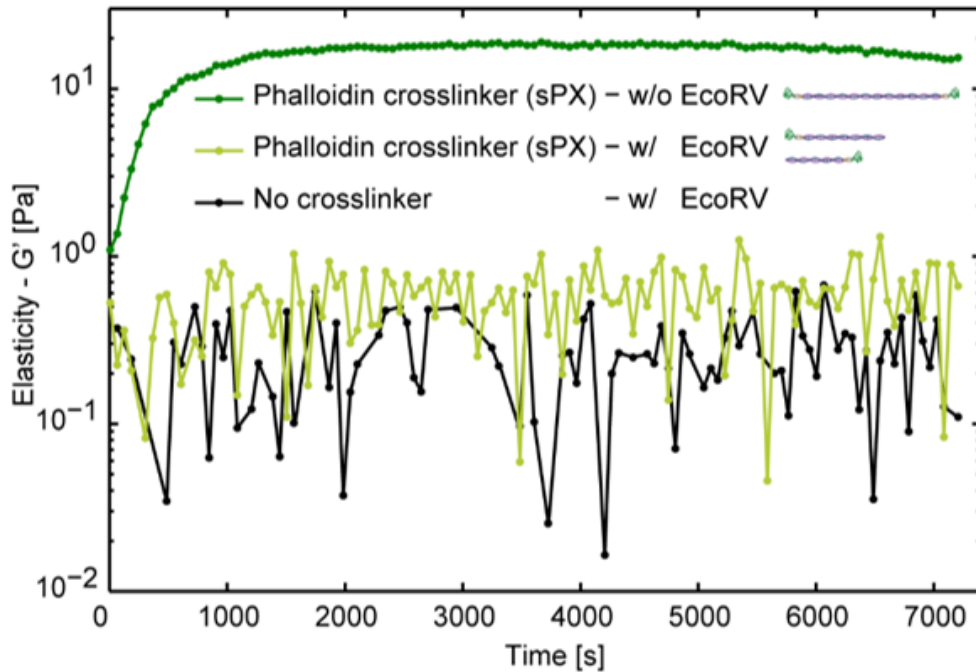


**Figure 42 | Reversibility of synthetic actin crosslinkers.** Time-dependent elasticity of actin polymerization in presence of intact sPX (dark green,  $c = 0.24\mu\text{M}$  ( $R = 0.01$ )), *EcoRV*-HF<sup>®</sup>-cleaved sPX (light green,  $c = 0.24\mu\text{M}$  ( $R = 0.01$ )) and actin which was incubated with just *EcoRV*-HF<sup>®</sup> (black) was investigated via shear rheology. The actin concentration was  $24\mu\text{M}$  for all experiments and the cleavage of sPX through *EcoRV*-HF<sup>®</sup> was additionally verified via native PAGE (supplemental Figure S 3).

Moreover, the mechanical impact of crosslinker-induced stiffening and enzyme-based regulation of actin networks could be also seen in macroscopic gels. As explained in section 4.35, TRITC-Phalloidin-labeled actin was polymerized in a cuvette in presence of intact sPX, *EcoRV*-HF<sup>®</sup>-cleaved sPX as well as without any crosslinker for 40 min. Right after, the cuvette with the respective sample was placed on an inclined plane with a  $20^\circ$  angle. The flow down of the samples over time is illustrated in Figure 42 B. Purely entangled, viscoelastic actin flowed down the gradient within seconds (left column) whereas an addition of intact sPX resulted in a more than five-fold slowing of the flow (middle column) indicating the increased elastic behavior of the system. However, the inclusion of enzyme-cut crosslinkers (right column) restored the dominance of the fluid-like behavior as the flow rate was undistinguishable from the actin only control.

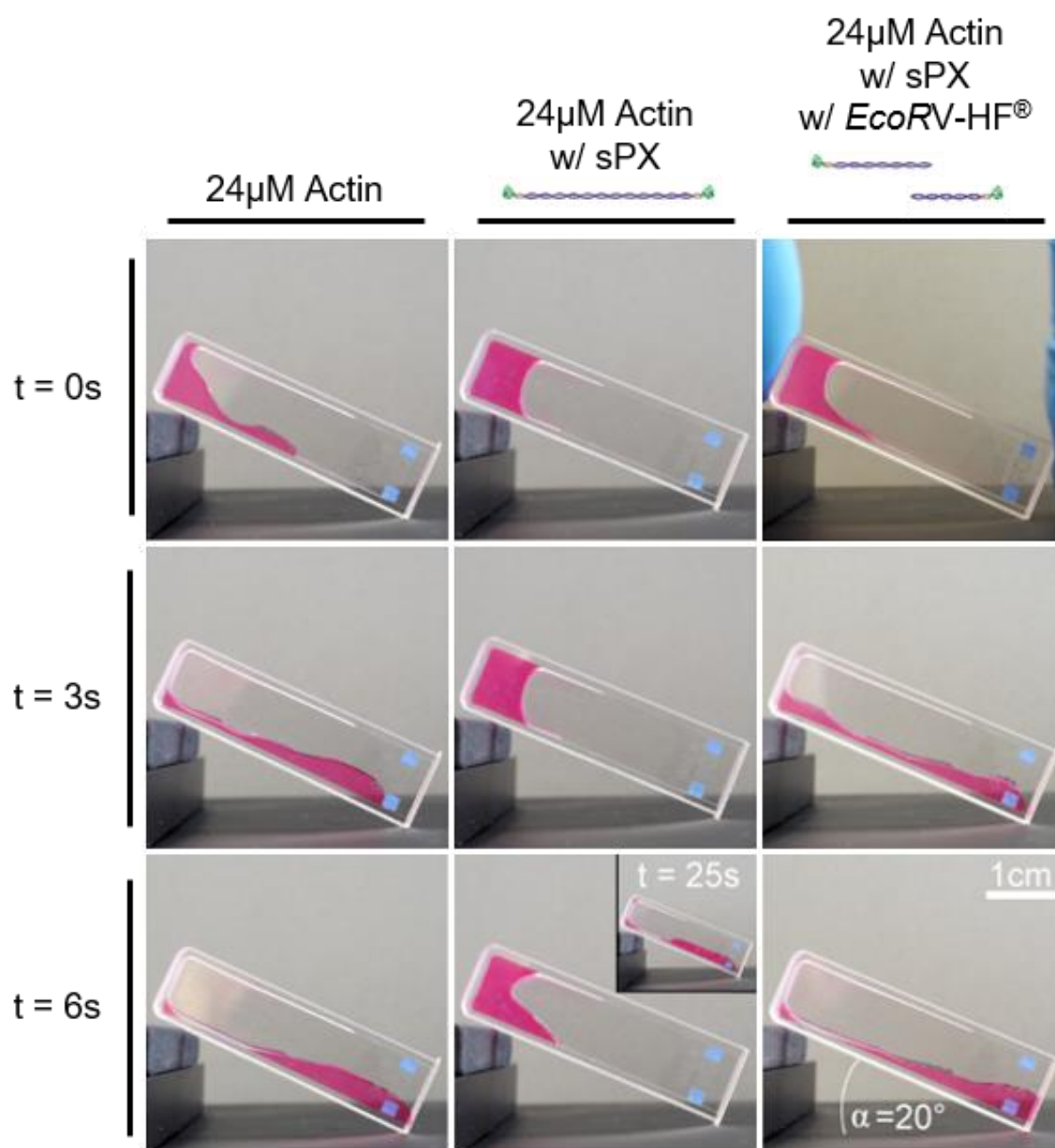


**Figure 43 | Reversibility of synthetic actin crosslinkers.** Macroscopic behavior of actin in an inclined cuvette over time. Actin was polymerized at 24 μM (**left**) w/o actin crosslinkers, (**middle**) with 9.6 μM sPX and (**right**) 9.6 μM sPX pre-incubated with 300 U *EcoRV*-HF<sup>®</sup>.

### 5.4 Interaction of synthetic crosslinkers with actin filaments

#### 5.4.1 Polymerization / Depolymerization of actin filaments (pyrene assay)

A well-established method to monitor actin polymerization and depolymerization *in vitro* is the standard pyrene assay, in which the fluorescence intensity is a measure for the degree of polymerization<sup>170,241</sup>. Schmoller *et al.* reported that natural occurring crosslinking proteins, such as fascin, suppress actin depolymerization in a concentration dependent manner and that this would be a generic effect for all actin-binding proteins which simultaneously bind to two F-actin subunits<sup>241</sup>.

In order to investigate the effect of synthetic actin crosslinkers on *in vitro* polymerization and depolymerization, a pyrene assay was conducted as explained in section 4.36. Pyrene-actin was polymerized at 6  $\mu\text{M}$  in presence of different concentrations of wLX (i.e.  $R = 1$ ,  $R = 0.2$ ,  $R = 0.1$ ,  $R = 0.08$ ,  $R = 0.02$  and  $R = 0.01$ ) as well as the LifeAct<sup>®</sup> peptide only ( $R = 1$ ). These results were compared to the polymerization of pyrene-actin alone. Actin depolymerization was induced after 90 min by the addition of latrunculin B (latB), which sequesters monomeric actin and thus causes a depolymerization at both the barbed and pointed ends<sup>241</sup>. Corresponding fluorescence intensities at 407 nm were recorded over time and are plotted in Figure 44. Typically, fluorescence intensity increases over time and reaches a plateau. When latB is added, this plateau suddenly drops and actin depolymerizes. Here, fluorescence intensities of all samples increased until reaching a peak after about 30 min but without the addition of latB, fluorescence intensity suddenly decreased over time. This could be due to bleaching effects and the rather low amount of pyrene-actin used. However, it could be clearly observed that wLX inhibited polymerization rates in a concentration-dependent fashion. At a wLX concentration of  $R = 1$  polymerization was suppressed the most, and at the lowest concentration of  $R = 0.01$  polymerization was almost similar to that of pyrene-actin alone. LifeAct<sup>®</sup> by itself did not cause an inhibition of polymerization rate when used at the same high concentration as wLX ( $R = 1$ ), which is coincident to the findings of Riedl *et al.*<sup>161</sup>.

After 90 min, latB was added and depolymerization of pyrene-actin induced. Unfortunately, since fluorescence signal already had dropped, no clear differences between samples were observed. Still, a slight concentration dependency might be assumed as wLX at  $R = 1$  showed the lowest fluorescence signal compared to wLX at  $R = 0.01$ , which is again in the range of pyrene-actin alone. However, it not possible to conclude from these results that synthetic crosslinkers also inhibit depolymerization rates as Schmoller *et al.* found for naturally occurring actin crosslinkers<sup>241</sup>.

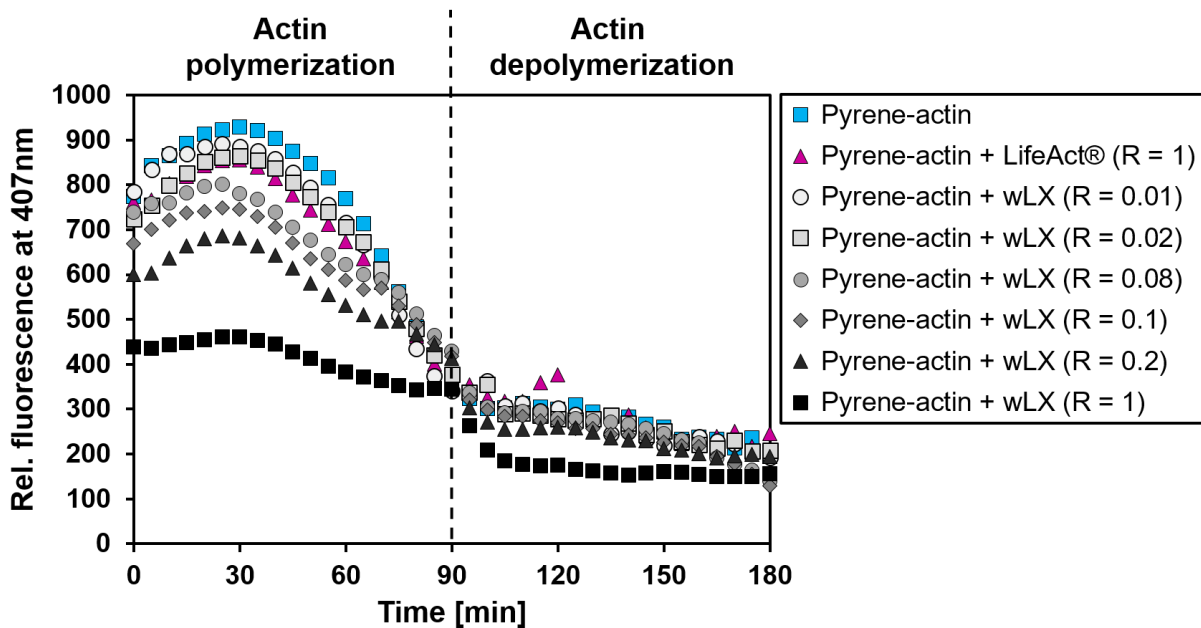


**Figure 44 | Polymerization and depolymerization of actin in presence of LifeAct® and wLX.** Polymerization and depolymerization of pyrene-actin (6  $\mu\text{M}$ ) in presence of LifeAct® as well as different ratios of wLX ( $R = 1$ ,  $R = 0.2$ ,  $R = 0.1$ ,  $R = 0.08$ ,  $R = 0.02$  and  $R = 0.01$ ) was monitored over time. Polymerization was induced by the addition of 20X KME buffer (4.3). After 90 min, depolymerization was initiated by the addition of Latrunculin B to a final concentration of 200  $\mu\text{M}$ . Emitted fluorescence was measured at 407 nm. A detailed experimental setup is described in 4.36.

#### 5.4.2 Impact of wLX on actin remodeling dynamics in cells

The actin cytoskeleton is highly dynamic, with ABP attaching and detaching from the actin meshwork and the constituent actin filaments turning over due to addition and removal of monomers at the filament ends<sup>242</sup>. As it was shown that wLX impact the actin polymerization *in vitro*, it is was of great interest whether synthetic crosslinkers also interfere with the actin remodeling dynamics inside of cells. Therefore, the influence of wLX on the actin dynamics were investigated the via fluorescence recovery after photobleaching (FRAP) with collaborator Tobias Zech (Cellular and Molecular Physiology, University of Liverpool). Normal mouse mammary gland epithelial cells (NMuMG) were transfected for 24 h with EGFP-actin and either 50 nM wLX or, as a control, 50 nM single LifeAct® 60bp DNA using Lipofectamine 2000 (Invitrogen) according to manufacturers' instructions. After transfection, EGFP fluorescence of actin in regions of interest (ROI) were imaged using a spinning disk confocal microscope and bleached with a brief pulse of 405 nm Diode laser. The recovery of the EGFP-fluorescence was recorded over time and is depicted in Figure 45. The control sample, i.e. 50 nM single LifeAct® 60bp DNA, which should not interfere with actin dynamics as it is not able to connect actin filaments, showed a fast increase up to 20 % of recovered fluorescence within half a

minute. In contrast, the actin-EGFP-fluorescence did not even recover to 5 % within the same time in wLX-transfected cells, which indicates that wLX is capable of slowing down actin remodeling dynamics. Still it remains unclear whether this effect can be attributed to a slowed down actin polymerization/depolymerization or an interference with either diffusion or myosin transport due to an enhancement of glassy characteristics in the networks. However this will be further investigated in future experiments.

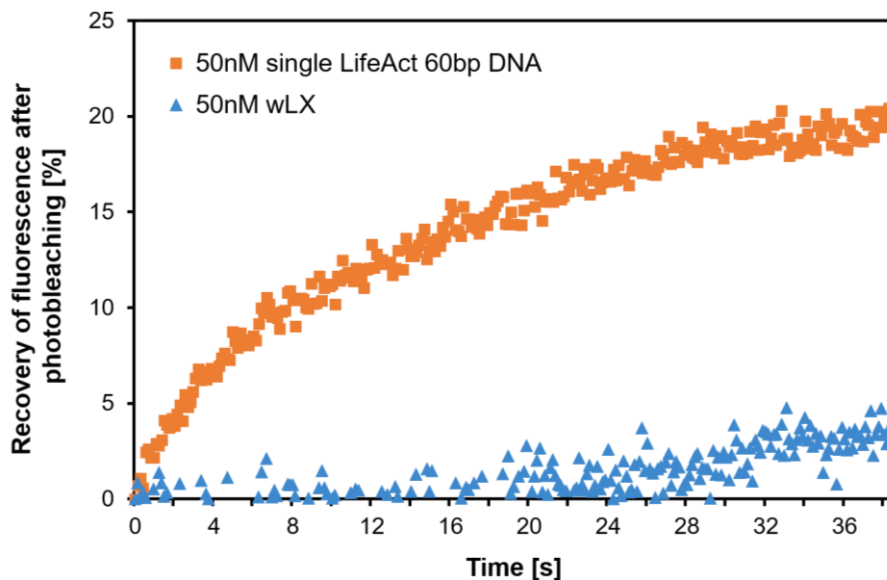


**Figure 45 | Influence of wLX on actin remodeling dynamics in NMuMG cells.** Normal mouse mammary gland epithelial (NMuMG) cells were co-transfected with EGFP-actin and either 50 nM wLX or, as a control, 50 nM single LifeAct® 60bp DNA using Lipofectamine 2000 (Invitrogen) according to manufacturers' instructions. Cells were imaged 24 h after transfection with a Marianas spinning disk confocal microscope (3i) using a 63 x 1.4NA or 10x 0.45NA Zeiss Plan-Apochromat lens. EGFP fluorescence in regions of interest (ROI) was bleached with a brief pulse of 405nm laser and recovery was recorded over time. Slidebook software (3i) was used to analyze the fluorescence recovery in ROIs and to deduct background bleaching of rest of cell with a control non-bleach ROI. The experiment was conducted and data kindly provided by Tobias Zech (University of Liverpool).

### 5.4.3 Labeling of actin filaments within cells

Synthetic wLX were extensively studied in *in vitro* experiments. Additionally, it was of general interest to see where fluorescently labeled wLX, i.e. Cy3-wLX, localize within cells and if it is possible to stain single actin filaments, as it was shown for LifeAct®-GFP fusions<sup>161</sup>. Cy3-wLX were generated as described in section 4.28 and, as already discussed (5.2, Figure 34), produced at high yields.

To compare localization of fluorescently labeled wLX, a LifeAct-GFP fusion, encoded on pTag-LifeAct-GFP-N (4.7), was generated as described in sections 4.18 to 4.21. The hybridized LifeAct®-DNA fragment was inserted into previously linearized 4.73 kb pTagGFP-N (supplemental Figure S 6 A) and subsequently *E. coli* DH5α cells were transformed with the

ligation mixture. Four of five picked clones were identified as positive clones, since these showed the estimated PCR product of 325bp (supplemental Figure S 6 B and Figure S 7). Additional sequence analysis verified the correctness of the sequence (not shown).

To visualize intracellular actin structures, HeLa cells were transfected (4.37.8) for 6 h with Cy3-wLX or pTag-LifeAct-GFP-N as described in 4.39. Corresponding LSM images, shown in Figure 46, illustrate that filamentous actin structures were stained with Cy3-wLX, comparable to staining with conventional LifeAct<sup>®</sup>-GFP fusions<sup>161</sup>, depicted in Figure 46 B, D and F. Figure 46 A and E nicely show the Cy3-wLX staining of lamellipodia that appear as branched “dendritic” actin filament networks or quasi 2D actin mesh at the front, leading edge of the cell<sup>243</sup>. Filopodia (also known as microspikes), which are exploratory extensions from the plasma membrane that contain parallel bundles of actin filaments<sup>244</sup>, were visualized within all Cy3-wLX transfected cells.

Additionally, some vesicular structures were noticeable. These vesicles presumably were Lipofectamine/Cy3-wLX complexes, which were up taken by endocytosis. However, since Cy3-labeled wLX were able to actively stain the actin cytoskeleton, it can be assumed, that most of these complexes were released from endosomes and translocated into the cytosol. This is consistent to what Cardarelli *et al.* recently found. They observed that Lipofectamine/DNA complexes enter cells by endocytosis and that a significant number of these complexes are released into the cytosol as they did not show a co-localization with lysosomal markers<sup>245</sup>.

Since synthetic crosslinkers are both, peptide- and DNA-based, Cy3-wLX were additionally investigated for co-localization with 4',6-diamidino-2-phenylindole, short DAPI. DAPI is a DNA-specific probe which forms a fluorescent complex by attaching in the minor groove of A-T rich sequences of DNA<sup>246</sup>. Thus DAPI is extensively used as DNA-specific probe for flow cytometry, chromosome staining, DNA visualization as well as quantitation in histochemistry and biochemistry. Here, DAPI was applied to stain the nuclei of Cy3-wLX-transfected as well as untreated, FITC-Phalloidin stained HeLa cells (Figure 47). Interestingly, when increasing the gamma of DAPI signal to 0.01 during image processing, afore mentioned F-actin structures could be visualized with DAPI in Cy3-wLX transfected cells, seen in Figure 47 B. In contrast, actin structures stained with FITC-Phalloidin did not co-localize with DAPI in control cells (Figure 47 D). This phenomenon served as an extra proof, that fluorescently labeled synthetic crosslinkers bound to actin structures within cells.

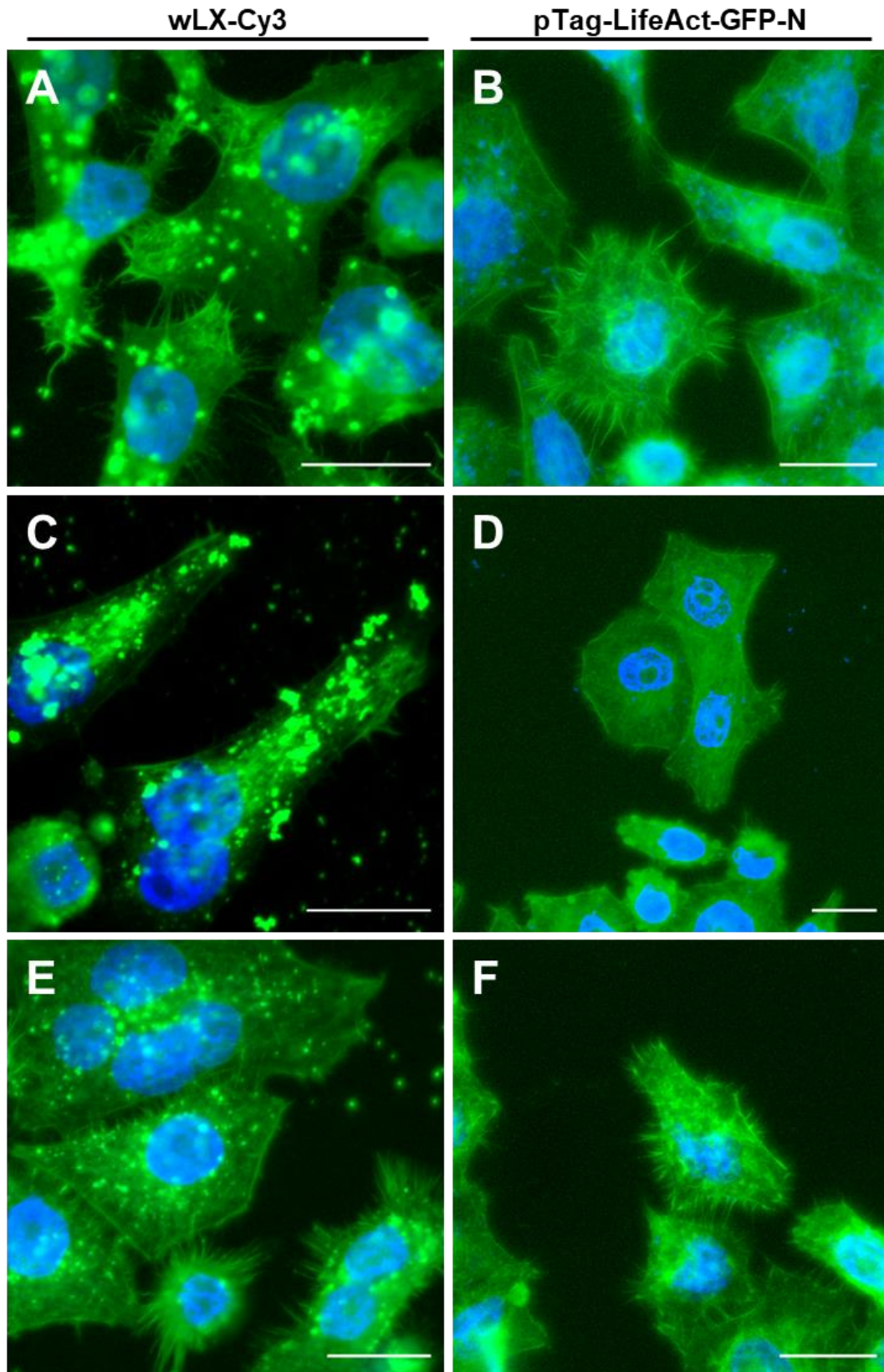


**Figure 46 | Labeling of actin filaments within HeLa cells.** (Left) Labeling of intracellular actin structures with Cy3-labeled wLX was compared to (Right) conventional staining with LifeAct-GFP through plasmid transfection with pTag-LifeAct-GFP-N (4.18). HeLa cells were transfected with (A) 75 nM, (C) 150 nM and (E) 300 nM Cy3-wLX for 6 h. (B, D, F) HeLa cells were transfected with 1000 ng pTag-LifeAct-GFP-N plasmid DNA for 6 h. Cells were fixed and nuclei were stained with DAPI (shown in blue). Equal laser intensities and gains were applied. LSM Images were pseudo colored using ZEN blue software and scale bars set to 20  $\mu$ m.

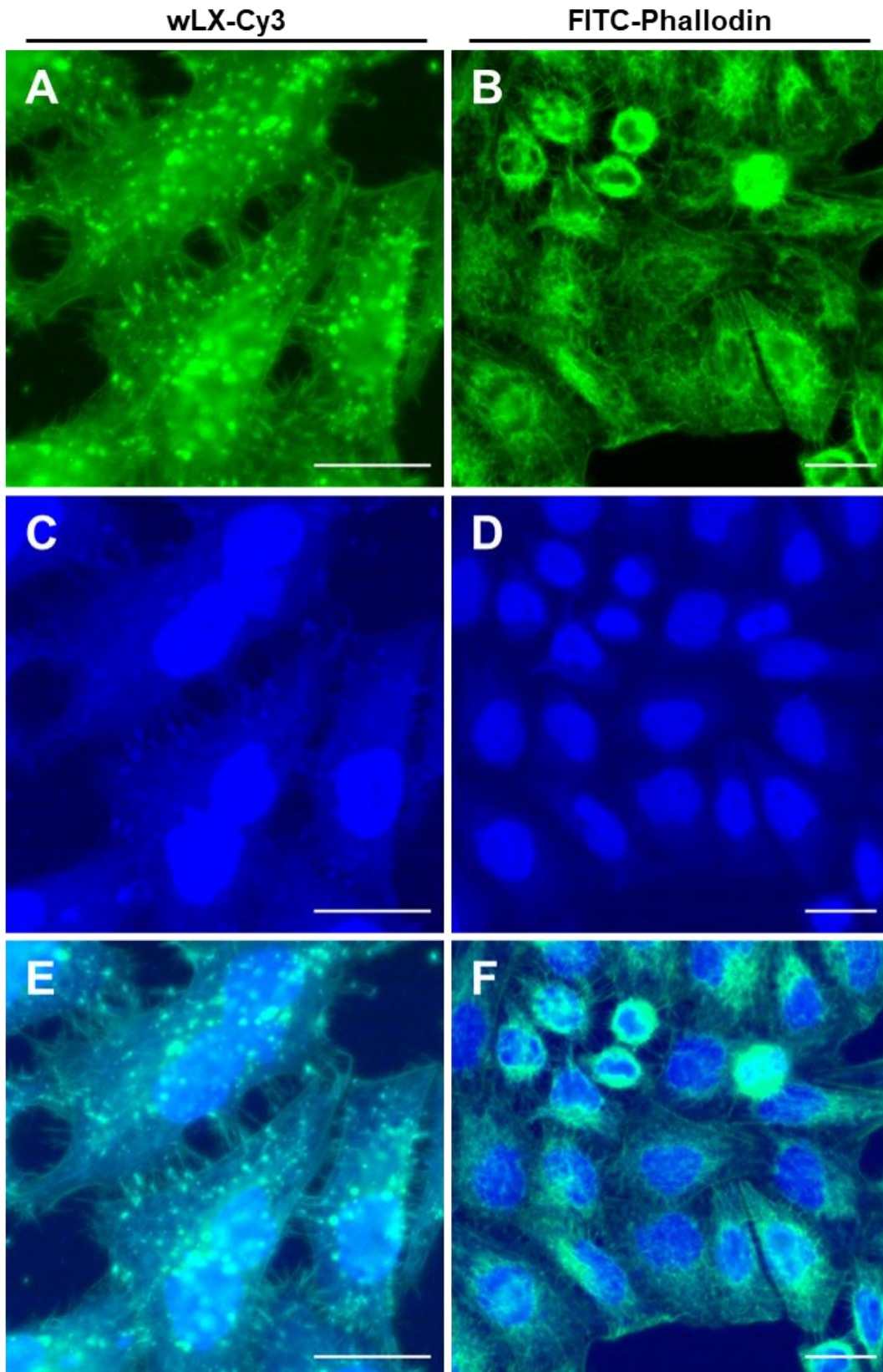


**Figure 47 | Co-localization of DNA and actin structures in HeLa cells transfected with wLX. (Left)** HeLa cells were transfected with 300 nM Cy3-labeled wLX for 6 h and fixed prior to LSM imaging. **(Right)** As a control, untreated cells were stained with 100 nM FITC-Phalloidin after fixation. In order to determine whether DNA-based Cy3-wLX (green fluorescence) merge with DNA staining (DAPI), gamma of blue channel was upregulated to 0.01 during image processing with ZEN blue software. **(A, B)** shows green fluorescence of **(A)** Cy3-wLX and **(B)** FITC-Phalloidin, **(C, D)** fluorescence of DAPI staining (blue), **(E, F)** merged pictures. LSM Images were pseudo colored and scale bars set to 20  $\mu\text{m}$ .

### 5.5 Functional effects of wLX on cells

After having shown that synthetic crosslinkers strongly interact with actin *in vitro*, e.g. inhibition of actin polymerization rates as well as stiffening of reconstituted actin networks, and that they specifically interact with actin filaments within cells, it was of strong interest, to investigate the functional effects of crosslinkers on cells stemming from these interactions. Obviously, actin-dependent processes such as proliferation, migration and invasion were in focus at the beginning. Additionally, the cytotoxic effect of these synthetic constructs was examined.

#### 5.5.1 Proof of concept

As a first proof of principle, the effect of synthetic crosslinkers on the migration of HeLa cells was tested. The process of cell migration is extremely dependent upon actin dynamics, as the rapid polymerization of actin at the barbed end of a branch in lamellipodia pushes the cell forward and therefore mediates migration (2.4). Since synthetic crosslinkers were shown to inhibit actin polymerization rates *in vitro*, it was of great interest to study migratory processes within cells. The two-dimensional migration of HeLa cells was investigated performing a simple wound healing or scratch assay, as described in section 4.40.3. HeLa cells were either treated with Lipofectamine™ 3000 only, or transfected with 300 nM 60bp DNA, 300 nM wLX or 300 nM sPX, respectively. After removing the culture insert, cell migration into the free gap was microscopically monitored over 48 h and a typical experimental run is shown in Figure 48 A. Whereas Lipofectamine as well as 60bp DNA control cells closed the gap within 48 h, cells treated with wLX and sPX moved slower and cell fronts did not reach each other within the same time. In order to gain a better understanding of the relative areas that are covered with cells during the process, images were quantitatively analyzed with the ImageJ plugin MITOBO. Figure 48 B shows the percentages of cells migrated into the cell-free area over 36 h. Cells treated with 300 nM wLX showed up to a 30 % decrease in migration over 36 h compared to the Lipofectamine control. Similar results were achieved for sPX: cells treated with 300 nM sPX migrated approximately 25 % slower than control cells. DNA-treated cells showed similar migratory course to Lipofectamine-treated cells. This observation nicely matches the findings Glück *et al.* reported in 1994. They found that modulations in the expression of  $\alpha$ -actinin, one of the previously introduced natural occurring actin crosslinkers (2.5.1) that were to be mimicked by wLX, were reported to have a major effect on the motile and tumorigenic properties of a cell. An overexpression of  $\alpha$ -actinin in 3T3 fibroblasts showed a significant reduction in cell motility, as seen by their slower movement into the cell free area of a standard wound healing assay. In contrast, a downregulation of  $\alpha$ -actinin led to an increased cell motility<sup>137</sup>.

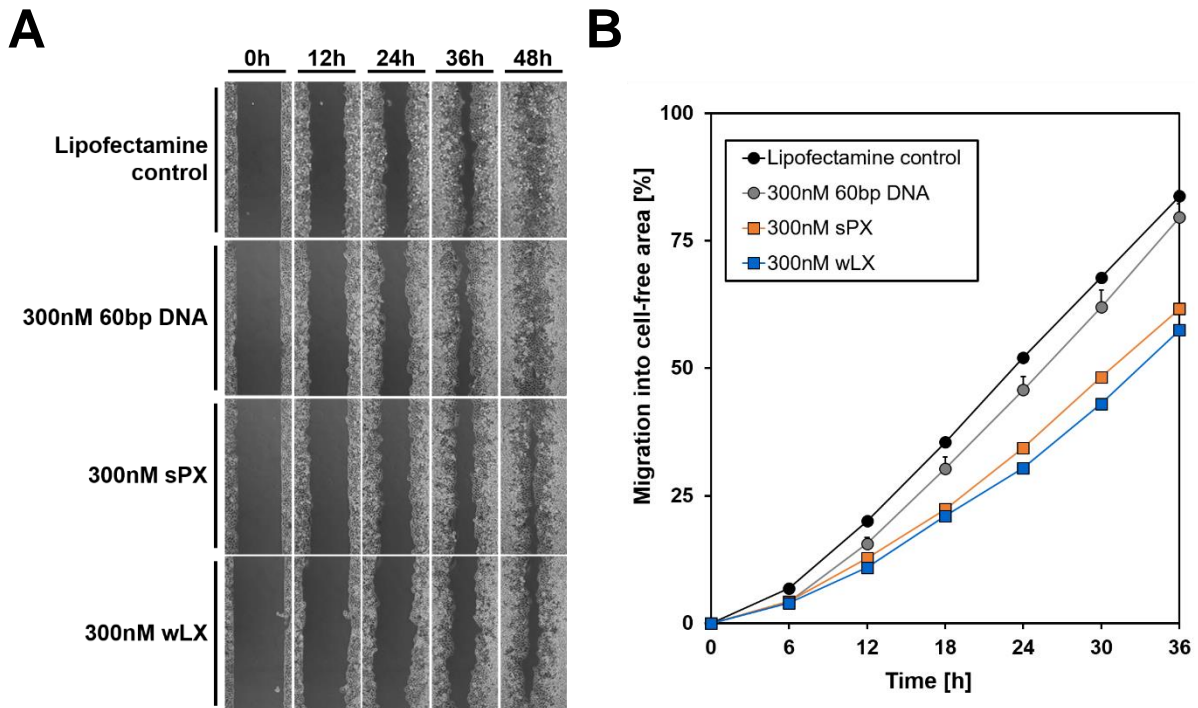


**Figure 48 | 2D migration of crosslinker-transfected HeLa cells into cell-free area over time.** (A) HeLa cells were transfected with 300 nM wLX, 300 nM sPX, 300 nM 60bp DNA as well as Lipofectamine only for 4 h. The time-dependent migration into the cell-free gap was imaged with an inverted Leica DM IRB phase contrast microscope. (B) Subsequent image analysis was conducted using ImageJ plugin MITOBO and received sample values were plotted against time. The experimental setup is described in 4.40.3.

Two-dimensional migration behavior is a combination of cells moving into the cell-free gap as well as cells proliferating to create the confluent layer. Since synthetic crosslinkers were shown to slow down cell migration in HeLa cells, it was of great interest whether the observed phenomenon simply occurred due to decreased proliferation or alternatively cell death and moreover, how wLX effects migration and invasion in 3D. However, HeLa cells are not suitable for invasion assays since they are noninvasive tumor cells. Thus, MDA-MB-231 cells, which are highly invasive and also considered a model system for cells that have undergone the process of epithelial-mesenchymal-transition (EMT), were utilized for the following experiments.

### 5.5.2 Impact of wLX on vital functions of cells

Initially, the proliferation of MDA-MB-231 cells, as described in 4.40.2, was investigated. WST-1 proliferation agent was added 24 h, 48 h and 72 h post transfection with wLX and corresponding controls. Results are plotted in Figure 49. Since DMSO is cytotoxic and cells did not proliferate any more after its addition, this was used as a suitable positive control. After three days, most of the DMSO-treated cells died, seen as red bars. After 72 hours, cells that were either transfected with 150 nM or 300 nM wLX showed a negligibly decreased

## Results and Discussion

proliferation activity compared to control samples with single-LifeAct® 60bp DNA, and a slightly decreased proliferation compared to the 60 bp DNA connector strand without any peptides (Figure 49 C). Cells, which were treated w/ and w/o Lipofectamine™3000, did show the highest proliferation rates. In general, any differences in the proliferation of cells treated with wLX compared to control cells were effectively negligible, and would not be expected to lead to functional changes as significant as those reported in the previous section.

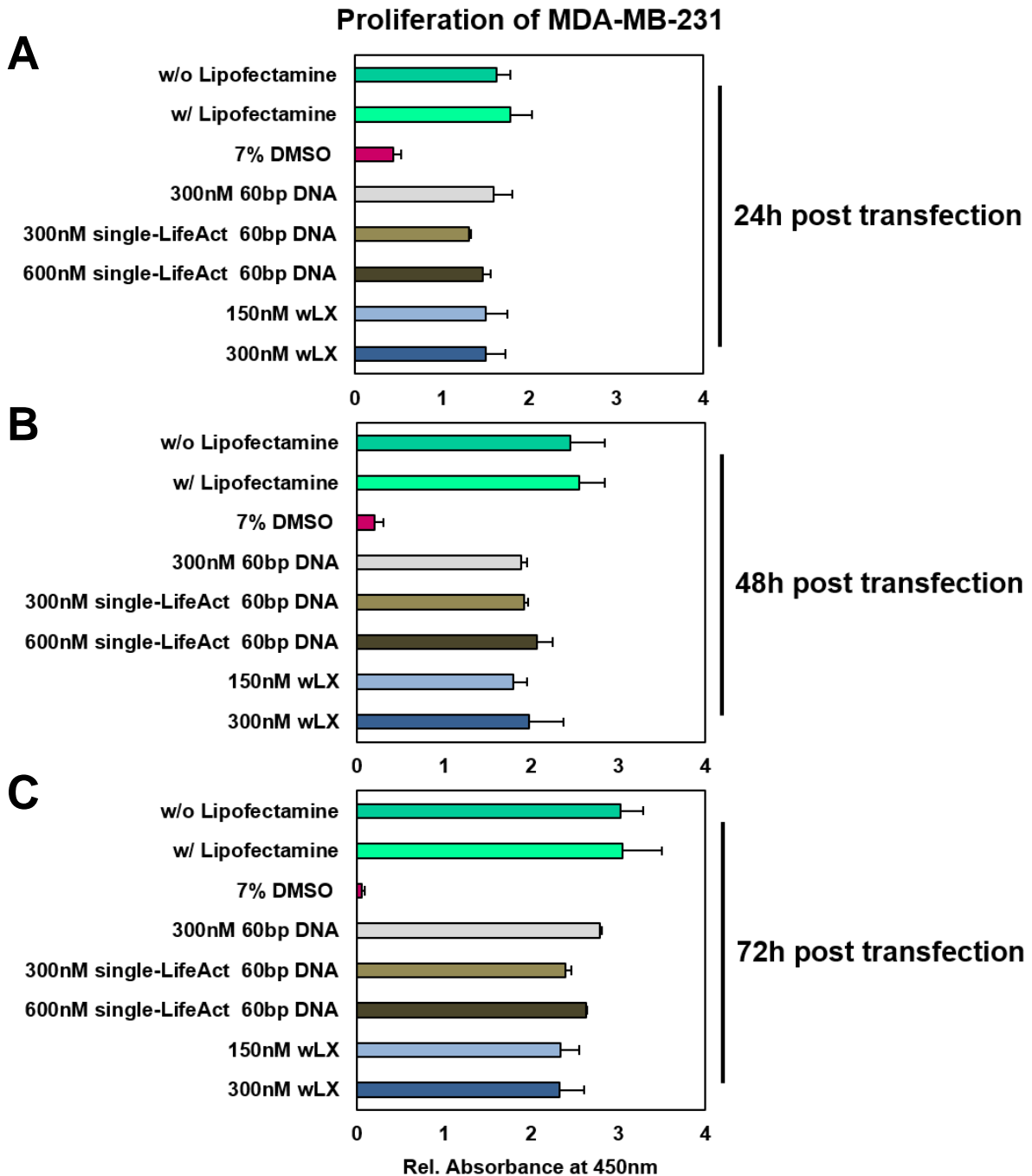


**Figure 49 | Proliferation of crosslinker-treated MDA-MB-231 cells.** MDA-MB-231 cells were transfected for 4 h with different concentrations of 60bp DNA, half-PTO 60bp DNA, wLX and full-PTO wLX, as well as Lipofectamine only. Proliferation was measured with WST-1 proliferation agent **(A)** 24 h, **(B)** 48 h and **(C)** 72 h post transfection. Cells treated with 7 % (v/v) DMSO served as positive control. Proliferation analysis was conducted as described in 4.40.2.

## Results and Discussion

Corresponding apoptosis analysis, as described in 4.40.1, is depicted in Figure 50. As seen in Figure 50 A, 60bp DNA as well as single LifeAct® 60bp DNA control showed very similar amounts of apoptotic cells compared to 150 nM and 300 nM wLX transfected cells. All of them were in the range of about 80 % to 85 % of vital cells, and showed approximately 10 % early apoptotic as well as 5 % to 7 % late apoptotic cells. However, non-treated cells, as well as cells treated only with Lipofectamine, showed a slightly lower apoptosis rate, with vitality rates of about 90 %, early apoptotic cells of 6 % to 7 % and late apoptotic cells of 3 % to 4 %. The DMSO control sample, shown as red bar, showed about 20 % early and more than 55 % late apoptotic cells after 24 h incubation. Only approximately 23 % cell incubated with 7 % DMSO were vital. In summary, it can be assumed, that synthetic crosslinkers do not initiate any significant amount of apoptosis in MDA-MB-231 cells and are not cytotoxic at those concentrations that were applied.

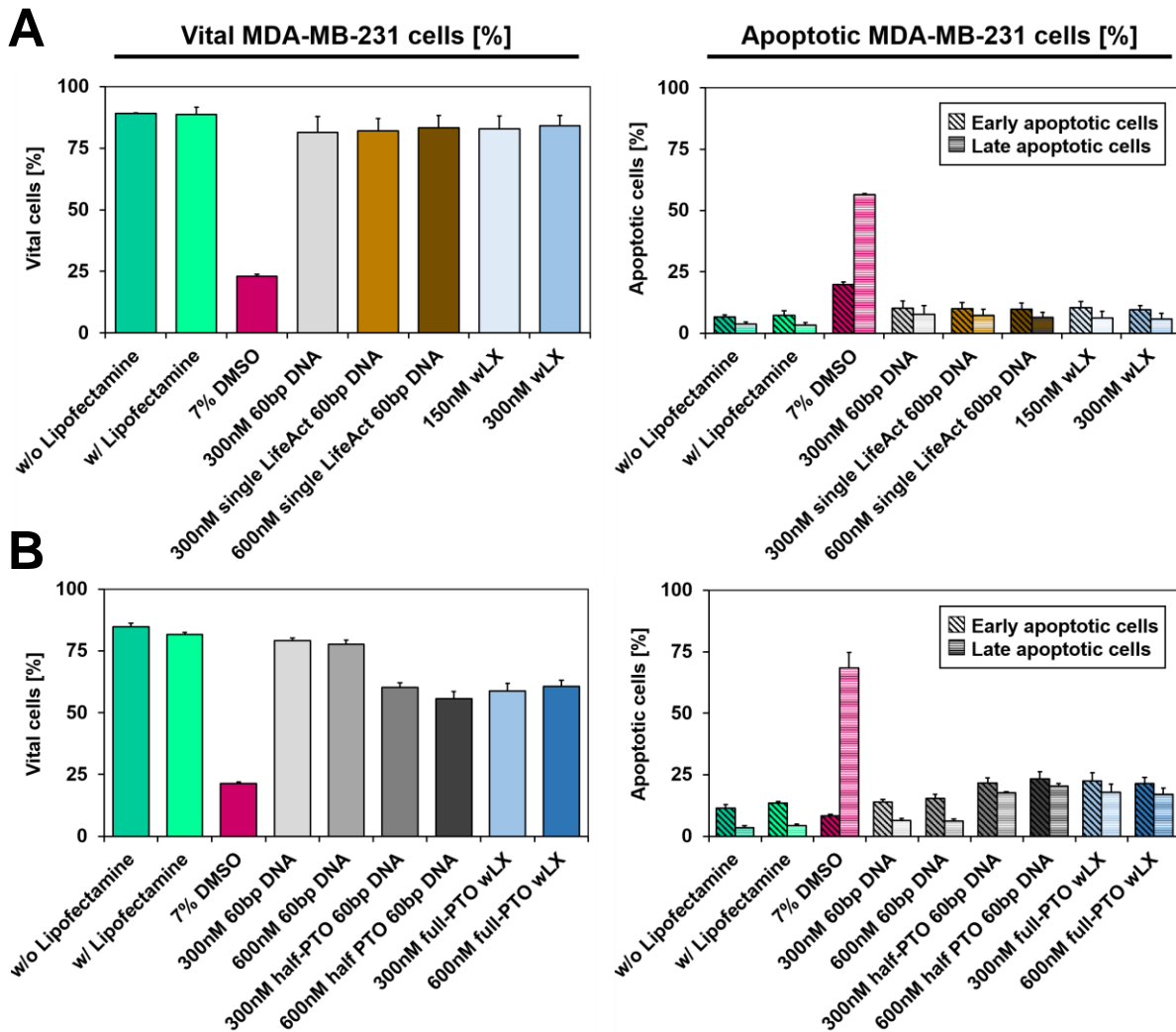


**Figure 50 | Apoptosis assay of crosslinker-treated MDA-MB-231 cells.** MDA-MB-231 cells were transfected for 4 h with different concentrations of 60bp DNA, half-PTO 60bp DNA, (A) wLX and (B) full-PTO wLX, as well as Lipofectamine only and incubated another 24 h prior to flow cytometry analysis. Cells treated with 7 % (v/v) DMSO served as positive control. Apoptosis analysis was conducted as described in 4.40.1.

Since PTO-modified DNA is known to be more stable against nuclease degradation<sup>237</sup>, two types of PTO-protected spacer segments were used in the cell culture experiments described in the following. Half-PTO 60bp DNA consisted of one fully protected strand and an unmodified complement, with no peptide modifications, and were used as a control. Full-PTO wLX were also used, where both strands were fully protected. These structures were investigated to assess influence of PTO modifications on apoptosis<sup>247</sup>. The results of this apoptosis assay, conducted similarly to the previously described apoptosis assay, are plotted in Figure 50 B. Compared to cells that were transfected with 300 nM and 600 nM 60bp DNA w/o PTO-modification, which showed vitality rates of about 80 %, cells transfected with either 300 nM or 600 nM half-PTO protected 60bp DNA as well as 300 nM and 600 nM full-PTO wLX showed about 20 % less vital cells. This included up to 24 % early and up to 20 % late apoptotic cells. Similarly, the half-PTO modified 60bp DNA also caused this significant effect. Due to the apparent and significant triggering of apoptosis from even a single PTO-protected strand, synthetic fully-PTO-protected crosslinkers were considered to be unsuitable for further cell experiments as they are more cytotoxic than unmodified DNA.

### 5.5.3 Effect of wLX on motile functions and invasiveness of cells

Migration of MDA-MB-231 cells was investigated in 3D utilizing a simple Boyden-chamber<sup>248</sup> approach, where cells squeeze through micron-sized pores at the bottom of the chamber towards a chemoattractant, in this case serum-containing medium. The full experimental setup is explained in section 4.40.4. Here, the 3D migration of cells after being treated for 48 h with only Lipofectamine was compared to cells transfected with either 300 nM 60bp DNA, 300 nM wLX, or 300 nM full-PTO wLX. Figure 51 A shows the percentages of cells that migrated through pores including the number of seeded cells. The data was normalized according to the cells treated with only Lipofectamine, which were set to 100 % in the presented data. All other samples were scaled according to this control. MDA-MB-231 cells, transfected with 300 nM wLX showed a decrease in 3D migration of around 12 % compared to Lipofectamine treated control cells. Full-PTO-protected wLX treated cells in contrast did not show a decrease in migration, and migrated similarly to control cells. However, cells that were transfected with unmodified 60bp DNA showed a decreased migration of around 12 %, similar to those described above that were treated with wLX.

Initial, earlier experiments had shown a decreased 3D migration of about 25 % of MDA-MB-231 cells treated with 300 nM wLX compared to cells that were treated either with only Lipofectamine or 300 nM single LifeAct 60bp DNA (supplemental Figure S 8 A). However, since the experimental setup was not exactly the same, those results are rather difficult to compare.

The initial response of a cell to a migration-promoting agent or trigger is polymerization and extension of protrusions towards the direction of migration. These protrusions can be large, broad lamellipodia or spike-like filopodia, are usually driven by actin polymerization, and are stabilized by adhering to the extracellular matrix (ECM) or adjacent cells via transmembrane receptors linked to the actin cytoskeleton. These adhesions serve as traction sites for migration as the cell moves forward over them, and they are disassembled at the cell rear, allowing it to detach<sup>83</sup>. In order to drive membrane protrusion and therefore initiate migration, actin filaments are polarized with fast-growing “barbed” ends and slow-growing “pointed” ends<sup>83</sup> as described in section 2.4. Additionally, it was reported that several actin-binding proteins regulate the rate and organization of actin polymerization in protrusions by affecting the pool of available monomers and free ends<sup>100,249</sup>. As seen in the pyrene assay, reported in 5.4.1, wLX caused an inhibition of polymerization rates in a concentration-dependent manner. Since actin polymerizes at the edge of a cell and thus promotes migration, an inhibition or decrease in polymerization could be an explanation why cells transfected with wLX migrated slower, both in 2D (Figure 48) and 3D (Figure 51 A and supplemental Figure S 8 A). For both, sPX and full-PTO wLX, pyrene assays are still lacking. Since it is unknown whether they inhibit or reduce actin polymerization rates as well, it is rather difficult to make conclusions about the cause for their previously observed effect on migrative behavior.

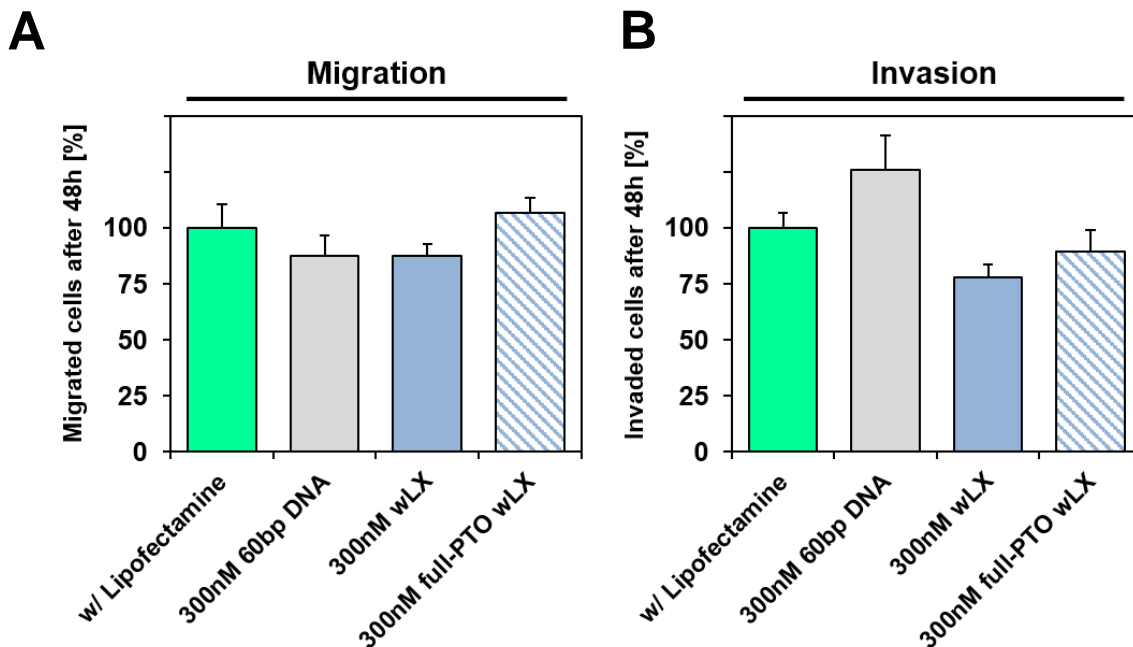


**Figure 51 | 3D migration and 3D invasion of crosslinker-transfected MDA-MB-231 cells.** (A) MDA-MB-231 cells were transfected with 300 nM 60bp DNA, 300 nM wLX, 300 nM full-PTO wLX, as well as Lipofectamine only for 4 h. Cells were detached and seeded into (A) uncoated culture wells to investigate 3D migration and (B) 0.5X BME-coated culture wells to analyze 3D invasion. Cells were incubated for 48 h and migrated and invaded cells subsequently stained via Calcein AM fluorescent dye. Under consideration of a Calcein AM standard curve as well as the seeded cell count, the number of cells was calculated from measured fluorescence intensities. The detailed experimental setup is to be found in 4.40.4. The percentage of migrated and invaded cells that were treated with Lipofectamine only was set to 100 %. All other samples were normalized to this control, respectively.

Similarly to 3D migration, a 3D invasion assay was conducted. Here, cells were seeded into chamber inserts that were additionally coated with a basement membrane extract (BME) layer. Only invasive cells that are able to degrade this BME layer with special, secreted enzymes (e.g. matrix metalloproteinases, short MMPs) are finally able to cross the barrier and reach the serum-containing medium on the other side. The detailed experimental setup is described in section 4.40.4. Figure 51 B shows the percentages of cells that successfully invaded through the BME layer and pores, which were either treated with Lipofectamine only or transfected with 300 nM 60bp DNA, 300 nM wLX or 300 nM full-PTO-protected wLX, respectively. Again, the percentages of invaded cells that were only treated with Lipofectamine were set to 100 % and all other samples normalized to this control. Transfection of MDA-MB-231 cells with 300 nM wLX led to nearly 25 % decreased invasiveness, compared to Lipofectamine control. Also full-PTO wLX-treated cells invaded approximately 10 % less than the corresponding control. However, this result might also be an effect of increased apoptosis rates, as seen previously (Figure 50 B). Unexpectedly, 60bp DNA treated cells showed an increased invasiveness of more than 25 % compared to the Lipofectamine control. However, the standard deviation was also rather high in this case.

Earlier 3D invasion studies, depicted in supplemental Figure S 8 B, had shown an inhibition of invasion of more than 90 % in wLX-treated MDA-MB-231 cells compared to corresponding controls. However, since different BME batches and BME concentrations were used as well as experiments were conducted in a self-made setup several months apart, larger differences in the very basic parameter of BMD layer thickness are expected. These preliminary results indicate that invasion is inhibited, however it requires further investigation to reveal to which extent it is inhibited. In order to better quantify the effect, future experiments need to be repeated on a standardized setup and a single BME batch.

Since 3D migration and invasion experiments were only performed once (in triplicates) with this particular setup, it was not possible to define whether differences in migration and invasion were significant compared to control cells. This could be determined in future experiments as well.

### **5.5.4 Possible impact of synthetic crosslinkers on EMT**

The results of the 3D invasion assays inevitably raised the question as to why wLX-treated cells showed a decreased invasiveness (e.g. decreased mesenchymal characteristic) through the BME layer as compared to the respective control cells. As described in section 2.9, the mesenchymal transformation of cells is not only associated with cancer, but generally with natural development and non-oncogenic diseases such as tissue fibrosis. Therefore, the potential inhibitory effect that these constructs generally have upon the epithelial to

## Results and Discussion

mesenchymal transition (EMT) was explored in preliminary experiments in conjunction with the collaborating group of Judith West-Mays (McMaster University, Hamilton, Canada). Here, synthetic crosslinkers were applied to a model system of human lens epithelial primary cells (FHL-124)<sup>250</sup>, which are often used as a model system for fibrosis-derived secondary cataracts. It is possible to induce epithelial-mesenchymal-transition (EMT) through stimulation with transforming growth factor beta (TGF- $\beta$ ) in those cells (2.9). It was found that cells, which were treated with 300 nM wLX for 3 h before stimulation with TGF- $\beta$  for 48 h, did not form criss-cross stress fibers, a key signature of EMT. The staining for F-actin, depicted in Figure 52, revealed that stress-fiber formation strongly increased in control cells treated with 300 nM 60bp DNA as well as buffer only before TGF- $\beta$  stimulation, indicating EMT was induced in those cells. Same was reported to happen for sPX-treated cells (data not shown). This observation can also be correlated to the previously described findings from FRAP experiments of wLX-transfected NMuMG cells, as it was shown that wLX slowed down actin remodeling dynamics (5.4.2), which is important for stress fiber formation.

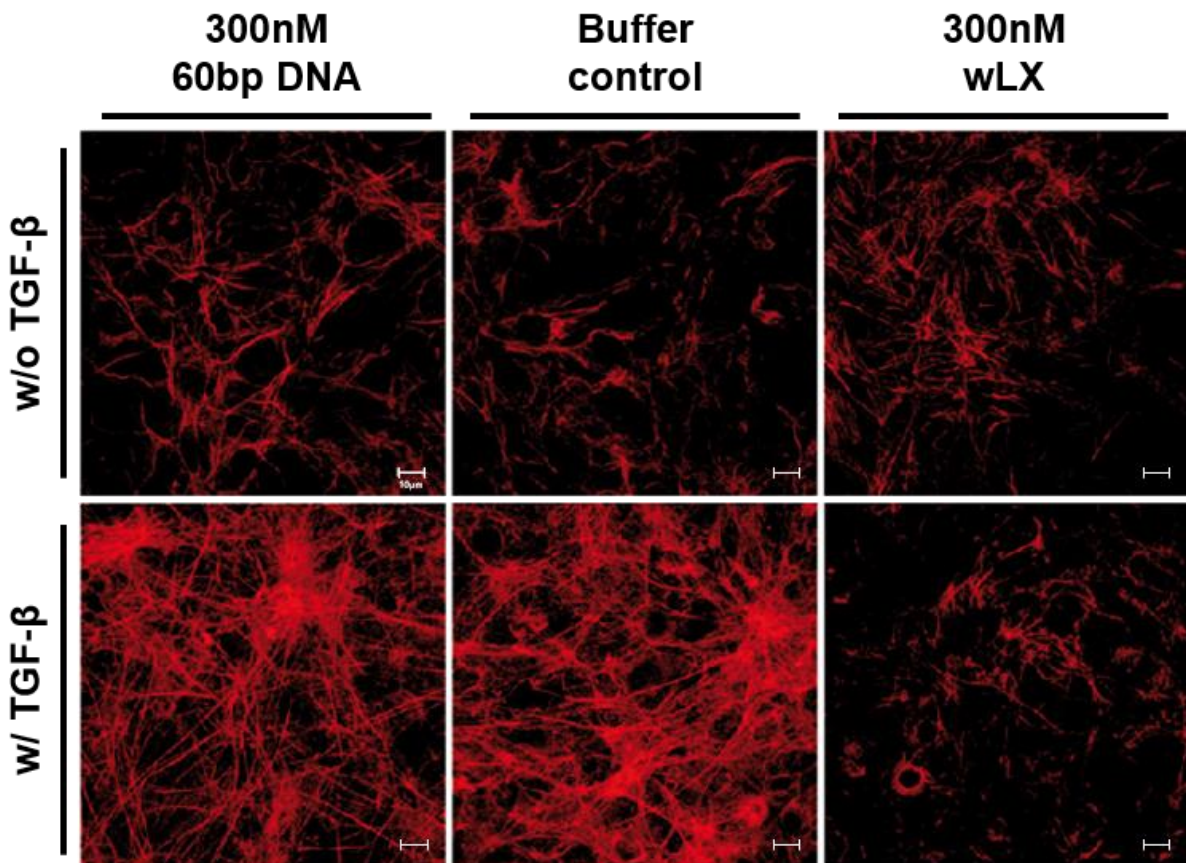


**Figure 52 | Influence of wLX on EMT induction in human lens epithelial cells (FHL-124).** Human lens epithelial cells (FHL-124) were either treated with buffer or transfected with 300 nM 60bp DNA or 300 nM wLX prior to treatment w/ or w/o transforming growth factor beta (TGF- $\beta$ ) for 48 h. Cells were fixed and stained for F-actin using Rhodamine-Phalloidin (red). Images were pseudo colored during image processing. Scale bars were set to 10  $\mu$ m. Experiments were conducted and pictures kindly provided by Aftab Taiyab, Post-Doctoral Fellow of the group of Judith West-Mays (McMaster University, Hamilton, Canada).

## Results and Discussion

Motivated by these experiments, wLX were investigated concerning their possible role within the process of EMT (2.9). Since Kim *et al.* showed that TGF -  $\beta$  induced EMT, invasion and migration in MCF-10A cells<sup>251</sup>, this human breast epithelial cell line (4.4.2) was utilized for these purposes. As a first anchor point, the influence of wLX on matrix metalloproteinase (MMP) expression was investigated. MMPs are calcium-dependent zinc-containing endopeptidases which are responsible for the tissue remodeling and degradation of the extracellular matrix<sup>252</sup>. Moreover, MMPs were reported to be connected to metastatic behavior *in vivo* and associated in breast cancer progression<sup>253</sup>.

Since wLX-treated cells showed a decreased 3D invasion, one possible explanation would be that wLX somehow mediated the downregulation of MMP expression levels and thus cells were less able to degrade the utilized Cultrex<sup>®</sup> BME layer, which mainly contained laminin, collagen IV, entactin, and heparan sulfate proteoglycan. Several MMPs are capable of degrading components of the BME layer. However, since both MMP-2 (gelatinase A, 72 kDa) and MMP-9 (gelatinase B, 92 kDa) are able to degrade collagen IV and gelatin, and were additionally reported to be upregulated in TGF -  $\beta$  stimulated MCF-10A cells<sup>251,252</sup>, a gelatin zymography assay was conducted. Gelatin zymography is a very simple assay to specifically detect gelatinase activity in conditioned medium. As reported in sections 4.40.5 and 4.40.5.1, MCF-10A cells were transfected with Lipofectamine only, 300 nM 60bp DNA or 300 nM wLX for 6 h and subsequently stimulated w/ or w/o TGF- $\beta$  for 48 h. The received gelatin zymogram is depicted in Figure 53.

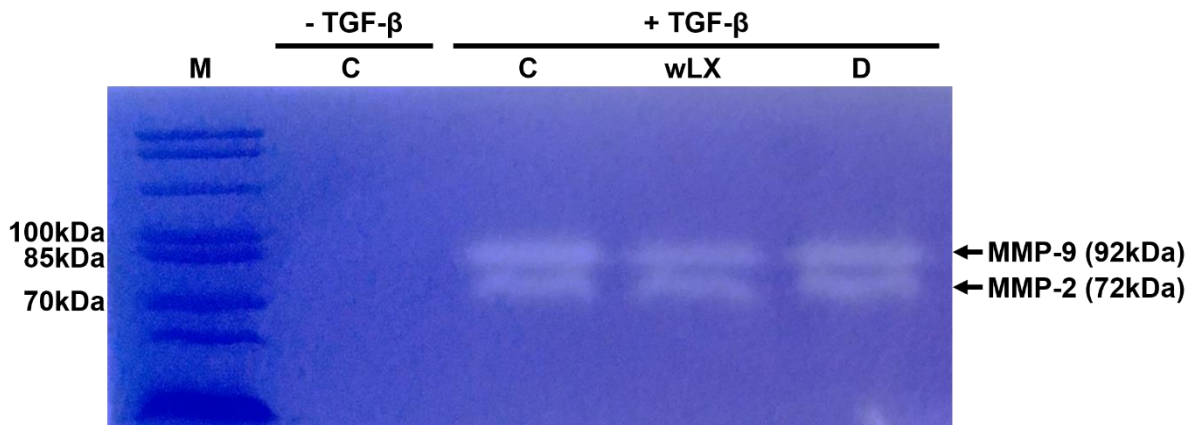


**Figure 53 | Detection of MMP-2 and MMP-9 levels via gelatin zymography.** Conditioned medium of MCF-10A cells stimulated for 48 h with or without 10 ng/ml TGF-beta after transfection for 6 h with **(C)** Lipofectamine only, **(wLX)** 300 nM wLX or **(D)** 300 nM 60bp DNA was analyzed for MMP activity. Samples were run on 10 % (v/v) SDS-PAGE containing 0.2 % (v/v) gelatin. **M**, PageRuler™ Unstained Protein Ladder. The detailed experimental setup is described in 4.40.5 and 4.40.5.1.

Conditioned medium of MCF-10A cells, which were not stimulated with TGF- $\beta$  for 48 h, did not show bands for MMP-2 and MMP-9 in the gelatin zymogram (lane C, - TGF- $\beta$ ). In contrast, conditioned media of cells which were stimulated with TGF- $\beta$  for 48 h showed bands

## Results and Discussion

---

for both MMP-2 and MMP-9. This nicely fits with what Kim *et al.* found in 2004, as they reported an upregulation of MMP-2 and MMP-9 expression in TGF- $\beta$ -stimulated MCF-10A cells<sup>251</sup>. Band intensities of MMP-2 and MMP-9 were almost equal in media of stimulated cells pretreated with Lipofectamine only as well as 300 nM 60bp DNA (lanes C and D, + TGF- $\beta$ ). The media of stimulated cells which were previously transfected with 300 nM wLX showed a slightly less intense MMP-9 band (lane wLX, + TGF- $\beta$ ). However, this effect is, if at all, very minor and would require further investigations. The MMP-2 level of stimulated cells that were treated with wLX was similar to controls which were also TGF- $\beta$ -stimulated.

Besides the analysis of MMP expression levels of TGF- $\beta$ -stimulated, wLX-treated cells, MCF-10A cells were also investigated regarding their up- or downregulated expression of several typical EMT markers. As described in sections 4.40.5 and 4.40.5.2, MCF-10 cells were transfected with Lipofectamine only, 300 nM 60bp DNA or 300 nM wLX and further treated w/o or w/ TGF- $\beta$  for 48 h. Prior to LSM imaging, cells were immunocytochemically stained for E-cadherin and snail. Corresponding results are shown in Figure 54. MCF-10A cells which were not stimulated with TGF- $\beta$  grew in a mosaic-like, epithelial fashion, as seen Figure 54 A - C. In comparison, cells which were TGF- $\beta$ -stimulated (Figure 54 D - L) did not grow in this previously mentioned pattern and appeared as more spindle-like cells with fewer cell-cell contacts, indicating the transition from an epithelial to a mesenchymal phenotype. Furthermore, those cells appeared larger compared to unstimulated cells. The fluorescence signal of E-cadherin was higher in unstimulated cells, compared to TGF- $\beta$ -treated cells. Snail staining in contrast, showed slightly increased intensities in TGF- $\beta$ -stimulated MCF-10A cells. It was reported that transcription factors, such as Snail, are induced by TGF- $\beta$  exposure and, once expressed, repress E-cadherin expression<sup>254</sup>. This would match the previously described observations, yet the differences in expression observed here were rather minor. Furthermore, there was no evidence for differences in E-cadherin and Snail expression of stimulated cells pretreated with either Lipofectamine only, 60bp DNA or wLX.

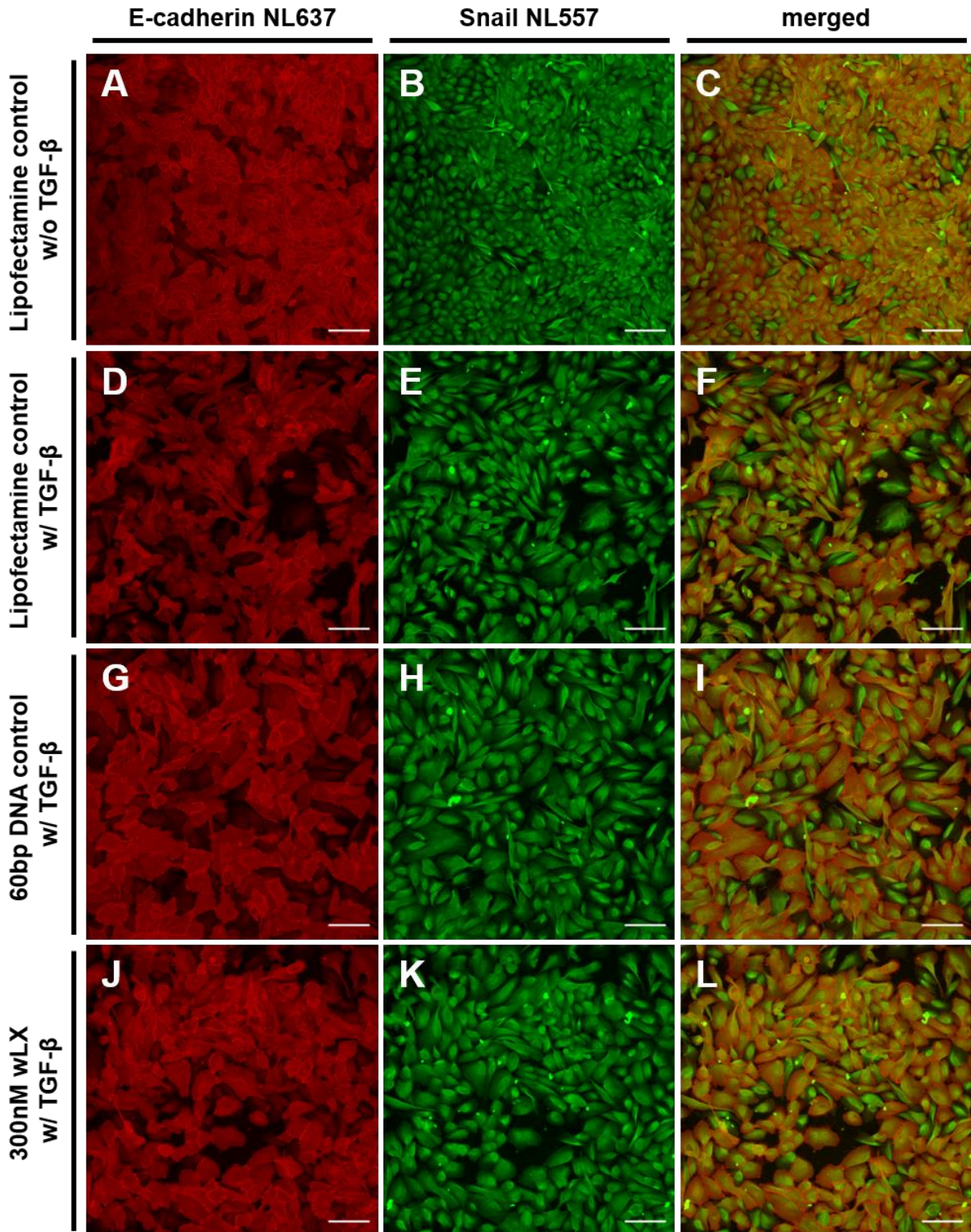


**Figure 54 | Immunocytochemistry staining for EMT markers after induction with TGF- $\beta$ .** MCF-10A cells were transfected with (J – L) 300 nM wLX, (G – I) 300 nM 60bp DNA as well as (A – F) Lipofectamine only for 6 h prior to stimulation w/ and w/o 10 ng/ml TGF- $\beta$  for 48 h in serum-free medium. Cells were fixed, permeabilized and stained for EMT markers E-cadherin and Snail utilizing fluorochrome-labeled antibodies (4.40.5.2). LSM images were pseudo colored using image processing software ZEN blue and scale bars set to 100  $\mu$ m.

In recent years, the elastic properties of non-cancerous, non-motile breast epithelial MCF-10A, cancerous but non-metastatic MCF-7 as well as highly invasive, motile

MDA-MB-231 cells have been investigated by various whole-cell rheology methods. Guck *et al.* reported in 2005 that non-cancerous MCF-10 cells deformed less than cancerous MCF-7 cells<sup>255</sup>. Furthermore it was reported that the elastic moduli of non-metastatic MCF-7 cells were significantly higher than those of metastatic MDA-MB-231 cells<sup>256</sup>. Since EMT was reported to be associated with cancer progression and metastasis<sup>189</sup>, unstimulated or TGF- $\beta$ -stimulated MCF-10A cells, which were pretreated with wLX as well as the corresponding controls, were investigated regarding their elastic moduli. On one hand, it was of great interest whether wLX have a direct influence on the cell mechanical properties by itself by stiffening the underlying actin network through crosslinking, while on the other hand, whether they somehow interfere with the biochemical process of EMT was also a valid line of inquiry. In this regard, cells were either pretreated with Lipofectamine only, 60bp DNA or wLX and were stimulated for 48 h with TGF- $\beta$ . The whole-cell elasticity was measured by microfluidic squeezing, i.e. real-time deformability cytometry (RT-DC)<sup>234</sup>, as described in section 4.40.6. The corresponding averaged Young's moduli are plotted in Figure 55, whereby the Young's modulus  $E$  is defined as the ratio of tensile stress to tensile strain.

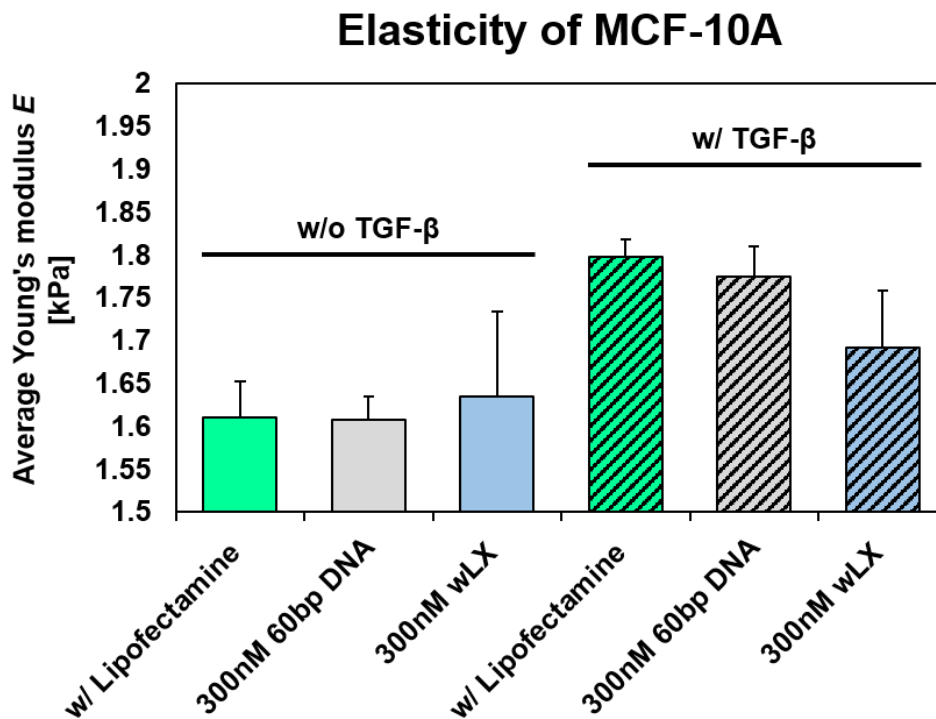


**Figure 55 | Mean elastic moduli of MCF-10 treated w/ or w/o TGF- $\beta$  post transfection with wLX and corresponding controls.** MCF-10A cells stimulated for 48 h with or without 10 ng/ml TGF- $\beta$  after transfection for 6 h with Lipofectamine only, 300 nM 60bp DNA or 300 nM wLX were analyzed via RT-DC<sup>234</sup> at a flow rate of 0.04  $\mu$ l/s. Mean Young's moduli were calculated using ShapeOut software provided by Zellmechanik Dresden GmbH. A detailed experimental setup is to be found in 4.40.5 and 4.40.6.

Looking at the direct influence of the synthetic crosslinker on unstimulated MCF-10A cells, wLX did not appear to stiffen the cells. While the bar (light blue) is in fact slightly increased, it is within the corresponding error bar. Cells treated with 60bp DNA showed an equal elasticity compared to the Lipofectamine control. Interestingly, cells which were stimulated for 48 h with TGF- $\beta$  showed an increased whole-cell elasticity compared to uninduced cells. Whereas the elasticity of Lipofectamine only and 300 nM 60bp DNA transfected cells increased of 11.6 % and 10.4 %, respectively, wLX-treated cells in showed a smaller increase of only 3.5 %. This result nicely correlates with the earlier described findings (5.5.4) where FHL-124 cells that were treated with wLX prior to TGF- $\beta$  stimulation showed a lack of stress fibers (Figure 52). This lack of the formation of cell-stabilizing criss-cross stress fibers in wLX-treated, TGF- $\beta$ -stimulated FHL-124 cells might be an explanation for the significantly smaller increase in elasticity compared to control cells. Corresponding contour plots also revealed that cells which were treated with TGF- $\beta$  were slightly bigger as curves were shifted to the right compared to unstimulated MCF-10A cells (supplemental Figure S 9), as also observed in previously discussed LSM images (Figure 54).

### 5.6 Hypotheses of how wLX effect actin-correlated processes

It still remains unclear exactly how wLX caused previously described effects such as a decreased migration and invasion as well as a decreased elasticity in EMT-induced cells. Some hypotheses of how wLX possibly acts within cells are given in the following.

#### 5.6.1 Interference with signaling pathways

One possible assumption is that the interaction of wLX with actin filaments interferes with actin-correlated signal pathways, schematically illustrated in Figure 56. It has been demonstrated that, for example, MMP-9 expression is linked to the myocardin-related transcription factor (MRTF) - serum-response factor (SRF) signaling pathway, which itself is dependent on actin polymerization and depolymerization processes<sup>201</sup> (2.9, Figure 15). High levels of G-actin retain the SRF cofactor protein MRTF in the cytosol. The incorporation of G-actin into the F-actin filament, i.e. actin polymerization, liberates MRTFs to enter the nucleus and interact with the transcription factor SRF<sup>205</sup>. This triggers the expression of a subset of SRF target genes, including MMP-9<sup>201</sup>. As wLX was shown to inhibit actin polymerization *in vitro*, it could possibly inhibit or reduce the nuclear translocation of MRTF, since more MRTF could probably remain bound to G-actin, and therefore decrease or suppress the expression of MMPs. A reduction of MMP levels could possibly explain the reduced migratory as well as invasive behavior of MDA-MB-231 cells. However, when MCF-10A cells were stimulated with

TGF- $\beta$  in order to induce EMT, MMP-9 levels of cells which were previously transfected with wLX only showed a minor, if any reduction. Further insights could be gained through the analysis of several other MMPs on the mRNA or protein level, also decoupled from TGF- $\beta$  stimulation.

Moreover, a downregulation of E-cadherin caused by an upregulation of snail was not conclusively detectable. However, wLX-transfected FHL-124 cells showed a suppression of criss-cross stress fibers, which are a signature of EMT. In addition to that, wLX-transfected, TGF- $\beta$ -stimulated MCF-10A cells were softer than control cells, which might be an indicator that wLX indeed interact with EMT-related processes.

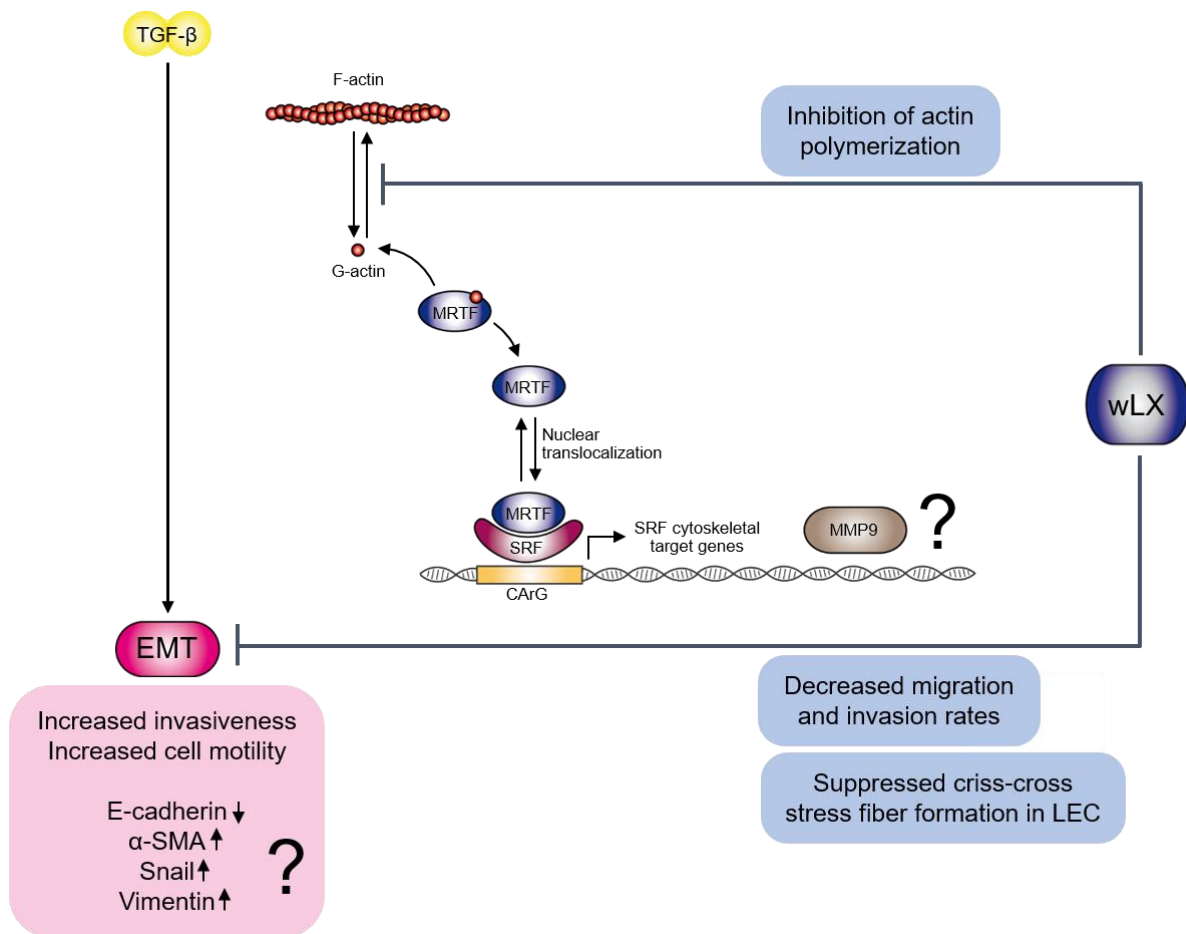


**Figure 56 | Possible influence of wLX in MRTF-mediated SRF signal transduction during EMT.** The synthetic actin crosslinker wLX showed a concentration-dependent inhibition of actin polymerization *in vitro*, which could also impact the MRTF-dependent SRF signal transduction of cytoskeletal target genes (2.9). Moreover, wLX caused a decreased migration and invasion as well as a lack of stress fiber formation in lens epithelial cells, which indicates a possible impact of wLX on EMT. Whether wLX indeed interferes with EMT, for instance, in the expression level of MMP-9 or the up- and downregulation of mesenchymal markers, however still requires further investigation.

More information could be achieved through investigations of other EMT markers such as vimentin,  $\alpha$ -smooth muscle actin, N-cadherin including immunocytochemistry staining as well as western blot analysis of wLX treated cells. In order to attain information, which genes

are possibly influenced by wLX application, microarrays could be conducted as well. Beyond this, it could be the case that wLX do not affect MRTF-SRF pathways; instead, they could also impact other actin-dependent signal transduction pathways or impact cell behavior by a different mechanism.

### 5.6.2 Mechanical influence of wLX on cells

Another assumption could be that crosslinkers directly influence cell behavior through a primarily mechanical effect as they possibly stiffen cells through linkage of actin filaments. This hypothesis is supported by the stiffening of reconstituted actin networks discussed in section 5.3. In 2008, furthermore, Jackson *et al.* reported that an  $\alpha$ -actinin overexpression in human osteoblasts led to an increased whole-cell stiffness, as measured by AFM indentation<sup>257</sup>. Moreover, Ehrlicher *et al.* reported that  $\alpha$ -actinin mutants, which had a three-fold higher affinity for actin due to a point mutation in the actin-binding domain, displayed slowed down intracellular dynamics as internalized micron-sized particles moved slower. Additionally, they found that these mutants generated higher contractile forces<sup>1</sup> compared to wild type cells. However, an increased elasticity of MCF-10A cells treated with wLX could not be conclusively proven with RT-DC measurements in this work. Future experiments will aim to provide insights into whether wLX as well as sPX connect actin filaments by their crosslinking properties and therefore intrinsically stiffen the whole cell. The influence of synthetic crosslinkers on adhesion forces as well as contractile forces could also be investigated via AFM and traction force microscopy, respectively.

### 5.6.3 Steric interference of actin dynamics caused by wLX

One final hypothesis is that since wLX interfere with actin polymerization and depolymerization, they generally slow down actin dynamics. This could be one reason for the observed decreased migration and invasion of MDA-MB-231 cells or the lack of the formation of criss-cross stress fibers in wLX-treated TGF- $\beta$ -stimulated FHL-124 cells. As already mentioned, wLX was seen to suppress actin polymerization in a concentration-dependent fashion *in vitro*. Since polymerization was inhibited, it was not possible to clearly state the influence of wLX on actin depolymerization. However, depolymerization was reported to be inhibited by natural crosslinkers such as fascin<sup>241</sup>. Thus it could be possible that synthetic crosslinkers interfere with both actin polymerization and depolymerization, which are two of the primary cellular processes that comprise the engine of cell motion and force generation. Assuming that wLX could decrease polymerization at the barbed ends and depolymerization at the pointed ends, the actin retrograde flow could be slowed down which in turn could have led to previously stated phenomena. Since MRTF-SRF signaling is related to actin

polymerization and depolymerization as well, the effect of wLX on filaments could also interfere with this pathway due to generally slowed down actin dynamics, which was indeed shown by FRAP experiments.

Further experiments could provide insights into how synthetic crosslinkers affect actin kinetics *in vitro*. These could be investigated by changing the actin binding peptide and/or the geometry of the DNA structure, e.g. increasing the number of binding sites for actin. Moreover, actin retrograde flow could be imaged and analyzed.



### 6 Conclusion and Outlook

One general aim of this work was to establish an efficient method to covalently link peptides to DNA nanostructures. Therefore, different conjugation methods were tested in which the copper-free click chemistry approach (SPAAC) was the most powerful tool as it gave the highest yields of the final product.

Within a smaller subproject, DNA nanostructures should serve as carrier platforms for functional biomolecules. In order to increase their cellular uptake, so-called cell-penetrating peptides were covalently conjugated to both structures. The utilized CPP sC18 is strongly cationic and enters cells via endocytotic pathways. It was shown that CPP-coupled DNA structures were internalized more efficiently than unconjugated controls. Additionally, it was demonstrated that CPP retain their functionality when they were bound to DNA structures, which was one of the main aims of this study. Both DNA tetrahedra and DNA trimers ended up in endosomes when they were conjugated to CPP as well as unconjugated, albeit to a lesser degree. However, to use them as a carrier platform for biomedical applications, it would be necessary to release them from endosomes following their initial uptake. In order to mediate the translocation into the cytosol, CPP that promote endosomal escape such as the chimeric version of sC18, named N-E5L-sC18, could be attached. In case an effective translocalization in the cytosol is warranted, these structures could be developed further and also functionalized with other biomolecules or therapeutic agents to serve as multifunctional carriers.

The fact that bifunctional molecules, such as peptides, retain their functionality when they are covalently attached to DNA structures, was also shown for the second subproject, in which actin crosslinkers such as  $\alpha$ -actinin or fascin were mimicked by purely synthetic actin crosslinkers fabricated from DNA and peptides. This was done due to the fact that naturally occurring actin crosslinkers, attributable to their empirical nature and complexity, do not allow systemic studies, in which different key parameters (e.g. affinity) can be varied in a decoupled fashion. By using synthetic crosslinkers, this natural limitation was resolved: whereas the basic geometry was kept constant, the affinity of the crosslinker was tuned independently by either attaching a weak (LifeAct<sup>®</sup>) or a strong (Phalloidin) actin-binding peptide on both sites of the 20 nm DNA spacer, referred as to wLX and sPX, respectively. High yields of both wLX and sPX as well as fluorescently labeled or PTO-protected alternatives were achieved by utilizing a SPAAC approach.

One of the major questions was also whether peptide-DNA conjugates could be applied to tune reconstituted biological systems. For this purpose, the impact of synthetic actin crosslinkers on reconstituted actin networks was investigated. Studies of actin polymerization

and depolymerization (via pyrene assay) revealed that actin polymerization was inhibited by wLX in a concentration-dependent manner. A reliable assumption as to whether depolymerization was also impacted by wLX could not be made, even though naturally occurring crosslinkers have previously been shown to inhibit depolymerization. Interestingly, both wLX and sPX displayed the same mechanical fingerprint as  $\alpha$ -actinin and fascin within rheological measurements. Moreover, both synthetic crosslinkers induced different structural morphologies within actin networks dependent on the crosslinker concentration applied. Thereby, it is noteworthy that the threshold bundle concentration was reduced for actin/sPX networks compared to actin/wLX networks due to a higher affinity of sPX towards F-actin. Furthermore, it was shown that crosslinking can be switched. A switching mechanism based on severing the DNA linker segment by the enzyme *EcoRV* clearly reversed the stiffening of actin/sPX networks, and the system became softer. This was nicely illustrated on the macroscopic scale within the inclined cuvette, as actin/*EcoRV*-cleaved sPX networks flowed out of the cuvette way faster than networks enriched with the intact sPX. The ability to switch crosslinkers from an "on" to an "off" state represents a promising feature, which could be further developed in future experiments. Moreover, it would be of great interest to explore the impact of different DNA spacer lengths as well as number of binding domains on *in vitro* actin networks. Altogether, these experiments indicate how effectively reconstituted actin networks can be manipulated in their biomechanical properties by using synthetic actin crosslinkers.

The last major aim of this dissertation was to investigate whether functionalized DNA-based biomimetic structures can function on specific target systems inside of living cells. One aspect was to ensure that synthetic crosslinkers are released into the cytosol after transfection to interfere with the actin cytoskeleton. As Cy3-labeled wLX were able to stain filamentous actin structures within cells similar to conventional staining methods using LifeAct<sup>®</sup>-GFP conjugates, it can be assumed that synthetic crosslinkers act in the cytosol. This assumption can be further strengthened by the results of actin remodeling dynamics experiments, as it was shown that the intracellular actin dynamics was slowed down by wLX. However, since actin remodeling in cells is a combination of polymerization, depolymerization, diffusion and myosin-driven translocation, a slowed down actin dynamics cannot be simply attributed to the inhibited polymerization that was shown for wLX in *in vitro* pyrene assays. Other factors, such as an increased crosslinking between actin structures would for instance inhibit diffusion and myosin translocation. Further fluorescence recovery after photobleaching (FRAP) experiments could gain insights in which of the named factors leads to a decrease in actin remodeling dynamics. Therefore, it would be of importance to compare the velocities of processes such as retrograde flow and myosin-based translocation/remodeling of actin filaments to those of fluorescence recovery. Moreover, in order to conclusively state that the slowed actin remodeling dynamics can be attributed to slowed polymerization/depolymerization, myosin II-inhibiting drugs like

## Conclusion and Outlook

---

blebbistatin could be used to determine whether the recovery dynamics are affected by the crosslinkers without the influence of the motor protein.

The impact of synthetic crosslinkers on actin-driven cellular processes such as migration, invasion or proliferation were investigated as well. Within a first “proof of concept” experiment, both wLX and sPX-transfected HeLa cells were observed to migrate slower into the cell-free gap of a simple 2D wound-healing assay. However, it still needed to be investigated in more detail whether this resulted from a decreased proliferation and/or increased apoptosis rates. In order to be also capable of studying 3D migration and invasion, a highly invasive breast tumor cell line (MDA-MB-231) was utilized for the following experiments. Both proliferation and apoptosis were not affected by wLX. However, PTO-modified wLX induced apoptosis and were, even though they were more stable against endo- and exonucleases in previous experiments, therefore excluded from further cell culture experiments. Furthermore, the 3D migration and invasion of wLX-transfected MDA-MB-231 cells was slowed down. The gain of invasive properties is associated with the process of epithelial-mesenchymal-transition (EMT), which involves signaling pathways that rely on the status of actin polymerization and depolymerization. Together with a collaborating group in Canada, who specialize in studying EMT during fibrosis, the synthetic crosslinkers were tested on a lens epithelial cell model (FHL-124). It was found that a key signature of EMT mediated by transforming growth factor- $\beta$  (TGF- $\beta$ ) was inhibited by both wLX and sPX, since criss-cross stress fibers were not observed. Subsequently, MCF-10A cells, which serve as a model cell line to study inducible EMT, were utilized to investigate the impact of synthetic crosslinkers in more detail, i.e. the level of MMP-2 and MMP-9, the expression levels of E-cadherin and snail as well as the elasticity of cells before and after stimulation with TGF- $\beta$ . Both MMP-2 and MMP-9 levels were increased in TGF- $\beta$  induced cells compared to unstimulated cells. However, no significant decrease of MMP-levels, which could explain a decreased 3D invasion, was observed. Similar results were seen with immunocytochemistry staining. No evidence for an impact of wLX on expression levels of E-cadherin and snail cells was seen, compared to other TGF- $\beta$ -induced control samples. In terms of biomechanical properties, TGF- $\beta$ -stimulated MCF-10A cells were stiffer than unstimulated cells. The synthetic crosslinker wLX did not cause a clear stiffening of unstimulated MCF-10A cells, however this requires further exploration. Interestingly, wLX caused less stiffening of TGF- $\beta$ -stimulated MCF-10A cells compared to controls, which might be an indicator that wLX indeed interact with EMT-related processes. For instance, the lack of formation of criss-cross stress fibers, as seen for wLX-transfected FHL-124 cells, could be a hint for cells being softer. However, whether wLX-transfected, TGF- $\beta$ -stimulated MCF-10A cells are also inhibited from forming extensive stress fibers still needs to be investigated.

Thus, these results clearly indicate that peptide-conjugated DNA structures are capable of functioning on particular systems inside of living cells. However, it still remains unclear how

exactly synthetic crosslinkers interfere with cellular processes. Different hypotheses of how these synthetic constructs act in cells were shown. First, crosslinkers could interfere with signaling pathways, such as the MRTF-dependent SRF signaling pathway, which is responsible for the expression of mostly cytoskeletal genes. In order to gain more information about possible interaction partners as well as up- or downregulated genes or proteins, microarrays and typical biochemical assays such as western blotting could be conducted. Second, synthetic actin crosslinkers could cause a mechanical effect on cellular systems, as these could physically link two actin filaments together and thus stiffen the whole cell. Therefore, the influence of synthetic crosslinkers on adhesion and contraction forces could be explored via AFM and traction force microscopy, respectively. One third, last assumption could be that synthetic crosslinkers sterically interfere with actin dynamics in cells and therewith cause a decrease in migration and invasion of MDA-MB-231 cells or the lack of the formation of criss-cross stress fibers in wLX-treated, TGF- $\beta$ -stimulated MCF-10A cells. Therefore, pyrene assays would need to be repeated and, as mentioned above, actin remodeling dynamics could be studied in more detail via FRAP. Further insights into how synthetic crosslinkers affect actin kinetics *in vitro* could be achieved by investigations of crosslinkers with an altered affinity towards F-actin as well as a change in geometry, e.g. an increased number of binding domains. This highlights a particular strength of this synthetic system, as such systematic changes would only involve choosing a different actin-binding peptide or altering the underlying DNA template. Ideally, all these studies should be conducted on one specific cell line to be finally able to combine all the different clues in one model.

The work presented here nicely illustrates how DNA-based biomimetics can be used to study reconstituted and cellular systems. For instance, by changing one single parameter of a synthetically fabricated actin crosslinker, i.e. binding affinity, the bulk properties of reconstituted actin networks were drastically altered. Biological systems comprise proteins with many other geometries, sizes or strengths, which could be immediately studied in more detail by functionalized DNA nanostructures to determine their impact. Linking this to changes in the cellular function could possibly provide tools to develop a clean model system for assessing the impact of these properties on whole-cell function. This could provide insights into specific diseases linked to the natural counterparts. Moreover, DNA nanotechnology provides a playground of various possible functionalization, which allows one to even go beyond the limits of natural crosslinks. Completely new bio-inspired materials could be designed, for example by changing the number of binding domains (valency) or the addition of different signal-responsive switching mechanisms. For instance, the development of an artificial DNA-based hydrogel which can be reversibly switched from stiff to soft by changing its mesh size could provide insights in the behavior of cells and would be an interesting tool for both researchers as well as bioengineers. Generally, this work shows the validity of this overall approach of

## **Conclusion and Outlook**

---

using programmable nanofabrication in order to engineer biocompatible, biomimetic constructs which could be used to help to unravel the complexity of life.



## 7 References

1. Ehrlicher, A. J. *et al.* Alpha-actinin binding kinetics modulate cellular dynamics and force generation. *Proceedings of the National Academy of Sciences of the United States of America* **112**, 6619–6624 (2015).
2. Rees, D. C., Williams, T. N. & Gladwin, M. T. Sickle-cell disease. *The Lancet* **376**, 2018–2031 (2010).
3. Walsh, R., Rutland, C., Thomas, R. & Loughna, S. Cardiomyopathy. A Systematic Review of Disease-Causing Mutations in Myosin Heavy Chain 7 and Their Phenotypic Manifestations. *Cardiology* **115**, 49–60 (2010).
4. Mandelkern, M., Elias, J. G., Eden, D. & Crothers, D. M. The dimensions of DNA in solution. *Journal of Molecular Biology* **152**, 153–161 (1981).
5. Biffi, G., Tannahill, D., McCafferty, J. & Balasubramanian, S. Quantitative visualization of DNA G-quadruplex structures in human cells. *Nature Chem* **5**, 182–186 (2013).
6. Seeman, N. C. Nucleic acid junctions and lattices. *J. Theoretical Biol.*, 237–247 (1982).
7. Watson, J. D. & Crick, F. H. C. Molecular Structure of Nucleic Acids. A Structure for Deoxyribose Nucleic Acid. *Nature* **171**, 737–738 (1953).
8. Kallenbach, N. R., Ma, R.-I. & Seeman, N. C. An immobile nucleic acid junction constructed from oligonucleotides. *Nature* **305**, 829–831 (1983).
9. J. Chen and N. C. Seeman. Synthesis from DNA of a molecule with the connectivity of a cube. *Nature*, 631–633 (1991).
10. Zhang, Y. & Seeman, N. C. Construction of a DNA-truncated octahedron. *J. Am. Chem. Soc.*, 1661–1669 (1994).
11. Winfree, E., Liu, F., Wenzler, L. A. & Seeman, N. C. Design and self-assembly of two-dimensional DNA crystals. *Nature* **394**, 539–544 (1998).
12. Seeman, N. C. DNA nanotechnology. Novel DNA constructions. *Annual Review of Biophysics and Biomolecular Structure* **27**, 225–248 (1998).
13. He, Y., Chen, Y., Liu, H., Ribbe, A. E. & Mao, C. Self-assembly of hexagonal DNA two-dimensional (2D) arrays. *J. Am. Chem. Soc.* **127**, 12202–12203 (2005).
14. He, Y. & Mao, C. Balancing flexibility and stress in DNA nanostructures. *Chemical communications (Cambridge, England)*, 968–969 (2006).
15. Zheng, J. *et al.* From molecular to macroscopic via the rational design of a self-assembled 3D DNA crystal. *Nature* **461**, 74–77 (2009).
16. Goodman, R. P. *et al.* Rapid chiral assembly of rigid DNA building blocks for molecular nanofabrication. *Science (New York, N.Y.)* **310**, 1661–1665 (2005).

## References

---

17. Erben, C. M., Goodman, R. P. & Turberfield, A. J. Single-Molecule Protein Encapsulation in a Rigid DNA Cage. *Angew. Chem.* **118**, 7574–7577 (2006).
18. Smith, D., Schüller, V., Engst, C., Rädler, J. & Liedl, T. Nucleic acid nanostructures for biomedical applications. *Nanomedicine (London, England)* **8**, 105–121 (2013).
19. Pinheiro, A. V., Han, D., Shih, W. M. & Yan, H. Challenges and opportunities for structural DNA nanotechnology. *Nature nanotechnology* **6**, 763–772 (2011).
20. Rothmund, P. W. K. Folding DNA to create nanoscale shapes and patterns. *Nature* **440**, 297–302 (2006).
21. Ke, Y., Ong, L. L., Shih, W. M. & Yin, P. Three-dimensional structures self-assembled from DNA bricks. *Science (New York, N.Y.)* **338**, 1177–1183 (2012).
22. Wei, B., Dai, M. & Yin, P. Complex shapes self-assembled from single-stranded DNA tiles. *Nature* **485**, 623–626 (2012).
23. Schuldt, C. *et al.* Tuning Synthetic Semiflexible Networks by Bending Stiffness. *Physical review letters* **117**, 197801 (2016).
24. Schnauß, J. *et al.* DNA Nanotubes as a Versatile Tool to Study Semiflexible Polymers. *JoVE* (2017).
25. Hariadi, R. F. *et al.* Mechanical coordination in motor ensembles revealed using engineered artificial myosin filaments. *Nature nanotechnology* **10**, 696–700 (2015).
26. Gu, Q. *et al.* DNA nanowire fabrication. *Nanotechnology* **17**, R14-R25 (2006).
27. Tan, S. J., Campolongo, M. J., Luo, D. & Cheng, W. Building plasmonic nanostructures with DNA. *Nature nanotechnology* **6**, 268–276 (2011).
28. Voigt, N. V. *et al.* Single-molecule chemical reactions on DNA origami. *Nature nanotechnology* **5**, 200–203 (2010).
29. Douglas, S. M., Chou, J. J. & Shih, W. M. DNA-nanotube-induced alignment of membrane proteins for NMR structure determination. *Proceedings of the National Academy of Sciences of the United States of America* **104**, 6644–6648 (2007).
30. Li, J., Fan, C., Pei, H., Shi, J. & Huang, Q. Smart drug delivery nanocarriers with self-assembled DNA nanostructures. *Advanced materials (Deerfield Beach, Fla.)* **25**, 4386–4396 (2013).
31. Schüller, V. J. *et al.* Cellular immunostimulation by CpG-sequence-coated DNA origami structures. *ACS nano* **5**, 9696–9702 (2011).
32. Li, Z. *et al.* DNA nanostructure-based universal microarray platform for high-efficiency multiplex bioanalysis in biofluids. *ACS applied materials & interfaces* **6**, 17944–17953 (2014).
33. Lee, H. *et al.* Molecularly self-assembled nucleic acid nanoparticles for targeted in vivo siRNA delivery. *Nature nanotechnology* **7**, 389–393 (2012).

## References

---

34. Crawford, R. *et al.* Non-covalent single transcription factor encapsulation inside a DNA cage. *Angewandte Chemie (International ed. in English)* **52**, 2284–2288 (2013).
35. Xie, N. *et al.* A DNA tetrahedron-based molecular beacon for tumor-related mRNA detection in living cells. *Chemical communications (Cambridge, England)* **52**, 2346–2349 (2016).
36. Chan, M. S. *et al.* Mitochondrial Delivery of Therapeutic Agents by Amphiphilic DNA Nanocarriers. *Small (Weinheim an der Bergstrasse, Germany)* **12**, 770–781 (2016).
37. Kim, K.-R. *et al.* Drug delivery by a self-assembled DNA tetrahedron for overcoming drug resistance in breast cancer cells. *Chemical communications (Cambridge, England)* **49**, 2010–2012 (2013).
38. Le Liang *et al.* Single-particle tracking and modulation of cell entry pathways of a tetrahedral DNA nanostructure in live cells. *Angewandte Chemie (International ed. in English)* **53**, 7745–7750 (2014).
39. Agard, N. J., Prescher, J. A. & Bertozzi, C. R. A strain-promoted [3 + 2] azide–alkyne cycloaddition for covalent modification of biomolecules in living systems. *J. Am. Chem. Soc.* **126**, 15046–15047 (2004).
40. Kolb, H. C., Finn, M. G. & Sharpless, K. B. Click Chemistry. Diverse Chemical Function from a Few Good Reactions. *Angew. Chem. Int. Ed.* **40**, 2004–2021 (2001).
41. Baskin, J. M. *et al.* Copper-free click chemistry for dynamic in vivo imaging. *Proceedings of the National Academy of Sciences of the United States of America* **104**, 16793–16797 (2007).
42. Jewett, J. C. & Bertozzi, C. R. Cu-free click cycloaddition reactions in chemical biology. *Chemical Society reviews* **39**, 1272–1279 (2010).
43. Pooga, M. *et al.* Cellular translocation of proteins by transportan. *Biochim. Soc. Trans.* **28**, A364.3-A364 (2000).
44. Astriab-Fisher, A., Sergueev, D., Fisher, M., Shaw, B. R. & Juliano, R. L. Conjugates of antisense oligonucleotides with the Tat and antennapedia cell-penetrating peptides: Effects on cellular uptake, binding to target sequences, and biologic actions. *Pharmaceutical Research* **19**, 744–754 (2002).
45. Torchilin, V. P., Rammohan, R., Weissig, V. & Levchenko, T. S. TAT peptide on the surface of liposomes affords their efficient intracellular delivery even at low temperature and in the presence of metabolic inhibitors. *Proceedings of the National Academy of Sciences of the United States of America* **98**, 8786–8791 (2001).
46. Lewin, M. *et al.* Tat peptide-derivatized magnetic nanoparticles allow in vivo tracking and recovery of progenitor cells. *Nat. Biotechnol.*, 410–414 (2000).

## References

---

47. Vivès, E., Brodin, P. & Lebleu, B. A Truncated HIV-1 Tat Protein Basic Domain Rapidly Translocates through the Plasma Membrane and Accumulates in the Cell Nucleus. *Journal of Biological Chemistry* **272**, 16010–16017 (1997).
48. Frankel, A. D. & Pabo, C. O. Cellular uptake of the tat protein from human immunodeficiency virus. *Cell* **55**, 1189–1193 (1988).
49. Derossi, D., Joliot, A. H., Chassaing, G. & Prochiantz, A. The third helix of the Antennapedia homeodomain translocates through biological membranes. *Journal of Biological Chemistry* **269**, 10444–10450 (1994).
50. Elliott, G. & O'Hare, P. Intercellular Trafficking and Protein Delivery by a Herpesvirus Structural Protein. *Cell* **88**, 223–233 (1997).
51. Pooga, M., Hällbrink, M., Zorko, M. & Langel, Ü. Cell penetration by transportan. *Faseb Journal*, 67–77 (1998).
52. Mitchell, D. J., Steinman, L., Kim, D. T., Fathman, C. G. & Rothbard, J. B. Polyarginine enters cells more efficiently than other polycationic homopolymers. *J Pept Res* **56**, 318–325 (2000).
53. Florian Reichart *Zyklisierte zellpenetrierende Peptide für den Wirkstofftransport: Auswirkung auf Stabilität und Internalisierungsmechanismus* (2015).
54. Henriques, S. T., Melo, M. N. & Castanho, M. A. R. B. Cell-penetrating peptides and antimicrobial peptides. How different are they? *The Biochemical journal* **399**, 1–7 (2006).
55. Larrick, J. W., Morgan, J. G., Palings, I., Hirata, M. & Yen, M. H. Complementary DNA sequence of rabbit CAP18—A unique lipopolysaccharide binding protein. *Biochemical and biophysical research communications* **179**, 170–175 (1991).
56. Tossi, A., Scocchi, M., Skerlavaj, B. & Gennaro, R. Identification and characterization of a primary antibacterial domain in CAP18, a lipopolysaccharide binding protein from rabbit leukocytes. *FEBS Letters* **339**, 108–112 (1994).
57. Kichler, A., Mason, A. J. & Bechinger, B. Cationic amphipathic histidine-rich peptides for gene delivery. *Biochimica et biophysica acta* **1758**, 301–307 (2006).
58. Neundorff, I. *et al.* Fusion of a Short HA2-Derived Peptide Sequence to Cell-Penetrating Peptides Improves Cytosolic Uptake, but Enhances Cytotoxic Activity. *Pharmaceuticals (Basel, Switzerland)* **2**, 49–65 (2009).
59. Conner, S. D. & Schmid, S. L. Regulated portals of entry into the cell. *Nature* **422**, 37–44 (2003).
60. Mukherjee, S., Ghosh, R. N. & Maxfield, F. R. Endocytosis. *Physiological reviews* **77**, 759–803 (1997).
61. Swanson, J. A. & Watts, C. Macropinocytosis. *Trends in cell biology* **5**, 424–428 (1995).
62. Johannes, L. & Lamaze, C. Clathrin-dependent or not. Is it still the question? *Traffic* **3**, 443–451 (2002).

## References

---

63. Di Fiore, P. P. & Camilli, P. de. Endocytosis and Signaling. *Cell* **106**, 1–4 (2001).
64. Seto, E. S., Bellen, H. J. & Lloyd, T. E. When cell biology meets development. Endocytic regulation of signaling pathways. *Genes & development* **16**, 1314–1336 (2002).
65. Parton, R. G. & Richards, A. A. Lipid Rafts and Caveolae as Portals for Endocytosis. New Insights and Common Mechanisms. *Traffic* **4**, 724–738 (2003).
66. Razani, B., Woodman, S. E. & Lisanti, M. P. Caveolae. From cell biology to animal physiology. *Pharmacological reviews* **54**, 431–467 (2002).
67. Rothberg, K. G. *et al.* Caveolin, a protein component of caveolae membrane coats. *Cell* **68**, 673–682 (1992).
68. Hansen, C. G. & Nichols, B. J. Exploring the caves. Cavins, caveolins and caveolae. *Trends in cell biology* **20**, 177–186 (2010).
69. Pelkmans, L., Püntener, D. & Helenius, A. Local actin polymerization and dynamin recruitment in SV40-induced internalization of caveolae. *Science (New York, N.Y.)* **296**, 535–539 (2002).
70. Hayer, A. *et al.* Caveolin-1 is ubiquitinated and targeted to intraluminal vesicles in endolysosomes for degradation. *The Journal of Cell Biology* **191**, 615–629 (2010).
71. Mayor, S. & Pagano, R. E. Pathways of clathrin-independent endocytosis. *Nature reviews. Molecular cell biology* **8**, 603–612 (2007).
72. Holm, T. *Cell-penetrating peptides. Uptake, stability and biological activity* (Department of Neurochemistry, Stockholm University, Stockholm, 2011).
73. Fletcher, D. A. & Mullins, R. D. Cell mechanics and the cytoskeleton. *Nature* **463**, 485–492 (2010).
74. Alberts, B. *et al.* *Molecular biology of the cell* (Garland Science Taylor and Francis Group, New York, NY, 2015).
75. Pollard, T. D. & Cooper, J. A. Actin, a central player in cell shape and movement. *Science (New York, N.Y.)* **326**, 1208–1212 (2009).
76. Pollard, T. D., Blanchoin, L. & Mullins, R. D. Molecular Mechanisms Controlling Actin Filament Dynamics in Nonmuscle Cells. *Annual Review of Biophysics and Biomolecular Structure* **29**, 545–576 (2000).
77. Condeelis, J. Life at the leading edge: The formation of cell protrusions. *Annual review of cell biology* **9**, 411–444 (1993).
78. Suetsugu, S. & Takenawa, T. *Regulation of Cortical Actin Networks in Cell Migration* vol. **229**. International Review of Cytology 245–286 (Elsevier, 2003).
79. Welch, M. D. & Mullins, R. D. Cellular control of actin nucleation. *Annual review of cell and developmental biology*, 247–288 (2002).
80. Le Clainche, C. & Carlier, M.-F. Regulation of actin assembly associated with protrusion and adhesion in cell migration. *Physiological reviews* **88**, 489–513 (2008).

## References

---

81. Svitkina, T. M. & Borisy, G. G. Arp2/3 Complex and Actin Depolymerizing Factor/Cofilin in Dendritic Organization and Treadmilling of Actin Filament Array in Lamellipodia. *J Cell Biol* **145**, 1009–1026 (1999).
82. Vignjevic, D. *et al.* Role of fascin in filopodial protrusion. *J Cell Biol* **174**, 863–875 (2006).
83. Ridley, A. J. *et al.* Cell migration. Integrating signals from front to back. *Science (New York, N.Y.)* **302**, 1704–1709 (2003).
84. Ponti, A., Machacek, M., Gupton, S. L., Waterman-Storer, C. M. & Danuser, G. Two distinct actin networks drive the protrusion of migrating cells. *Science (New York, N.Y.)* **305**, 1782–1786 (2004).
85. Kreis, T. E. & Birchmeier, W. Stress fiber sarcomeres of fibroblasts are contractile. *Cell* **22**, 555–561 (1980).
86. Lazarides, E. & Burridge, K.  $\alpha$ -Actinin: Immunofluorescent localization of a muscle structural protein in nonmuscle cells. *Cell* **6**, 289–298 (1975).
87. Tojkander, S., Gateva, G. & Lappalainen, P. Actin stress fibers-assembly, dynamics and biological roles. *Journal of cell science* **125**, 1855–1864 (2012).
88. Pellegrin, S. & Mellor, H. Actin stress fibres. *Journal of cell science* **120**, 3491–3499 (2007).
89. Wachsstock, D. H., Schwartz, W. H. & Pollard, T. D. Affinity of  $\alpha$ -actinin for actin determines the structure and mechanical properties of actin filament gels. *Biophysical Journal* **65**, 205–214 (1993).
90. Machesky, L. M. Purification of a cortical complex containing two unconventional actins from *Acanthamoeba* by affinity chromatography on profilin-agarose. *J Cell Biol* **127**, 107–115 (1994).
91. Ma, L., Rohatgi, R. & Kirschner, M. W. The Arp2/3 complex mediates actin polymerization induced by the small GTP-binding protein Cdc42. *Proceedings of the National Academy of Sciences of the United States of America* **95**, 15362–15367 (1998).
92. Winter, D., Podtelejnikov, A. V., Mann, M. & Li, R. The complex containing actin-related proteins Arp2 and Arp3 is required for the motility and integrity of yeast actin patches. *Current Biology* **7**, 519–529 (1997).
93. Welch, M. D., Iwamatsu, A. & Mitchison, T. J. Actin polymerization is induced by Arp2/3 protein complex at the surface of *Listeria monocytogenes*. *Nature* **385**, 265–269 (1997).
94. Yasar, D., To, W., Abo, A. & Welch, M. D. The Wiskott–Aldrich syndrome protein directs actin-based motility by stimulating actin nucleation with the Arp2/3 complex. *Current Biology* **9**, 555–S1 (1999).
95. Winter, D., Lechler, T. & Li, R. Activation of the yeast Arp2/3 complex by Bee1p, a WASP-family protein. *Current Biology* **9**, 501–505 (1999).

## References

---

96. Machesky, L. M. *et al.* Scar, a WASp-related protein, activates nucleation of actin filaments by the Arp2/3 complex. *Proceedings of the National Academy of Sciences of the United States of America* **96**, 3739–3744 (1999).
97. Rohatgi, R. *et al.* The Interaction between N-WASP and the Arp2/3 Complex Links Cdc42-Dependent Signals to Actin Assembly. *Cell* **97**, 221–231 (1999).
98. Pollitt, A. Y. & Insall, R. H. WASP and SCAR/WAVE proteins. The drivers of actin assembly. *Journal of cell science* **122**, 2575–2578 (2009).
99. Mullins, R. D., Heuser, J. A. & Pollard, T. D. The interaction of Arp2/3 complex with actin. Nucleation, high affinity pointed end capping, and formation of branching networks of filaments. *Proceedings of the National Academy of Sciences of the United States of America* **95**, 6181–6186 (1998).
100. Pollard, T. D. & Borisy, G. G. Cellular motility driven by assembly and disassembly of actin filaments. *Cell* **112**, 453–465 (2003).
101. Mullins, R.D. & Pollard, T. D. Rho-family GTPases require the Arp2/3 complex to stimulate actin polymerization in *Acanthamoeba* extracts. *Current Biology* **9**, 405–415 (1999).
102. Maciver, S. K. Characterization of actin filament severing by actophorin from *Acanthamoeba castellanii*. *J Cell Biol* **115**, 1611–1620 (1991).
103. Schafer, D. A. Dynamics of capping protein and actin assembly in vitro. Uncapping barbed ends by polyphosphoinositides. *J Cell Biol* **135**, 169–179 (1996).
104. Blanchoin, L., Robinson, R. C., Choe, S. & Pollard, T. D. Phosphorylation of *Acanthamoeba* actophorin (ADF/cofilin) blocks interaction with actin without a change in atomic structure. *Journal of Molecular Biology* **295**, 203–211 (2000).
105. Edwards, D. C., Sanders, L. C., Bokoch, G. M. & Gill, G. N. Activation of LIM-kinase by Pak1 couples Rac/Cdc42 GTPase signalling to actin cytoskeletal dynamics. *Nature cell biology* **1**, 253–259 (1999).
106. Niwa, R., Nagata-Ohashi, K., Takeichi, M., Mizuno, K. & Uemura, T. Control of Actin Reorganization by Slingshot, a Family of Phosphatases that Dephosphorylate ADF/Cofilin. *Cell* **108**, 233–246 (2002).
107. Akin, O. & Mullins, R. D. Capping protein increases the rate of actin-based motility by promoting filament nucleation by the Arp2/3 complex. *Cell* **133**, 841–851 (2008).
108. Bear, J. E. & Gertler, F. B. Ena/VASP: Towards resolving a pointed controversy at the barbed end. *Journal of cell science* **122**, 1947–1953 (2009).
109. Sun, H. Q., Yamamoto, M., Mejillano, M. & Yin, H. L. Gelsolin, a Multifunctional Actin Regulatory Protein. *Journal of Biological Chemistry* **274**, 33179–33182 (1999).
110. Gardel, M. L. *et al.* Traction stress in focal adhesions correlates biphasically with actin retrograde flow speed. *The Journal of Cell Biology* **183**, 999–1005 (2008).

## References

---

111. Stossel, T. P. *et al.* Filamins as integrators of cell mechanics and signalling. *Nature reviews. Molecular cell biology* **2**, 138–145 (2001).
112. Way, M. Sequence and domain organization of scruin, an actin-cross-linking protein in the acrosomal process of *Limulus* sperm. *J Cell Biol* **128**, 51–60 (1995).
113. Bartles, J. R. Parallel actin bundles and their multiple actin-bundling proteins. *Current opinion in cell biology* **12**, 72–78 (2000).
114. Otey, C. A. & Carpen, O. Alpha-actinin revisited. A fresh look at an old player. *Cell Motil. Cytoskeleton* **58**, 104–111 (2004).
115. Bryan, J. & Kane, R. E. Separation and interaction of the major components of sea urchin actin gel. *Journal of Molecular Biology* **125**, 207–224 (1978).
116. Adams, J. C. Roles of fascin in cell adhesion and motility. *Current opinion in cell biology* **16**, 590–596 (2004).
117. Blanchard, A., Ohanian, V. & Critchley, D. The structure and function of  $\alpha$ -actinin. *J Muscle Res Cell Motil* **10**, 280–289 (1989).
118. Suzuki, A. *et al.* Some properties of purified skeletal muscle alpha-actinin. *Journal of Biological Chemistry* **251**, 6860–6870 (1976).
119. Endo, T. & Masaki, T. Molecular Properties and Functions *In Vitro* of Chicken Smooth-Muscle  $\alpha$ -Actinin in Comparison with Those of Striated-Muscle  $\alpha$ -Actinins. *The Journal of Biochemistry* **92**, 1457–1468 (1982).
120. Podlubnaya, Z. A., Tskhovrebova, L. A., Zaalishvili, M. M. & Stefanenko, G. A. Electron microscopic study of  $\alpha$ -actinin. *Journal of Molecular Biology* **92**, 357–359 (1975).
121. Mimura, N. & Asano, A. Isolation and characterization of a conserved actin-binding domain from rat hepatic actinogelin, rat skeletal muscle, and chicken gizzard alpha-actinins. *Journal of Biological Chemistry* **261**, 10680–10687 (1986).
122. Tang, J., Taylor, D. W. & Taylor, K. A. The three-dimensional structure of alpha-actinin obtained by cryoelectron microscopy suggests a model for  $\text{Ca}^{2+}$ -dependent actin binding. *Journal of Molecular Biology* **310**, 845–858 (2001).
123. Noegel, A., Witke, W. & Schleicher, M. Calcium-sensitive non-muscle  $\alpha$ -actinin contains EF-hand structures and highly conserved regions. *FEBS Letters* **221**, 391–396 (1987).
124. Burridge, K. & Feramisco, J. R. Non-muscle  $\alpha$ -actinins are calcium-sensitive actin-binding proteins. *Nature* **294**, 565–567 (1981).
125. Bennett, J. P., Zaner, K. S. & Stossel, T. P. Isolation and some properties of macrophage alpha-actinin. Evidence that it is not an actin gelling protein. *Biochemistry* **23**, 5081–5086 (1984).
126. Duhaime, A. S. & Bamberg, J. R. Isolation of brain alpha-actinin. Its characterization and a comparison of its properties with those of muscle alpha-actinins. *Biochemistry* **23**, 1600–1608 (1984).

## References

---

127. Landon, F., Gache, Y., Touitou, H. & Olomucki, A. Properties of two isoforms of human blood platelet alpha-actinin. *European journal of biochemistry* **153**, 231–237 (1985).
128. Sjöblom, B., Salmazo, A. & Djinović-Carugo, K. Alpha-actinin structure and regulation. *Cellular and molecular life sciences : CMLS* **65**, 2688–2701 (2008).
129. Mills, M. Differential expression of the actin-binding proteins, alpha-actinin-2 and -3, in different species. Implications for the evolution of functional redundancy. *Human Molecular Genetics* **10**, 1335–1346 (2001).
130. Edlund, M., Lotano, M. A. & Otey, C. A. Dynamics of  $\alpha$ -actinin in focal adhesions and stress fibers visualized with  $\alpha$ -actinin-green fluorescent protein. *Cell Motil. Cytoskeleton* **48**, 190–200 (2001).
131. Honda, K. *et al.* Actinin-4, a Novel Actin-bundling Protein Associated with Cell Motility and Cancer Invasion. *J Cell Biol* **140**, 1383–1393 (1998).
132. Araki, N., Hatae, T., Yamada, T. & Hirohashi, S. Actinin-4 is preferentially involved in circular ruffling and macropinocytosis in mouse macrophages: Analysis by fluorescence ratio imaging. *Journal of cell science* **113**, 3329–3340 (2000).
133. Pavalko, F. M., Schneider, G., Burridge, K. & Lim, S. S. Immunodetection of alpha-actinin in focal adhesions is limited by antibody inaccessibility. *Experimental cell research* **217**, 534–540 (1995).
134. Knudsen, K. A. Interaction of alpha-actinin with the cadherin/catenin cell-cell adhesion complex via alpha-catenin. *J Cell Biol* **130**, 67–77 (1995).
135. Otey, C. A. An interaction between alpha-actinin and the beta 1 integrin subunit in vitro. *J Cell Biol* **111**, 721–729 (1990).
136. Glück, U., Kwiatkowski, D. J. & Ben-Ze'ev, A. Suppression of tumorigenicity in simian virus 40-transformed 3T3 cells transfected with alpha-actinin cDNA. *Proceedings of the National Academy of Sciences of the United States of America* **90**, 383–387 (1993).
137. Glück, U. & Ben-Ze'ev, A. Modulation of alpha-actinin levels affects cell motility and confers tumorigenicity on 3T3 cells. *Journal of cell science* **107**, 1773–1782 (1994).
138. Yamashiro-Matsumura, S. & Matsumura, F. Purification and characterization of an F-actin-bundling 55-kilodalton protein from HeLa cells. *Journal of Biological Chemistry* **260**, 5087–5097 (1985).
139. Lieleg, O., Kayser, J., Brambilla, G., Cipelletti, L. & Bausch, A. R. Slow dynamics and internal stress relaxation in bundled cytoskeletal networks. *Nat Mater* **10**, 236–242 (2011).
140. Tseng, Y., Fedorov, E., McCaffery, J. M., Almo, S. C. & Wirtz, D. Micromechanics and ultrastructure of actin filament networks crosslinked by human fascin: A comparison with  $\alpha$ -actinin. *Journal of Molecular Biology* **310**, 351–366 (2001).
141. Elkhatab, N. *et al.* Fascin plays a role in stress fiber organization and focal adhesion disassembly. *Current Biology* **24**, 1492–1499 (2014).

## References

---

142. Kureishy, N., Sapountzi, V., Prag, S., Anilkumar, N. & Adams, J. C. Fascins, and their roles in cell structure and function. *BioEssays : news and reviews in molecular, cellular and developmental biology* **24**, 350–361 (2002).
143. Hashimoto, Y., Skacel, M. & Adams, J. C. Roles of fascin in human carcinoma motility and signaling. Prospects for a novel biomarker? *The international journal of biochemistry & cell biology* **37**, 1787–1804 (2005).
144. Arcangelis, A. de, Georges-Labouesse, E. & Adams, J. C. Expression of fascin-1, the gene encoding the actin-bundling protein fascin-1, during mouse embryogenesis. *Gene expression patterns : GEP* **4**, 637–643 (2004).
145. Wada, Y. *et al.* Mutation of human retinal fascin gene (FSCN2) causes autosomal dominant retinitis pigmentosa. *Investigative ophthalmology & visual science* **42**, 2395–2400 (2001).
146. Tubb, B. *et al.* Testis fascin (FSCN3). A novel paralog of the actin-bundling protein fascin expressed specifically in the elongate spermatid head. *Experimental cell research* **275**, 92–109 (2002).
147. Ono, S. *et al.* Identification of an Actin Binding Region and a Protein Kinase C Phosphorylation Site on Human Fascin. *Journal of Biological Chemistry* **272**, 2527–2533 (1997).
148. Anilkumar, N., Parsons, M., Monk, R., Ng, T. & Adams, J. C. Interaction of fascin and protein kinase Calpha. A novel intersection in cell adhesion and motility. *The EMBO Journal* **22**, 5390–5402 (2003).
149. Lieleg, O., Schmoller, K. M., Claessens, Mireille M. A. E. & Bausch, A. R. Cytoskeletal polymer networks: viscoelastic properties are determined by the microscopic interaction potential of cross-links. *Biophysical Journal* **96**, 4725–4732 (2009).
150. Lieleg, O., Claessens, Mireille M. A. E. & Bausch, A. R. Structure and dynamics of cross-linked actin networks. *Soft Matter* **6**, 218–225 (2010).
151. Wachsstock, D. H., Schwarz, W. H. & Pollard, T. D. Cross-linker dynamics determine the mechanical properties of actin gels. *Biophysical Journal* **66**, 801–809 (1994).
152. Gardel, M. L. *et al.* Elastic behavior of cross-linked and bundled actin networks. *Science (New York, N.Y.)* **304**, 1301–1305 (2004).
153. Borukhov, I., Bruinsma, R. F., Gelbart, W. M. & Liu, A. J. Structural polymorphism of the cytoskeleton: a model of linker-assisted filament aggregation. *Proceedings of the National Academy of Sciences of the United States of America* **102**, 3673–3678 (2005).
154. Strehle, D. *et al.* Transiently crosslinked F-actin bundles. *European biophysics journal : EBJ* **40**, 93–101 (2011).
155. Limozin, L. & Sackmann, E. Polymorphism of cross-linked actin networks in giant vesicles. *Physical review letters* **89**, 168103 (2002).

## References

---

156. Meyer, R. K. & Aebi, U. Bundling of actin filaments by alpha-actinin depends on its molecular length. *The Journal of Cell Biology* **110**, 2013–2024 (1990).
157. Ward, S. M. V., Weins, A., Pollak, M. R. & Weitz, D. A. Dynamic viscoelasticity of actin cross-linked with wild-type and disease-causing mutant alpha-actinin-4. *Biophysical Journal* **95**, 4915–4923 (2008).
158. Wagner, B., Tharmann, R., Haase, I., Fischer, M. & Bausch, A. R. Cytoskeletal polymer networks: the molecular structure of cross-linkers determines macroscopic properties. *Proceedings of the National Academy of Sciences of the United States of America* **103**, 13974–13978 (2006).
159. Asakura, T. *et al.* Isolation and characterization of a novel actin filament-binding protein from *Saccharomyces cerevisiae*. *Oncogene* **16**, 121–130 (1998).
160. Yang, H.-C. & Pon, L. A. Actin cable dynamics in budding yeast. *Proceedings of the National Academy of Sciences of the United States of America* **99**, 751–756 (2002).
161. Riedl, J. *et al.* Lifeact: a versatile marker to visualize F-actin. *Nature methods* **5**, 605–607 (2008).
162. Lynen, F. & Wieland, U. Über die Giftstoffe des Knollenblätterpilzes. IV. *Justus Liebigs Ann. Chem.* **533**, 93–117 (1937).
163. Wieland, T., Faulstich, H. & Fiume, L. Amatoxins, Phallotoxins, Phallolysin, and Antamanide. The Biologically Active Components of Poisonous Amanita Mushroom. *CRC Critical Reviews in Biochemistry* **5**, 185–260 (1978).
164. De La Cruz, E M & Pollard, T. D. Kinetics and thermodynamics of phalloidin binding to actin filaments from three divergent species. *Biochemistry* **35**, 14054–14061 (1996).
165. Lorenz, M., Popp, D. & Holmes, K. C. Refinement of the F-actin model against X-ray fiber diffraction data by the use of a directed mutation algorithm. *Journal of Molecular Biology* **234**, 826–836 (1993).
166. Estes, J. E., Selden, L. A., & Gershman, L. C. Mechanism of Action of Phalloidin on the Polymerization of Mechanism of action of phalloidin on the polymerization of muscle actin. *Biochemistry*, 708–712 (1981).
167. Blanchoin, L. & Pollard, T. D. Mechanism of Interaction of Acanthamoeba Actophorin (ADF/Cofilin) with Actin Filaments. *Journal of Biological Chemistry* **274**, 15538–15546 (1999).
168. Doolittle, L. K., Rosen, M. K. & Padrick, S. B. Measurement and analysis of in vitro actin polymerization. *Methods in molecular biology (Clifton, N.J.)* **1046**, 273–293 (2013).
169. Kouyama, T. & Mihashi, K. Fluorimetry Study of N-(1-Pyrenyl)iodoacetamide-Labelled F-Actin. *European journal of biochemistry* **114**, 33–38 (1981).

## References

---

170. Cooper, J. A., Walker, S. B. & Pollard, T. D. Pyrene actin: documentation of the validity of a sensitive assay for actin polymerization. *Journal of Muscle Research & Cell Motility* **4**, 253–262 (1983).
171. Tseng, Y. & Wirtz, D. Mechanics and Multiple-Particle Tracking Microheterogeneity of  $\alpha$ -Actinin-Cross-Linked Actin Filament Networks. *Biophysical Journal* **81**, 1643–1656 (2001).
172. Lieleg, O. *et al.* Structural polymorphism in heterogeneous cytoskeletal networks. *Soft Matter* **5**, 1796–1803 (2009).
173. Schmoller, K. M., Lieleg, O. & Bausch, A. R. Structural and viscoelastic properties of actin/filamin networks: cross-linked versus bundled networks. *Biophysical Journal* **97**, 83–89 (2009).
174. Schmoller, K. M., Lieleg, O. & Bausch, A. R. Cross-linking molecules modify composite actin networks independently. *Physical review letters* **101**, 118102 (2008).
175. Tseng, Y., An, K. M., Esue, O. & Wirtz, D. The bimodal role of filamin in controlling the architecture and mechanics of F-actin networks. *Journal of Biological Chemistry* **279**, 1819–1826 (2004).
176. Yao, N. Y. *et al.* Nonlinear viscoelasticity of actin transiently cross-linked with mutant  $\alpha$ -actinin-4. *Journal of Molecular Biology* **411**, 1062–1071 (2011).
177. Pelletier, O. *et al.* Structure of actin cross-linked with alpha-actinin: a network of bundles. *Physical review letters* **91**, 148102 (2003).
178. Schmoller, K. M., Lieleg, O. & Bausch, A. R. Internal stress in kinetically trapped actin bundle networks. *Soft Matter* **4**, 2365 (2008).
179. Lieleg, O., Claessens, M. M. A. E., Heussinger, C., Frey, E. & Bausch, A. R. Mechanics of bundled semiflexible polymer networks. *Physical review letters* **99**, 88102 (2007).
180. Purdy, K. R., Bartles, J. R. & Wong, G. C. L. Structural polymorphism of the actin-espino system: A prototypical system of filaments and linkers in stereocilia. *Physical review letters* **98**, 58105 (2007).
181. Lowey, S., Slayter, H. S., Weeds, A. G. & Baker, H. Substructure of the myosin molecule. *Journal of Molecular Biology* **42**, 1–29 (1969).
182. Tharmann, R., Claessens, M. M. A. E. & Bausch, A. R. Viscoelasticity of isotropically cross-linked actin networks. *Physical review letters* **98**, 88103 (2007).
183. Bernstein, B. W. & Bamberg, J. R. Tropomyosin binding to F-actin protects the F-actin from disassembly by brain actin-depolymerizing factor (ADF). *Cell Motility* **2**, 1–8 (1982).
184. Wegner, A. Equilibrium of the actin-tropomyosin interaction. *Journal of Molecular Biology* **131**, 839–853 (1979).
185. Luan, Y., Lieleg, O., Wagner, B. & Bausch, A. R. Micro- and macrorheological properties of isotropically cross-linked actin networks. *Biophysical Journal* **94**, 688–693 (2008).

## References

---

186. Pollard, T. D. Rate constants for the reactions of ATP- and ADP-actin with the ends of actin filaments. *The Journal of Cell Biology* **103**, 2747–2754 (1986).
187. Aratyn, Y. S., Schaus, T. E., Taylor, E. W. & Borisy, G. G. Intrinsic dynamic behavior of fascin in filopodia. *Molecular biology of the cell* **18**, 3928–3940 (2007).
188. Tsuda, Y., Yasutake, H., Ishijima, A. & Yanagida, T. Torsional rigidity of single actin filaments and actin-actin bond breaking force under torsion measured directly by in vitro micromanipulation. *Proceedings of the National Academy of Sciences of the United States of America* **93**, 12937–12942 (1996).
189. Kalluri, R. & Weinberg, R. A. The basics of epithelial-mesenchymal transition. *The Journal of clinical investigation* **119**, 1420–1428 (2009).
190. Thiery, J. P. & Sleeman, J. P. Complex networks orchestrate epithelial-mesenchymal transitions. *Nature reviews. Molecular cell biology* **7**, 131–142 (2006).
191. Yilmaz, M. & Christofori, G. EMT, the cytoskeleton, and cancer cell invasion. *Cancer metastasis reviews* **28**, 15–33 (2009).
192. Nieto, M. A. The ins and outs of the epithelial to mesenchymal transition in health and disease. *Annual review of cell and developmental biology* **27**, 347–376 (2011).
193. Katsuno, Y., Lamouille, S. & Derynck, R. TGF- $\beta$  signaling and epithelial-mesenchymal transition in cancer progression. *Current opinion in oncology* **25**, 76–84 (2013).
194. Shi, Y. & Massagué, J. Mechanisms of TGF- $\beta$  Signaling from Cell Membrane to the Nucleus. *Cell* **113**, 685–700 (2003).
195. Feng, X.-H. & Derynck, R. Specificity and versatility in tgf-beta signaling through Smads. *Annual review of cell and developmental biology* **21**, 659–693 (2005).
196. Peinado, H., Olmeda, D. & Cano, A. Snail, Zeb and bHLH factors in tumour progression. An alliance against the epithelial phenotype? *Nature reviews. Cancer* **7**, 415–428 (2007).
197. Vincent, T. *et al.* A SNAIL1-SMAD3/4 transcriptional repressor complex promotes TGF-beta mediated epithelial-mesenchymal transition. *Nature cell biology* **11**, 943–950 (2009).
198. Derynck, R. & Zhang, Y. E. Smad-dependent and Smad-independent pathways in TGF-beta family signalling. *Nature* **425**, 577–584 (2003).
199. Bishop, A. & Hall, A. Rho GTPases and their effector proteins. *Biochem. J.* **348**, 241–255 (2000).
200. Edlund, S., Landström, M., Heldin, C.-H. & Aspenström, P. Transforming growth factor-beta-induced mobilization of actin cytoskeleton requires signaling by small GTPases Cdc42 and RhoA. *Molecular biology of the cell* **13**, 902–914 (2002).
201. Olson, E. N. & Nordheim, A. Linking actin dynamics and gene transcription to drive cellular motile functions. *Nature reviews. Molecular cell biology* **11**, 353–365 (2010).

## References

---

202. Charbonney, E., Speight, P., Masszi, A., Nakano, H. & Kapus, A.  $\beta$ -catenin and Smad3 regulate the activity and stability of myocardin-related transcription factor during epithelial-myofibroblast transition. *Molecular biology of the cell* **22**, 4472–4485 (2011).
203. Jaffe, A. B. & Hall, A. Rho GTPases. Biochemistry and biology. *Annual review of cell and developmental biology* **21**, 247–269 (2005).
204. Pollard, T. D. Regulation of actin filament assembly by Arp2/3 complex and formins. *Annual Review of Biophysics and Biomolecular Structure* **36**, 451–477 (2007).
205. Posern, G. & Treisman, R. Actin' together. Serum response factor, its cofactors and the link to signal transduction. *Trends in cell biology* **16**, 588–596 (2006).
206. Vartiainen, M. K., Guettler, S., Larijani, B. & Treisman, R. Nuclear actin regulates dynamic subcellular localization and activity of the SRF cofactor MAL. *Science (New York, N.Y.)* **316**, 1749–1752 (2007).
207. Perez-Moreno, M. & Fuchs, E. Catenins. Keeping cells from getting their signals crossed. *Developmental cell* **11**, 601–612 (2006).
208. Schrott, G. *et al.* Serum response factor is crucial for actin cytoskeletal organization and focal adhesion assembly in embryonic stem cells. *J Cell Biol* **156**, 737–750 (2002).
209. Gey G.O., Coffman W.D., Kubicek M.T. Tissue culture studies of the proliferative capacity of cervical carcinoma and normal epithelium. *Cancer Research*, 264-265 (1952).
210. Cailleau, R., Young, R., Olivé, M. & Reeves, W. J. Breast Tumor Cell Lines From Pleural Effusions 2. *JNCI: Journal of the National Cancer Institute* **53**, 661–674 (1974).
211. Cailleau, R., Olivé, M. & Cruciger, Q. V. J. Long-term human breast carcinoma cell lines of metastatic origin. Preliminary characterization. *In Vitro* **14**, 911–915 (1978).
212. Soule, H. D. *et al.* Isolation and Characterization of a Spontaneously Immortalized Human Breast Epithelial Cell Line, MCF-10. *Cancer Research* **50**, 6075 (1990).
213. Ausubel, F. M. (ed) *Current protocols in molecular biology* (John Wiley & Sons, New York, 1994).
214. Hanahan, D. Studies on transformation of Escherichia coli with plasmids. *Journal of Molecular Biology* **166**, 557–580 (1983).
215. Green, R. & Rogers, E. J. Transformation of chemically competent E. coli. *Methods in enzymology* **529**, 329–336 (2013).
216. Levison, M. E., Josephson, A. S. & Kirschenbaum, D. M. Reduction of biological substances by water-soluble phosphines. Gamma-globulin (IgG). *Experientia* **25**, 126–127 (1969).
217. Han, J. C. & Han, G. Y. A procedure for quantitative determination of tris(2-carboxyethyl)phosphine, an odorless reducing agent more stable and effective than dithiothreitol. *Analytical biochemistry* **220**, 5–10 (1994).

## References

---

218. Getz, E. B., Xiao, M., Chakrabarty, T., Cooke, R. & Selvin, P. R. A comparison between the sulfhydryl reductants tris(2-carboxyethyl)phosphine and dithiothreitol for use in protein biochemistry. *Analytical biochemistry* **273**, 73–80 (1999).
219. Dmitrenko, O., Thorpe, C. & Bach, R. D. Mechanism of SN2 disulfide bond cleavage by phosphorus nucleophiles. Implications for biochemical disulfide reducing agents. *J. Org. Chem.* **72**, 8298–8307 (2007).
220. Gentry, B., Smith, D. M. & Käs, J. A. Buckling-induced zebra stripe patterns in nematic F-actin. *Physical review. E, Statistical, nonlinear, and soft matter physics* **79**, 31916 (2009).
221. Pardee, J. D. & Spudich, J. A. *Purification of Muscle Actin* vol. **24**. In *The Cytoskeleton Part A. Cytoskeletal Proteins, Isolation and Characterization*. Methods in Cell Biology 271–289 (Elsevier, 1982).
222. van Oosten, A. S. G. *et al.* Uncoupling shear and uniaxial elastic moduli of semiflexible biopolymer networks: compression-softening and stretch-stiffening. *Scientific reports* **6**, 19270 (2016).
223. Vahabi, M. *et al.* Elasticity of fibrous networks under axial prestress.
224. Tang, J. X. & Janmey, P. A. The polyelectrolyte nature of F-actin and the mechanism of actin bundle formation. *Journal of Biological Chemistry* **271**, 8556–8563 (1996).
225. Morris, C. B. Cryopreservation of animal and human cell lines. *Methods in molecular biology (Clifton, N.J.)* **368**, 227–236 (2007).
226. Fadok, V. A. *et al.* Exposure of phosphatidylserine on the surface of apoptotic lymphocytes triggers specific recognition and removal by macrophages. *The Journal of Immunology* **148**, 2207 (1992).
227. Berridge, M. V., Tan, A. S., McCoy, K. D. & Wang, R. The biochemical and cellular basis of cell proliferation assays that use tetrazolium salts. *Biochemica* **4**, 14–19 (1996).
228. Berridge, M. V., Herst, P. M. & Tan, A. S. *Tetrazolium dyes as tools in cell biology. New insights into their cellular reduction* vol. **11**. Biotechnology Annual Review 127–152 (Elsevier, 2005).
229. Ishiyama, M., Shiga, M., Sasamoto, K., Mizoguchi, M. & He, P.-g. A New Sulfonated Tetrazolium Salt That Produces a Highly Water-Soluble Formazan Dye. *Chem. Pharm. Bull.* **41**, 1118–1122 (1993).
230. Moon, A. *et al.* H-ras, but not N-ras, induces an invasive phenotype in human breast epithelial cells. A role for MMP-2 in the h-ras-induced invasive phenotype. *Int. J. Cancer* **85**, 176–181 (2000).
231. Kim, M.-S., Lee, E.-J., Kim, H.-R. C. & Moon, A. p38 kinase is a key signaling molecule for H-Ras-induced cell motility and invasive phenotype in human breast epithelial cells. *Cancer Research* **63**, 5454–5461 (2003).

## References

---

232. Leber, T. M. & Balkwill, F. R. Zymography. A single-step staining method for quantitation of proteolytic activity on substrate gels. *Analytical biochemistry* **249**, 24–28 (1997).
233. LAEMMLI, U. K. Cleavage of Structural Proteins during the Assembly of the Head of Bacteriophage T4. *Nature* **227**, 680–685 (1970).
234. Otto, O. *et al.* Real-time deformability cytometry. On-the-fly cell mechanical phenotyping. *Nature methods* **12**, 199–202, 4 p following 202 (2015).
235. Navarro-Quiroga, I. *et al.* Improved neurotensin-vector-mediated gene transfer by the coupling of hemagglutinin HA2 fusogenic peptide and Vp1 SV40 nuclear localization signal. *Molecular Brain Research* **105**, 86–97 (2002).
236. Michiue, H. *et al.* The NH2 terminus of influenza virus hemagglutinin-2 subunit peptides enhances the antitumor potency of polyarginine-mediated p53 protein transduction. *Journal of Biological Chemistry* **280**, 8285–8289 (2005).
237. Putney, S. D., Benkovic, S. J. & Schimmel, P. R. A DNA fragment with an alpha-phosphorothioate nucleotide at one end is asymmetrically blocked from digestion by exonuclease III and can be replicated in vivo. *Proceedings of the National Academy of Sciences of the United States of America* **78**, 7350–7354 (1981).
238. Janmey, P. A., Hvidt, S., Lamb, J. & Stossel, T. P. Resemblance of actin-binding protein/actin gels to covalently crosslinked networks. *Nature* **345**, 89–92 (1990).
239. Tempel, M., Isenberg, G. & Sackmann, E. Temperature-induced sol-gel transition and microgel formation in  $\alpha$ -actinin cross-linked actin networks. A rheological study. *Phys. Rev. E* **54**, 1802–1810 (1996).
240. Chelakkot, R. & Gruhn, T. Length dependence of crosslinker induced network formation of rods. A Monte Carlo study. *Soft Matter* **8**, 11746 (2012).
241. Schmoller, K. M., Semmrich, C. & Bausch, A. R. Slow down of actin depolymerization by cross-linking molecules. *Journal of structural biology* **173**, 350–357 (2011).
242. Fritzsche, M., Lewalle, A., Duke, T., Kruse, K. & Charras, G. Analysis of turnover dynamics of the submembranous actin cortex. *Molecular biology of the cell* **24**, 757–767 (2013).
243. Ridley, A. J. Life at the leading edge. *Cell* **145**, 1012–1022 (2011).
244. Mattila, P. K. & Lappalainen, P. Filopodia. Molecular architecture and cellular functions. *Nature reviews. Molecular cell biology* **9**, 446–454 (2008).
245. Cardarelli, F. *et al.* The intracellular trafficking mechanism of Lipofectamine-based transfection reagents and its implication for gene delivery. *Scientific reports* **6**, 25879 (2016).
246. Kapuscinski, J. DAPI: A DNA-Specific Fluorescent Probe. *Biotechnic & Histochemistry* **70**, 220–233 (1995).
247. Drygin, D., Barone, S. & Bennett, C. F. Sequence-dependent cytotoxicity of second-generation oligonucleotides. *Nucleic Acids Research* **32**, 6585–6594 (2004).

## References

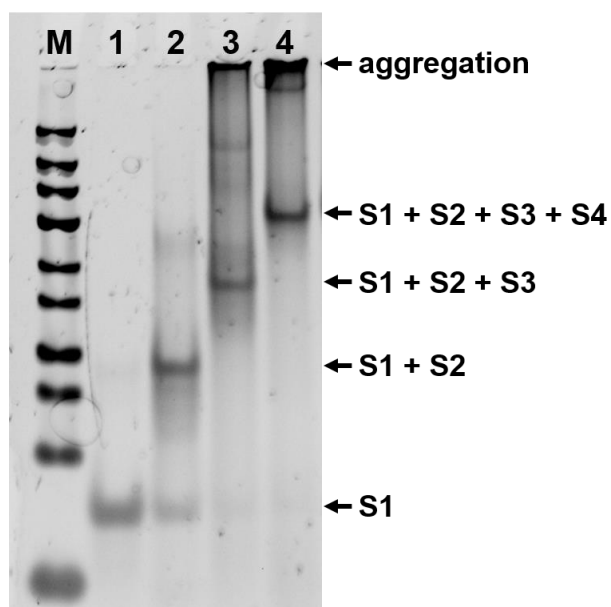
---

248. Boyden, S. The chemotactic effect of mixtures of antibody and antigen on polymorphonuclear leucocytes. *Journal of Experimental Medicine* **115**, 453–466 (1962).
249. dos Remedios, C. G. *et al.* Actin binding proteins. Regulation of cytoskeletal microfilaments. *Physiological reviews* **83**, 433–473 (2003).
250. Nathu, Z. *et al.* Temporal changes in MMP mRNA expression in the lens epithelium during anterior subcapsular cataract formation. *Experimental eye research* **88**, 323–330 (2009).
251. Kim, E.-S., Kim, M.-S. & Moon, A. TGF- $\beta$ -induced upregulation of MMP-2 and MMP-9 depends on p38 MAPK, but not ERK signaling in MCF10A human breast epithelial cells. *Int J Oncol* (2004).
252. Verma, R. P. & Hansch, C. Matrix metalloproteinases (MMPs). Chemical-biological functions and (Q)SARs. *Bioorganic & medicinal chemistry* **15**, 2223–2268 (2007).
253. Himelstein, B. P., Canete-Soler, R., Bernhard, E. J., Dilks, D. W. & Muschel, R. J. Metalloproteinases in tumor progression. The contribution of MMP-9. *Invasion & metastasis* **14**, 246–258 (1994).
254. Medici, D., Hay, E. D. & Olsen, B. R. Snail and Slug promote epithelial-mesenchymal transition through beta-catenin-T-cell factor-4-dependent expression of transforming growth factor-beta3. *Molecular biology of the cell* **19**, 4875–4887 (2008).
255. Guck, J. *et al.* Optical deformability as an inherent cell marker for testing malignant transformation and metastatic competence. *Biophysical Journal* **88**, 3689–3698 (2005).
256. Park, S. & Lee, Y. J. AFM-based dual nano-mechanical phenotypes for cancer metastasis. *Journal of biological physics* **40**, 413–419 (2014).
257. Jackson, W. M., Jaasma, M. J., Baik, A. D. & Keaveny, T. M. Over-expression of alpha-actinin with a GFP fusion protein is sufficient to increase whole-cell stiffness in human osteoblasts. *Annals of biomedical engineering* **36**, 1605–1614 (2008).



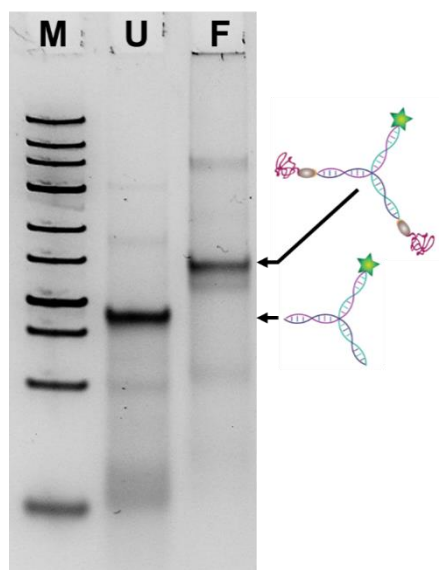
## 8 Supplemental information

### I Step-wise assembly of DNA tetrahedra

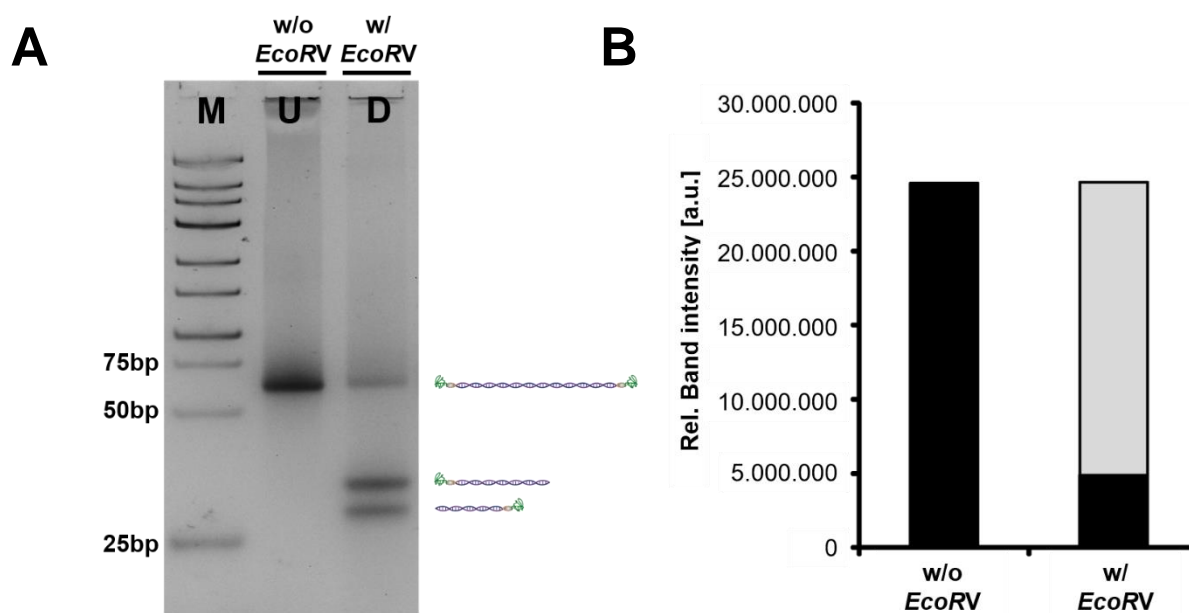


**Figure S 1 | Step-wise assembly of DNA tetrahedra.** Step-wise formation of DNA tetrahedra was monitored via 6 % (v/v) native polyacrylamide gel electrophoresis (PAGE) and visualized by SYBR® Gold Nucleic Acid Gel Stain staining. **M**, GeneRuler™ Low Range DNA Ladder; **1**, TetS1; **2**, TetS1 + TetS2; **3**, TetS1 + TetS2 + TetS3; **4**, full DNA tetrahedron. Aggregations are indicated at the top of the gel. DNA sequences are to be found in Table 4. The assembly conditions are described in 4.23.1.

## II Assembly of PTO-capped, CPP-functionalized DNA trimers



**Figure S 2 | CPP-conjugation to PTO-capped DNA trimers.** PTO-capped DNA trimers labeled with a Cy3 dye were covalently coupled to two CPP (azide - sC18) utilizing a copper free click chemistry approach (2.2.4). The conjugation procedure was observed via 6 % (v/v) native PAGE and visualized by SYBR<sup>®</sup> Gold Nucleic Acid Gel Strain staining. **M**, GeneRuler™ Low Range DNA Ladder; **U**, unmodified PTO-capped Cy3-labeled DNA trimer; **F**, PTO-capped Cy3-labeled DNA trimer carrying two CPP. These samples were applied to cells later on (Figure 33).

III *EcoRV*-HF<sup>®</sup> digestion of sPX

**Figure S 3 | Cleavage of sPX by *EcoRV*-HF<sup>®</sup>.** (A) Digestion of sPX through *EcoRV*-HF<sup>®</sup> was analyzed via 10 % (v/v) native PAGE and visualized by SYBR<sup>®</sup> Gold Nucleic Acid Gel Stain staining. **M**, GeneRuler<sup>™</sup> Low Range DNA Ladder; **U**, sPX w/o *EcoRV*-HF<sup>®</sup> incubation; **D**, sPX incubated for 1 h at 37 °C with *EcoRV*-HF<sup>®</sup> according to manufacturers' manual. (B) Band intensities were analyzed using ImageJ.

## IV Elasticity burst occurring with the natural occurring actin crosslinker fascin

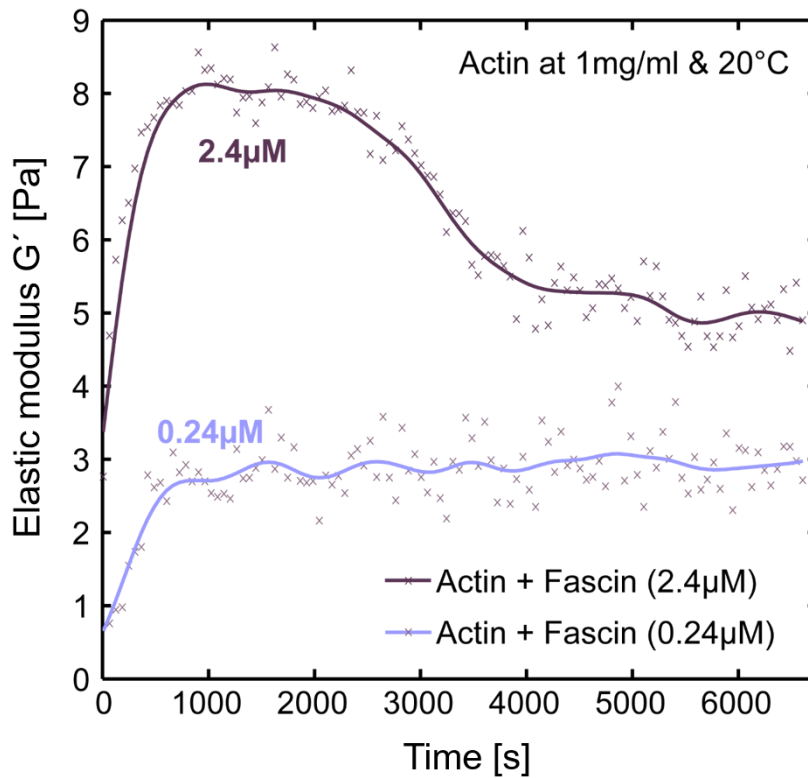


**Figure S 4 | Evolution of the elasticity during actin polymerization in presence of fascin over time.** Actin polymerization in presence of fascin was investigated via dynamic shear rheology. The elastic modulus  $G'$  of actin enriched with different concentrations of the natural occurring actin crosslinker fascin ( $R = 0.1, 0.01$ ) was measured over time as explained in 4.32.

V Structural morphologies induced by different sPX concentrations

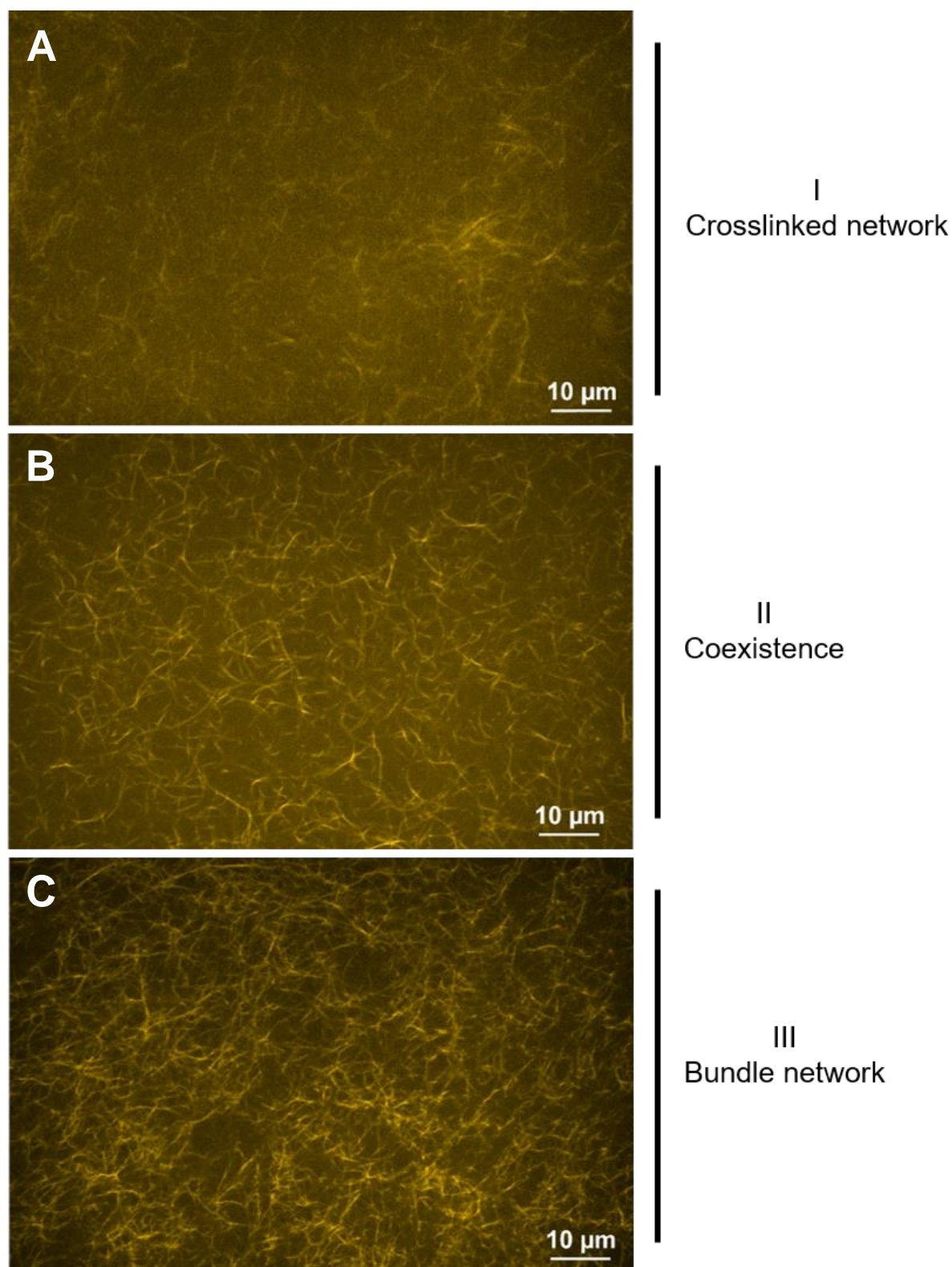


**Figure S 5 | Structural phases of actin networks polymerized in presence of sPX.** Actin was polymerized at 3  $\mu\text{M}$  in presence of wLX at (A)  $R = 0.01$ , (B)  $R = 0.1$  and (C)  $R = 1$ , respectively. Actin was mixed with TRITC-Phalloidin at a molar ratio of 3 : 1 for visualization with spinning disc confocal microscopy. The detailed experimental setup is explained in 4.34.

## VI Cloning of pTagGFP-N

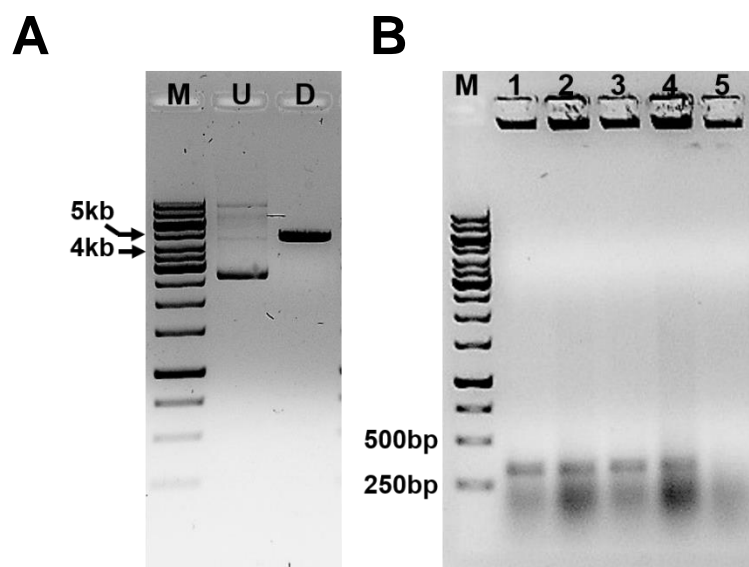


**Figure S 6 | Cloning of pTag-LifeAct-GFP-N.** (A) The linearization of pTagGFP-N through restriction digest with *Bam*HI and *Eco*RI was analyzed by 1 % (w/v) agarose gel electrophoresis (4.15.1). **M**, GeneRuler™ 1 kb DNA Ladder; **U**, undigested pTagGFP-N; **D**, pTagGFP-N digested with *Bam*HI and *Eco*RI. (B) Colony PCR of five selected clones. The resulting PCR product was expected to be 325 bp. **M**, GeneRuler™ 1 kb DNA Ladder; **1 - 5**, PCR fragment resulting from colony PCR of clones 1 - 5.

## VII DNA sequence of pTag-LifeAct-GFP-N

TAGTTATTAATAGTAATCAATTACGGGGTCATTAGTTCATAGCCCATATATGGAGTTCGCGTTACATA  
ACTTACGGTAAATGGCCCGCTGGCTGACCGCCCAACGACCCCGCCATTGACGTCAATAATGACGTATGT  
TCCCATAGTAACGCCAATAGGGACTTTCCATTGACGTCAATGGGTGGAGTATTTACGGTAAACTGCCCACTTG  
GCAGTACATCAAGTGTATCATATGCCAAGTACGCCCCCTATTGACGTCAATGACGGTAAATGGCCCGCTGG  
CATTATGCCCAGTACATGACCTTATGGGACTTTCTACTTTGGCAGTACATCTACGTATTAGTGCACCTATTAC  
CATGGTGTGCGGTTTTGGCAGTACATCAATGGGCGTGGATAGCGGTTTGACTCACGGGGATTTCCAAGTCT  
CCACCCATTGACGTCAATGGGAGTTTGTGGTGGCACCAAAATCAACGGGACTTTCCAAAATGTCGTAACAAC  
TCCGCCCCATTGACGCAATGGGCGGTAGGCGTGTACGGTGGGAGGTCTATATAAGCAGAGCTGGTTTGTAGT  
GAACCGTCAGATCCGCTAGCGCTACCGGACTCAGATCTCGAGCTCAAGCTTCGAATTCATGGCGCTGGCCG  
ACCTGATCAAGAAGTTCGAGAGCATCAGCAAGGAGGAGGATCCACCGGTCGCCACCATGAGCGGGGGCGA  
GGAGCTGTTGCGCGGCATCGTGGCCGTGCTGATCGAGCTGGACGGCGACGTGCACGGCCACAAGTTTCAAG  
GTGCGCGCGGAGGCGAGGGCGACGCGGACTACGGCAAGCTGGAGATCAAGTTTCACTGCACCCACCGCA  
AGCTGCCCGTGGCTGGCCACCCTGGTGACCACTTCTGCTACGGCATCCAGTGTTCGCCCCCTACCCC  
GAGCACATGAAGATGAACGACTTCTTCAAGAGCGCCATGCCCGAGGGCTACATCCAGGAGCGCACCATCTT  
CTTCCAGGACGACGGCAAGTACAAGACCCGCGGCGAGGTGAAGTTCGAGGGCGACACCCTGGTGAACCGC  
ATCGAGCTGAAGGGCAAGGACTTCAAGGAGGACGGCAACATCTGGGCCACAAGCTGGAGTACAGCTTCAA  
CAGCCACAACGTGTACATCATGCCCGACAAGGCCAACACGGCCTGGAGGTGAAGTTCAGACCCGCCACA  
ACATCGAGGGCGGCGCGTGCAGCTGGCCGACCACTACCAGACCAACGTGCCCTGGGCGACGGCCCGG  
TGCTGATCCCCATCAACCACTACCTGAGCACTCAGACCGCCATCAGCAAGGACCGCAAGCGCCCGGAC  
CACATGGTCTCCTGGAGTCTTTCAGCGCTGCTGCCACACCCACGGCATGGACGAGTAAAG  
CGGCCGCGACTCTAGATCATAATCAGCCATACCACATTTGTAGAGGTTTTACTTGTCTTAAAAAACCTCCCAC  
ACCTCCCCCTGAACCTGAAACATAAAATGAATGCAATTGTTGTTGTTAACTTGTATTGCAGCTTATAATGGT  
TACAAATAAAGCAATAGCATCACAAATTTACAAATAAAGCATTTTTTTCACTGCATTCTAGTTGTGGTTTTGTCC  
AAACTCATCAATGTATCTTAAGGCGTAAATTTGTAAGCGTTAATATTTTGTAAAAATTCGCGTAAATTTTTGTTA  
AATCAGTCAATTTTTTAAACCAATAGGCCGAAATCGGCAAAATCCCTTATAAATCAAAGAATAGACCGAGATA  
GGTTGAGTGTGTTCCAGTTTGGAAACAAGATCCAATTAAGAACGTGGACTCCAAGTCAAAGGGCGA  
AAAACCGTCTACAGGCGATGGCCCACTACGTGAACCACTACCCCTAATCAAGTTTTTGGGGTGCAGGTGC  
CGTAAAGCACTAAATCGGAACCCTAAAGGGAGCCCCGATTTAGAGCTTGACGGGGAAAGCCGGCGAACGT  
GGCGAGAAAGGAAGGGAAGAAAGCGAAAGGAGCGGGCGCTAGGGCGCTGGCAAGTGTAGCGGTACGCT  
GCGCGTAACCACCACACCCCGCCGCTTAATGCGCCGCTACAGGGCGCGTCAGGTGGCACTTTTCGGGGA  
AATGTGCGCGGAACCCCTATTTGTTATTTTCTAAATACATTCAAATATGTATCCGCTCATGAGACAATAACC  
CTGATAAATGCTTCAATAATATTGAAAAAGGAAGATCCTGAGGCGGAAAGAACCAGCTGTGGAATGTGTGT  
CAGTTAGGGTGTGGAAGTCCCCAGGCTCCCCAGCAGGCGAGAAGTATGCAAAGCATGCATCTCAATTAGTCA  
GCAACCATAGTGGAAAGTCCCCAGGCTCCCCAGGACGGCAGAAGTATGCAAAGCATGCATCTCAATTAGTCA  
AGCAACCATAGTCCCGCCCCTAACTCCGCCCATCCCGCCCCTAACTCCGCCAGTTCCGCCCATTTCCCGC  
CCCATGGCTGACTAATTTTTTTTTATTTATGCAGAGGCGGAGGCCGCTCGGCCTCTGAGCTATTCCAGAAGTA  
GTGAGGAGGCTTTTTTGGAGGCCTAGGCTTTTCAAAGATCGATCAAGAGACAGGATGAGGATCGTTTCGCA  
TGATTGAACAAGATGATTGCACGCAGTTCTCCGGCCGCTTGGGTGGAGAGGCTATTCGGCTATGACTGG  
GCACAACAGACAATCGGCTGCTCTGATGCCGCCGTGTTCCGGCTGTCAGCGCAGGGGCGCCCGGTTCTTTT  
TGTCAGAGAGCTTCCGGTCCGCTGACCTGAATGAACTGCAAGACGAGGCGAGCGGCTATCGTGTGGCCA  
CGAGGGCGTTCTTCCGAGCTGTGCTCGACGTTGCTACTGAAGCGGGAAGGGACTGCTGCTATTGGG  
CGAAGTCCCGGGGCGAGATCTCCTGTCTACCTTGTCTCCTGCCGAGAAAGTATCCATGCTGCTGATGC  
AATGCGGCGGCTGCATACGCTTGATCCGGCTACCTGCCATTGACCACCAAGCGAAACATCGCATCGAGC  
GAGCACGTACTCGGATGGAAGCCGGTCTTGTGATCAGGATGATCTGGACGAAGAGCATCAGGGGCTCGCG  
CCAGCCGAAGTGTTCGCCAGGCTCAAGGCGAGCATGCCCGACGGCGAGGATCTCGTCTGACCCATGGCG  
ATGCCTGCTTGCCTGAATATCATGGTGGAAAATGGCCGCTTTTCTGGATTATCGACTGTGGCCGGCTGGGTG  
TGGCGGACCGCTATCAGGACATAGCGTTGGCTACCGGTGATATTGCTGAAGAGCTTGGCGCGAATGGGCT  
GACCGCTTCTCGTCTTTACGGTATCGCCGCTCCCGATTCCGACGCGCATCGCCTTCTATCGCCTTCTTGAC  
GAGTTCTTAAAGCGGGACTCTGGGTTTCGAAATGACCCAAAGCAGCAGCCCAACCTGCCATCACGAGAT  
TTCGATTCCACCGCCGCTTCTATGAAAGTTGGGCTTCGGAATCGTTTTCCGGGACGCCGGCTGGATGATC  
CTCCAGCGCGGGGATCTCATGCTGGAGTTCTTCGCCACCCTAGGGGGAGGCTAACTGAAACACGGAAGGA  
GACAATACCGGAAGGAACCCGCGCTATGACGGCAATAAAAAGACAGAATAAAACGCACGGTGTGGGTCGT  
TTGTTTATAAACCGGGGTTCCGTTCCAGGGCTGGCACTCTGTGATACCCACCGAGACCCATTGGGGC  
CAATACGCCCGGCTTTCTTCTTTTCCCAACCCACCCCAAGTTCCGGTGAAGGCCAGGGCTCGCAGC  
CAACGTCGGGGCGGACGGCCCTGCCATAGCTCAGTTACTCATATATACTTTAGATTTTAAAACTTCAT  
TTTTAATTTAAAGGCTAGGTGAAGATCTTTTTGATAATCTCATGACCAAAATCCCTTAACTGAGTTTTT  
GTTCCACTGAGCGTCAGACCCGTAGAAAAGATCAAAGGATCTTCTTGGAGATCTTTTTTTCTGCGGTAATC  
TGCTGCTTCAAACAAAAAACCCGCTACCAGCGGTGGTTTGTGGCGGATCAAGAGCTACCAACTCTT  
TTTCCGAAGGTAAGTGGCTTACGAGAGCGCAGATACCAAAATACTGTCTTCTAGTGTAGCCGTAGTTAGGC  
CACCATTCAAGAACTCTGTAGCACCGCTACATACCTCGCTCTGTAATCTGTTACCAAGTGGCTGCTGCC  
AGTGGCGATAAGTCGTGCTTACCGGGTTGACTCAAGACGATAGTTACCGGATAAGGGCGACGGTCCGG  
CTGAACGGGGGTTCTGTCACACAGCCAGCTGGAGCGAAGACCTACACCGAAGTGAATCACTACCTACAGC  
GTGAGCTATGAAAGCGCCACGCTTCCCGAAGGAGAAAGCGGACAGGATCCGGTAAAGCGGAGGTT  
CGGAACAGGAGAGCGCACGAGGGAGCTTCCAGGGGAAACGCCTGGTATCTTTATAGTCTGTGCGGTTTT  
GCCACTCTGACTTGAGCGTCGATTTTTGTGATGCTCGTACGGGGGCGGAGCCTATGGAAAACGCCAGC

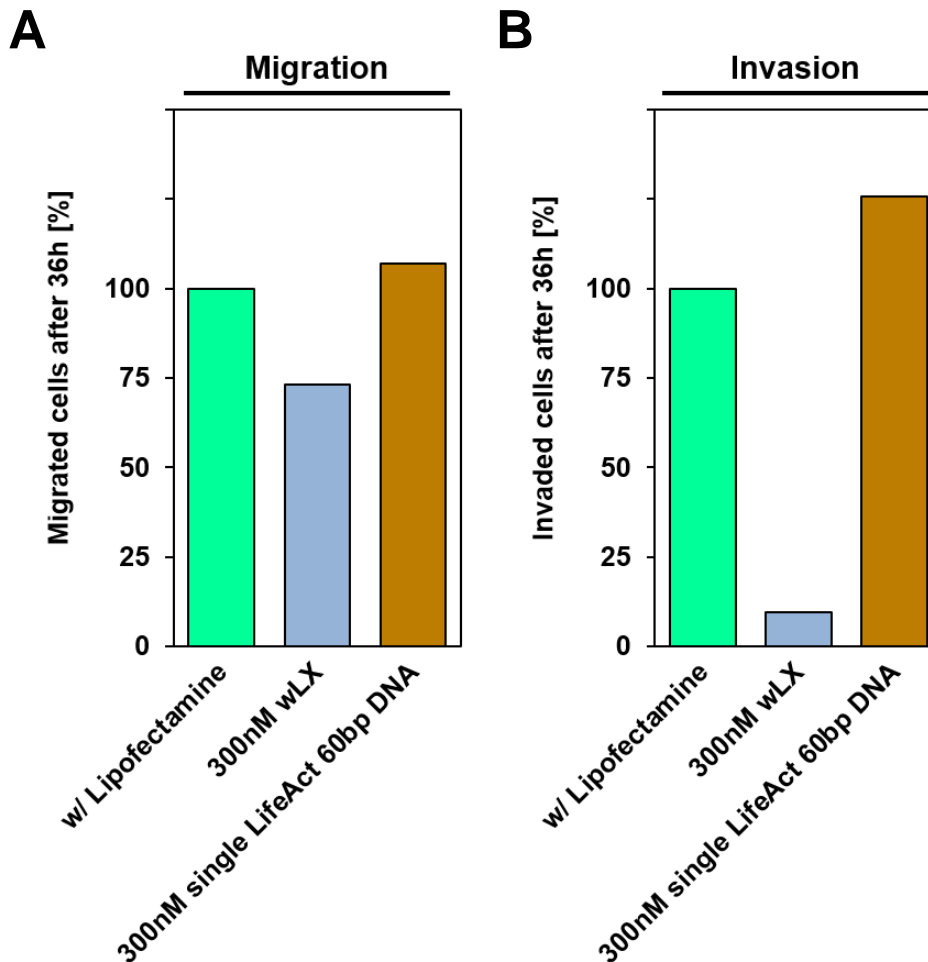
## Supplemental information

---

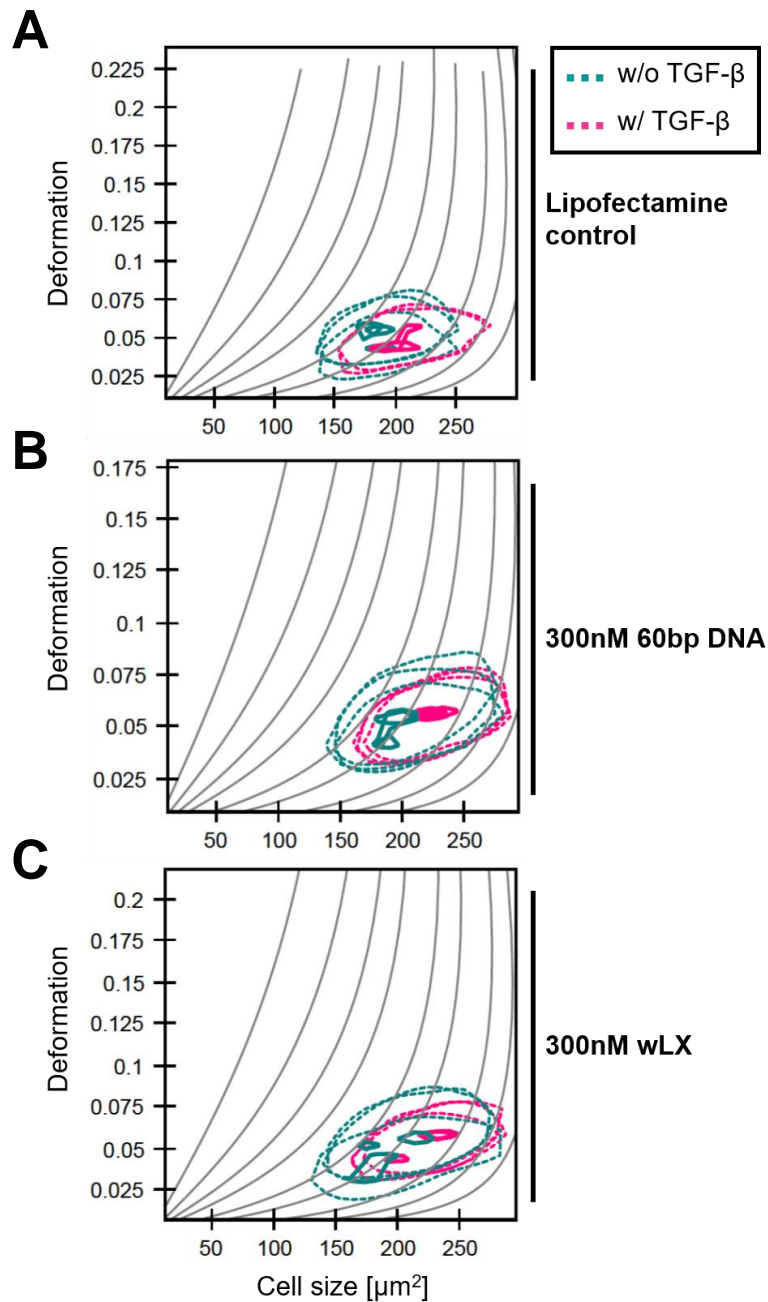
AACGCGGCCTTTTTACGGTTCCTGGCCTTTTGCTGGCCTTTTGCTCACATGTTCTTTCCTGCGTTATCCCCTG  
ATTCTGTGGATAACCGTATTACGCCATGCAT

**Figure S 7 | DNA sequence of pTag-LifeAct-GFP-N.** DNA sequence encoding LifeAct<sup>®</sup> (purple) was inserted into MCS of pTag-GFP-N via *EcoRI* (yellow) and *BamHI* (turquoise) overhangs. Sequence encoding GFP is shown in grey. Colony-PCR was conducted in order to identify positive clones. Corresponding sequences, where forward and reverse colony PCR primers bound, are underlined.

## VIII 3D migration and invasion of wLX-treated MDA-MB-231 cells after 36 h



**Figure S 8 | 3D migration and invasion of wLX-treated MDA-MB-231 cells after 36 h.** (A) MDA-MB-231 cells were transfected with 300 nM wLX, 300 nM single LifeAct® 60bp DNA and Lipofectamine only for 4 h. Cells were detached and seeded into (A) uncoated culture wells to investigate 3D migration and (B) 1X BME-coated culture wells to analyze 3D invasion. Cells were incubated for 36 h and migrated and invaded cells subsequently stained via Calcein AM fluorescent dye. Under consideration of a Calcein AM standard curve as well as the seeded cell count, the number of cells was calculated from measured fluorescence intensities. The detailed experimental setup is to be found in 4.40.4. The percentage of migrated and invaded cells that were treated with Lipofectamine only was set to 100 %. All other samples were normalized to this control, respectively.

IX Contour plots of RT-DC measurements for MCF-10A treated w/ or w/o TGF- $\beta$ 

**Figure S 9 | Real-time deformability cytometry (RT-DC) of MCF-10A treated w/ or w/o TGF- $\beta$ .** MCF-10A cells stimulated for 48 h with or without 10 ng/ml TGF- $\beta$  after transfection for 6 h with Lipofectamine only, 300 nM wLX or 300 nM 60bp DNA were analyzed via RT-DC<sup>234</sup> at a flow-rate of 0.12  $\mu\text{l/s}$ . Contours of MCF-10A cells transfected with (A) Lipofectamine only, (B) 300 nM 60bp DNA and (C) 300 nM wLX are shown as dotted lines, i.e. cells treated w/ TGF- $\beta$  in green and w/o TGF- $\beta$  in magenta. The detailed experimental setup is to be found in 4.40.5 and 4.40.6.

X Toxicity of Lipofectamine™ 3000

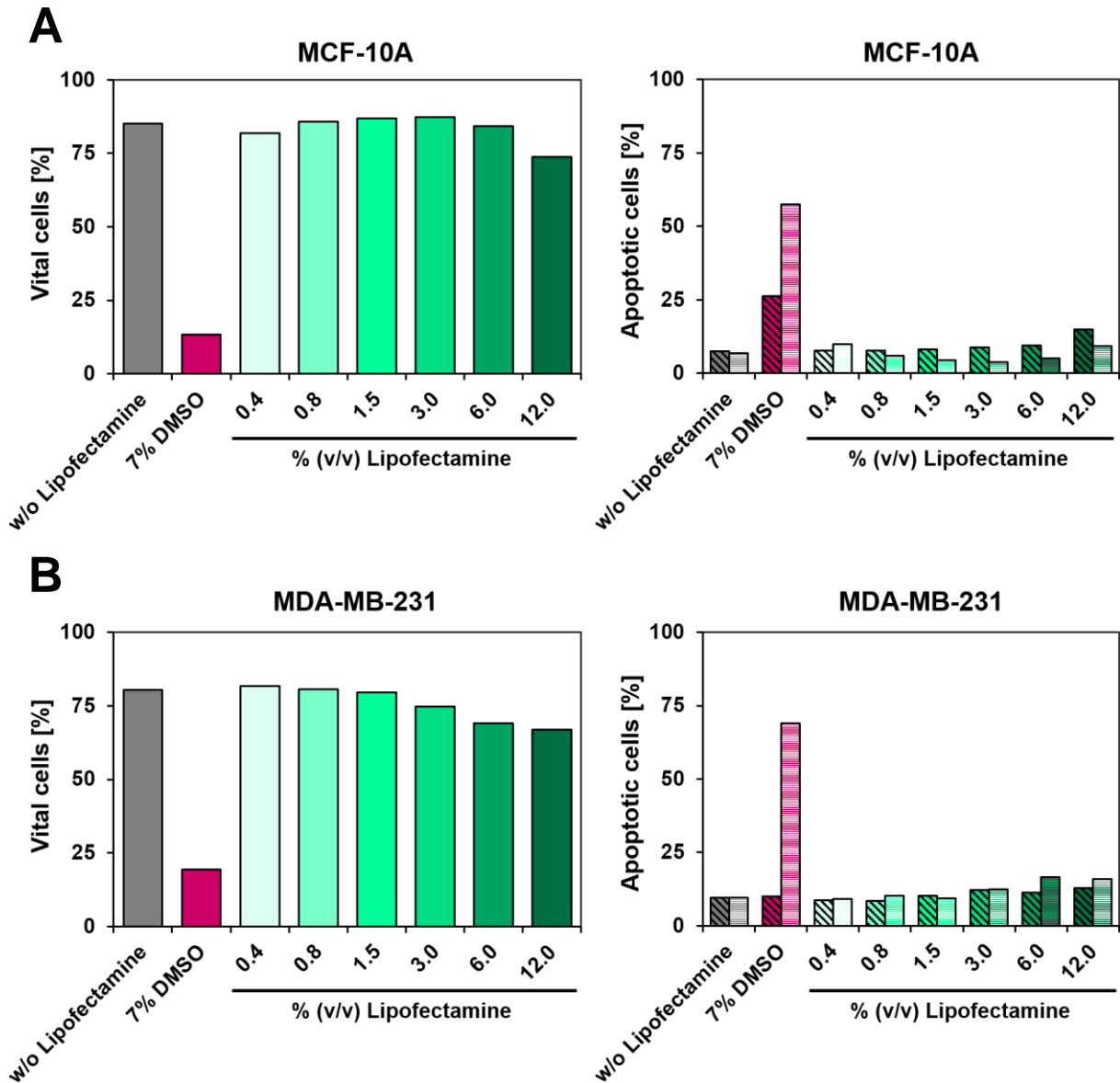


**Figure S 10 | Cytotoxic effect of Lipofectamine™ 3000 in MCF-10A and MDA-MB-231 cells.** MCF-10A as well as MDA-MB-231 cells were incubated for 2 h w/o and w/ different concentrations of Lipofectamine™ 3000. The toxicity of Lipofectamine was determined via apoptosis assay, as described in 4.40.1, 24 h post treatment. Cells incubated with 7 % (v/v) DMSO served as positive control. The experimental setup is explained in 4.37.7.2.

## XI Internalization of DNA at different Lipofectamine™ 3000 concentrations

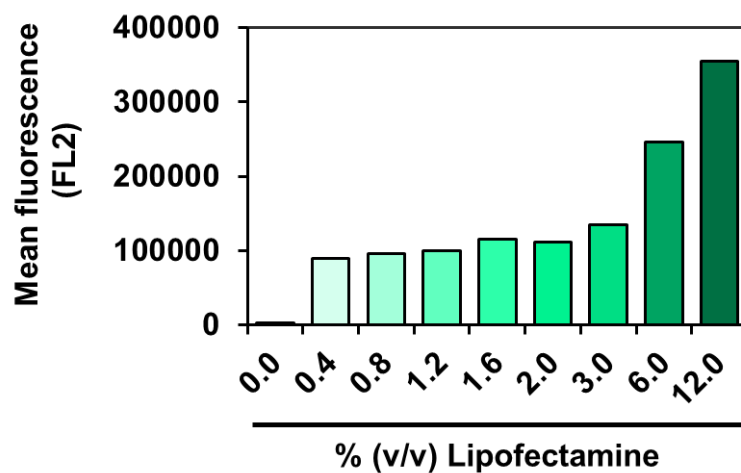


**Figure S 11** | Internalization of DNA at different Lipofectamine™ 3000 concentrations. MDA-MB-231 cells were incubated for 2 h with Cy3-labeled 60nt DNA complexed w/o and w/ different concentrations of Lipofectamine™ 3000. The mean fluorescence intensity of cell populations was determined via flow cytometry (iQue Screener). The experimental setup is described in 4.37.7.1.

## XII DNA internalization efficacies

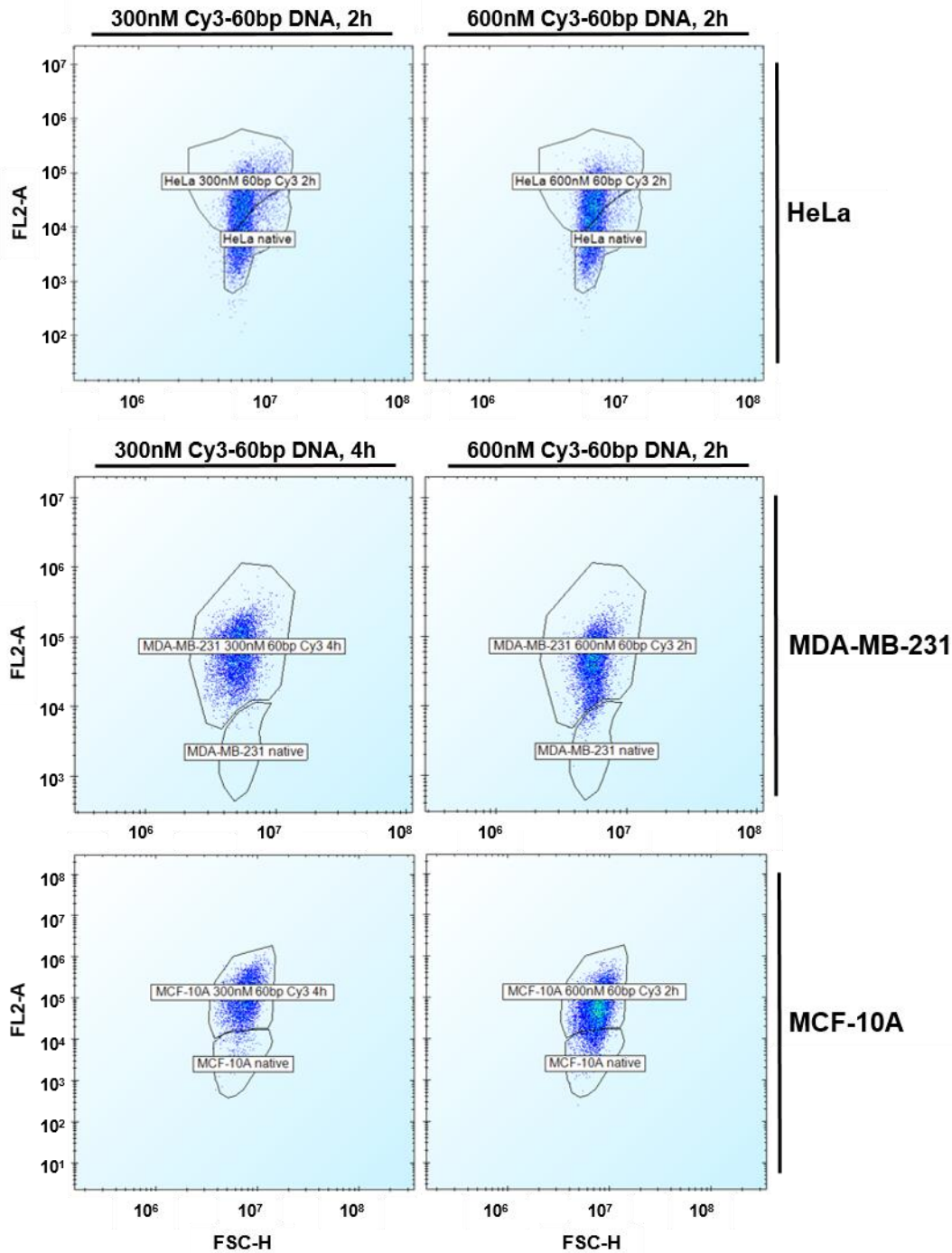


**Figure S 12 | Internalization efficacies of Cy3-labeled 60bp DNA in different cell lines. (A)** HeLa, **(B)** MDA-MB-231 and **(C)** MCF-10A cells were incubated for 2 h to 4 h with 300 nM and 600 nM Cy3-labeled 60nt DNA complexed with 0.75 % (v/v) Lipofectamine™ 3000. Cells treated with only Lipofectamine served as control. Cells were analyzed via flow cytometry and internalization efficacies were calculated by the relative number of positively classified cells compared to negative control populations. Internalization efficacies are listed in Table S 1.

**XIII DNA internalization efficacies (statistical analysis)**

**Table S 1 | Internalization efficacies of Cy3-labeled 60bp DNA in different cell lines**

Concentration of Cy3-60bp DNA	Transfection time	Cell lines		
		HeLa	MDA-MB-231	MCF-10A
300 nM	2 h	59.32 %		
300 nM	4 h		99.46 %	95.21 %
600 nM	2 h	59.54 %	96.68 %	87.34 %

## 9 Publications

Jessica S. Lorenz\*, Jörg Schnauß\*, Martin Glaser, Martin Sajfutdinow, Carsten Schuldt, Josef A. Käs and David M. Smith (2017): Synthetic transient crosslinks program the mechanics of soft, biopolymer based materials, *Advanced Materials*, in press

Doi: 10.1002/adma.201706092

Jörg Schnauß\*, Martin Glaser\*, Jessica S. Lorenz, Carsten Schuldt, Christin Möser, Martin Sajfutdinow, Tina Händler, Josef A. Käs and David M. Smith (2017): DNA Nanotubes As a Versatile Tool to Study Semiflexible Polymers. *Journal of Visualized Experiments*.

Doi: 10.3791/56056

Carsten Schuldt, Jörg Schnauß, Tina Händler, Martin Glaser, Jessica Lorenz, Tom Golde, Joseph A. Käs and David M. Smith (2016): Tuning Synthetic Semiflexible Networks by Bending Stiffness. *Physical review letters* 117, 197801.

Doi: 10.1103/PhysRevLett.117.197801



### 10 Danksagung

An erster Stelle möchte ich mich bei meiner Doktormutter Ines Neundorf für ihre Bereitschaft, mich als externe Doktorandin zu betreuen, bedanken. Ich danke ihr für ihr stets offenes Ohr, ihre Hilfsbereitschaft sowie ihre stetige Unterstützung in allen Fragen und Belangen.

Ich möchte mich ebenso recht herzlich bei Karsten Niefind für seine Bereitschaft, als Zweitgutachter einzutreten, bedanken.

Einen ganz besonderen Dank möchte ich meinem externen Betreuer David Smith aussprechen. Ich danke ihm für sein Vertrauen in meine Arbeit, sein Verständnis in allen Lebenslagen, und sein Engagement, das wesentlich zum Gelingen dieser Arbeit beigetragen hat. Danke, dass du unsere junge Arbeitsgruppe zur Family Smith machst.

Ein großes Dankeschön geht auch an Jörg Schnauß, der mir immer mit Rat und Tat zur Seite stand, mich stets unterstützt und mich immer wieder motiviert hat.

Aftab Taiyab und Tobias Zech danke ich für die Durchführung ergänzender Experimente meiner Arbeit, die Kooperation sowie die vielen hilfreichen fachlichen Gespräche.

Ebenso möchte ich mich bei Maik Herbig und der Firma Zellmechanik Dresden GmbH für die Unterstützung bei diversen Zellmessungen sowie deren Hilfe bei der Auswertung der Daten bedanken, insbesondere bei Christoph Herold, Daniel Klaue und Oliver Otto.

Ein Dankeschön geht auch an Steve Pawlizak und Steffen Grosser, die mir stets gern bei der Durchführung meiner 2D Migrationsexperimente weitergeholfen haben.

Ich bedanke mich des Weiteren von ganzem Herzen bei Christin Möser und Martin Glaser, die mir immer mit einer helfenden Hand zur Seite standen und mich immer unterstützt haben. Außerdem möchte ich an dieser Stelle Christoph Schneider danken, der maßgeblich dazu beigetragen hat, dass ich heute der Mensch bin der ich bin.

Außerdem danke ich Martin Sajfutdinow, Alexander Spaeth, Hans Kubitschke, Carsten Schuldt, sowie der gesamten AG DNA Nanosysteme für ihre stetige Unterstützung im Arbeitsalltag, die tolle Arbeitsatmosphäre und die vielen unvergesslichen privaten Aktivitäten in Leipzig. Auch wegen euch, bin ich jeden Tag gern im Labor.

Besonders möchte ich Pierre Tangermann, Cornelia Gruhle und Annegret Shaw danken, die mich seit Beginn im Fraunhofer IZI begleitet haben. Ich danke ihnen für ihre unermüdliche Ausdauer, für mich da zu sein, ihren Zuspruch und ihre Schultern, an die ich mich immer anlehnen konnte.

Ich danke vor allem meinen Freunden Dörthe Marie Wolter, Martina Conrad, Kristina Helbig, Daniela Raboldt, Eva Nossa, Elisabeth Wenzel sowie Friederike Eßbach für ihren

## **Danksagung**

---

unermüdlichen Glauben an mich, die zahlreichen schönen Abende und die Ablenkung, die ich ab und zu brauchte.

Ein ganz besonderes Dankeschön möchte ich auch meiner lieben Familie aussprechen, die mich, seit ich denken kann, auf meinem Weg unterstützt hat und immer für mich da ist.

Zu guter Letzt danke ich von ganzem Herzen meinem Freund Carsten Freitag für die unendliche Geduld, die er für mich aufbringt, seine aufheiternden Worte, seinen Rückhalt in allen Situationen und die Liebe, die er mir täglich schenkt.

## 11 Eidesstattliche Erklärung

Ich versichere, dass ich die von mir vorgelegte Dissertation selbständig angefertigt, die benutzten Quellen und Hilfsmittel vollständig angegeben und die Stellen der Arbeit – einschließlich Tabellen, Karten und Abbildungen –, die anderen Werken im Wortlaut oder dem Sinn nach entnommen sind, in jedem Einzelfall als Entlehnung kenntlich gemacht habe; dass diese Dissertation noch keiner anderen Fakultät oder Universität zur Prüfung vorgelegen hat; dass sie – abgesehen von unten angegebenen Teilpublikationen – noch nicht veröffentlicht worden ist, sowie, dass ich eine solche Veröffentlichung vor Abschluss des Promotionsverfahrens nicht vornehmen werde.

Die Bestimmungen der Promotionsordnung sind mir bekannt. Die von mir vorgelegte Dissertation ist von Frau Prof. Dr. Ines Neundorf betreut worden.

Nachfolgend genannte Teilpublikationen liegen vor:

Jessica S. Lorenz\*, Jörg Schnauß\*, Martin Glaser, Martin Sajfutdinow, Carsten Schuldt, Josef A. Käs and David M. Smith (2017): Synthetic transient crosslinks program the mechanics of soft, biopolymer based materials, *Advanced Materials*, in press  
Doi: 10.1002/adma.201706092

Jörg Schnauß\*, Martin Glaser\*, Jessica S. Lorenz, Carsten Schuldt, Christin Möser, Martin Sajfutdinow, Tina Händler, Josef A. Käs and David M. Smith (2017): DNA Nanotubes As a Versatile Tool to Study Semiflexible Polymers. *Journal of Visualized Experiments*.  
Doi: 10.3791/56056

Carsten Schuldt, Jörg Schnauß, Tina Händler, Martin Glaser, Jessica Lorenz, Tom Golde, Joseph A. Käs and David M. Smith (2016): Tuning Synthetic Semiflexible Networks by Bending Stiffness. *Physical review letters* 117, 197801.  
Doi: 10.1103/PhysRevLett.117.197801

---

Ort, Datum

---

Jessica Sophie Lorenz



## 12 Curriculum vitae

### Persönliche Angaben

Name	Jessica Sophie Lorenz
Geburtsdatum	20. Februar 1989
Geburtsort	Karl-Marx-Stadt (jetzt Chemnitz)
Nationalität	Deutsch

### Akademische Ausbildung

Seit 06/2013	Promotion am Fraunhofer Institut für Zelltherapie und Immunologie (IZI) in Leipzig in der von Herrn Dr. David Michael Smith geleiteten Arbeitsgruppe DNA-Nanosysteme, und universitäre Betreuung durch Frau Prof. Dr. Ines Neundorf am Institut für Biochemie der Universität zu Köln
10/2010 - 11/2012	Studium der Biochemie an der Martin-Luther-Universität Halle-Wittenberg <u>Abschluss:</u> Master of Science
10/2007 - 07/2010	Studium der Biochemie an der Martin-Luther-Universität Halle-Wittenberg <u>Abschluss:</u> Bachelor of Science

### Schulbildung

08/1999 - 07/2007	Matthes-Enderlein-Gymnasium Zwönitz <u>Abschluss:</u> Allgemeine Hochschulreife
08/1995 - 08/1999	Grundschule Hormersdorf

